

TIRE-PAVEMENT INTERACTION, EXPERIMENTAL MEASUREMENTS AND MODELING

A Dissertation

Presented in Partial Fulfillment of the Requirements for the

Degree of Doctor of Philosophy

with a

Major in Civil Engineering

in the

College of Graduate Studies

University of Idaho

by

Mohammad O. Al-Assi

Major Professor: Emad Kassem, Ph.D., P.E.

Committee Members:

Richard Nielsen, Ph.D., P.E.

S.J. Jung, Ph.D., P.E.

Gabriel Potirniche, Ph.D., P.E.

Department Administrator: Patricia J. S. Colberg, Ph.D., P.E.

December 2019

Authorization to Submit Dissertation

This dissertation of Mohammad O. Al-Assi, submitted for the degree of Doctor of Philosophy with a Major in Civil Engineering and titled "TIRE-PAVEMENT INTERACTION, EXPERIMENTAL MEASUREMENTS AND MODELING" has been reviewed in final form. Permission, as indicated by the signatures and dates below, is now granted to submit final copies to the College of Graduate Studies for approval.

Major Professor: _____ Date: _____
Emad Kassem, Ph.D., P.E.

Committee Members: _____ Date: _____
Richard Nielsen, Ph.D., P.E.

_____ Date: _____
S. J. Jung, Ph.D., P.E.

_____ Date: _____
Gabriel Potirniche, Ph.D., P.E.

Department
Administrator: _____ Date: _____
Patricia J. S. Colberg, Ph.D., P.E.

ABSTRACT

Providing an adequate level of skid resistance is essential for the safety of motorists. Previous studies demonstrated that the number of crashes is reduced if pavements have sufficient friction, especially in wet conditions. Adequate pavement friction prevents the vehicle from sliding on the pavement surface and provides the grip needed to maintain control over the vehicle. The first phase of this study investigated experimentally the two major friction mechanisms (i.e., adhesion and hysteresis) that contribute to tire-pavement friction. It is postulated that the adhesion between rubber tires and pavements is highly influenced by the surface free energy. However, there are no previous studies carried out to investigate the adhesion between rubber tires and pavements using the surface free energy. The results demonstrated that adhesion friction can be quantified by measuring the surface free energy components of pavement surface aggregates and rubber materials. There was a fair correlation between the adhesive bond energy and the measured coefficient of friction. Higher adhesion between rubber materials and pavement surface provided higher friction. These results provide a fundamental understanding of the mechanisms of rubber-pavement friction and verification of the relationship between adhesion and friction. In addition, there was a strong correlation between friction and rubber rheological properties. Rubber materials with lower elasticity modulus provided higher friction compared to those with higher modulus. These results explain the change in skid resistance with temperature throughout the year.

The second phase of this study examined different factors that affect skid resistance of pavement surfaces. These parameters included macrotexture, microtexture, and driving speed. The macrotexture of the pavement is related to aggregate gradation of the mix or surface texture pattern. The microtexture is influenced by the roughness of the aggregate particles and their resistance to abrasion and polishing under traffic. This study proposed a new model that can be used to estimate the skid number at a given speed between 20 mph and 60 mph as a function of both macrotexture and microtexture of pavement surface. This model was developed based on the measured frictional characteristics of field test sections. The proposed model can be used if the full-scale friction tester is not available or cannot be used due to the limited length of the test section (e.g., bridge deck). In addition, the model provides a tool to the pavement engineers to ensure adequate skid resistance at various operation speeds during the mix design stage and before the mix is used in the field. A given mix design can be modified

to improve its frictional characteristics at early stage which leads to cost savings often spent on the application of surface treatments.

The third phase of this study utilized the close-range photogrammetry (CRP) technique to measure the pavement macrotexture and microtexture. Texture parameters were calculated from the collected and analyzed images of the pavement surface. The results of the CRP texture measurements were compared to standard test methods. The CRP texture measurements had excellent correlation with the standard methods; however, the CRP offers a simple and accurate, yet inexpensive alternative to the current methods used to measure surface macrotexture and microtexture. In addition, the CRP texture parameters were incorporated in the Persson friction model to predict skid friction as a function of rubber properties. The results demonstrated excellent correlation between measured and predicted friction. This study greatly simplified the texture parameter calculations needed in the Persson friction model with good accuracy.

The last component of this study developed a 3D finite element model to investigate the effect of surface characteristics along with rubber properties on the contact stress between the standard skid test tire and pavement surface. Such simulation provides an in-depth understanding of tire-pavement interaction that would require expensive resources to examine in the field. Study parameters included various coefficients of friction, texture (e.g., smooth, and grooved), tire rolling conditions (fully skidding and free rolling) as well as temperature. The developed 3D FE model of the test tire was first validated with laboratory measurements before it was used to examine the effect of the study parameters on tire-pavement contact stresses. The results of the finite element simulations demonstrated that the stress distribution at the tire-pavement interface is non-uniform with maximum values towards the edges of the tire. These findings were consistent with the wearing pattern of the test tire in the field. In addition, the results also demonstrated that the shear stresses increased with surface friction while there was no significant change in the vertical stresses. The grooved surface exhibited higher vertical and shear stresses compared to pavement with smooth texture. The grooved texture is used to improve skid resistance and reduce the noise of pavement surfaces. In addition, temperature was found to have significant impact on the stresses at the tire-pavement

interface. The finite element simulation results agreed with the laboratory and field measurements of pavement friction.

Acknowledgements

I would like to express my utmost gratitude to Dr. Emad Kassem, who has provided me with unlimited support during my journey at the University of Idaho. I am honored to have him as an advisor. Words fall short to express how grateful I am for everything he has done to make this work possible.

I would like to thank the committee members: Dr. Richard Nielsen, Dr. S. J. Jung, and Dr. Gabriel Potirniche for their guidance and continuous feedback towards my Ph.D. dissertation.

Many thanks to Mr. Don Parks for all the help and for always being there in the lab providing assistance with designing and maintaining our research equipment.

Additional thanks to all my friends at the University of Idaho for being a second family for me when I was away from home. Hamza, Simpson, Wahid, Niyi, Mohammad, Robinour, Sandarva, Bikash, Charles, Sabreena, and Ebenezer. I will never forget the moments we have shared during our years of study.

Dedication

To my Father,

My Mother,

My Wife,

My brothers and sister,

Whom it would have been impossible to complete this dissertation without your love and support.

Table of Contents

Authorization to Submit Dissertation	ii
Abstract	iii
Acknowledgements	vi
Dedication	vii
Table of Contents	viii
List of Tables	xi
List of Figures	xii
Chapter 1. Introduction	1
1.1 Overview	1
1.2 Problem Statement	2
1.3 Research Goal and Objectives	4
1.4 Research Tasks	4
1.5 Dissertation Organization	6
1.6 References	8
Chapter 2. Evaluation of Adhesion Friction of Rubber-Pavement System	10
2.1 Abstract	10
2.2 Introduction	10
2.3 Objectives and Research Tasks	11
2.4 Methods and Materials	14
2.5 Results	23
2.6 Conclusions and Recommendations	30
2.7 References	32

Chapter 3. Pavement Skid Number Prediction Using Surface Texture Characteristics	34
3.1 Abstract.....	34
3.2 Introduction.....	34
3.3 Research Objectives.....	41
3.4 Research Tasks	41
3.5 Research Methodology	42
3.6 Data Analysis and Results	49
3.7 Conclusions and Recommendations	63
3.8 References.....	65
Chapter 4. Using Close-Range Photogrammetry to Measure Pavement Texture Characteristics and Predict Pavement Friction	68
4.1 Abstract.....	68
4.2 Introduction.....	68
4.3 Research Objectives.....	77
4.4 Research Methodology	77
4.5 Results and Analysis.....	92
4.6 Conclusions and Recommendations	106
4.7 References.....	107
Chapter 5. Finite Element Simulation of ASTM E 524 Standard Test Tire	111
5.1 Abstract.....	111
5.2 Introduction.....	112
5.3 Research Motivation.....	115
5.4 Research Objectives.....	116

5.5 Methods and Materials	116
5.6 Results and Analysis.....	129
5.7 Discussion and Conclusions	145
5.8 References.....	147
Chapter 6. Conclusions and Recommendations.....	149
6.1 Summary.....	149
6.2 Findings	152
6.3 Recommendations for Future Research.....	153
Appendix A – Improving Pavement Friction Through Aggregate Blending	155
Appendix B – Flow Curves for Rubber Materials	170
Appendix C – Summary of Skid and Texture Measurements in Idaho	173
Appendix D – CRP Measurements and Pearson Friction Model Parameters.....	178
Appendix E – Letters of Permission	190

List of Tables

Table 2-1. Surface free energy components for selected probe liquids.....	17
Table 2-2. Rubber properties as provided by the manufacturer.....	18
Table 2-3. Aggregate gradation used for asphalt mixture slabs.....	19
Table 2-4. Average contact angle between rubbers and probe liquids using Sessile drop device (degrees)	24
Table 2-5. Measured surface energy of rubber materials using the Sessile drop device	25
Table 2-6. Measured surface energy of aggregates using universal sorption device (USD) device, (adapted from Kassem et al., 2016 [20])	25
Table 3-1. Characteristics of evaluated pavement sections in this study.....	44
Table 3-2. Analysis of variance between measured SN50 and DFT20 and MTD	51
Table 4-1. Testing matrix for the laboratory experiments	78
Table 4-2. Testing matrix for the field test sections	80
Table 4-3. Sigmoid function coefficients for the rubber master curves	98
Table 5-1. Material properties for the tire parts	119
Table 5-2. Study parameters used in the second stage of the analysis	128
Table 5-3. Maximum contact stress at the tire-pavement interface	137
Table 5-4. Change in the normal and shear contact stress with temperature.....	142

List of Figures

Figure 2-1. Contact angle between liquid and solid surfaces	15
Figure 2-2. a) Sessile drop device; b) Sketch of Sessile drop contact angle measurement	16
Figure 2-3. Preparing hot mix asphalt (HMA) slabs.....	20
Figure 2-4. Prepared rubber sliders from test rubber materials	21
Figure 2-5. (a) Dynamic friction tester (DFT) device; (b) Bottom of the DFT with three rubber sliders.....	21
Figure 2-6. Three-wheel polisher device	22
Figure 2-7. Testing rubber specimen in the dynamic mechanical analyzer (DMA) device inside a temperature-control chamber	23
Figure 2-8. Adhesive bond energy between rubbers and aggregates materials.....	26
Figure 2-9. Measured coefficient of friction vs. the adhesive bond energy for a) limestone and gabbro slabs separately b) both gabbro and limestone slabs	28
Figure 2-10. Master curves of the rubber materials	29
Figure 2-11. Relationship between the rubber dynamic modulus and the coefficient of friction	30
Figure 3-1. Examples of different pavement types examined in this study	43
Figure 3-2. Schematic of location of texture measurements	43
Figure 3-3. Measuring surface coefficient of friction using DFT device	45
Figure 3-4. An example of the change in coefficient of friction with DFT test speed	46
Figure 3-5. Measuring pavement macrotexture using; a) CTMeter device, b) sand patch test, c) laser profiler	47
Figure 3-6. Typical measurement of pavement macrotexture using the sand patch test	48
Figure 3-7. Locked wheel skid trailer and standard smooth test tire used in Idaho	49

Figure 3-8. Measured skid number at 50 mph vs. measured coefficient of friction at 20 km/h	50
Figure 3-9. Measured skid number at 50 mph vs. measured surface MTD	50
Figure 3-10. Measured MPD vs. MTD for test section in Idaho	51
Figure 3-11. Measured skid number vs. calculated skid number using Equation 3-7	53
Figure 3-12. Relationship between measured and calculated skid number	53
Figure 3-13. Residual vs. predicted values for the SN prediction model Q-Q plot	54
Figure 3-14. Distribution of the residuals	54
Figure 3-15. Sensitivity analysis of the developed SN50 prediction model	55
Figure 3-16. Correlation between MTD and DFT20 with SN measures at 50 mph	57
Figure 3-17. Change of SN with speed for sections with low and high macrotexture	58
Figure 3-18. Typical change of measured SN with speed for test sections with lower and higher microtexture.....	58
Figure 3-19. Relationship between measured and calculated skid number at different speeds	60
Figure 3-20. Diagnostic check of the normality of the developed model.....	61
Figure 3-21. Combined effect of MTD and DFT20 on the predicted SN at a given speed.....	62
Figure 3-22. Combined effect of speed and DFT20 on the predicted SN	62
Figure 3-23. Combined effect of speed and MTD on the predicted SN	63
Figure 4-1. Preparation of HMA slabs; a) placing HMA inside the slab for compaction b), Compaction of the HMA slab, and c) HMA slab surface after compaction.....	79
Figure 4-2. Measuring pavement macrotexture using the sand patch test.	81
Figure 4-3. Polishing of HMA slabs using the three-wheel polisher	83
Figure 4-4. Typical set of 2D images captured using a hand-held camera from close proximity	84
Figure 4-5. Example of sparse point cloud distribution for HMA slab	85

Figure 4-6. a) Densification process into a 3D dense point cloud; b) 3D sharp features mesh of the surface model; c) Textured mesh of the 3D surface model; d) Resize the 3D surface model	86
Figure 4-7. Example of a typical 3D surface model before and after applying the level and remove form operators	88
Figure 4-8. Example of a typical pavement profile height and separating the macrotexture and microtexture using a Gaussian filter	88
Figure 4-9. Calculating the CRP mean texture depth according to the ASTM E 1845	89
Figure 4-10. Metal mold used to cut the rubber sliders to the desired shape	90
Figure 4-11. DFT rubber sliders	90
Figure 4-12. ITD Pavement Friction Tester	92
Figure 4-13. Examples of different macrotexture measured using Sand patch test and CRP	93
Figure 4-14. Examples of different microtexture measured using DFT and CRP	94
Figure 4-15. Correlation between CRP macrotexture and MTD measured using the sand patch test	95
Figure 4-16. Correlation between CRP microtexture and DFT20 measurements	96
Figure 4-17. DMA curves for the Butyl rubber material	97
Figure 4-18. Master curves for the rubber materials	97
Figure 4-19. Examples of typical pavement surface power spectral density	99
Figure 4-20. Measured coefficient of friction using DFT vs. predicted coefficient of friction using Persson model	101
Figure 4-21. Histogram of the predicted coefficient of friction residuals	102
Figure 4-22. Q-Q plot for the model prediction of the coefficient of friction	102
Figure 4-23. Correlation between the field measurements of the SN and the predicted SN using Persson friction model	104
Figure 4-24. Histogram of the predicted SN residuals	105
Figure 4-25. Q-Q plot for the model prediction of the coefficient of friction	105

Figure 5-1. Cross section of the ASTM E 524 standard test tire model in Abaqus	117
Figure 5-2. Stress-Strain curve for SBR Rubber at 20 °C	119
Figure 5-3. Contact between the tire part and two plates	121
Figure 5-4. Loads and boundary conditions for the first stage of the analysis	122
Figure 5-5. Loads and boundary conditions for the tire model sliding over pavement slab .	123
Figure 5-6. Mesh sensitivity analysis for the tire	124
Figure 5-7. Mesh used for the 3D tire model	124
Figure 5-8. Measuring the contact area of the ASTM E 524 standard test tire using the MTS machine	126
Figure 5-9. Change in contact area with applied load	127
Figure 5-10. Comparing the load displacement curve between the experimental test data and the FE simulation results.....	128
Figure 5-11. Contact stress distribution for a fully skidding tire on a grooved pavement surface	131
Figure 5-12. Wearing pattern of the ASTM E 524 standard test tire	132
Figure 5-13. Vertical contact stress for grooved pavement at different levels of μ	133
Figure 5-14. Vertical contact stress for smooth pavement at different levels of μ	134
Figure 5-15. Shear contact stress for grooved pavement at different levels of μ	134
Figure 5-16. Shear contact stress for smooth pavement at different levels of μ	135
Figure 5-17. Pavement surfaces modeled in this study	137
Figure 5-18. Comparing the vertical contact stress for smooth and grooved pavement slab	138
Figure 5-19. Effect of the coefficient of friction and surface texture on the maximum contact shear stress	139
Figure 5-20. Comparing the vertical contact stress distribution for a fully skidding tire and a freely rolling tire	140

Figure 5-21. Contact stress distribution for a freely-rolling tire	141
Figure 5-22. Contact stress distribution for a tire fully skidding	141
Figure 5-23. Stress strain curves for SBR rubber at different temperatures	143
Figure 5-24. Vertical contact stress distribution at different temperatures	144
Figure 5-25. Comparison between the finite element calculated shear stress at different temperatures and SN measurements	145

Chapter 1. Introduction

1.1 Overview

Tire-pavement friction or skid resistance is one of the main factors that contribute to road safety. An adequate level of friction between vehicle tire and pavement surface reduces the number of crashes, especially in wet pavement conditions [1, 2]. Providing an appropriate level of traction between rubber tires and pavements is essential for safe driving. Pavement friction is often expressed in terms of a dimensionless parameter called coefficient of friction (μ). The coefficient of friction is expressed mathematically as the ratio between the friction force (opposite to the direction of motion) to the normal applied force (from the wheel axle) [3].

Rubber is the main component of vehicle tires. It is an elastomer that exhibits unique physical and chemical properties. It has low Young's modulus and high yield strain compared to other materials. The theory of rubber friction recognizes three major friction forces: adhesion force, bulk deformations (hysteresis), and cohesion losses due to wearing of the rubber [4]. The adhesion friction force is formed due to rubber-pavement interaction at a microtexture level and is highly dependent on the true area of contact; thus the adhesion friction is dominant for smooth contact at low speed and dry conditions [5]. The hysteresis component of friction is caused by the bulk deformation of rubber material as it comes into contact with pavement asperities. Such deformation causes energy losses as rubber slides over the pavement surface. These energy losses are caused by the hysteretic losses in the rubber material due to loading and unloading [5]. The third major component of friction (cohesion losses) is caused by the wearing of rubber as it slides over the pavement surface.

Pavement texture has an important role in the friction components; higher pavement microtexture and macrotexture result in higher frictional properties [6]. The friction between the surface of the pavement and vehicle tires is dependent on the macrotexture and microtexture of pavement surface. The macrotexture of asphalt pavement is dependent on the aggregate gradation used in the mix design where coarse mixes have higher macrotexture than finer mixes, while the microtexture is dependent on the petrography of aggregate particles. Angular aggregates with rough texture provide higher levels of pavement friction compared to rounded aggregates with smooth surface texture. In addition, aggregates with higher resistance to polishing and abrasion provide higher pavement friction over the pavement life compared

to those with lower resistance to polishing and abrasion as they maintain higher microtexture [7, 8]. Hall et al., [5] indicated that microtexture dictates the magnitude of skid resistance, while macrotexture controls the slope of the skid resistance reduction as the speed increases. Skid resistance decreases with time due to the polishing of pavement surface under traffic. The polishing action affects both microtexture and macrotexture of pavement surface [9, 10].

1.2 Problem Statement

Skid resistance of pavements is a key component in road safety, and it depends on several factors including surface macrotexture and microtexture, tire material properties, and temperature. It was documented that rubber generates three different forms of friction: adhesion, hysteresis, and wear. Previous studies have shown that the adhesion force is the most influential component in rubber friction in dry conditions and low speed [5, 11, 12]. It is postulated that the adhesion between rubber tires and pavements is highly influenced by the surface free energy, which depends on the chemical composition of rubbers. Yet, no studies have been carried out to investigate the effect of surface free energy of rubber on traction with pavements. One of the objectives of this research was to investigate the effect of adhesion between rubber and pavement surface on friction at low speed in addition to the effect of rubber rheological properties on friction. This outcome will provide a fundamental understanding of the mechanisms of rubber-pavement friction.

It is important for highway agencies to be able to predict pavement skid resistance to identify locations where surface friction restoration is needed to enhance safety. Although previous studies demonstrated that it is possible to predict skid resistance as a function of macrotexture and microtexture [7, 8, 13]; there is no existing method to predict skid number at various speeds as a function of macrotexture and microtexture. This study conducted a comprehensive field investigation of skid resistance. A full-scale skid trailer was used to measure the skid resistance or skid number. In addition, the dynamic friction tester and laser profiler were used to measure the surface microtexture and macrotexture, respectively. Various pavement surfaces including hot mix asphalt, seal coat, and concrete were evaluated. The results of this field investigation were used to develop statistical models to predict the skid resistance as a function of microtexture and macrotexture at different speeds. It is well known

that skid resistance changes with speed and such models will be helpful to transportation agencies to ensure adequate friction at different speeds.

The use of close-range photography (CRP) and image analysis to measure surface macrotexture and microtexture has been recently proposed [14-17]. At this time, the macrotexture is typically measured using expensive methods such as the laser profiler, while the microtexture is measured indirectly by measuring the coefficient of friction using the dynamic friction tester. The CRP offers a viable alternative for measuring both macrotexture and microtexture. It is relatively much cheaper considering that it only requires a hand-held camera. This study investigates the use of CRP to generate a three-dimensional (3D) dense-point cloud model of a pavement surface. Such 3D models were used to describe pavement roughness, waviness, and wavelengths. Surface parameters derived from the CRP can be used along with rubber properties to predict the coefficient of friction between the pavement surface and the rubber.

Finally, in order to achieve an in-depth understanding of the tire-pavement contact mechanisms, finite element methods were used to study the tire-pavement interaction at various conditions that would require more resources to investigate in the field. Finite element models provide better understanding of the effect of various parameters including coefficient of friction, pavement texture (e.g., smooth, and grooved), tire rolling conditions (fully skidding and free rolling) as well as temperature (i.e., 0 °C, 20 °C, 50 °C) on the tire-pavement interaction and pavement response.

1.3 Research Goal and Objectives

The primary goal of this dissertation is to advance the current state of knowledge of tire-pavement interaction mechanisms and modeling. This dissertation has four primary objectives in order to meet this goal:

1. Investigate the effect of adhesion between rubber and pavement surface as well as rubber rheological properties on pavement friction.
2. Develop statistical-based models to predict the skid resistance as a function of pavement texture and testing speed.
3. Explore the use of the close-range photogrammetry (CRP) to develop 3D models of pavement surface texture and proposed parameters derived from the CRP along with rubber properties to predict friction level.
4. Develop a 3D finite element model and evaluate the effects of surface texture and rubber properties on the tire-pavement interaction.

1.4 Research Tasks

This study involved conducting several tasks to achieve the above-mentioned research objectives. These tasks include:

Task 1: Conduct literature review. A comprehensive literature review was conducted to collect relevant information and review the findings of previous studies on the following topics:

- Theory of rubber friction and rubber friction mechanisms,
- Theory of surface energy and its correlation to the adhesive bond energy,
- Effect of pavement surface texture on rubber-pavement friction,
- Methods and techniques used to measure pavement friction,
- Effect of external factors (i.e., temperature and speed) on tire-pavement friction,
- Statistical models for skid resistance prediction,
- Applications of close-range photography (CRP) in measuring surface roughness, and
- Finite element modeling of tire-pavement interaction.

Task 2: Assess adhesion and hysteresis friction mechanisms of various rubber compounds. In this task, a series of lab experiments were designed to investigate and study how the

adhesion and hysteresis friction mechanisms contribute to the frictional forces at the rubber-pavement interface. Adhesion and hysteresis are the two major components contributing to pavement friction. The adhesion mechanism is more dominant at low sliding speeds, while the hysteresis mechanism is more dominant at higher sliding speeds.

Task 3: Collect skid measurements and measure pavement surface characteristics in the field. Under this task, a series of field measurements was performed to collect skid resistance measurements on various pavement surfaces (e.g., HMA, seal coat, and concrete) at various test speeds (e.g., 20, 30, 40, 50, and 60 mph). These measurements were collected on the left wheel-path of the outermost lane (in case of multiple lanes) of the pavement section where most of traffic passes. It is well documented that wheel path is more polished due to traffic when compared to between the wheel paths. The field tests included 22 test sections distributed across Idaho. These sections covered typical pavements in the state.

Task 4: Develop statistical models for skid resistance using pavement surface texture measurements. Two subtasks were performed under Task 4. The first subtask included validating the ASTM E 274 equation to predict the skid number at a standard test speed of 50 mph and developing a revised model to better predict the skid number at this speed based on surface texture measurements. The second subtask included developing a new regression-based model to study and predict skid number at any speed between 20 mph and 60 mph as a function of pavement texture characteristics.

Task 5: Predict pavement friction using close-range photography and rubber properties. This task utilized close-range photography (CRP) to generate three dimensional textured models of a pavement surface and proposed parameters to describe the pavement surface macrotexture and microtexture. These texture parameters along with the rheological properties of rubber were used to predict pavement friction. Close-up images of the pavement surface from several angles were captured using a hand-held camera. These images were used to reconstruct 3D models of the pavement surface. Texture parameters were calculated from the 3D surface models to describe both surface microtexture and macrotexture. The texture parameters along with rubber properties were incorporated in the Persson friction model to predict pavement friction. The field and laboratory measurements were compared to those predicted by the model.

Task 6: Perform finite element simulations of tire-pavement interaction. Under this task, finite element simulations were conducted to investigate the effect of pavement surface characteristics and rubber properties on the contact stress (normal and shear) distributions. First, a 3D model for the standard skid test tire was developed and tire geometry properties as well as the contact area between the tire and surface were verified under various loads in the laboratory. After validating the 3D model of the test tire, the model was used to study the effect of various parameters including coefficient of friction, texture (e.g., smooth, and grooved), tire rolling conditions (fully skidding and free rolling) as well as temperature (i.e., 0 °C, 20 °C, 50 °C) on the tire-pavement interaction.

1.5 Dissertation Organization

The dissertation consists of six chapters. Chapter 1 represents an overview, problem statement, research goal and objectives, research tasks and the organization of the dissertation.

Chapter 2 presents a laboratory study to evaluate the two major components of friction for a rubber-pavement system (i.e., adhesion and hysteresis). The chapter investigated the effect of adhesion between the pavement surface and different rubber materials on surface friction at low speeds. In addition, the effect of rubber rheological properties on the hysteresis component of pavement friction was also investigated.

Chapter 3 introduced two proposed statistical-based models that were developed based on comprehensive field measurements to predict the skid number (SN) of pavement surfaces. Both models utilized field measurements of pavement texture characteristics (macrotexture and microtexture), in addition to measurements skid numbers using the locked wheel skid trailer. The first model was used to accurately predict the skid number as a function of the surface macrotexture and microtexture at a standard measurement speed of 50 mph. The second model was used to predict the skid number at any speed between 20 mph and 60 mph as a function of pavement texture and test speed.

Chapter 4 investigated the use of close-range photogrammetry (CRP) to measure the pavement surface frictional characteristics. The CRP method uses 2D images of the pavement surface to develop 3D models of the texture of pavement surfaces. The pavement surface texture measurements along with rheological properties of rubber materials were incorporated in the Persson model to predict pavement friction.

Chapter 5 presented the development of a 3D finite element simulation for a full-scale standard smooth test tire. The finite element model was used to investigate the effect of different parameters on the tire-pavement interaction (i.e., contact stresses). These parameters included the effect of the coefficient of friction, rolling condition, pavement texture, and temperature on the contact stress distribution (vertical and shear) at the tire-pavement interface.

Chapter 6 presented the conclusions and recommendations of this research study as well as proposed future research.

Appendix A presented additional work performed by the author to investigate the effect of aggregate blending on improving the frictional characteristics of asphalt pavements. This study used aggregates from the State of Qatar. The outcome of this study showed that aggregate blending can be used whenever good quality rocks are limited. Local materials can be blended with good quality aggregates to improve pavement friction which leads to cost savings and maximizes the use of natural resources in Qatar.

Appendices B, C, and D provide various test results and field measurements cited in the dissertation.

1.6 References

- [1] Noyce, D.A., Bahia, H.U., Yambo, J.M. and Kim, G., 2005. Incorporating road safety into pavement management: maximizing asphalt pavement surface friction for road safety improvements. Draft Literature Review and State Surveys, Midwest Regional University Transportation Center (UMTRI), Madison, Wisconsin.
- [2] Najafi, S., Flintsch, G. and Medina, A., Linking Roadway Crashes and Tire–Pavement Friction: A Case Study. *International Journal of Pavement Engineering*. 2017, 18(2), pp.119-127.
- [3] Wallman, C.-G. and Åström, H. (2001). Friction measurement methods and the correlation between road friction and traffic safety. A literature review; Swedish National Road and Transport Research Institute, Technical Report., p. 47. ISSN: 0347-6049.
- [4] Kummer, H., 1966. *Unified Theory of Rubber and Tire Friction*, 1st ed.; College of Engineering, Pennsylvania State University: University Park, PA, USA.
- [5] Hall, J., Smith K., Titus-Glover, L., Wambold, J., Yager, T. and Rado. Z. (2009). Guide for pavement friction. National Cooperative Highway Research Program, Final Report for NCHRP project 01-43. doi: 10.17226/23038.
- [6] Woodward, D., Millar, P., Lantieri, C., Sangiorgi, C. and Vignali, V., 2016. The wear of Stone Mastic Asphalt due to slow speed high stress simulated laboratory trafficking. *Construction and Building Materials*, 110, pp.270-277.
- [7] Masad, E., Rezaei, A., Chowdhury, A. and Freeman, T. J. (2011). Field evaluation of asphalt mixture skid resistance and its relationship to aggregate characteristics (No. 0-5627-3). Texas Transportation Institute.
- [8] Kassem, E., Awed, A., Masad, E., and Little, D. Development of Predictive Model for Skid Loss of Asphalt Pavements. *Transportation Research Record: Journal of the Transportation Research Board*. 2013, 2372 (1), pp. 83-96.
- [9] Flintsch, G. W. et al. (2010). Speed Adjustment Factors for Locked-Wheel Skid Trailer Measurements; *Transportation Research Record: Journal of the Transportation Research Board*, 2155(1), pp. 117–123. doi: 10.3141/2155-13.

- [10] Kogbara, R.B., Masad, E.A., Kassem, E., Scarpas, A.T. and Anupam, K., 2016. A state-of-the-art review of parameters influencing measurement and modeling of skid resistance of asphalt pavements. *Construction and Building Materials*, 114, pp.602-617.
- [11] Roberts, A.D., 1988. *Natural rubber science and technology*. Oxford University Press.
- [12] Mataei, B., Zakeri, H., Zahedi, M. and Nejad, F.M., Pavement Friction and Skid Resistance Measurement Methods: A Literature Review. *Open Journal of Civil Engineering*. 2016, 6, pp. 537-565.
- [13] Chowdhury, A., Kassem, E., Aldagari, S., and Masad, E. (2017) Validation of Asphalt Mixture Pavement Skid Prediction Model and Development of Skid Prediction Model for Surface Treatments. Technical Report. Report FHWA/TX-17/0-6746-01-1. Texas Department of Transportation. College Station, TX.
- [14] McQuaid, G., Millar, P., Woodward, D., Friel, S. (2013). Use of Close Range Photogrammetry to Assess the Micro-Texture of Asphalt Surfacing Aggregate. *International Journal of Pavements Conference*, Sao Paulo, Brazil.
- [15] Millar, P., Woodward, D., Woodside, A. (2009). Use of Close Range Terrestrial Photogrammetry to Assess Accelerated Wear of Asphalt Concrete Surface Course Mixes. *6th International Conference on Maintenance and Rehabilitation of Pavements and Technological Control (MAIREPAVE6)*, pp. 734-740.
- [16] Kogbara, R., Masad, E., Woodward, D. and Millar, P. (2018). Relating surface texture parameters from close range photogrammetry to Grip-Tester pavement friction measurements. *Construction and Building Materials*, 166, pp.227-240.
- [17] Woodward, D., Millar, P., McQuaid, G. (2014). Use of 3D modelling techniques to better understand road surface textures. In *International Safer Roads Conference*, 4th, 2014, Cheltenham, United Kingdom.

Chapter 2. Evaluation of Adhesion and Hysteresis Friction of Rubber-Pavement System

This Chapter is published in Applied Sciences Journal “Al-Assi, M. and Kassem, E., 2017. Evaluation of adhesion and hysteresis friction of rubber–pavement system. Applied Sciences, 7(10), p.1029.”

2.1 Abstract

Tire-pavement friction is a key component in road safety. Adhesion and hysteresis are the two main mechanisms that affect the friction between rubber tires and pavements. This study experimentally examined the relationship between rubber–pavement adhesion and friction. The adhesive bond energy between rubber and pavement surfaces was calculated by measuring the surface energy components of rubber and aggregates. The friction was measured in the laboratory using a dynamic friction tester. The results revealed that there is a fair correlation between the adhesive bond energy and the measured coefficient of friction. A rubber–pavement system with higher adhesion provided higher friction at low speed. In addition, the results demonstrated that there is a strong correlation between rubber–pavement friction and rubber properties. Softer rubber provided higher friction and vice versa. The results of this study provide experimental verification of the relationship between adhesion and pavement surface friction. The adhesive bond energy and rubber rheological properties could be incorporated in computational models to study tire-pavement friction in different conditions (e.g., speed and temperature).

2.2 Introduction

Tire-pavement friction is one of the main factors that contribute to road safety. An adequate level of friction between the vehicle tire and pavement surface reduces the number of crashes, especially in wet pavement conditions [1]. Therefore, an appropriate level of traction between rubber tires and pavements is essential for safe driving. Rubber is the main component of vehicle tires. Rubber materials are known to exhibit unique physical and chemical properties. Generally, rubber materials exhibit high yield strain at failure and have relatively low Young’s modulus when compared with other materials.

It is documented that rubber generates three different forms of friction: adhesion, deformation, and wear. Previous studies have shown that the adhesion force is the most influential component in rubber friction in dry conditions and low speed [2,3]. It is postulated that the adhesion between rubber tires and pavements is highly influenced by the surface free energy, which depends on the chemical composition of rubbers. Yet, to the best of the authors' knowledge, no studies have been carried out to investigate the effect of surface free energy of rubber on traction with pavements.

According to the theory of rubber friction there are three major friction forces: adhesion force, bulk deformations (hysteresis), and cohesion losses that are caused by the wearing of rubber [4]. The adhesion friction force is formed at a microtexture level and highly dependent on the true area of contact, and thus the adhesion friction is dominant for smooth contact at low speeds and dry conditions [3]. The hysteresis component of friction is caused by the bulk deformation of rubber material as it slides over pavement asperities. The energy losses due rubber deformation are referred to as hysteresis energy losses. These energy losses are caused by the hysteretic losses in the rubber material due to loading and unloading [3]. The third major component of friction (cohesion losses) is caused by the shear forces that caused rubber to wear while sliding over the pavement surface. Pavement texture has an important role in the friction components. A recent study showed that higher pavement microtexture and macrotexture result in higher frictional properties [5]. The study also showed that pavement surfaces initially had lower frictional properties due to the thin film of asphalt coating the aggregates at the surface. The friction increased as the binder film was removed by traffic, exposing the microtexture. Then, the friction decreased due to polishing and abrasion of the aggregates at the surface.

2.3 Objectives and Research Tasks

The main goal of this part of the study was to investigate the effect of adhesion between rubber and pavement surface on friction at low speed. In addition, the authors evaluated the effect of rubber rheological properties on friction with pavements. These objectives were achieved by conducting the following tasks:

1. Measure the surface energy components of different rubber and aggregate materials.
2. Calculate the adhesive bond energy between rubber materials and aggregates.

3. Measure the rheological properties of test rubber materials at different temperatures and loading frequencies.
4. Measure the coefficient of friction between rubber and hot mix asphalt (HMA) substrates.
5. Investigate the correlation between the calculated adhesive bond energy and the measured coefficient of friction between rubber and pavement surfaces.
6. Investigate the correlation between the rubber dynamic modulus and the coefficient of friction.

The surface free energy of test rubber materials was measured using a Sessile drop device, while the surface energy components of aggregates were measured using a universal sorption device (USD). The surface free energy of the rubber materials and aggregates was used to calculate the adhesion between the rubber materials and aggregates used in preparing the HMA test substrates. The friction between rubber sliders prepared using test rubber materials and HMA substrates was measured using the dynamic friction tester (DFT) in dry conditions at low speed. In addition, we measured the dynamic modulus of test rubber materials at different temperatures and loading frequencies using a dynamic mechanical analyzer (DMA).

2.3.1 Theory of Surface Energy

There are two major components contributing to pavement friction: adhesion and hysteresis. The adhesion component of pavement friction is dominant at low speeds in dry conditions, while the hysteresis component is dominant at higher speeds in wet conditions [6]. The adhesion between any materials is a function of their surface free energy components, where the adhesion force is developed at the molecular level [7,8]. The atoms at the surface have a lower level of bond energy compared to the atoms in bulk. As molecules in the material bulk are surrounded by other molecules from all sides, an external work must be applied to create a new surface area [7]. This work is known as the total surface free energy of the material and is denoted with Greek letter gamma (γ); the surface free energy is measured in units of ergs/cm² or mJ/m². The two most recognized theories to explain the surface free energy are: the two-component theory, and the acid-base theory. According to the two-component theory, the total surface free energy is caused by dispersion forces (e.g., Lifshitz-van der Waals forces)

and specific forces (e.g., H-bonding). The total surface free energy is the sum of these two forces as shown in Equation 2-1 [9,10].

$$\gamma = \gamma^{\text{Dispersive}} + \gamma^{\text{Specific}} \quad (2-1)$$

According to the acid-base theory, the total surface free energy for any material has three components; nonpolar component also known as Lifshitz-van der Waals (γ^{LW}), and two polar components: Lewis acid (γ^+), and Lewis base (γ^-) [11,12]. The total surface energy can be calculated from these three components as given in Equation 2-2.

$$\gamma^{\text{Total}} = \gamma^{\text{LW}} + 2\sqrt{\gamma^+\gamma^-} \quad (2-2)$$

Several theories explain the adhesion between two materials by studying the interfacial forces between the materials [13]. The adhesion between rubber tires and pavement surface is one mechanism leading to friction and is dominant at low speeds. The adhesion between rubber and aggregate can be measured if the surface free energies of both materials are known. The adhesion between two materials (A and B) is a function of the surface free energy components of these two materials, as given in Equation (2-3) [7].

$$W_{\text{AB}} = 2\sqrt{\gamma_{\text{A}}^{\text{LW}}\gamma_{\text{B}}^{\text{LW}}} + 2\sqrt{\gamma_{\text{A}}^+\gamma_{\text{B}}^-} + 2\sqrt{\gamma_{\text{A}}^-\gamma_{\text{B}}^+} \quad (2-3)$$

The amount of work required to separate the two materials at the interface in vacuum is referred as the adhesive bond energy (W_{AB}). The adhesive bond energy between rubber sample (subscript A) and an aggregate (subscript B) can be calculated using Equation (2-3), while the cohesive bond energy of a single material (e.g., rubber) (W_{AA}) can be calculated according to Equation 2-4 [7].

$$W_{\text{AA}} = \gamma_{\text{A}}^{\text{LW}} + 2\sqrt{\gamma_{\text{A}}^{\text{LW}}\gamma_{\text{B}}^{\text{LW}}} \quad (2-4)$$

2.4 Methods and Materials

2.4.1 *Methods for Measuring Surface Energy*

The surface energy components of various rubber materials were measured using a Sessile drop device, while surface energy components of aggregates were measured using the USD. Both USD and Sessile drop devices at Texas A&M University were used for surface energy measurements. This section provides background and demonstrates the test procedure for the surface energy testing.

2.4.1.1 Sessile Drop Method

The Sessile drop method is commonly used to measure the surface free energy between a probe liquid and solid surface by means of measuring the contact angle between a droplet of a selected probe liquid and material surface [14]. The Sessile drop test measures the contact angle between a drop of liquid of known surface energy and a solid material, to calculate the surface free energy (SFE) of solid material surfaces. The Young's equation (Equation 2-5), defines the equilibrium at the three-phase contact of solid-liquid and gas [15].

$$\gamma_{SV} = \gamma_{SL} + \gamma_{LV} \cos(\theta) \quad (2-5)$$

where,

θ is the contact angle between a solid surface and a drop of probe liquid.

The contact angle is measured from a static image using a charged-coupled device (CCD) camera as shown in Figure 2-1. The Young's equation assumes that the surface is chemically homogeneous and topographically smooth.

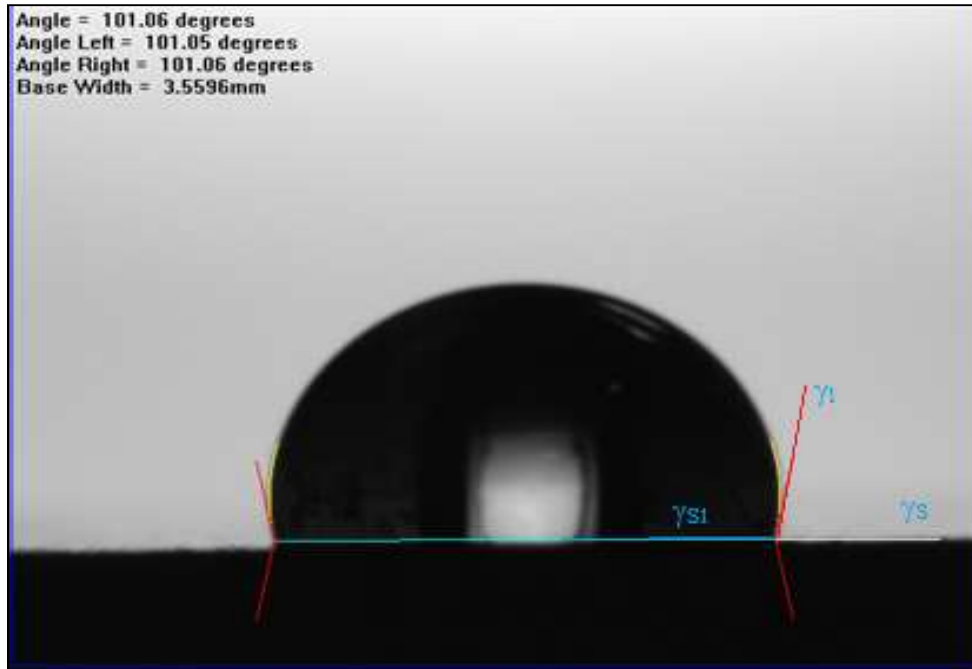
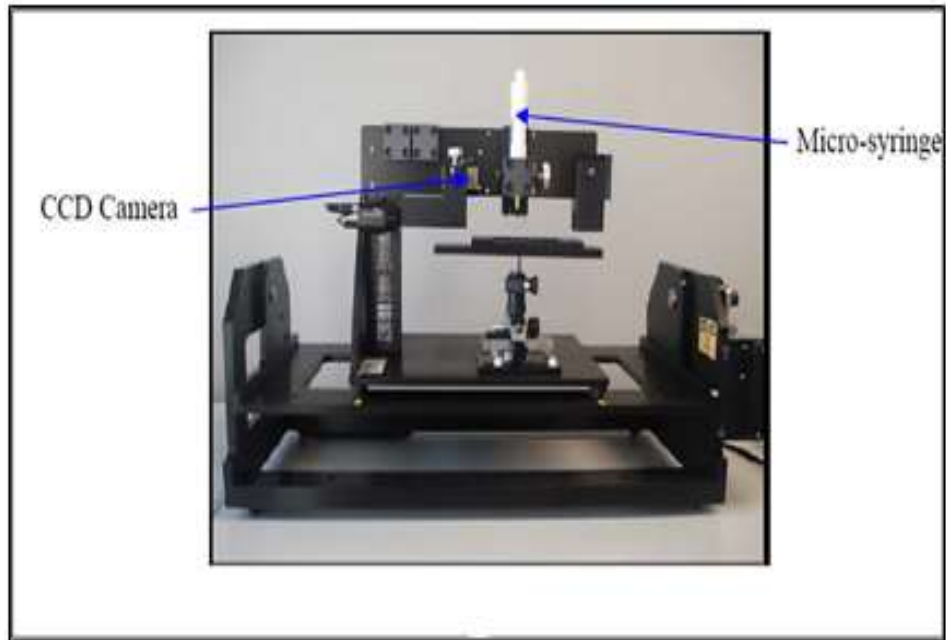
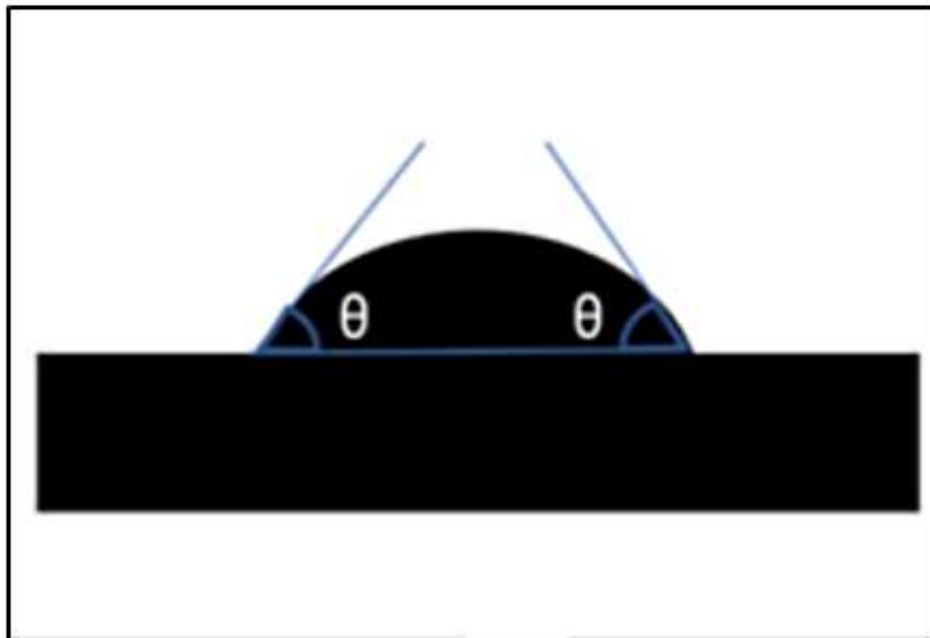


Figure 2-1. Contact angle between liquid and solid surfaces

In the Sessile drop technique, a droplet of probe liquid is placed on the test surface using a micro-syringe. The Sessile drop device (Figure 2-2a) uses a CCD camera static image to measure the contact angle between the used probe liquid of known surface energy and the rubber surface. The contact angle is the average value of the measured right and left contact angles (Figure 2-2b).



(a)



(b)

Figure 2-2. a) Sessile drop device; b) Sketch of Sessile drop contact angle measurement

To determine the surface energy components of a material, three different probe liquids are used in the test. However, in order to minimize experimental error in calculating the surface energy components, Little and Bhsain [7] recommended using five different probe liquids

(water, glycerol, ethylene glycol, formamide, and diiodomethane) with known surface energy components. Table 2-1 summarizes the surface energy components of the five probe liquids used in this study.

Table 2-1. Surface free energy components for selected probe liquids (ergs/cm²)

Probe Liquid	γ^{LW}	γ^+	γ^-	γ^{Total}
Water	21.80	25.50	25.50	72.80
Glycerol	34.00	3.92	57.40	64.00
Formamide	39.00	2.28	39.60	58.00
Methylene Iodide	50.80	0.00	0.00	50.80
Ethylene Glycol	29.00	1.92	47.00	47.99

2.4.1.2 Universal Sorption Device

The surface free energy components of aggregates are often measured using the universal sorption device (USD). In this method, the aggregate particles are placed in a sealed cell under vacuum and controlled temperature. The USD uses a magnetic suspension balance to measure the mass of the aggregate particle and probe vapor adsorbed on the aggregate surface when aggregates are subjected to different pressures of probe vapor. The relationship between the amount of probe vapor adsorbed on aggregate surface and the partial pressure is called the adsorption isotherm which is used to determine the spreading pressure (π_e) [7]. The spreading pressure (π_e) is a function of the surface energy components of aggregate particles (S) and probe vapor (V), as given in Equation 2-6.

$$\pi_e + 2\gamma_V^{Tot} = 2\sqrt{\gamma_S^{LW}\gamma_V^{LW}} + 2\sqrt{\gamma_S^+\gamma_V^-} + 2\sqrt{\gamma_S^-\gamma_V^+} \quad (2-6)$$

Several researchers used the USD to measure the surface free energy components of aggregates [16–18]. In this study, the USD test was used to determine the surface free energy of the gabbro and limestone aggregates. The surface energy components of rubber and aggregates are used to calculate the adhesive bond energy or work of adhesion (W_{AB}), (Equation 2-3) between rubber sliders and HMA surfaces.

2.4.2 Test Materials and Laboratory Experiments

In this study, six different rubber materials were used to investigate the frictional properties between laboratory-prepared rubber sliders and HMA slabs prepared from limestone and gabbro aggregates. The rubber materials used in this study included pure gum, Styrene Butadiene Rubber (SBR), Nitrile, Ethylene Propylene Diene Monomer (EPDM), Neoprene, and Butyl. These materials were selected in testing as they cover a wide range of rubber properties in terms of dynamic modulus, elongation, and durability. Table 2-2 summarizes the rubber properties as provided by the manufacturer.

Table 2-2. Rubber properties as provided by the manufacturer

Rubber Type	Tensile Strength (PSI)	Elongation (%)	Composition	Durometer
Pure Gum	3000	600	Organic Gum	40 A Nominal
SBR	800	250	Styrene Butadiene	65 Shore A
EPDM	800	400	Synthetic	60 A Nominal
Nitrile	950	250	Synthetic	50 A Nominal
Neoprene	1000	220	Synthetic	60 A Nominal
Butyl	1000	350	Isobutylene Isoprene	55 Shore A

Two sources of aggregates were evaluated in this study (i.e. gabbro and limestone). The gabbro and limestone aggregates were used to prepare HMA slabs. The gabbro is an igneous

rock while the limestone is a sedimentary rock. Gabbro has rough surface compared to limestone [19]. These aggregates are used in road construction in the State of Qatar. Table 2-3 presents the aggregate gradation used to prepare both gabbro and limestone substrates. It should be noted that the same aggregate gradation and binder type (Pen 60–70) were used in preparing the asphalt mixture substrates. The optimum binder content was found to be 4.3% for gabbro and 4.7% for limestone. The mixing and compaction temperatures were 143 °C and 135 °C, respectively.

The asphalt mixtures were prepared following the AASHTO T-312, and the test slabs were compacted using a small vibratory compactor as shown in Figure 2-3

Table 2-3. Aggregate gradation used for asphalt mixture slabs

Sieve Size	% Passing
1.5"	100.0
1"	98.6
3/4"	88.2
1/2"	76.9
3/8"	68.9
No. 4	47.1
No. 8	26.5
No. 16	15.8
No. 30	10.5
No. 50	7.9
No. 100	6.1
No. 200	4.2
Pan	0.0



Figure 2-3. Preparing hot mix asphalt (HMA) slabs

2.4.3 Measuring Frictional Properties for HMA Slabs

We used a dynamic friction tester (DFT) to measure the coefficient of friction between rubber sliders (Figure 2-4) prepared using the test rubber materials, and HMA substrate at low speed (20 km/h) in dry conditions. The DFT uses three rubber sliders attached to a rotating desk (Figure 2-5). The rotating desk is lowered on the surface once the specified speed is reached and the coefficient of friction is measured with speed until the rotating desk comes to a complete stop.

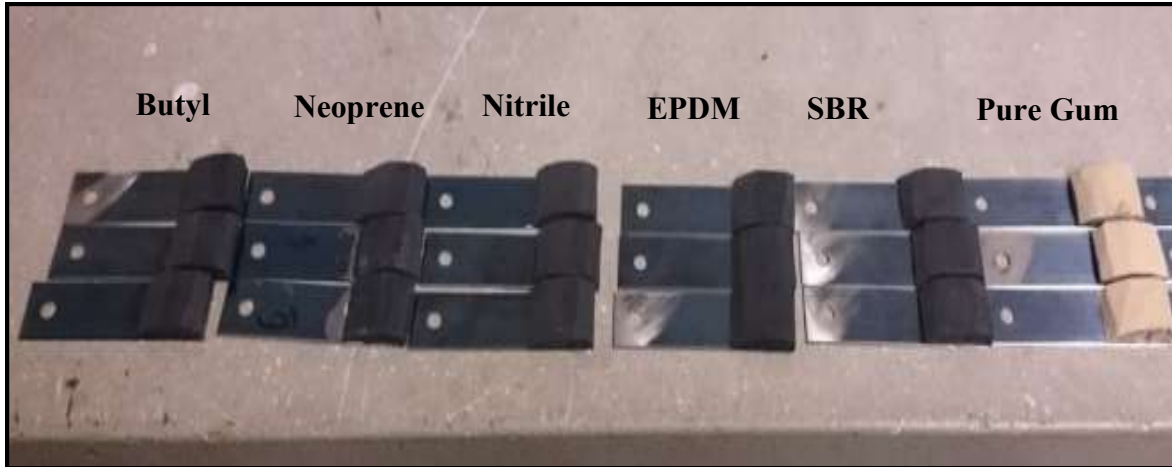
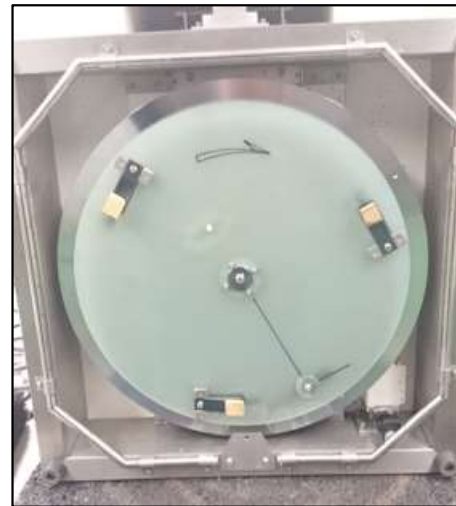


Figure 2-4. Prepared rubber sliders from test rubber materials



(a)



(b)

Figure 2-5. (a) Dynamic friction tester (DFT) device; (b) Bottom of the DFT with three rubber sliders

For the prepared HMA substrates, the aggregates on the surface were coated with a thin asphalt binder. The authors used a three-wheel polisher to remove this thin film of binder to ensure direct contact between rubber sliders and aggregates. The surface energy components of asphalt binder are different than those of aggregate samples and thus it may affect the adhesive bond energy between rubber and surface aggregates. In the field, this thin layer of

asphalt binder is typically removed under traffic in a short period of time. The three-wheel polisher consists of pneumatic rubber wheels that rotate over the test HMA substrate as shown in Figure 2-6. The DFT device was used to measure the coefficient of friction between the prepared rubber sliders (Figure 2-4) and HMA substrates.



Figure 2-6. Three-wheel polisher device

2.4.4 Measuring Rubber Properties

The dynamic mechanical analyzer (DMA) device at Texas A&M University was used to measure the dynamic modulus of rubber samples tested in this study (Figure 2-7). The rubber test sample for the DMA testing was 50 mm in length, 16.8 mm in width, and 6.4 mm thick. The test was performed at different test temperatures (0 °C to 70 °C) and frequencies (0.1 to 70 Hz). The temperature was controlled during the test by placing the DMA inside an environmental chamber. The dynamic modulus is calculated by dividing the maximum applied cyclic tensile stress by the resulting strain.



Figure 2-7. Testing rubber specimen in the dynamic mechanical analyzer (DMA) device inside a temperature-control chamber

2.5 Results

2.5.1 Adhesion Friction

The average contact angle between rubber samples and the test probe liquids was recorded using the Sessile drop device. Each measurement represents the average contact angle measured from right and left. The results for the measured contact angles in degrees are presented in Table 2-4. Based on the contact angle measurements, the surface energy components were calculated for each rubber material using Equation 2-7, which is discussed in detail by Little and Bhasin [7].

$$W_{LS} = \gamma_L (1 + \cos \theta) = 2\sqrt{\gamma_s^{LW}\gamma_V^{LW}} + 2\sqrt{\gamma_s^+\gamma_V^-} + 2\sqrt{\gamma_s^-\gamma_V^+} \quad (2-7)$$

The surface free energy components are summarized in Table 2-5. The surface free energy components of the aggregates were measured using a Universal Sorption Device (USD) from a previous study [20]. The surface free energy components for the gabbro and limestone aggregates are shown in Table 2-6. It was found that gabbro rock has the higher total surface free energy compared to limestone.

Table 2-4. Average contact angle between rubbers and probe liquids using Sessile drop device (degrees)

Probe Liquid	Water	Glycerol			Ethylene Glycol			Formamide			Diiodomethane		
		Contact Angle	Std. Dev	Contact Angle	Std. Dev	Contact Angle	Std. Dev	Contact Angle	Std. Dev	Contact Angle	Std. Dev	Contact Angle	Std. Dev
Pure gum	89.47	0.69	120.18	0.86	87.14	0.74	83.03	1.21	67.43	0.76			
SBR	100.98	0.86	101.28	1.47	87.16	1.05	84.19	0.66	71.74	0.55			
Nitrile	89.04	0.74	94.77	0.82	84.32	0.89	90.35	0.99	63.03	1.04			
EPDM	108.36	0.74	112.45	0.67	89.61	0.75	93.29	0.87	72.22	13.12			
Neoprene	124.58	0.89	112.02	0.74	90.23	0.95	87.54	1.75	69.63	1.64			
Butyl	111.32	0.96	117.02	1.21	92.49	0.71	107.16	0.93	64.43	0.98			

Table 2-5. Measured surface energy of rubber materials using the Sessile drop device

Rubber	Surface Energy Components (ergs/cm ²)				Standard Deviation (ergs/cm ²)		
	γ^{LW}	γ^+	γ^-	γ^{Total}	γ^{LW}	γ^+	γ^-
Pure gum	21.21	0.00	2.26	21.21	0.44	0.00	0.42
SBR	22.11	0.00	2.24	22.11	0.46	0.00	0.40
Nitrile	17.08	0.00	10.33	17.08	0.54	0.00	0.67
EPDM	16.77	0.00	0.35	16.77	1.53	0.00	0.17
Neoprene	15.30	0.00	0.00	15.30	0.69	0.00	0.00
Butyl	18.79	0.00	0.00	18.79	0.51	0.00	0.00

Table 2-6. Measured surface energy of aggregates using universal sorption device (USD) device, (adapted from Kassem et al., 2016 [20])

Material	Surface Energy Components (ergs/cm ²)			
	γ^{LW}	γ^+	γ^-	γ^{Total}
Limestone	69.35	0.28	1075.40	104.18
Gabbro	57.37	3.34	6277.96	346.85

The adhesive bond energy between different rubber and aggregate samples was calculated from their surface free energy components according to Equation 2-3. Figure 2-8 shows the calculated adhesive bond energies between the rubber and aggregates. The SBR and Pure Gum rubber materials were found to provide the highest adhesion with test substrates made with gabbro and limestone. The adhesive bond energy between limestone and SBR rubber was 79.91 ergs/cm². The Neoprene was found to provide the lowest adhesion with HMA substrates

compared to other rubber materials. Also, the limestone was found to provide higher adhesion with rubber materials compared to gabbro in most cases.

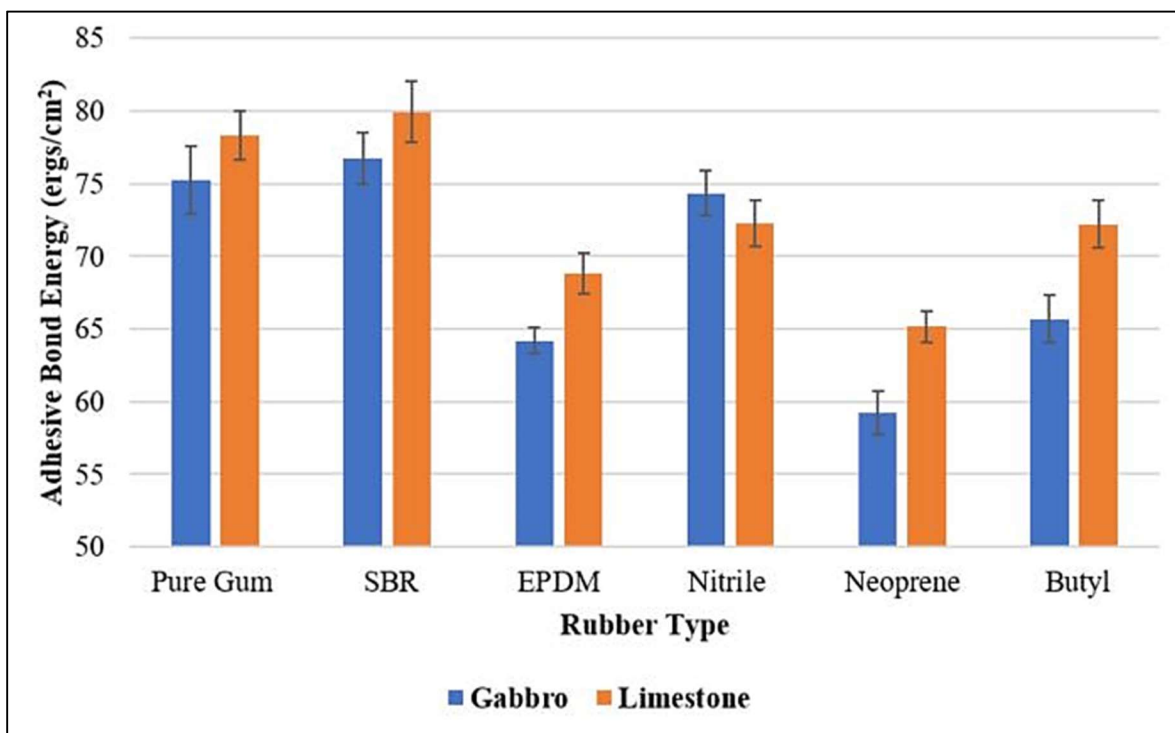
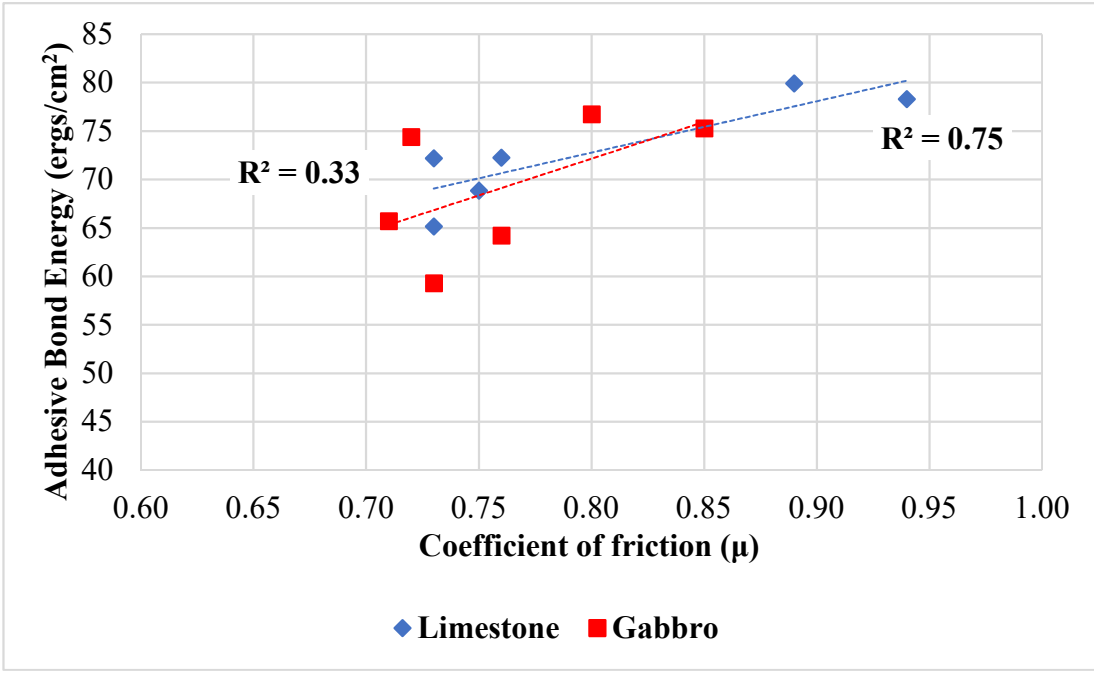


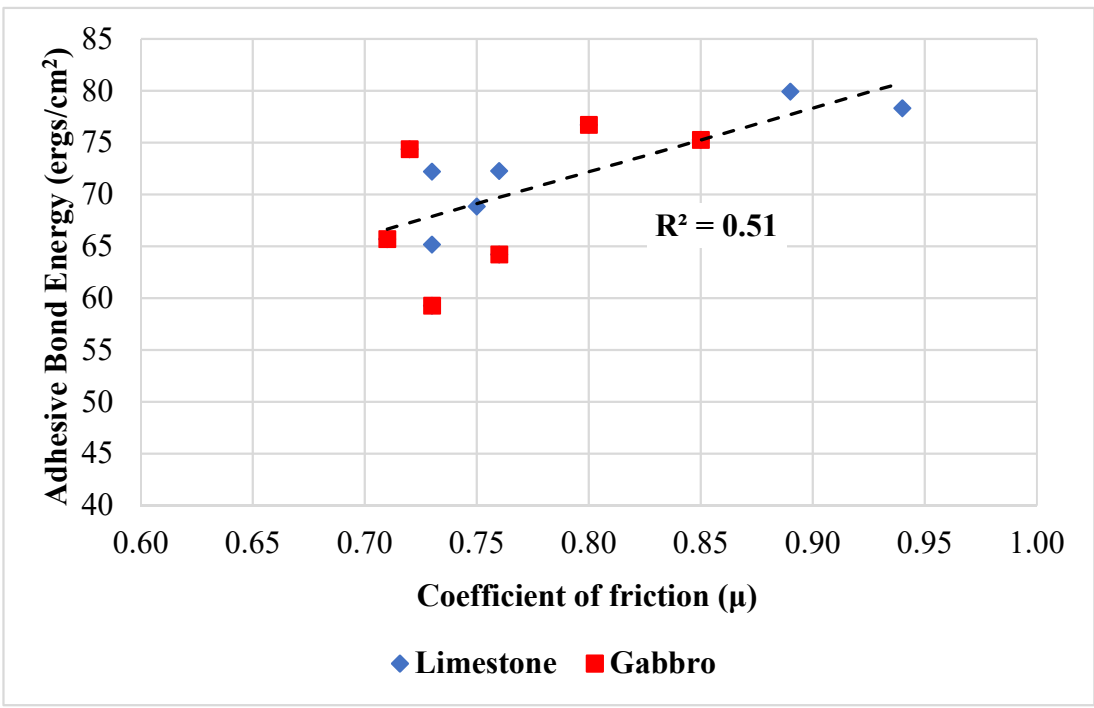
Figure 2-8. Adhesive bond energy between rubbers and aggregates materials

The coefficient of friction between rubber sliders and HMA substrates was measured using the DFT at low speed (20 km/h) in dry conditions. The adhesion component of the friction is dominant at low speed. Figure 2-9a show the relationship between the adhesive bond energy and the coefficient of friction for gabbro and limestone separately, while Figure 2-9b shows the relationship between the coefficient of friction versus the adhesive bond energy between test rubber materials and all the test HMA substrates (both gabbro and limestone). It was found that there is a fair correlation between the adhesive bond energy and measured coefficient of friction. This relationship demonstrates that higher adhesion between rubber and pavement surface increases the coefficient of friction at low speed as one expects; however, this study provided an experimental verification to such relationship. In the meantime, we believe that this relationship is affected by two experimental limitations. First, the asphalt binder film was not fully removed from the aggregates on the surface. We attempted to minimize this effect by

removing most of the film thickness by polishing the slab using the three-wheel polisher for 5000 cycles until the aggregate particles surface is exposed. The application of more cycles was found to polish the aggregates which should be avoided since the surface energy components of aggregate will change with change in the texture of the surface. Second, the surface energy components of rubber were calculated based on the contact angle between smooth rubber samples and probe liquids. Meanwhile, we observed that the surface of rubber sliders, used in DFT, was not completely smooth due to cutting the rubber sheet to prepare the sliders. These two limitations may contribute to this fair correlation between adhesive bond energy and measured coefficient of friction at low speed.



(a)



(b)

Figure 2-9. Measured coefficient of friction vs. the adhesive bond energy for a) limestone and gabbro slabs separately b) both gabbro and limestone slabs

2.5.2 Hysteresis Friction

The DMA results demonstrated that the dynamic modulus (E^*) of rubber material increased with the loading frequency and decreased with temperature as expected. Figure 2-10 shows the E^* master curves of the test rubber materials. The Pure Gum rubber provided the lowest E^* value compared to other rubber materials, while the Nitrile rubber had the highest E^* . From Figure 2-10, it can be clearly seen that the Pure Gum rubber is the softest followed by the SBR rubber while the Nitrile rubber is the stiffest. The rubbers' dynamic modulus at room temperature (20 °C) were correlated with the measured coefficient of friction.

Figure 2-11 shows the relationship between the dynamic modulus values of rubber samples and the coefficient of friction between rubber sliders and HMA substrates. There is a strong correlation between the complex modulus at room temperature (20 °C) and the coefficient of friction at 30 km/h. The researchers observed that there was no significant change in the coefficient of friction measured using DFT with speed greater than 30 km/h. Figure 2-11 demonstrates that softer rubbers provide higher coefficients of friction while stiffer rubbers provided lower coefficients of friction regardless the aggregate type.

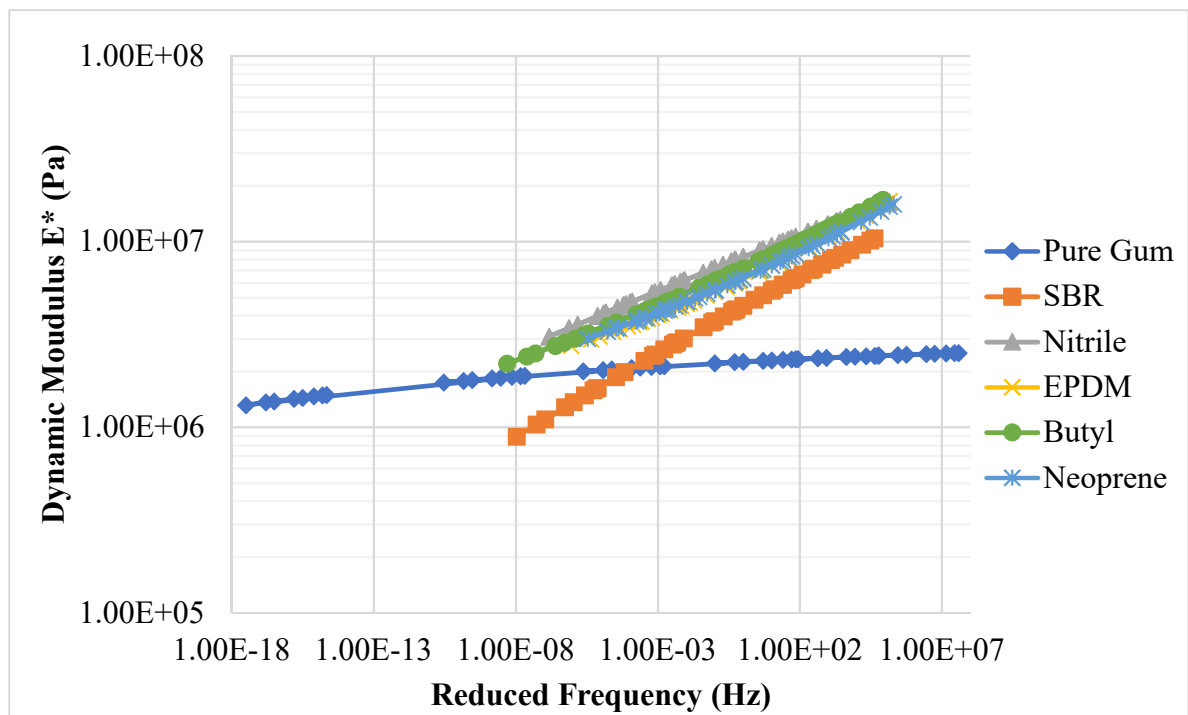


Figure 2-10. Master curves of the rubber materials

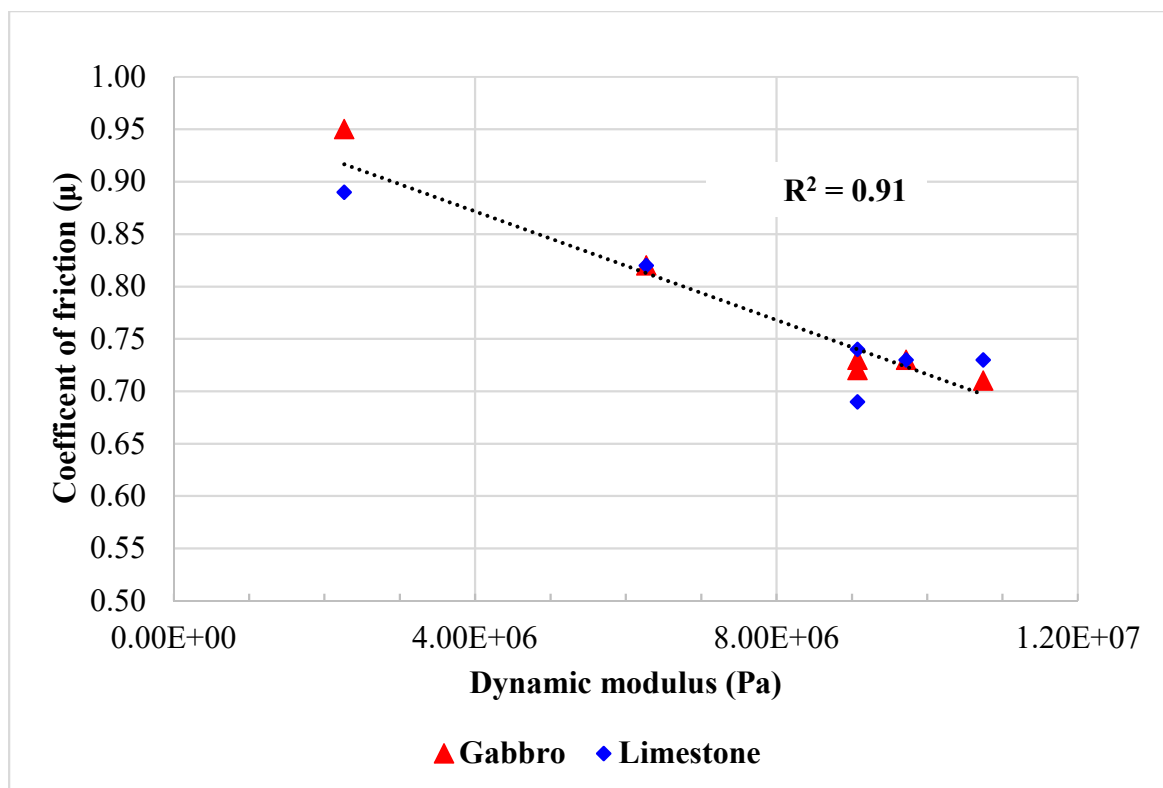


Figure 2-11. Relationship between the rubber dynamic modulus and the coefficient of friction

2.6 Conclusions and Recommendations

This part of the study experimentally examined the relationship between the rubber–pavement adhesion and friction. We calculated the surface energy components for rubber materials by measuring the contact angle between rubber materials and different probe liquids. The contact angle was measured using a Sessile drop device. Similarly, the surface energy components of aggregate samples were measured using a USD device. The adhesive bond energy between rubber and aggregates was calculated based on the surface energy components of both materials. In addition, we measured the coefficient of friction between different rubber materials and HMA substrates prepared using different rock types. The results showed that there is a fair correlation between adhesive bond energy and friction between rubber and pavement surfaces. In addition, the results demonstrated that there is a strong relationship between friction and rubber elastic modulus. Softer rubber provided higher friction. The results of this study provide an experimental verification of the relationship between adhesion and

friction of rubber and pavement surface. The adhesive bond energy and rubber rheological properties could be incorporated in computational models to study tire-pavement friction in different conditions (e.g., speed and temperature). We recommend testing more aggregate types and rubber materials to evaluate the adhesion friction.

2.7 References

- [1] Noyce, D.A., Bahia, H.U., Yambo, J.M. and Kim, G., 2005. Incorporating road safety into pavement management: maximizing asphalt pavement surface friction for road safety improvements. Draft Literature Review and State Surveys, Midwest Regional University Transportation Center (UMTRI), Madison, Wisconsin.
- [2] Roberts, A.D., 1988. Rubber Adhesion at High Rolling Speeds. *J. Nat. Rubber Res.* 3, 4.
- [3] Hall, J.W.; Smith, K.L.; Titus-Glover, L., 2009. Guide for Pavement Friction; Contractors final report for NCHRP Project 01-43; National Cooperative Highway Research Program. URL: <https://www.nap.edu/download/23038#> (accessed on 12/8/2017).
- [4] Kummer, H., 1966. Unified Theory of Rubber and Tire Friction, 1st ed.; College of Engineering, Pennsylvania State University: University Park, PA, USA.
- [5] Woodward, D., Millar, P., Lantieri, C., Sangiorgi, C. and Vignali, V., 2016. The wear of Stone Mastic Asphalt due to slow speed high stress simulated laboratory trafficking. *Construction and Building Materials*, 110, pp.270-277.
- [6] Dunford, A., 2013. Friction and the texture of aggregate particles used in the road surface course Doctoral dissertation, University of Nottingham, UK.
- [7] Little, D., Bhasin, A. and Hefer, A., 2006. Using surface energy measurements to select materials for asphalt pavement. NCHRP project 9–37. Transportation Research Board (TRB), Washington, DC, USA.
- [8] Berg, J.C., 2010. An introduction to interfaces & colloids: the bridge to nanoscience. World Scientific.
- [9] Fowkes, F.M., 1962. Determination of interfacial tensions, contact angles, and dispersion forces in surfaces by assuming additivity of intermolecular interactions in surfaces. *The Journal of Physical Chemistry*, 66(2), pp.382-382.
- [10] Fowkes, F.M., 1964. Attractive forces at interfaces. *Industrial & Engineering Chemistry*, 56(12), pp.40-52.
- [11] Van Oss, C.J., Chaudhury, M.K. and Good, R.J., 1988. Interfacial Lifshitz-van der Waals and polar interactions in macroscopic systems. *Chemical Reviews*, 88(6), pp.927-941.
- [12] Van Oss, C.J., 2002. Use of the combined Lifshitz–van der Waals and Lewis acid–base approaches in determining the apolar and polar contributions to surface and interfacial tensions and free energies. *Journal of adhesion science and technology*, 16(6), pp.669-677.

- [13] Adamson, A.; Gast, A., 1997. *Physical Chemistry of Surfaces*, 1st ed.; Wiley: New York.
- [14] Hejda, F., Solar, P. and Kousal, J., 2010, June. Surface free energy determination by contact angle measurements—a comparison of various approaches. In *WDS* (Vol. 10, pp. 25-30).
- [15] Bracco, G. and Holst, B., 2013. *Surface science techniques*. Springer Science & Business Media.
- [16] Cheng, D., 2002. *Surface Free Energy of Asphalt-Aggregate Systems and Performance Analysis of Asphalt Concrete Based on Surface Free Energy*. Ph.D. Thesis, Texas A&M University, College Station.
- [17] Hefer, A., 2004. *Adhesion in Bitumen-Aggregate Systems and Quantification of the Effects of Water on the Adhesive Bond*. Ph.D. Thesis, Texas A&M University, College Station.
- [18] Zollinger, C., 2005. *Application of Surface Energy Measurements to Evaluate Moisture Susceptibility of Asphalt and Aggregates*. Master's Thesis, Texas A&M University, College Station.
- [19] Masad, E., Rezaei, A., Chowdhury, A. and Harris, P., 2008. *Predicting asphalt mixture skid resistance based on aggregate characteristics* (No. FHWA/TX-09/0-5627-1). Texas. Dept. of Transportation. Research and Technology Implementation Office.
- [20] Kassem, E., Garcia Cucalon, L., Masad, E. and Little, D., 2016. Effect of warm mix additives on the interfacial bonding characteristics of asphalt binders. *International Journal of Pavement Engineering*, 19(12), pp.1111-1124.

Chapter 3. Pavement Skid Number Prediction Using Surface Texture

Characteristics

3.1 Abstract

The skid number of pavements is used by various transportation agencies to ensure adequate skid resistance of pavements. Higher skid numbers imply better skid resistance and improved safety, especially in wet conditions. Pavement texture characteristics can be used to estimate the skid number (SN). The SN is often measured using a skid trailer at a reference speed (e.g., 80.5 km/h [50 mph] or 64 km/h [40 mph]). The texture characteristics include both macrotexture and microtexture. The macrotexture is measured using laser-based techniques or volumetric sand patch test, while a dynamic friction tester is often used to indirectly measure the microtexture. The current standard model proposed in ASTM E 274 uses both macrotexture and microtexture to estimate the skid number. This study found that the current standard model underestimates the skid number predictions; therefore, a revised model was developed and proposed. The revised model improved the accuracy of skid number predictions. The revised model is a function of both macrotexture and microtexture. The model can be used to optimize the surface texture by selecting the proper aggregate type and mix design to ensure adequate skid resistance before pavement construction. In addition, another model was developed to predict the change in the skid number with speed as a function of pavement macrotexture and microtexture. The model was found to provide a good correlation with skid number measurements in the field at different speeds ($R^2 = 0.83$). This model can provide transportation agencies with a useful tool to predict skid number at the desired speed at a given location where there are restrictions for measuring skid number due to the geometry of the road or posted speed limits.

3.2 Introduction

Skid resistance is a major factor that contributes to road safety. Adequate friction between pavement surface and tires is essential to provide a minimum stopping distance which has the potential to reduce the number of vehicle crashes [1-3]. Previous research found that providing adequate skid resistance could reduce the total number of crashes on highways in wet conditions [4]. According to the National Highway Traffic Safety Administration (NHTSA)

report published in 2016, there were more than 34,000 fatalities and over 2.17 million people were injured in vehicle crashes [5]. Crash statistics showed that 14.2% of crashes occurred on wet pavement conditions and more than 23% of fatal crashes occurred on horizontal curves [5]. A recent study by Alhasan et al. [6] found that there is a significant correlation between pavement skid number (SN) and the number of roadway-departure crashes. Providing higher skid resistance significantly reduced the crash rates for all weather crashes [6]. According to the Federal Highway Administration (FHWA) [4], it was found that between 22% to 30% of single-vehicle crashes and 15% to 18% of multiple vehicles crashes occurred on wet pavement conditions where skid resistance is most critical.

Pavement friction is often expressed in terms of a dimensionless parameter called the coefficient of friction (μ). The coefficient of friction is expressed mathematically as the ratio between the friction force (opposite to the direction of motion) to the normal applied force (applied vertically to the wheel axle). The texture of the pavement surface is one of the major factors that contributes to pavement skid resistance [5]. It is well established that pavement surface texture plays a crucial role in tire-pavement friction [2, 7-9]. According to the Permanent International Association for Road Congress (PIARC), pavement surface texture is classified into four categories; 1) microtexture with wavelengths less than 0.5 mm, 2) macrotexture with wavelengths between 0.5 mm to 50 mm, 3) megatexture with wavelengths between 50 mm to 500 mm, and 4) unevenness with wavelengths greater than 500 mm) [7]. Both microtexture and macrotexture have a significant effect on skid resistance, while megatexture and unevenness affect the ride quality [1]. The macrotexture of asphalt pavements is related to the mix design characteristics (e.g., aggregate gradation), while the aggregate microtexture is dependent on the petrography of aggregate particles [8]. Angular aggregates with rough textures provide higher levels of skid resistance compared to rounded aggregates with smooth surface textures [9]. In addition, aggregates with higher resistance to polishing and abrasion provide higher pavement friction compared to those with lower resistance to polishing and abrasion as they maintain higher microtexture [10].

It is well known that pavement friction is highly influenced by surface microtexture and macrotexture characteristics [1]. Previous studies [2, 3, 9] showed that tire-pavement friction has two major components: adhesion and hysteresis friction. The adhesion component is

predominant at low speeds and dry pavement conditions [2] and it was found that the adhesion component of pavement friction is dependent on the microtexture of pavement surface. Pavements with higher microtexture have higher friction due to the adhesion friction component [2, 11, 12]. The hysteresis component of pavement friction is predominant at higher speeds and wet surface conditions [2, 9]. The hysteresis component of tire-pavement friction was found to be a function of pavement surface macrotexture. Pavements with higher macrotexture generally have higher friction due to the hysteresis component [9, 12].

There are several methods used to measure pavement surface macrotexture. One of these methods is the volumetric sand patch test. This test is conducted in accordance with the ASTM E 965-15 [13]. In this test, the surface is cleaned from debris and dust and then a known volume of silica sand is spread over pavement surface in a circular pattern. The mean texture depth (MTD), obtained using a volumetric measurement technique, represents the surface characteristics in three-dimensional space [2]. The average diameter of the sand patch is measured and the MTD is calculated using Equation 3-1.

$$\text{MTD} = 4V/(\pi D^2) \quad (3-1)$$

where,

MTD = mean texture depth (mm)

V = sand volume (mm³)

D = average diameter of sand patch circle (mm)

The Circular Texture Meter (CTMeter) is another device that is used to measure the surface macrotexture in accordance with ASTM E 2157-15 [14]. The CTMeter consists of a laser displacement sensor mounted on a moving arm that rotates on pavement surface. The CTMeter is used to measure the mean profile depth (MPD). The MPD is widely accepted as a measure of pavement surface macrotexture [2, 7-9]. The MPD measured using CTMeter is the average value of profile depth for all profile segments over a certain distance (baseline). Several studies found a strong correlation between MTD measured using the sand patch test and MPD measured using CTMeter [15-19]. Equation 3-2 presents the relationship between MPD and MTD as presented in ASTM E 2157-15 [14].

$$\text{MTD} = 0.947 \text{ MPD} + 0.069 \quad (3-2)$$

where,

MTD and MPD are both measured in millimeters

3.2.1 Pavement Friction Measurements

There are several test methods used to measure pavement friction. These methods include some stationary devices such as the British Pendulum Tester (BPT) (ASTM E303-93) [20] and the Dynamic Friction Tester (DFT) (ASTM E 1911) [21]. The DFT utilizes three rubber sliders attached to a rotating disk at the bottom of the device. The speed of the rotating disk can reach up to 100 km/h. Once the speed of the rotating disk reaches the desired speed, it drops to pavement surface and the coefficient of friction (μ) between the rubber sliders and pavement surface is measured. A normal force of 3.6 kg is applied to the rotating disk and a potentiometer records the tangential force in a spring attached to the rotating disk to calculate the coefficient of friction. The measured coefficient of friction at 20 km/h (DFT_{20}) is often used as indirect method to quantify the surface microtexture as no direct field measurement method has been yet established [22].

The locked-wheel trailer (skid trailer) is the most common method used by various departments of transportation (DOTs) for periodic pavement skid resistance measurements at the network level. The skid trailer is used to measure the skid number in accordance with ASTM E 274 [23]. The skid trailer is towed by a van that travels at a standard testing speed (i.e., 40 or 50 mph), the left wheel of the skid trailer is locked and dragged over the pavement surface while water is sprayed from a nozzle in front of the locked wheel. A force transducer measures the traction between the wheel and the pavement surface and the skid number is calculated as the ratio of friction force to normal force multiplied by 100 [2, 24].

Different friction measurement devices may report different friction values for the same pavement surface. Thus, harmonization of different friction measurements by different devices is necessary. The International Friction Index (IFI) was developed by the Permanent International Association of Road Congress (PIARC) to compare and harmonize different

methods of measuring pavement friction and texture. The IFI is calculated as presented in Equation 3-3 [25].

$$IFI = A + B \cdot FRS \cdot e^{(S-60)/S_p} + C \cdot MPD \quad (3-3)$$

where,

A, B, and C are calibration coefficients for various friction measurement devices

FRS = friction measurement at speed (S)

MPD = mean profile depth

S_p = speed parameter

The speed parameter (S_p) is calculated using Equation 3-4 [26].

$$S_p = 14.2 + 89.7MPD \quad (3-4)$$

The FRS is calculated using Equation 3-5.

$$FR60 = FRS e^{(S-60)/S_p} \quad (3-5)$$

where,

FR60 = friction number at 60 km/h

The IFI can be calculated as a function of coefficient of friction measured using DFT at 20 km/h (DFT_{20}) in accordance with ASTM E 1960-7 [25] (Equation 3-6). The IFI can be used to estimate the skid number measured at 50 mph (SN50) using the locked wheel skid trailer for a smooth standard test tire in accordance with ASTM E 274 [23] as presented in (Equation 3-7) [7].

$$IFI = 0.081 + 0.732 DFT_{20} e^{(-40/S_p)} \quad (3-6)$$

$$IFI = 0.0446 + 0.9255 \left(\frac{SN50}{100} \right) e^{(20/Sp)} \quad (3-7)$$

3.2.2 Previous Models to Predict the Skid Number

Several previous models were developed to predict the SN of pavements as a function of texture measurements. These models are often used to predict SN at the testing speed (e.g., 50 mph) [8]. Meanwhile, to the best of the authors' knowledge, there is no previous research to predict SN at different speeds as a function of texture measurements. Masad et al. [8] developed a model to predict the skid number at a speed of 50 mph (SN50) for asphalt pavements. The model included parameters that describe the aggregate texture and its resistance to polishing and abrasion, mixture gradation, and traffic level. It was found that the model provided good prediction ($R^2 = 0.75$) of SN50 when compared to the field measurement using a locked wheel skid trailer.

Wu et al. [27] developed a prediction model to estimate the friction number at 60 km/h (F60) for flexible pavements. The model was developed by investigating 12 laboratory-prepared mixtures that covered a variety of mix design types and multiple aggregate sources. The Micro-Deval test device was used to evaluate the aggregate resistance to polishing. The dynamic friction tester (DFT) and circular texture meter (CTMeter) were used to measure the microtexture and macrotexture of the test slabs, respectively. Equation 3-8 presents the model developed by Wu et al. [27]. The model is a function of the macrotexture of the pavement surface expressed in terms of MPD and microtexture of the pavement surface quantified by the DFT measurement at 20 km/h (DFT₂₀).

$$F60 = 0.081 + 0.732 DFT_{20} * \exp \left(\frac{-40}{14.2 + 89.7MPD} \right) \quad (3-8)$$

where,

F60 = friction number at 60 km/h

MPD = mean profile depth (mm)

DFT_{20} = measured coefficient of friction at 20 km/h

Rezaei and Masad [28] conducted a study to evaluate the effect of aggregate texture and mix type on asphalt pavement skid resistance. They proposed a statistical model to predict asphalt pavement skid resistance over time during the service life of asphalt pavements. The model incorporated parameters that describe aggregate texture, gradation, and traffic level. These parameters were used to calculate the IFI for different laboratory-prepared HMA slabs, after different intervals of polishing in the laboratory using the three-wheel polisher. In the field the locked wheel skid trailer was used to measure the SN at speed of 50 mph. The predicted skid number at 50 mph (SN50) from the model was found to be a function of IFI and speed parameter (S_p).

Kassem et al. [10] developed a model to predict friction loss of asphalt pavements. The model used parameters to describe the resistance of aggregates to abrasion and polishing, aggregate texture and angularity, aggregate gradation, number of polishing cycles. They used the Aggregate Imaging Measurement System (AIMS) to measure the texture and angularity of aggregates. They examined 24 laboratory-prepared HMA slabs. The HMA slabs were subjected to polishing using a three-wheel polisher for various polishing cycles. After each set of polishing, the DFT and CTMeter devices were used to measure the frictional characteristics of the HMA slabs and calculate the International Friction Index (IFI). Kassem et al. [10] found that the developed model was able to predict the IFI with good accuracy ($R^2 = 0.92$). Equation 3-9 presents the model developed by Kassem et al., [10]. The model parameters (a_{mix} , $a_{mix} + b_{mix}$, c_{mix}) were related to mix and aggregate characteristics.

$$IFI(N) = a_{mix} + b_{mix} * e^{(-c_{mix} * N)} \quad (3-9)$$

where

a_{mix} , $a_{mix} + b_{mix}$, c_{mix} = the terminal, initial, and rate of change of the IFI, respectively N = the number (in thousands) of polishing cycles using the three-wheel polisher.

Chowdhury et al. [29] developed prediction models for IFI and SN50 for both HMA and seal coat surfaces. The models consisted of parameters that described the aggregate shape

characteristics (i.e. texture and angularity), traffic level, aggregate resistance to polishing and abrasion due to traffic repetitions, and the aggregate gradation. The results showed good correlation between field measurements and model predictions.

3.3 Research Objectives

The main objectives of this part of the study were to:

- 1) evaluate the effect of both microtexture and macrotexture on pavement skid resistance of various pavement surfaces,
- 2) validate ASTM equations (Equations 3-6 and 3-7) for measuring IFI and predicting SN50,
- 3) develop a regression-based model to predict SN50 of asphalt pavements and sealcoat based on surface texture measurements to improve the accuracy of SN50 predictions,
- 4) develop a regression-based model to predict the SN change with speed as a function of the pavement macrotexture and microtexture.

3.4 Research Tasks

To achieve the objectives of this study, the researchers conducted the following tasks:

- Task 1: select field pavement test sections. These sites covered a wide range of pavement surface types, traffic levels, aggregate types, and climate conditions.
- Task 2: collect pavement surface macrotexture and microtexture measurements using various methods including the volumetric sand patch test, laser-based methods, and a dynamic friction tester.
- Task 3: collect pavement skid numbers using a locked-wheel skid trailer that used smooth standard tires.
- Task 4: analyze the collected pavement surface texture and friction number measurements and validate the ASTM equations for measuring IFI and predicting SN50.
- Task 5: develop a revised statistical model to predict SN50 as a function of pavement surface texture (i.e., MTD and DFT₂₀).
- Task 6: develop a regression-based model to predict SN of pavements at different speeds as a function of pavement macrotexture and microtexture.

3.5 Research Methodology

The frictional and surface characteristics of 83 test sections in Idaho and Texas were studied in this research. The research team conducted field testing for 22 test sections in Idaho as part of the ITD research project 266. In addition, the friction surface characteristics data for 61 sections in Texas, measured in a previous research project [TxDOT research project 0-6746 [29], were included in this study. These test sections included various pavement types. Figure 3-1 shows examples of various pavement types included in this study. The test sections included 41 Hot Mix Asphalt (HMA), 39 seal coat and three Portland Cement Concrete (PCC) sections. The HMA sections had various surface mix designs (e.g., dense-graded, stone matrix asphalt [SMA], porous friction courses [PFC], etc.). These sections were constructed using different aggregates, different traffic levels and were distributed across the two states as described in Table 3-1. A locked wheel skid trailer was used to measure the SN at 50 mph for all test sections in Texas included in this study. For the test sections in Idaho, the SN was also measured at four additional speeds (i.e. 20, 30, 40, and 60 mph) using the locked wheel skid trailer. Surface microtexture and macrotexture were measured at a minimum of four different locations along the left wheel path of the outside lane as show in Figure 3-2. The average value of these four measurements was reported for each test section. It should be noted that more measurements were taken on some sites.

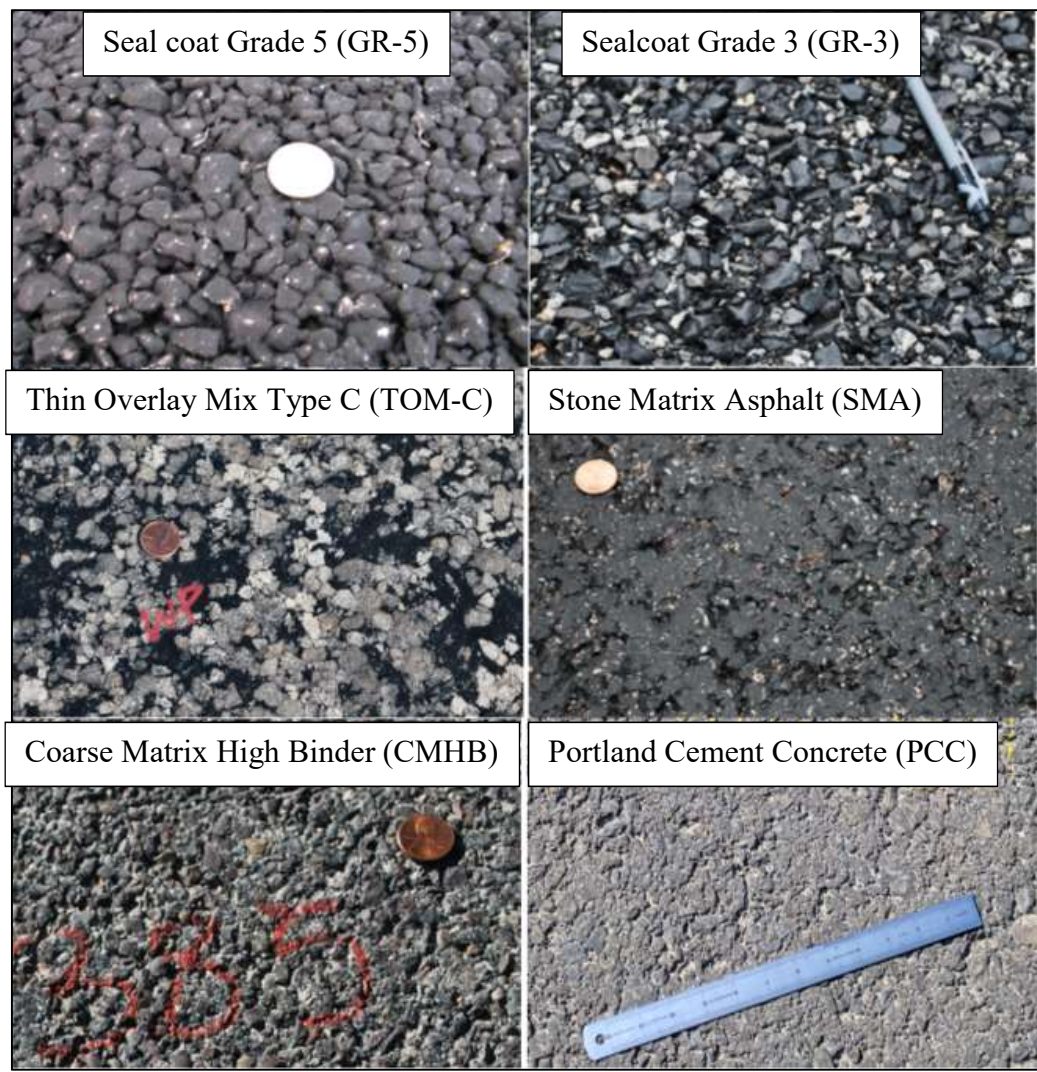


Figure 3-1. Examples of different pavement types examined in this study

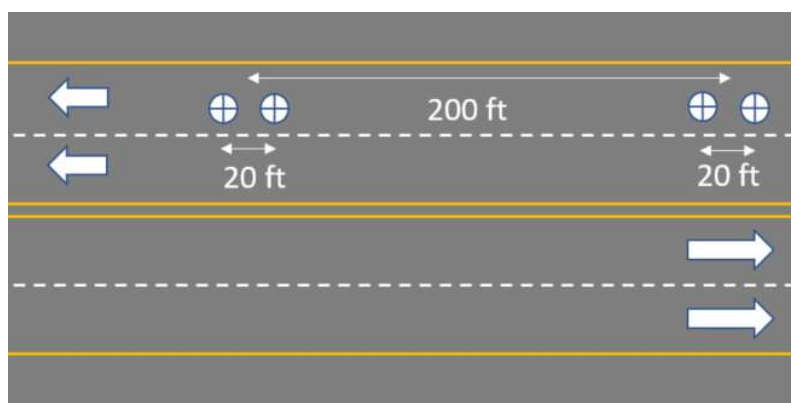


Figure 3-2. Schematic of location of texture measurements

Table 3-1. Characteristics of evaluated pavement sections in this study

Parameters	Levels
Aggregate Type	Limestone, basalt, river gravel, dolomite, quartzite, sandstone
Mix design	Superpave type 3 (SP3) [30], SP5 [30], Stone Matrix Asphalt (SMA-C) [31], SMA-D [31], Poursous Friction Coarse (PFC) [31], Sealcoat GR-3 [31], Sealcoat GR-5 [31], Thin Overlay Mix (TOM-C) [31], TOM-F [31], Coarse Matrix High Binder (CMHB-F) [31], Portland Cement Concrete (PCC) [30]
Traffic Level (AADT)	300 to 29,000
Geographic Location	Idaho and Texas
Roadway type	Interstate highways, U.S highways, state routes, farm to market roads

3.5.1 Measuring Pavement Surface Characteristics

3.5.1.1 Measuring Pavement Microtexture

The dynamic friction tester (DFT) is a stationary portable device that is used to measure friction in terms of the coefficient of friction (μ). The DFT device consists of a horizontal flywheel and disc that are connected to a drive motor. Three rubber sliders are attached to the bottom of the DFT disk as shown in Figure 3-3c. The rubber sliders consist of a steel plate and a piece of standard rubber (6 mm x 16 mm x 20 mm) attached to the plate. The drive motor rotates the DFT disk to the desired speed (up to 100 km/h). Once the disk reaches the desired speed, water is sprayed on the surface with a constant rate of 0.95 gal/min. Then the disk is dropped on the surface allowing the rubber sliders to be in contact with the surface, and the coefficient of friction is measured continuously as the speed of the rotating disk decreases. A computer connected to the DFT is used to record the results. There is no well-established method to measure pavement microtexture directly, instead pavement microtexture is

estimated indirectly by measuring the coefficient of friction (μ) using the dynamic friction tester (DFT) at 20 km/h (ASTM E 1911) [21]. In the field, the DFT device was placed on the left wheel path of the outermost lane (Figure 3-3). The test was conducted in wet conditions where water is sprayed from nozzles around the perimeter of the DFT device at a constant rate. The average value of the DFT_{20} (coefficient of friction at 20 km/h) was calculated and used as a measure of surface microtexture [22]. Figure 3-4 shows an example of the change of coefficient of friction with the speed of the DFT. In general, the coefficient of friction decreased slightly with increasing speed of the DFT. However, such change depends on both macrotexture and microtexture of pavement surface [31].

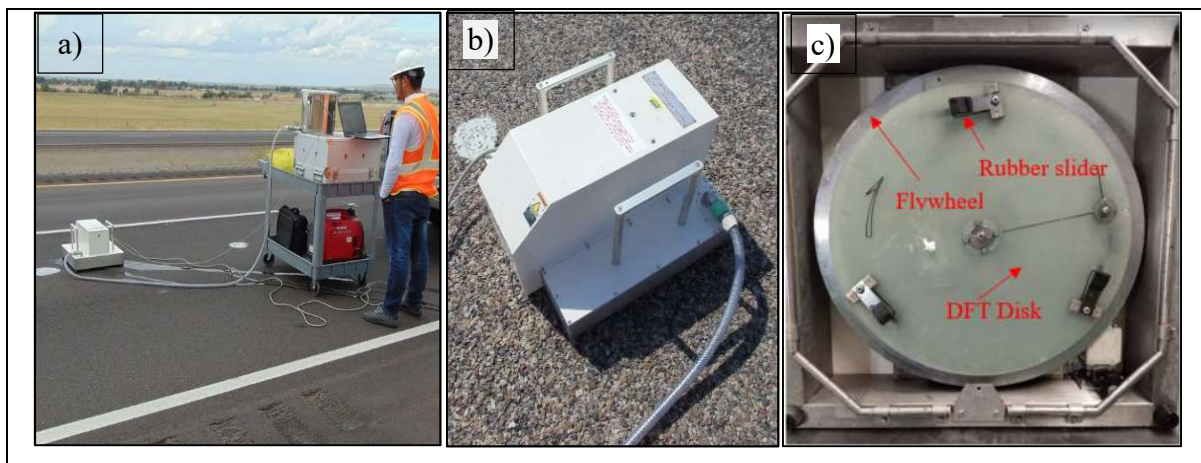


Figure 3-3. Measuring surface coefficient of friction using DFT device

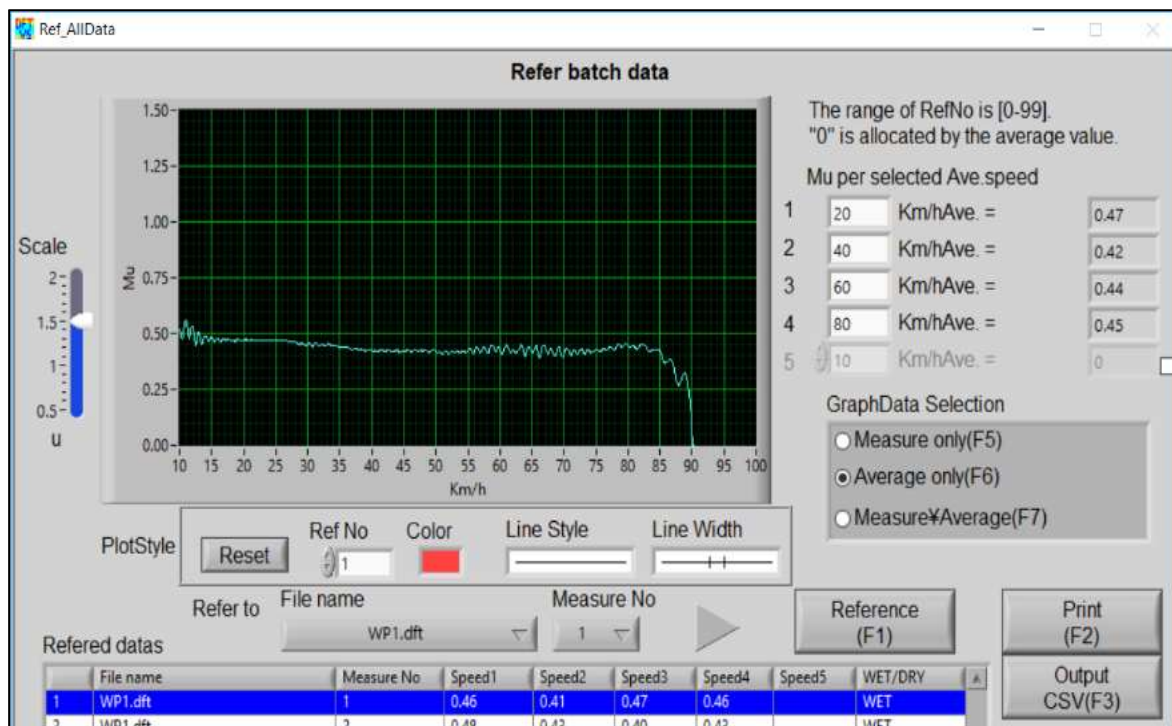


Figure 3-4. An example of the change in coefficient of friction with DFT test speed

3.5.1.2 Measuring Pavement Macrotexture

The skid van used in Idaho is equipped with a laser profiler to measure the macrotexture during skid testing, while the skid trailer used in Texas was not equipped with a laser profiler. Instead, a CTMeter device was used to measure the macrotexture of test sections in Texas. The MPD was measured at the same locations shown in Figure 3-2. The CTMeter uses a charged coupled device (CCD) laser displacement sensor to scan a circular strip of pavement surface. The average MPD in millimeters along with the root mean square (RMS) are calculated for each test section. In addition to the laser technique, the researchers used the volumetric sand patch test (ASTM E 965-15 [13]) to measure surface macrotexture for test sections in Idaho. The sand patch test measures the mean texture depth (MTD), while the laser profiler and CTMeter measure the MPD. Figure 3-5 shows test methods used to measure the surface macrotexture. The results of the macrotexture from both measurement methods were compared to observe any variations of the macrotexture measurements.

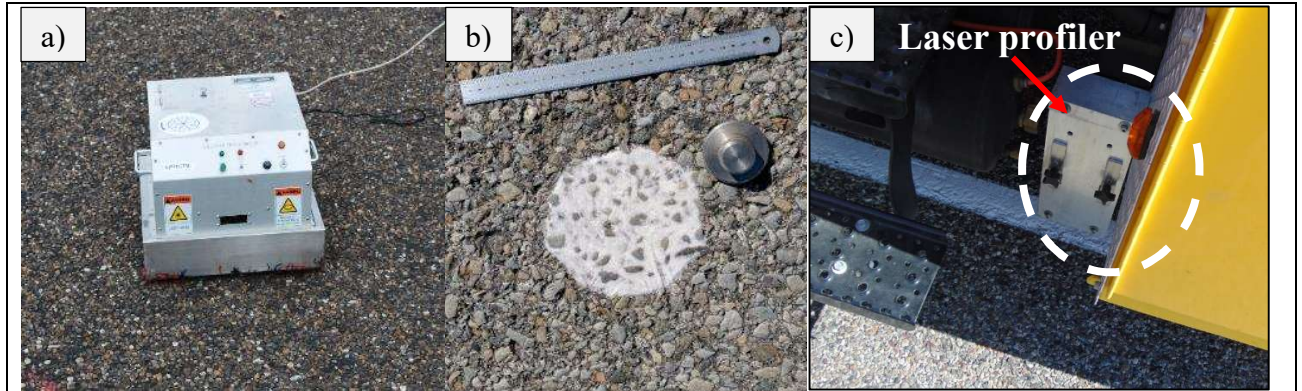


Figure 3-5. Measuring pavement macrotexture using; a) CTMeter device, b) sand patch test, c) laser profiler

The volumetric sand patch test (Figure 3-6) is a simple test method to measure the macrotexture of pavement surfaces. This test is conducted in accordance with ASTM E 965 [13]. The surface macrotexture is measured in terms of the mean texture depth (MTD). The tools and materials needed to perform this test include silica sand, graduated cylinder, cleaning brush, ruler, and spreader. The test surface is cleaned using a cleaning brush and a known volume of sand is spread over the surface uniformly in a circular motion to create a circular patch of silica sand. The diameter of the circular patch is measured at four different points using a ruler and the average diameter for the patch is calculated. The MTD is calculated using Equation 3-10.

$$\text{MTD} = 4V/(\pi D^2) \quad (3-10)$$

where,

MTD = mean texture depth (mm)

V = sand volume (mm³)

D = average diameter of sand patch circle (mm)

The sand patch test was performed at the same locations the DFT measurements were collected as shown in Figure 3-2. The average value of the MTD was reported for each test

section. The macrotexture for all the test sections in Idaho were reported in terms of the MTD. For the test sections in Texas, the measured MPD using the CTMeter was converted to corresponding MTD values using Equation 3-2 according to ASTM E 2157-15 [14].



Figure 3-6. Typical measurement of pavement macrotexture using the sand patch test

3.5.1.3 Measuring Skid Resistance Using Skid Trailer

In this study, the SN was measured using a locked-wheel skid trailer with a smooth tire in accordance with ASTM E 274 [23] (Figure 3-7). The SN was measured at 50 mph for all the test sections in this study (standard test speed in Texas). In Idaho, the SN was measured at additional speeds (i.e., 20, 30, 40, and 60 mph) with exception of two test sites where it was not possible for the crew to measure the skid number at 60 mph due to the speed limit and geometry of the test sections. The SN was measured at various speeds in Idaho to study the effect of test speed on SN. The SN measurements using the skid trailer were collected in wet conditions where water was sprayed in front of the tire of the skid trailer in accordance with ASTM E 274. In this test, the left wheel of the skid trailer is fully locked during the SN measurements. An automatic trigger system was placed by the side of the road to ensure that the skid number measurements were recorded over the same area where the DFT and sand patch data were collected.



Figure 3-7. Locked wheel skid trailer and standard smooth test tire used in Idaho

3.6 Data Analysis and Results

3.6.1 Predicting SN50 Using Surface Texture Characteristics

Pavement surface friction is affected by both microtexture and macrotexture. Pavement microtexture was quantified indirectly by measuring the value of DFT_{20} while macrotexture was measured in terms of the surface mean texture depth (MTD). Figure 3-8 and Figure 3-9 show the relationship between SN50 and microtexture and macrotexture, respectively for all test sections included in this study. The results demonstrated that microtexture had better correlation with SN50 for all test sections compared to macrotexture. The analysis of variance between the measured DFT_{20} and SN50 showed that there was a significant correlation between the two parameters (p -value = 0.001). Similarly, the analysis of variance between the measured MTD and SN50 was also significant (p -value = 0.024) as presented in Table 3-2. These findings are in agreement with the findings of previous studies where both microtexture and macrotexture have significant effect on skid resistance [2, 7, 10, 29]. The microtexture was found to control the magnitude of friction, while the macrotexture affects the speed gradient of friction [2].

The MTD measured using sand patch test was found to have a strong linear relationship with the MPD measured using laser as shown in Figure 3-10. The R^2 for this correlation was 0.99. It should be mentioned that two seal coat test sections in Idaho were excluded from this study due to bleeding of asphalt binder on the surface of the pavement.

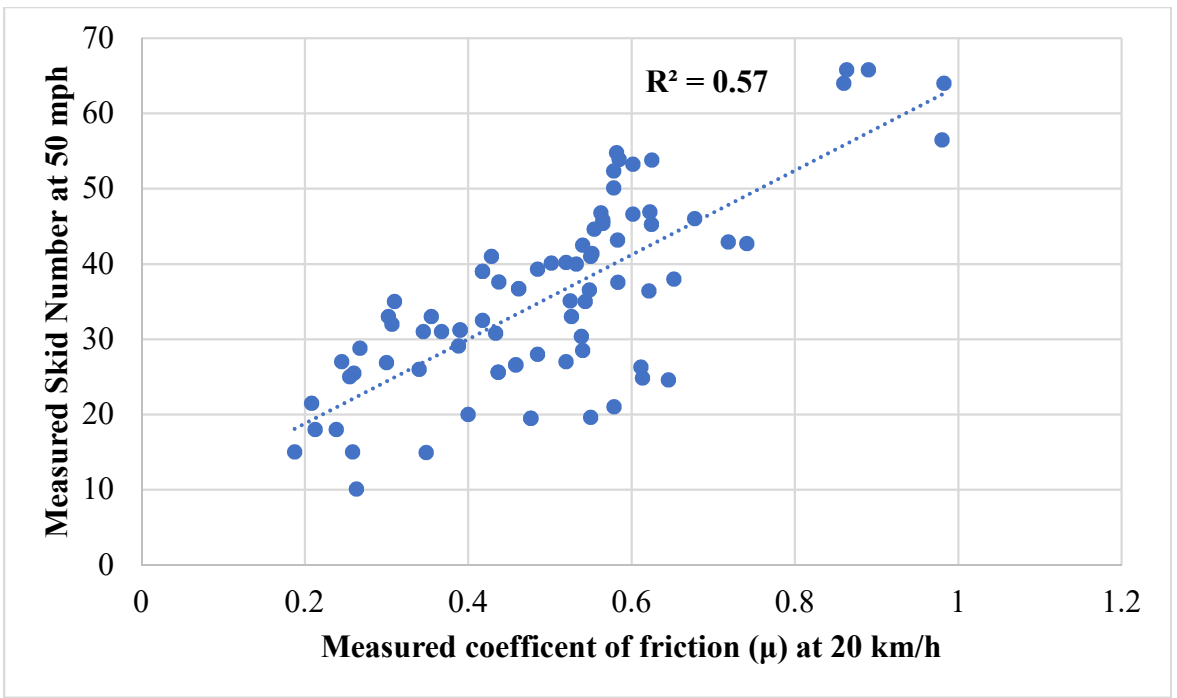


Figure 3-8. Measured skid number at 50 mph vs. measured coefficient of friction at 20 km/h (DFT₂₀)

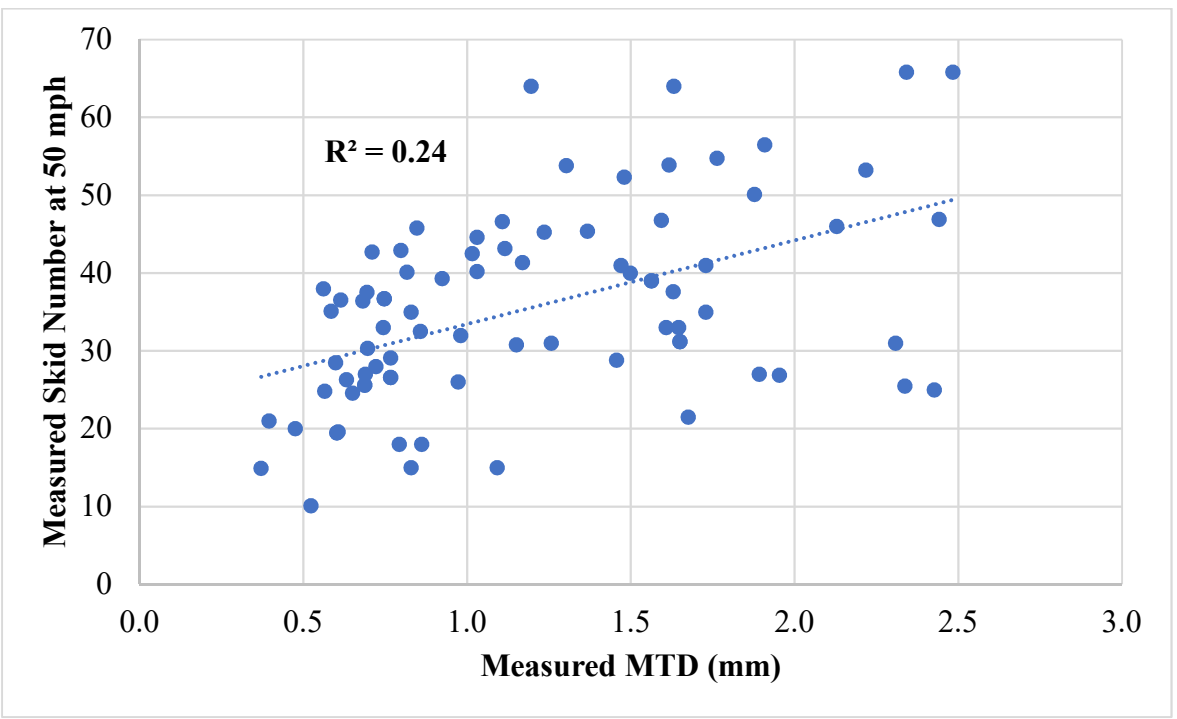
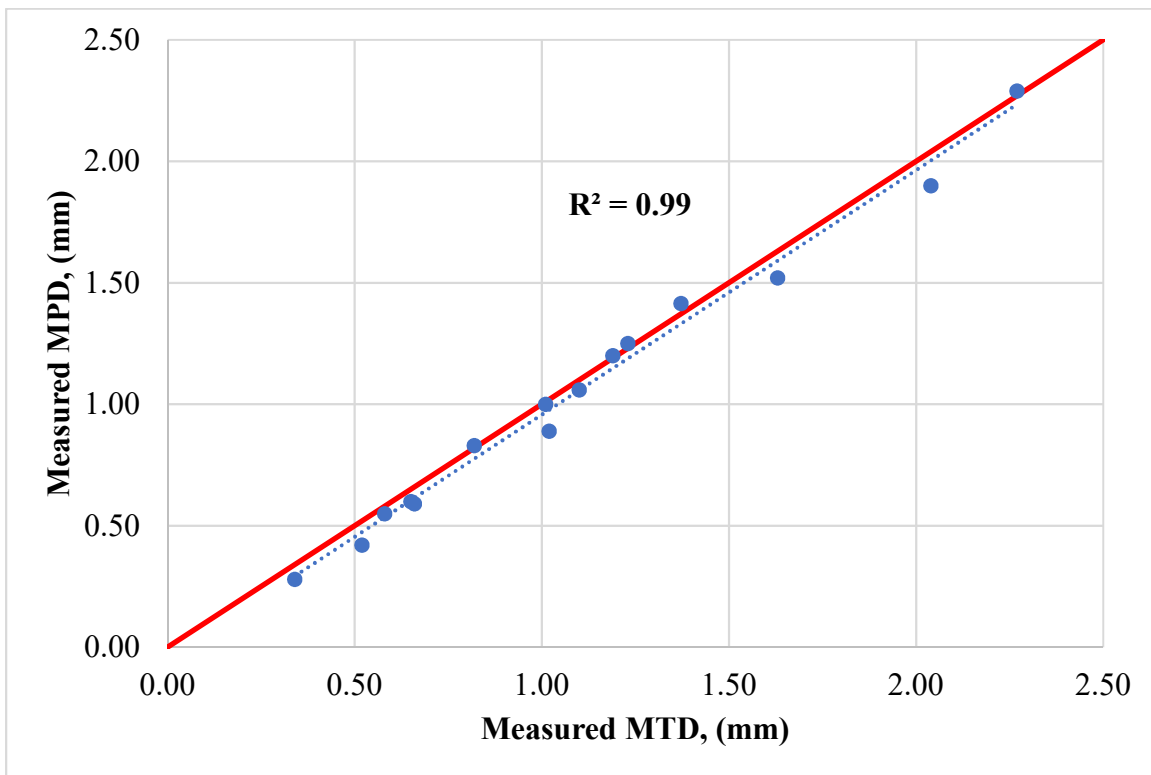


Figure 3-9. Measured skid number at 50 mph vs. measured surface MTD

Table 3-2. Analysis of variance (ANOVA) between measured SN50 and DFT₂₀ and MTD

Coefficient of friction (μ) (DFT₂₀)					
Source	Sum of Squares	Degrees of Freedom	Mean Squares	F	p-value
Measurement	2.158	65	0.034	4.864	0.001
Error	0.111	16	0.007		
Total	2.268	81			
Mean Texture Depth (MTD)					
Measurement	23.446	65	0.366	2.468	0.024
Error	2.375	16	0.148		
Total	25.821	81			

**Figure 3-10.** Measured MPD vs. MTD for test section in Idaho

The IFI was calculated as a function of microtexture and macrotexture in accordance with Equation 3-6. Then, the IFI values were used to calculate SN50 using Equation 3-7. The

calculated SN50 values were then compared to the measured ones in the field using the skid trailer as shown in Figure 3-11. The results demonstrated that the predicted SN50 values were lower than the ones measured in the field. In other words, Equations 3-6 and 3-7 underestimated SN50 values. Based on these results and in order to improve the accuracy of SN50 predictions, the researchers developed a revised equation to estimate the SN50 using nonlinear regression analysis. The revised model is also a function of MTD and DFT₂₀ measurements as presented in Equation 3-11.

$$\text{SN50} = -37.971 + (114.889 \text{ DFT}_{20}^{0.352}) e^{[-0.1805/(1.056\text{MTD} - 0.069)]} \quad (3-11)$$

where:

DFT₂₀ = coefficient of friction measured at 20 km/h

MTD = mean texture depth (mm)

Data from 71 test sections were selected randomly and included in the development of Equation 3-11, while, data from the remaining 10 test sections were used to validate the model as shown in Figure 3-12. The revised model provided improved accuracy with low bias and standard errors as shown in Figure 3-11 and Figure 3-12. The revised model (Equation 3-11) has lower bias (0.33) and standard error (4.487) compared to the original ASTM equations (Equations 3-6 and 3-7) which had higher bias (10.30) and standard error (5.233). The analysis also showed that both DFT₂₀ and MTD are statistically significant at a 95% confidence interval with p-value close to zero for both parameters ($p < 0.05$).

A diagnostic check of the regression model was performed to check for the normality and linearity of the model as shown in Figure 3-13 and Figure 3-14. The Q-Q plot of the residuals were linearly distributed along the normal quantile line which confirms the linearity of the model residuals. Similarly, the histogram of the residuals was symmetric with a mean close to zero (residuals mean = 0.09) and the residuals followed a normal distribution shape.

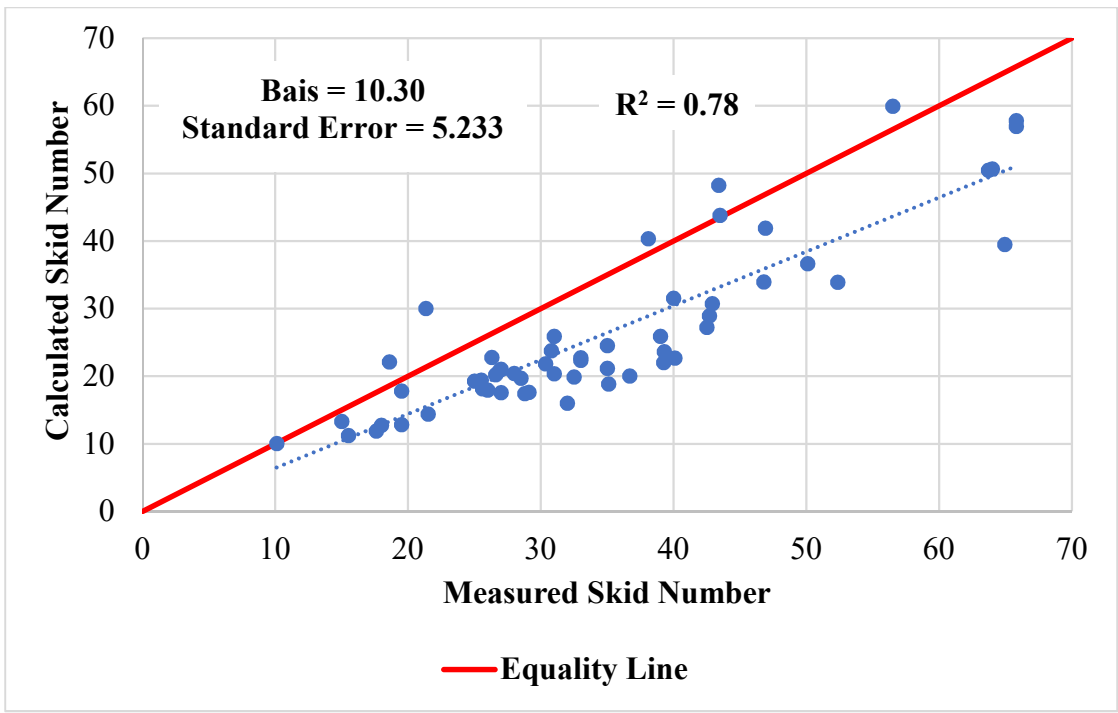


Figure 3-11. Measured skid number vs. calculated skid number using Equation 3-7

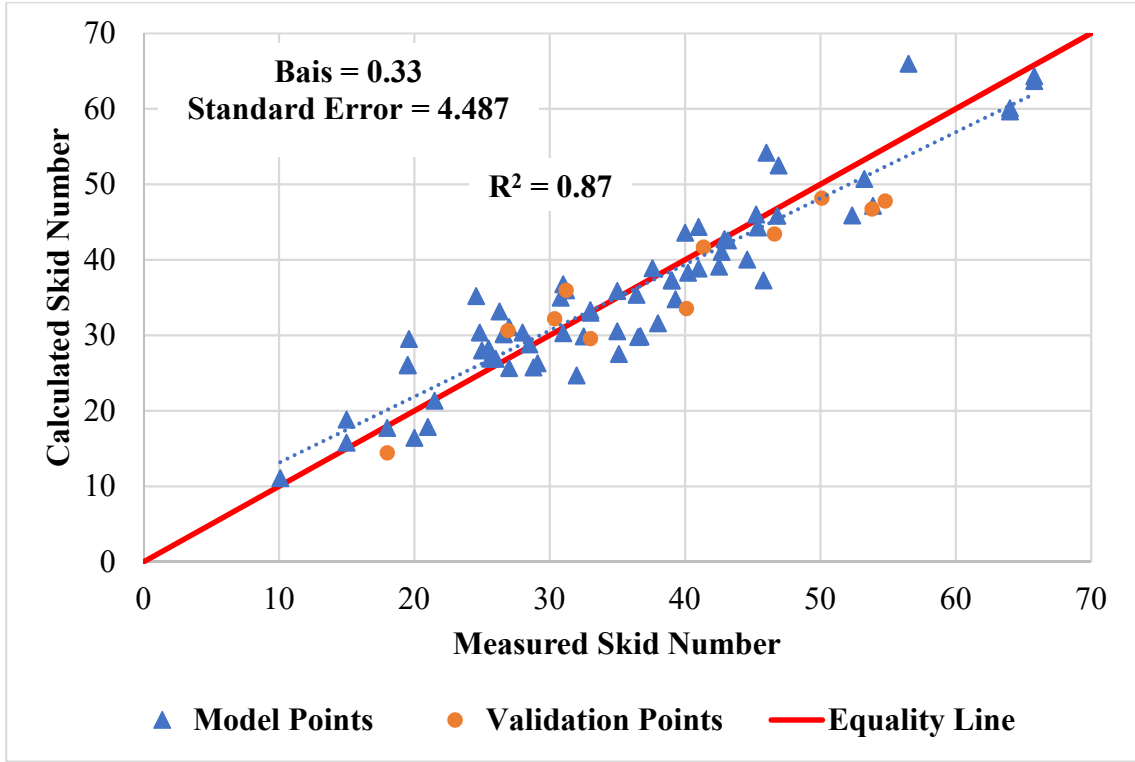


Figure 3-12. Relationship between measured and calculated skid number

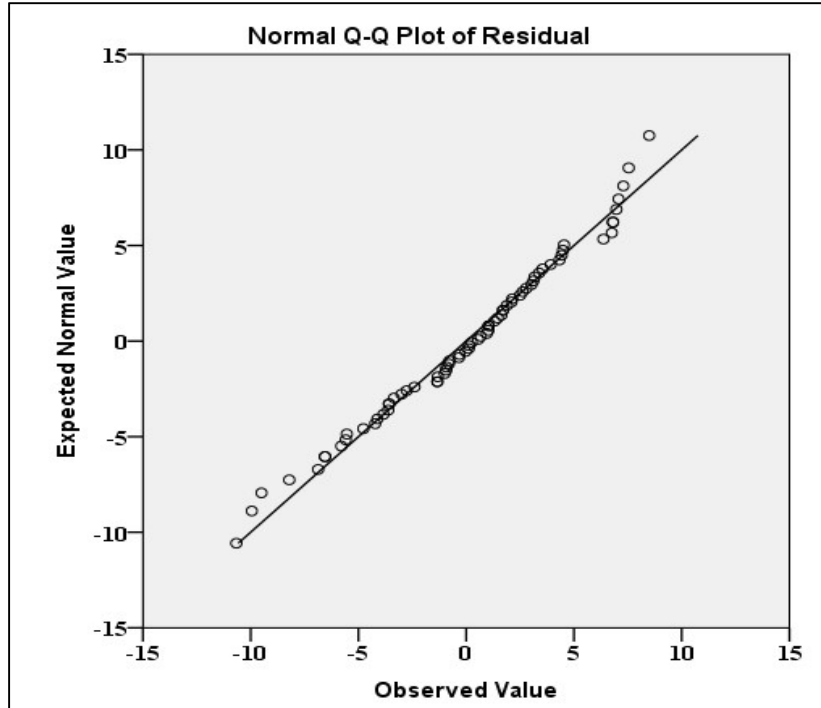


Figure 3-13. Residual vs. predicted values for the SN prediction model Q-Q plot

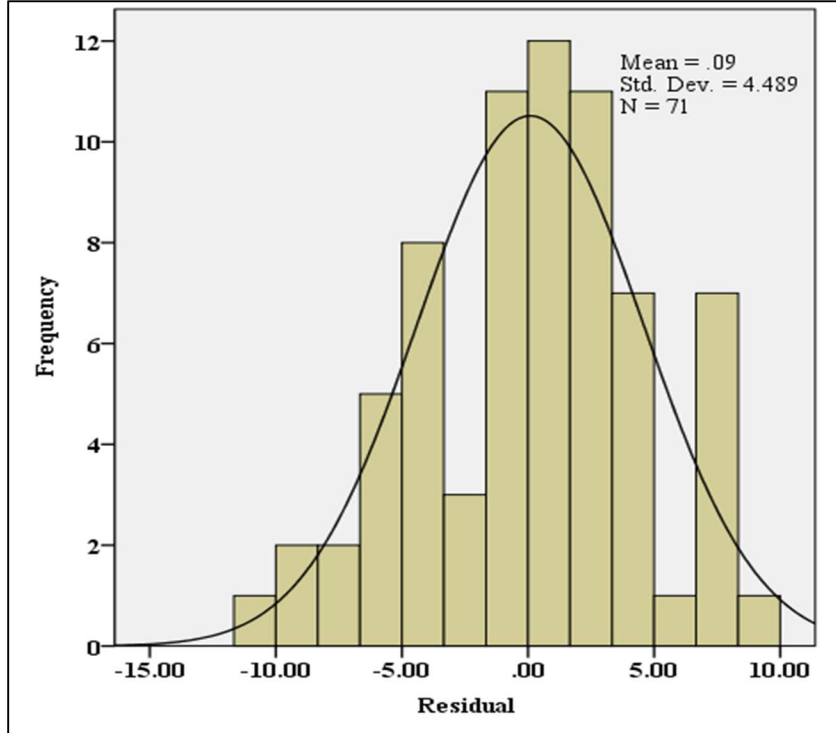


Figure 3-14. Distribution of the residuals

A sensitivity analysis of the model parameters was performed to investigate the effect of each parameter on the predicted SN50 as shown in Figure 3-15. The results show that SN50 increases nonlinearly with both DFT₂₀ and MTD. In addition, the microtexture or DFT₂₀ had a greater effect on the predicted SN50 compared to macrotexture or MTD which is in good agreement with previous studies [1-3]. Such models can be used in the mix design stage to ensure that a given pavement has adequate skid resistance or proper skid number. Microtexture or DFT₂₀ depends on aggregate type [10, 12, 29], while MTD is a function of aggregate gradation [28-29]. Thus, one can select a proper aggregate source or type and aggregate gradation or mix design to provide an adequate level of friction.

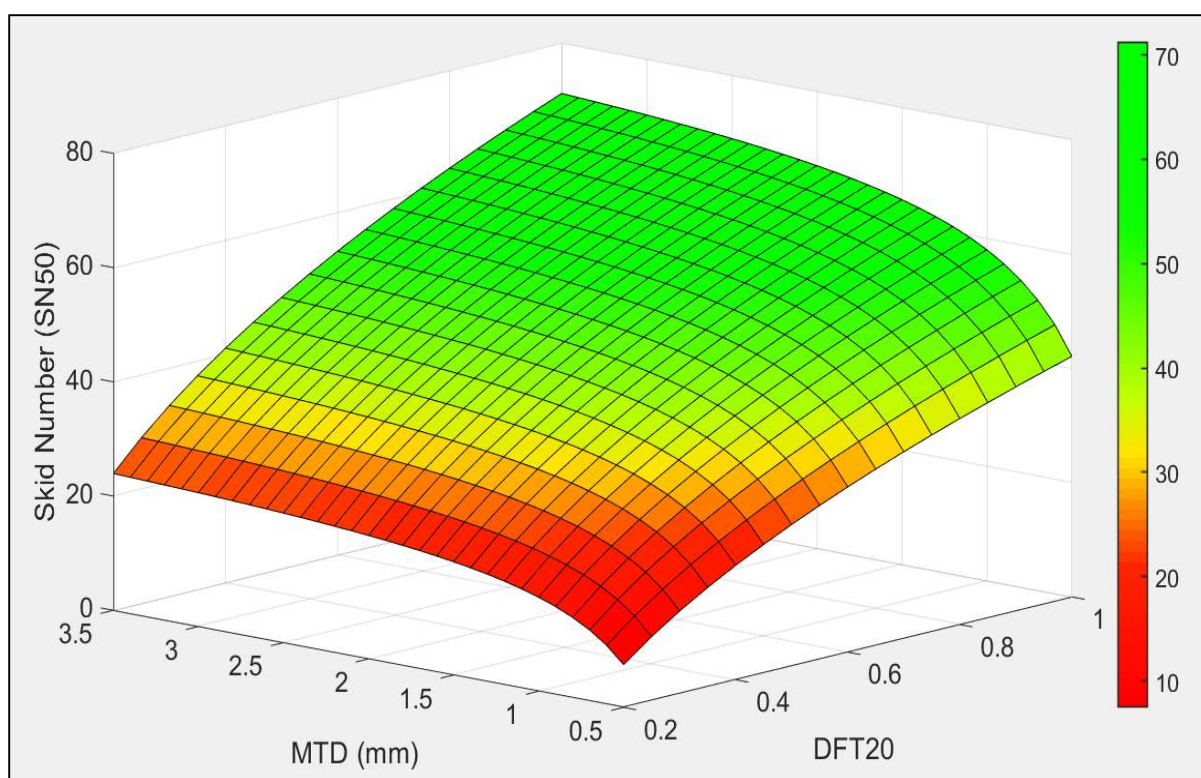


Figure 3-15 Parametric analysis of the developed SN50 prediction model

3.6.2 Predicting SN of Pavements at Different Speeds Using Surface Texture Characteristics

As mentioned earlier, the skid number was collected at different speeds (i.e., 20, 30, 40, 50, and 60 mph) for the test sections in Idaho. In addition, the measurements of macrotexture and microtexture using the sand patch test and the measured DFT₂₀ respectively, were used to

develop a prediction model for the SN as a function of speed and both macrotexture and microtexture.

It is well established that both microtexture and macrotexture are significant in determining the level of skid resistance of pavements [1, 2, 8-10, 14, 22, 29], and the SN is a function of the combined effect of both. Figure 3-16a shows the correlation between the measured MTD and SN while Figure 3-16b shows the correlation between the DFT₂₀ and SN for the Idaho test sections. It can be seen that the MTD had a better correlation ($R^2 = 0.71$) with SN while the DFT₂₀ did not exhibit correlation with SN. This could be attributed to the narrow range of the measured DFT₂₀ values in the field for the test sections in Idaho since most aggregates in Idaho have good microtexture. It should be noted that the SN is affected by the combination of both MTD and DFT₂₀.

Figure 3-17 shows an example of the change in SN with speed for two test sections; one with high macrotexture (2.29 mm) and the other with low macrotexture (0.56 mm). These two sections have comparable microtexture or DFT₂₀. The skid resistance decreased with speed for both sections; however, the test section with low macrotexture had a steep slope compared to the test section with higher macrotexture. These results are in good agreement with the findings of previous results where the macrotexture was found to control the rate of change of skid number in previous research studies [2].

Figure 3-18 shows the change of SN with speed for two test sections; one with higher microtexture (DFT₂₀ = 0.63) and the other with a lower microtexture (DFT₂₀ = 0.52). These two test sections have comparable macrotexture (1.22 and 1.30 mm). Both test sections showed a comparable rate of decrease in SN with speed. The section with higher microtexture had a higher SN when compared to the section with low microtexture. The results are in agreement with previous findings where the microtexture was found to dictate the magnitude of SN for pavement surfaces [2].

The collected SN measurements were found to have a standard deviation as high as 6.7 depending on pavement type and test speed. The error bars in Figures 3-17 and 3-18 present the standard deviation (\pm one standard deviation) of the collected SN in the field at each test speed.

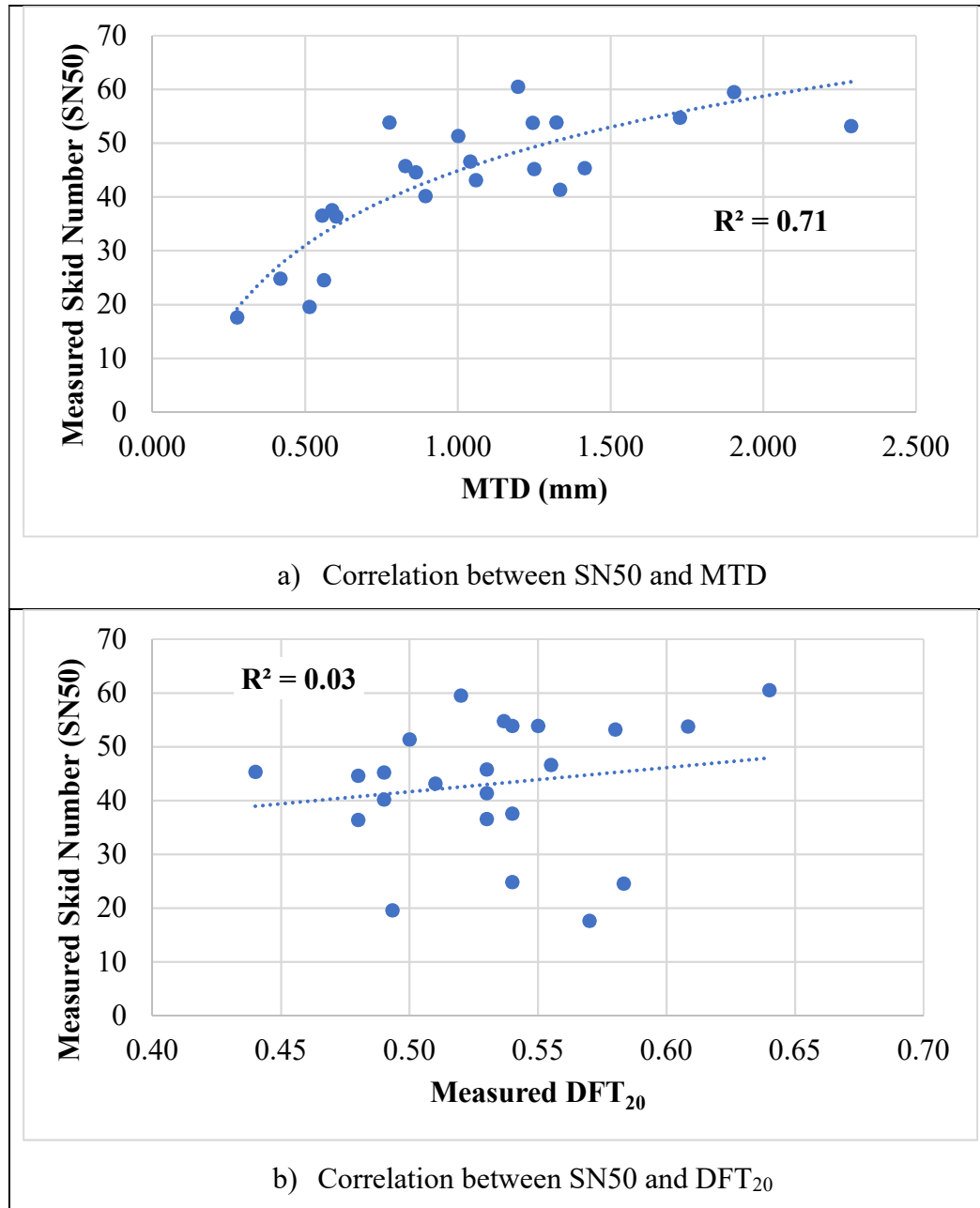


Figure 3-16. Correlation between MTD and DFT_{20} with SN measures at 50 mph

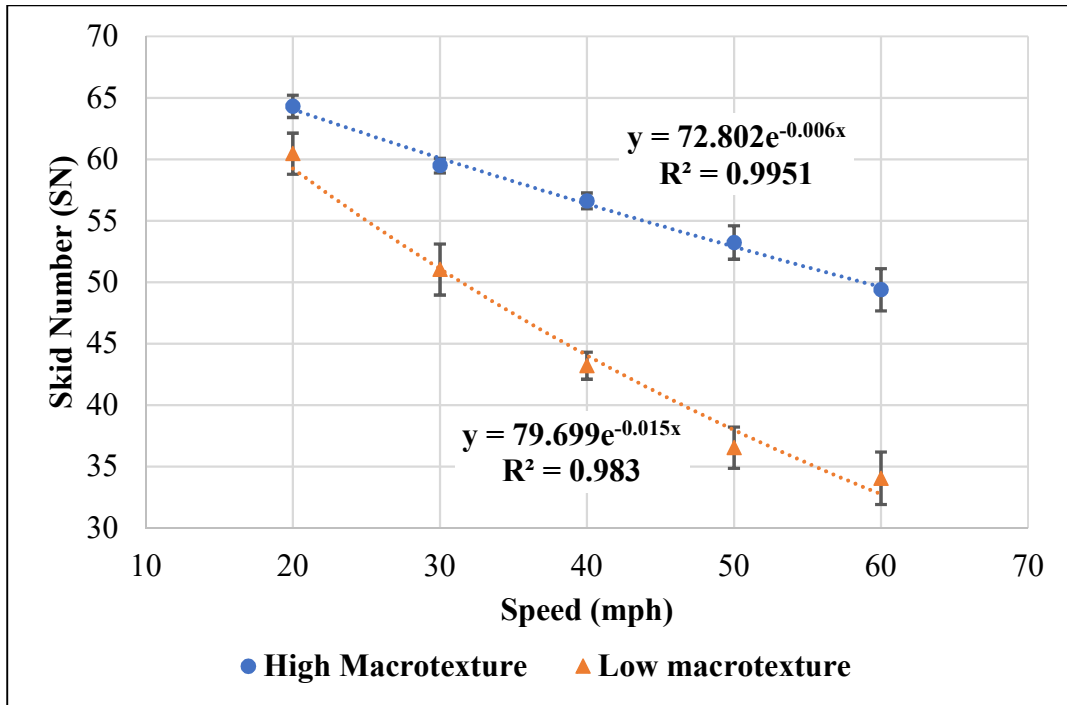


Figure 3-17. Change of SN with speed for sections with low and high macrotexture.

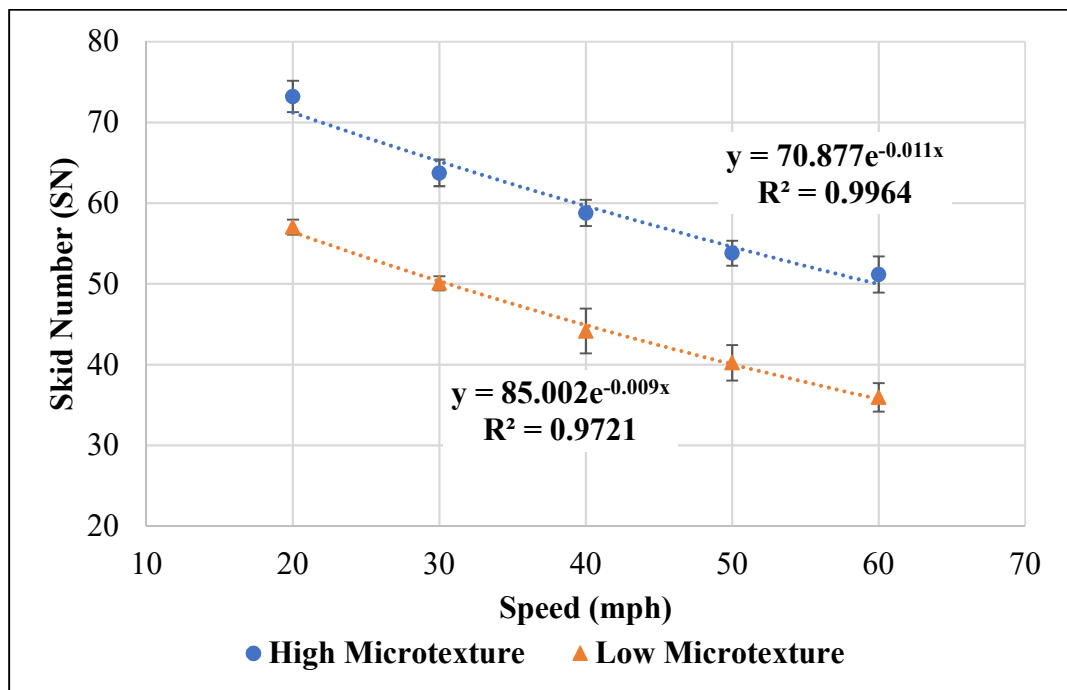


Figure 3-18. Typical change of measured SN with speed for test sections with lower and higher microtexture.

The author developed a statistical-based model to predict the skid number (SN) with speed. Equation 3-12 presents the proposed model for SN as a function of speed, and surface macrotexture and microtexture.

$$SN = 157.733 DFT_{20} e^{\left(\frac{-0.309(V/40)}{MTD}\right)} - 9.631 \quad (3-12)$$

where,

DFT_{20} = coefficient of friction measured at speed of 20 km/h

MTD = mean texture depth measured in mm

V = speed measured in mph

Figure 3-19 shows the correlation between predicted versus measured skid number at various test speeds for all test sections. The results demonstrate that there is a very good correlation ($R^2 = 0.83$) between predicted and measured skid number. The model provides a prediction interval of ± 9.6 at 95% confidence level. A diagnostic check was performed on the developed model as shown in Figure 3-20. The residuals were normally distributed with no significant skewness or bias and there is no pattern for the residuals as the measured SN changes.

The proposed model predicts the SN as a function of three parameters (i.e., speed, macrotexture, and microtexture). The author performed a sensitivity analysis on model parameters. Figure 3-21 shows that at a given speed, the SN increased with both macrotexture and microtexture. At low microtexture, the change in macrotexture had less effect on the predicted SN, while the effect of macrotexture was more evident at high microtexture. Figure 3-22 illustrates the effect of microtexture and speed on the predicted SN. The SN decreased with speed and the change in SN with speed was more evident at high microtexture compared to low microtexture. Figure 3-23 shows the effect of macrotexture and speed on predicted SN. It was found that the rate of change in SN with speed (speed gradient) is a function of the macrotexture where pavements with higher macrotexture had lower speed gradient when compared to pavement with lower macrotexture. These findings are in agreement with previous studies in the literature [2, 29].

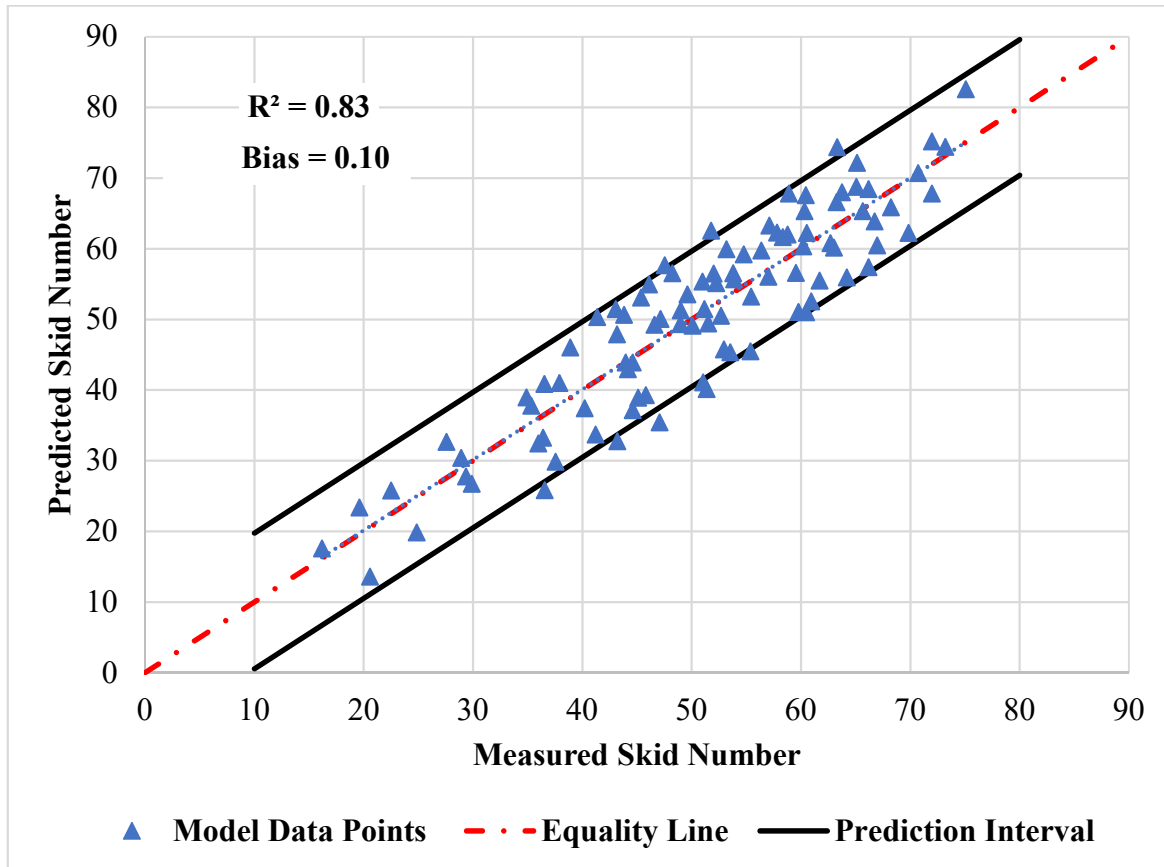
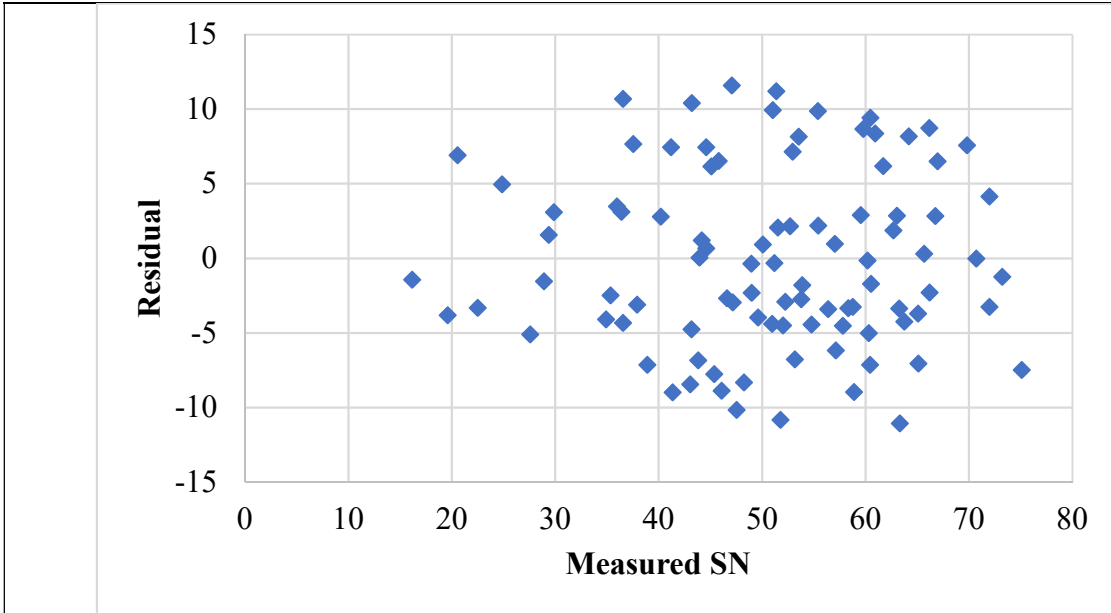
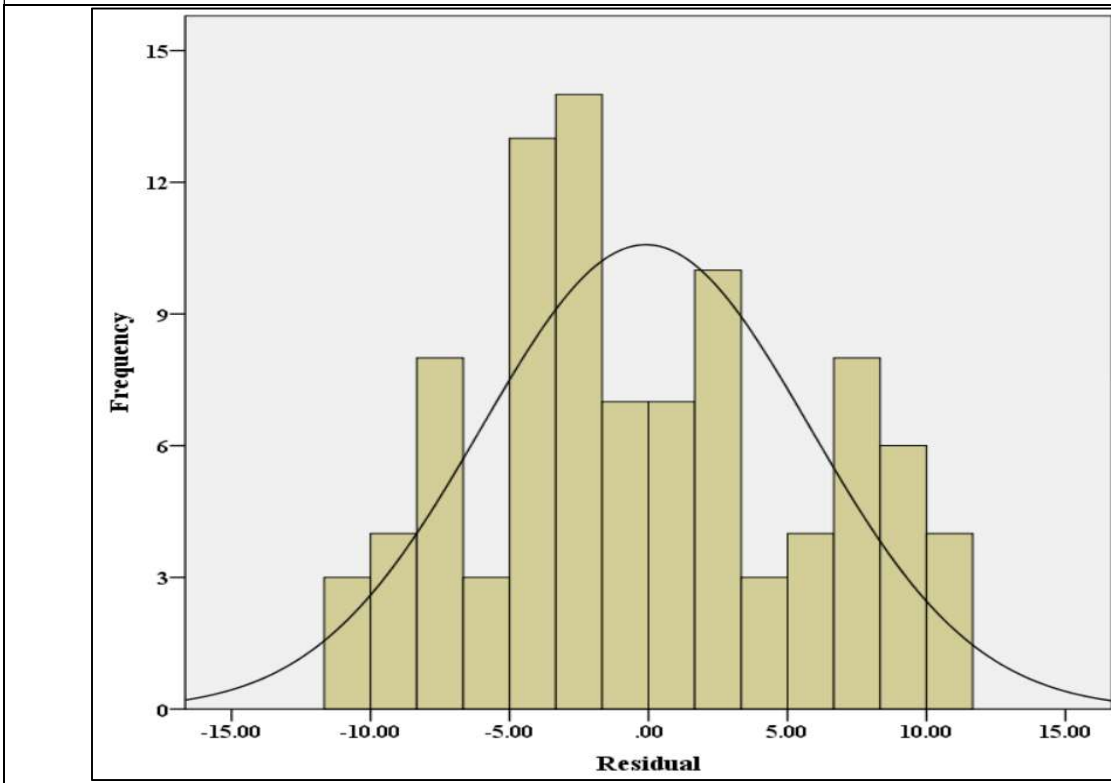


Figure 3-19. Relationship between measured and calculated skid number at different speeds



(a) Residual plot showing a random pattern of prediction errors



(b) Histogram of residuals distribution

Figure 3-20 Diagnostic check of the normality of the developed model

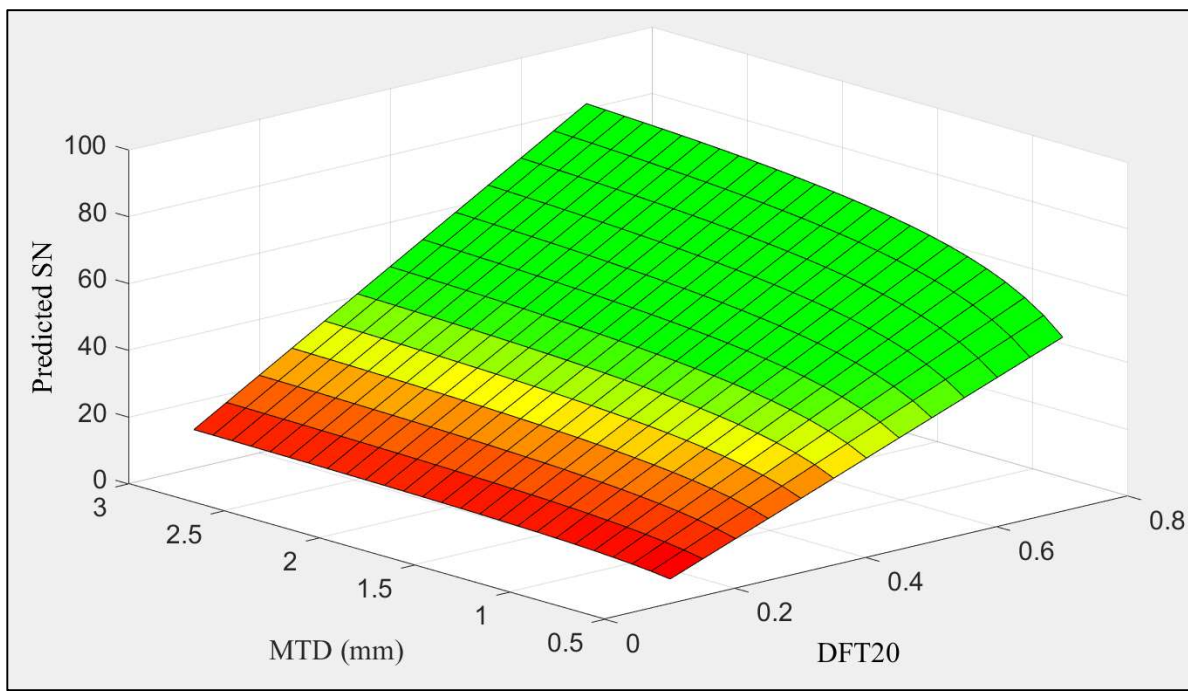


Figure 3-21. Combined effect of MTD and DFT₂₀ on the predicted SN at a given speed

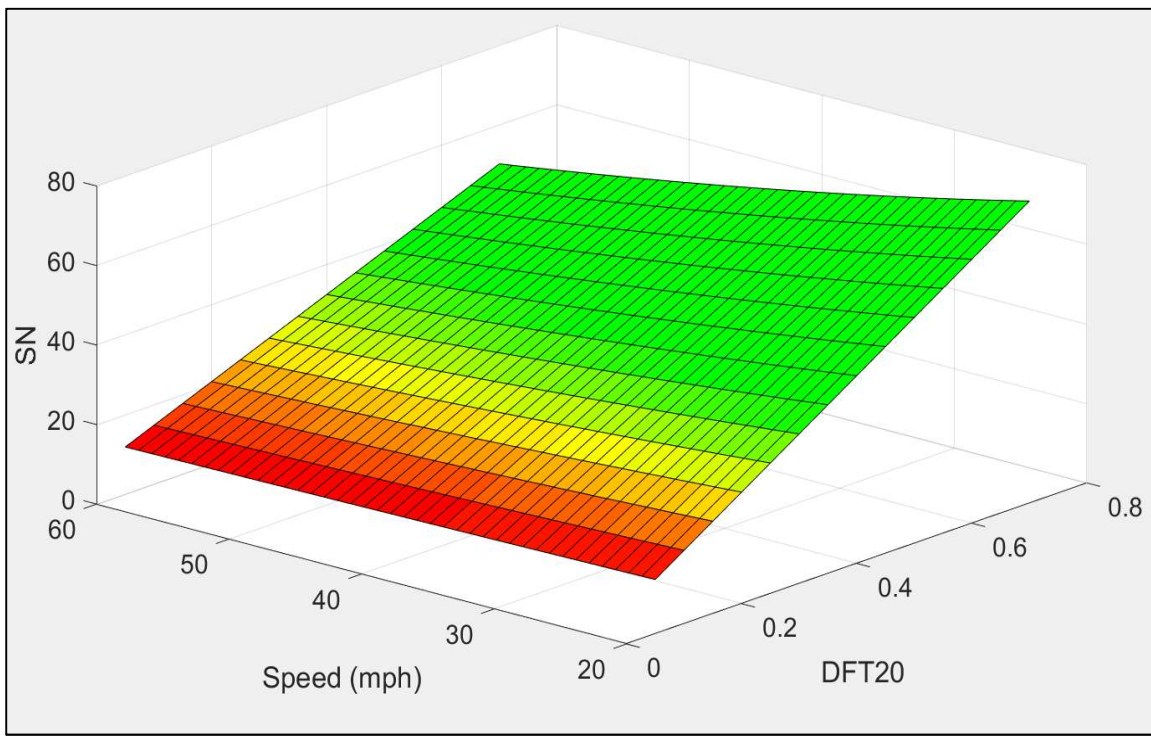


Figure 3-22. Combined effect of speed and DFT₂₀ on the predicted SN

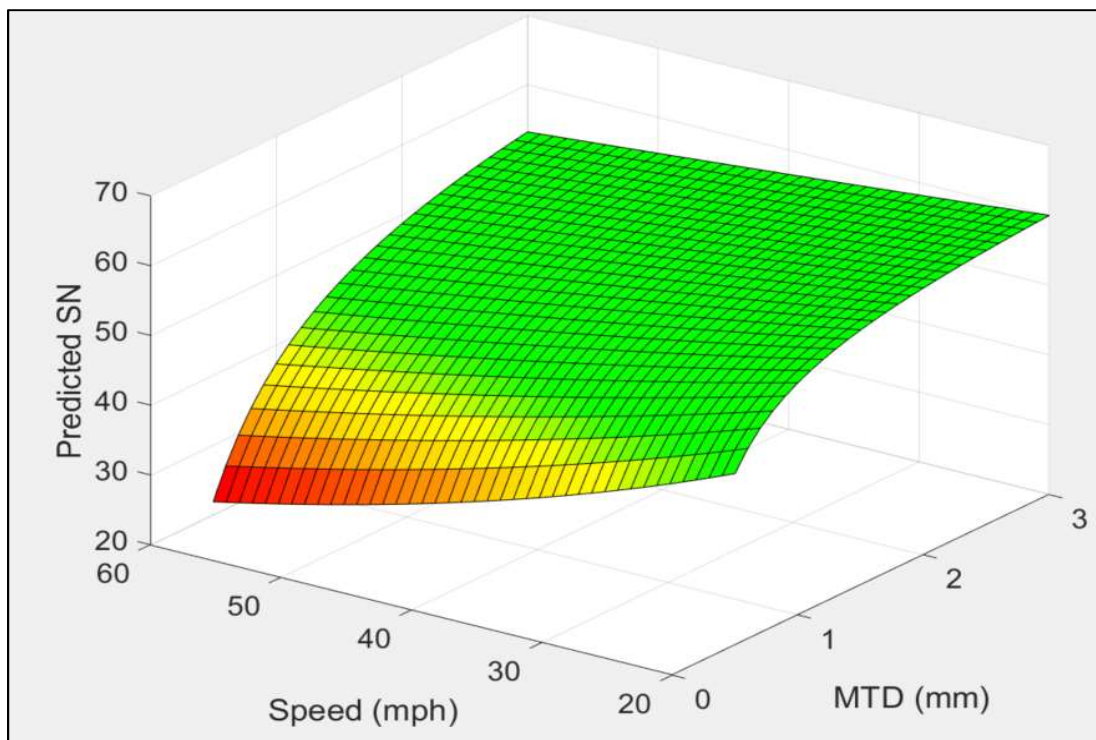


Figure 3-23 Combined effect of speed and MTD on the predicted SN

3.7 Conclusions and Recommendations

This study examined the frictional properties of pavement test sections with different characteristics. The MTD and DFT_{20} were used to describe the surface macrotexture and microtexture, respectively. The skid number was measured using a skid trailer with a smooth tire at 50 mph for all test sections. For the test sections in Idaho, the SN was measured at additional speeds of 20, 30, 40 and 60 mph. This study found that the current standard equation used in ASTM E 274 underestimates skid number predictions. The researchers developed a revised model that was found to correlate better with the measured skid number and reduce the bias in the existing model. The revised model was developed based on frictional surface characteristics of 71 test sections distributed in Idaho and Texas. The model was validated using frictional surface characteristics of 10 additional test sections. The revised model can be used to accurately predict the skid number as a function of both macrotexture and microtexture of a given surface. This is very useful to transportation agencies to ensure adequate skid resistance of pavements. Proper aggregate type and mix design can be selected at the mix design stage to ensure adequate skid resistance before pavement construction. In addition, this

model can be used whenever the use of skid trailer is not feasible due speed limit restrictions, short test sites (e.g., bridge deck), or geometry of roadways (e.g., sharp horizontal curves, steep vertical grades, pavement section with low speed limit, etc.).

The second part of this study investigated the effect of pavement texture parameters (i.e., macrotexture and microtexture) on the change of skid resistance with speed. The MTD and DFT_{20} were used to describe the surface macrotexture and microtexture, respectively. The skid number (SN) was measured at different speeds (i.e., 20, 30, 40, 50, and 60 mph) using a locked wheel skid trailer for various test sections in Idaho. The SN had an exponential relationship with speed. The author developed a predictive model to calculate the SN at different speed as a function of surface texture characteristics. The results demonstrated that there is good correlation between predicted skid number at different speeds using the proposed model and the measured skid number in the field. In addition, the macrotexture was found to control the speed gradient while, the microtexture was found to control the magnitude of SN. Higher microtexture contributes to higher skid resistance and vice versa. This model can be used to predict the skid number at the desired speed using parameters that describe pavement texture. The model is an alternative method that can be use whenever the skid trailer is not available or cannot be used to measure skid due to speed limit restrictions or limitations caused by the test section geometric design (e.g., sharp horizontal curves, steep slope grade, etc.). In addition, this model can be used during the mix design stage to ensure that a given mix or surface has adequate skid characteristics over the operation speeds.

3.8 References

- [1] Henry, J. J. NCHRP Synthesis of Highway Practice 291: Evaluation of Pavement Friction Characteristics. Transportation Research Board, National Research Council. 2000, Washington, D.C.
- [2] Hall, J. W., Smith K. L., and Littleton, P. Guide for pavement friction. National cooperative highway research program. 2008, final report for NCHRP project 10-67.
- [3] Najafi, S., Flintsch, G. and Medina, A., Linking Roadway Crashes and Tire–Pavement Friction: A Case Study. *International Journal of Pavement Engineering*. 2017, 18(2), pp.119-127.
- [4] Rizenbergs, R., Burchett, J. and Napier, C. (1972). Skid resistance of pavements. Report No. KYHPR-64-24, Part II. Lexington, KY: Kentucky Department of Highways.
- [5] National Highway Traffic Safety Administration (NHTSA) (2016). Traffic Safety Facts 2016 – A Compilation of Motor Vehicle Crash Data from the Fatality Analysis Reporting System and the General Estimates System.
- [6] Alhasan, A., Nlenanya, I., Smadi, O. and MacKenzie, C. (2018). Impact of Pavement Surface Condition on Roadway Departure Crash Risk in Iowa. *Infrastructures*, 3(2), p.14.
- [7] Wambold J. C., Antle C. E., Henry J. J., Rado Z., Descornet G., Sandberg U., Gothié M. and Huschek S. International PIARC Experiment to Compare and Harmonize Skid Resistance and Texture Measurements. 1995, (Paris: PIARC) Publication n 01.04.T.
- [8] Masad, E., Rezaei, A., Chowdhury, A. and Freeman, T. J. Field Evaluation of Asphalt Mixture Skid Resistance and Its Relationship to Aggregate Characteristics, Technical report No. 0-5627-3. 2011, Texas Transportation Institute, College Station, TX.
- [9] Kassem, E., Masad, E., Awed, A. and Little, D. (2012). Laboratory Evaluation of Friction Loss and Compactability of Asphalt Mixtures. Technical Report No. SWUTC/12/476660-00025-1. Texas Transportation Institute, College Station, TX.
- [10] Kassem, E., Awed, A., Masad, E. and Little, D. (2013). Development of Predictive Model for Skid Loss of Asphalt Pavements. *Transportation Research Record: Journal of the Transportation Research Board*, 2372(1), pp.83-96.
- [11] Little, D., Bhasin, A., NCHRP Report W104: Using Surface Energy Measurements to Select Materials for Asphalt Pavement. 2006, Transportation Research Board, Washington, D.C.

- [12] Al-Assi, M., Kassem, E., Evaluation of Adhesion and Hysteresis Friction of Rubber-Pavement System. *Applied Sciences SI Advanced Asphalt Materials and Paving Technologies*. 2017, 7(10), 1029.
- [13] ASTM E965-15, Standard Test Method for Measuring Pavement Macrottexture Depth Using a Volumetric Technique, ASTM International, West Conshohocken, PA, 2015.
- [14] ASTM E2157-15, Standard Test Method for Measuring Pavement Macrottexture Properties Using the Circular Track Meter, ASTM International, West Conshohocken, PA, 2015.
- [15] Yaacob, H., Abdul Hassan, N., Hainin, M. and Rosli, M. Comparison of Sand Patch Test and Multi Laser Profiler in Pavement Surface Measurement. *Jurnal Teknologi*. 2014, 70(4).
- [16] Hao, X., Sha, A., Sun, Z., Li, W. and Zhao, H., Evaluation and Comparison of Real-Time Laser and Electric Sand-Patch Pavement Texture-Depth Measurement Methods, *Journal of Transportation Engineering*. 2016, 142(7).
- [17] China, S. and James, D. Comparison of Laser-Based and Sand Patch Measurements of Pavement Surface Macrottexture. *Journal of Transportation Engineering*. 2012, 138(2), pp.176-181.
- [18] Praticò, F. and Vaiana, R. A Study on the Relationship between Mean Texture Depth and Mean Profile Depth of Asphalt Pavements. *Construction and Building Materials*. 2015, 101, pp.72-79.
- [19] Mataei, B., Zakeri, H., Zahedi, M. and Nejad, F.M., Pavement Friction and Skid Resistance Measurement Methods: A Literature Review. *Open Journal of Civil Engineering*. 2016, 6, pp. 537-565.
- [20] ASTM E303-93, Standard Test Method for Measuring Surface Frictional Properties Using the British Pendulum Tester, ASTM International, West Conshohocken, PA, 2018.
- [21] ASTM E1911-09ae1, Standard Test Method for Measuring Paved Surface Frictional Properties Using the Dynamic Friction Tester, ASTM International, West Conshohocken, PA, 2009.
- [22] Florková, Z. and Pepucha, L. Microtexture Diagnostics of Asphalt Pavement Surfaces. *IOP Conference Series: Materials Science and Engineering*. 2017, 236, 012025.

- [23] ASTM E274 / E274M-15, Standard Test Method for Skid Resistance of Paved Surfaces Using a Full-Scale Tire, ASTM International, West Conshohocken, PA, 2015.
- [24] Zimmer R., and Fernando E., Evaluation of skid measurements used by TXDOT: Technical report. 2013, Texas A&M Transportation Institute (TTI) Report 0-6619-1.
- [25] ASTM E1960-07, Standard Practice for Calculating International Friction Index of a Pavement Surface, ASTM International, West Conshohocken, PA, 2015.
- [26] ASTM E1845-15, Standard Practice for Calculating Pavement Macrotexture Mean Profile Depth, ASTM International, West Conshohocken, PA, 2015.
- [27] Wu, Z., King, B., Abadie, C. and Zhang, Z., 2012. Development of design procedure to predict asphalt pavement skid resistance. *Transportation Research Record*, 2306(1), pp.161-170.
- [28] Rezaei A., and Masad E., Experimental-based model for predicting the skid resistance of asphalt pavements, *International Journal of Pavement Engineering*. 2013, 14 (1), pp. 24-35.
- [29] Chowdhury, A., Kassem, E., Aldagari, S., and Masad, E. Validation of Asphalt Mixture Pavement Skid Prediction Model and Development of Skid Prediction Model for Surface Treatments. Technical Report. Report No.0-6746-01-1. 2017, Texas Transportation Institute (TTI), College Station, TX.
- [30] 2017 Standard Specifications for Highway Construction. 2017, Idaho Transportation Department. Boise, ID.
- [31] Standard Specifications for Construction and Maintenance of Highway, Streets, and Bridges. 2014, Texas Department of Transportation, Austin, TX.
- [31] Jackson, N. Harmonization of Texture and Skid-Resistance Measurements. Final Report No. 08-BDH-23. 2008, University of North Florida. Jacksonville, FL.

Chapter 4. Using Close-Range Photogrammetry to Measure Pavement Texture Characteristics and Predict Pavement Friction

4.1 Abstract

Pavement friction measurements are collected and used to assess the functional characteristics of pavements to ensure an adequate level of friction. There are several factors that affect pavement friction including the properties of the tire rubber materials and pavement surface texture characteristics. This study used the close-range photogrammetry (CRP) method to measure the surface texture characteristics of pavements. It was found that the CRP can be used to measure both the pavement macrotexture and microtexture. The CRP measurements of the pavement texture were found to be comparable to measurements using other standard methods. In addition, the researchers incorporated the texture measurements determined from the CRP method and the rheological properties of various rubber materials in the Persson friction model to predict pavement friction at different conditions. Furthermore, the CRP measurements were used to predict the skid number (SN) for the field sections at different speeds. The dynamic friction tester (DFT) and the skid trailer, were used to collect friction measurements in the laboratory and field, respectively. The predicted friction values were compared to the measurements collected in the field and laboratory. Good correlation was found between measured and predicted friction values in the field ($R^2 = 0.97$) and in the laboratory ($R^2 = 0.90$). The CRP was found to offer a simple and accurate, yet inexpensive alternative to the current methods used to measure surface macrotexture and microtexture. In addition, the use of the CRP method simplified the calculation of Persson friction model parameters, thus offering an alternative method to predict pavement friction and ensure safety of motorists.

4.2 Introduction

Pavement friction and skid resistance are often used interchangeably in the literature and used to refer to the force resisting the relative motion between the pavement surface and the vehicle tire. Pavement friction acts in the opposite direction of motion between the tire and pavement surface [1]. Skid resistance plays a major role in highway safety as it prevents the vehicle from sliding and slipping over the surface of the pavement when the driver attempts to

maneuver the vehicle by changing its speed, direction, or both. Skid resistance provides the grip needed to maintain control over the vehicle [2]. Pavement friction is often expressed in terms of the dimensionless parameter called coefficient of friction (μ). The coefficient of friction is expressed mathematically as the ratio between the friction force (opposite to the direction of motion) to the normal applied force (from the wheel axel) as given by Equation 4-1.

$$\mu = F_f / F_w \quad (4-1)$$

where,

F_f = friction force between the tire and pavement surface

F_w = normal force due to the weight of the tire axle

The mechanisms where friction forces are formed between the tire and pavement surface are complex and not yet fully understood [1]. However, there are two widely recognized components that contribute to pavement friction; these mechanisms are known as hysteresis and adhesion. Both hysteresis and adhesion are strongly correlated to pavement texture at different wavelengths [3]. Hysteresis is the result of energy dissipation when the tire rubber deforms due to pavement texture roughness and the internal friction of the rubber [4]. On the other hand, adhesion forces are formed as the rubber molecules slide across the surface of the pavement and are highly dependent on the real contact area between the rubber and pavement surface [5]. The hysteresis component of friction is caused by the bulk deformation of rubber material as it comes into contact with pavement asperities. Such deformation causes energy losses as rubber slides over the pavement surface. The energy losses are caused by the hysteretic losses in the rubber material due to loading and unloading [1]. It was found that the hysteresis friction is highly correlated to the rubber properties (e.g., dynamic modulus) [6]. Softer rubber with lower dynamic modulus exhibits higher friction as it undergoes higher deformations at the interface [6]. Also, hysteresis was found to be correlated to the macrottexture of pavement surface [1]. Generally, higher macrottexture wavelength will exhibit higher friction compared to those with lower macrottexture as the asperities of the surface cause the rubber to deform more causing higher energy loses at the interface [3]. It was found that hysteresis friction is more dominant at higher sliding speeds and especially in wet pavement

conditions [3]. The pavement macrotexture can be controlled by simply adjusting the aggregate gradation of the asphalt concrete mix [1].

Adhesion friction force is formed due to rubber–pavement interaction at the micro level and highly dependent on the true area of contact; therefore the adhesion friction is dominant for smooth contact at low speeds and dry conditions [7]. The adhesion component of the force of friction is highly related to the microtexture of the pavement surface which depends mainly on the surface texture properties of individual particles of coarse aggregate [7]. Aggregates that have higher (rough) surface microtexture provide higher friction compared to smooth aggregates [8]. In addition, aggregates lose some of their texture during the service life of the pavement surface due to polishing under repeated traffic loading [8]. Aggregates that have higher resistance to polishing and abrasion can retain higher friction during the service life of the pavement [9]. It was found that rubber properties (dynamic modulus) and both macrotexture (wavelengths 0.5 mm to 50 mm) and microtexture (wavelengths <0.5 mm) have a significant effect on pavement skid resistance [10].

Pavement surface texture characteristics can be controlled by changing some parameters during the mix design stage. The nominal maximum aggregate size selected for a given mix design has a great impact on pavement macrotexture as a larger nominal maximum aggregate size of the mix provides higher macrotexture [11]. Similarly, a dense graded mix provides lower macrotexture than the porous friction course (PFC) or open graded mix design [12]. In the meantime, the aggregate type selected for a given mix design also influences the microtexture of pavement surface. Aggregate characteristics including surface texture, shape, and resistance to polishing and abrasion have a significant effect on pavement surface microtexture and on maintaining adequate skid resistance over time. Rough, angular aggregates with good resistance to polishing and abrasion exhibit higher microtexture compared to smooth, rounded aggregate with poor resistance to abrasion and polishing aggregates [13].

Previous studies showed that the temperature has a significant effect on skid resistance and it contributes to the seasonal variation of skid resistance [14]. Skid resistance is typically lower in summer (hot weather) compared to winter (cold weather) [15]. This might be counter intuitive as the rubber material is softer (lower dynamic modulus) at higher temperatures. In

addition, it is known that softer rubber materials provide higher friction which holds true for different types of rubber materials at the same temperature [16]. However, for the same rubber material, as the temperature increases the modulus of the rubber decreases [17] but the ratio between the storage part of the dynamic modulus to the loss modulus decreases and the ability of the material to dissipate energy due to rubber deformation is less leading to lower hysteresis in the rubber material and thus lower skid resistance [17].

4.2.1 Measurements of Pavement Macrotexture and Microtexture

There are several standardized test methods to measure pavement macrotexture. One simple method is the volumetric sand patch test as standardized in ASTM E 965 [18], this method is used to measure the macrotexture of pavement surface in terms of a texture parameter called Mean Texture Depth (MTD). The advantages of using the sand patch test is that it is simple and can be done quickly and it is considered to have a relatively low cost compared to other methods to measure the pavement macrotexture. However, this method has some limitations when used to measure the macrotexture of porous friction course (PFC) mixes and open graded mixes as the sand passes through the connected voids in the HMA pavement [19].

The Circular Texture Meter (CTMeter) is a device that uses laser displacement sensors for stationary measurements of pavement macrotexture in the field and in the laboratory [30]. The standard test procedure for measuring macrotexture using CTMeter are specified in ASTM E 2157 [20]. The MPD of the surface is a measure of surface macrotexture [21]. Several studies found a strong correlation between MTD measured using the sand patch test and the MPD measured using CTMeter, and both MTD and MPD are accepted as measures of the pavement surface macrotexture [16, 21, 22]. However, one of the disadvantages of the CTMeter is the relatively high-cost of the test equipment.

Equation 4-2 presents the relationship between MPD and MTD as described in ASTM E 2157-15 [20].

$$\text{MTD} = 0.947 \text{ MPD} + 0.069 \quad (4-2)$$

where,

MTD and MPD are both measured in millimeters

The majority of commonly used methods to measure pavement texture are used to measure the macrotexture of pavement surface. Pavement microtexture is typically quantified indirectly using methods such as the British pendulum test (BPT) or the dynamic friction tester (DFT) and reported as British pendulum number (BPN) or coefficient of friction at 20 km/h (DFT₂₀), respectively as an indication of the pavement microtexture [23, 24]. The DFT₂₀ value is widely accepted as indirect measure of pavement microtexture

4.2.2 Use of Imaging Techniques to Measure Pavement Texture

Some high-end laser texture scanners can capture pavement macrotexture and a portion of the microtexture (0.02 mm to 0.5 mm) [25]. However, the downside of the laser texture scanners is the high cost. Therefore, some recent research considered using the close-range photogrammetry (CRP) method to measure the macrotexture and microtexture of pavement surfaces.

A study by McQuaid et al. [26] used the CRP method to capture stereo images of aggregate particles in the laboratory to evaluate the changes in surface microtexture before and after polishing. The study included six types of aggregates. The aggregates were arranged in a metal frame rig used for stereo imaging. Each of the aggregate samples was polished for 0, 3, 6, and 9 hours. A Canon EOS 400D digital SLR camera was used to take stereo images of the aggregate surface after each polishing time. Then the close-up images were processed using a photogrammetry software to create a Triangular Irregular Networks (TIN) of the aggregate surface. The TIN mesh was oriented and leveled before exported to MountainsMap 6 software (Digital Surf 2016) and a 3D model of the surface was developed and analyzed. The results showed that the CRP method can capture changes in aggregate texture at microtexture wavelengths. The accuracy of CRP measurements for the microtexture was found comparable to measurements of the laser texture scanner. [26].

Millar et al. [27] used the CRP method to measure the polishing and wear of asphalt pavement surfaces due to repeated wheel passes. Twelve-inch square-shaped slabs were prepared in the laboratory using a roller compactor. The slabs were subjected to accelerated

wear using the Road Test Machine (RTM) where up to 10 slabs can be placed inside the RTM and polisher at the same time reducing the time of the test. Two full-size car tires rotate at a constant speed of 10 rpm to simulate traffic. A set of two stereo image pairs were taken of the pavement slabs prior to wearing using a Canon SLR camera. Then the slabs were subjected to an increasing number of wheel passes up to 100,000. After each interval of wheel passes in the RTM, a set of stereo pair images were taken for each pavement slab. The stereo image pairs were processed using a digital photogrammetric software and transformed to generate 3D surface models of test slabs at a given number of wheel passes. The 3D surface models were found to capture changes in the slab texture profile depth due to wearing and polishing of the slab with an increasing number of wheel passes with accuracy up to 0.01 mm in the vertical contour interval.

In another study McQuaid et al. [28] used the CRP method to generate 3D surface models of pavement slabs to quantify the growth of potholes in asphalt pavements. The potholes were artificially manufactured into the surface of test slabs. The 3DF Zephyr photogrammetric software (3D Flow 2011) was used generate a TIN model of the slab surface with the pothole. 3DF Zephyr requires multiple images to be captured for the slab surface with at least 60% forward overlap and 30% side overlap between images. The TIN mesh is then exported into the MountainsMap 6 software for analysis and measurement of the volume of the pothole. The artificial pothole was enlarged at different stages and at each stage the volume of the pothole was measured. The results of this study showed a good correlation between the experimental measurements of the volume of the pothole and the 3D model obtained measurements of the pothole.

In a recent study Kogbara et al. [29] related the pavement texture parameters measured using the CRP method to pavement friction measurements using the Grip Tester device. The study was able to explain variations in the Grip Tester skid measurements based on measurements of the surface texture parameters obtained from images of the pavement surface using the CRP method. The texture parameters were calculated from the 3D surface models of the pavement surface. The best correlation of the measured grip numbers was found with both the peak material volume (V_{mp}) and the density of the peaks (S_{pd}). The study was limited to hot mix asphalt (HMA) pavements only with limited number of test sections (a total of six test

sections). The study found fair correlation between the coefficient of friction and surface texture indices measured using CRP. However, the study did not verify the surface measurements obtained from the CRP with other standard methods.

4.2.3 Persson Friction Model to Predict Pavement Friction

The theory of rubber friction and contact mechanics was used to describe the internal friction of the rubber and how the resulting friction force depends on the nature of the surfaces in contact. Persson [4] developed a model to provide a fundamental understanding of rubber friction when sliding over a self-affine fractal surface. A self-affine surface is a surface that does not change its morphology (i.e., the surface looks the same) when the scale of the surface is changed in any direction [31], and the statistical properties of the surface are invariant when the surface scale is transformed in each direction by a different magnitude as shown in Equation 4-3 [4].

$$x \rightarrow \xi x; y \rightarrow \xi y; z \rightarrow \xi^H z \quad (4-3)$$

where,

ξ = the scale factor in the xy-plane, ξ^H (where $0 < H < 1$) is the scale factor in the perpendicular z-direction

H = the Hurst exponent of the surface

Persson [4] showed that road surfaces are self-affine when viewed in a finite length scale λ , that is bounded by an upper and lower cutoff length scale λ_0 and λ_1 respectively (i.e., $\lambda_1 < \lambda < \lambda_0$). For pavement surfaces the upper cutoff length scale resembles the largest aggregate particle size in the pavement mix and can be in order of few millimeters [4]. However, not much information is known about the lower cutoff length scale λ_1 . However, Persson demonstrates that for rubber-pavement friction, it can be in order of few micrometers [31, 32]. When rubber is sliding over a pavement surface with surface roughness of the length scale λ , it experiences a sinusoidal fluctuating force with frequency (ω) that is directly proportional to the sliding speed (v) and inversely proportional to the roughness length scale ($\omega \sim v/\lambda$).

However, a typical pavement surface has a wide distribution of length scales (i.e., $\lambda_1 < \lambda < \lambda_0$) which results in a wide distribution of frequency components [32].

When the rubber slides over pavement surface, the normal applied pressure causes the rubber to squeeze into the large cavities of the surface. Persson explained that even if the rubber could make a direct contact with large pavement cavities, the contact pressure at the top of the cavity would be much greater than the bottom of the cavity. Thus, the wavelengths of the pavement surface contribute to the major part of the friction force and the apparent area of contact for a given wavelength $A(\lambda)$ should be considered in the analysis as given in Equation 4-4 [4].

$$P(q) = A(\lambda)/A(L) \quad (4-4)$$

where,

$P(q)$ = the relative area of contact between the rubber and pavement

$A(\lambda)$ = the area of real contact if the surface would be smooth for all length scales shorter than λ

$A(L)$ = the macroscopic contact area (L = diameter of the macroscopic contact area)

Persson developed Equation 4-5 to estimate the coefficient of friction between pavement and rubber [32].

$$\mu = \frac{1}{2} \int_{q_0}^{q_1} dq q^3 C(q) S(q) P(q) \times \int_0^{2\pi} d\phi \cos\phi \operatorname{Im} \frac{E(\omega)}{(1-\nu^2)\sigma_0} \quad (4-5)$$

where,

q = the surface wavenumber

q_0 = the lower cut-off length of the wavenumber

q_1 = the upper cut-off length of the wavenumber

$C(q)$ = the surface roughness power spectrum

$S(q)$ = surface correction factor

$P(q)$ = the relative contact area at the pavement-rubber interface

$E(\omega)$ = the rubber dynamic modulus

ν = Poisson's ratio of the rubber

σ_0 = the nominal contact normal pressure between the tested rubber slider and the pavement surface;

Φ = the cosine roughness profile of the surface; $\Phi = 0$ indicates perpendicular roughness to the sliding direction, and $\Phi = \pi/2$ indicates parallel roughness to sliding direction

For a fractal self-affined surface, the power spectral density of the surface can be expressed by Equation 4-6 [3].

$$C(q) = k q^{-2(1+H)} \quad (4-6)$$

where,

q = the wavenumber

k = a constant

H = the Hurst exponent of the surface

The Hurst exponent is related to the fractal dimension (D) of the surface as given in Equation 4-7. The Hurst exponent characterizes the roughness of the surface profile where lower H values represent a surface with higher roughness, and a value of 1 represents a fully smooth surface (straight line) [33].

$$D = 3-H \quad (4-7)$$

Lorenz et al. [32] defined $S(q)$ for pavement surfaces as shown in Equation 4-8.

$$S(q) = \gamma + (1 - \gamma)P(q)^2 \quad (4-8)$$

where,

γ = equal to 0.5 for pavement surfaces [32].

Previous studies used the Persson model to predict pavement friction with high accuracy. However, these studies used 3D laser scanners to characterize the texture of the pavement surface and determine the Hurst exponent [4]. Other researchers used atomic force microscopy (AFM) to characterize both the macrotexture and microtexture of the pavement surface [31, 32]. Such methods to measure pavement texture are costly and can be limited to laboratory measurements only.

4.3 Research Objectives

The main objectives of this part of study were to:

- 1- Explore the use of the close-range photogrammetry (CRP) to develop 3D models to measure pavement macrotexture and microtexture.
- 2- Use the proposed parameters derived from the CRP along with rubber properties to predict friction level using Persson friction model.
- 3- Examine the Persson friction model at various conditions including test speed, pavement surface characteristics, and rubber properties

4.4 Research Methodology

This section discusses the research methodology of this part of study followed to measure the coefficient of friction of pavement surfaces in the laboratory and field. In addition, the method for using CRP to measure the pavement macrotexture and microtexture was also discussed in detail. Finally, the use of CRP texture measurements of the surface texture along with rubber properties were incorporated in Persson's friction model to predict pavement friction.

In this study, the researchers evaluated field test sections as well as laboratory-prepared HMA slabs. The surface macrotexture and microtexture of the pavement surfaces were measured using the CRP method and the results were compared to the sand patch test and DFT₂₀ measurements used to quantify surface macrotexture and microtexture, respectively.

Table 4-1 summarizes the testing matrix for the laboratory experiments. A total of 134 friction data points were collected in the laboratory. The laboratory experiments included four HMA laboratory-prepared slabs using different combinations of gabbro and limestone aggregates (i.e., 100% gabbro, 50% gabbro + 50% limestone, 30% gabbro +70% limestone, and 100% limestone). Asphalt mixtures were prepared in the laboratory and then compacted in a 20-in square-shaped steel mold. A plate vibratory compactor was used to compact the HMA mix inside the mold. Figure 4-1 shows the steps of preparing the HMA slabs in the laboratory. A three-wheel polisher was used to polish the test slabs. Friction measurements were recorded at various polishing levels (e.g., 0, 5000, 10000, 20000, 30000, 50000, and 100000 cycles) and at different test temperatures (e.g., 0, 20, and 50 °C).

Table 4-1. Testing matrix for the laboratory experiments

Parameter	Description	Number
Slab type	100% Gabbro, 50% gabbro + 50% limestone, 30% gabbro +70% limestone, and 100% limestone	4
Rubber materials	Butyl, Neoprene, Nitrile, EPDM, SBR, and Pure Gum	6
Number of polishing cycles (Thousands)	0 (unpolished), 5, 10, 20, 30, 50, and 100	7
Test temperature	0 °C, 20 °C, and 50 °C	3
	Total number of data points	134

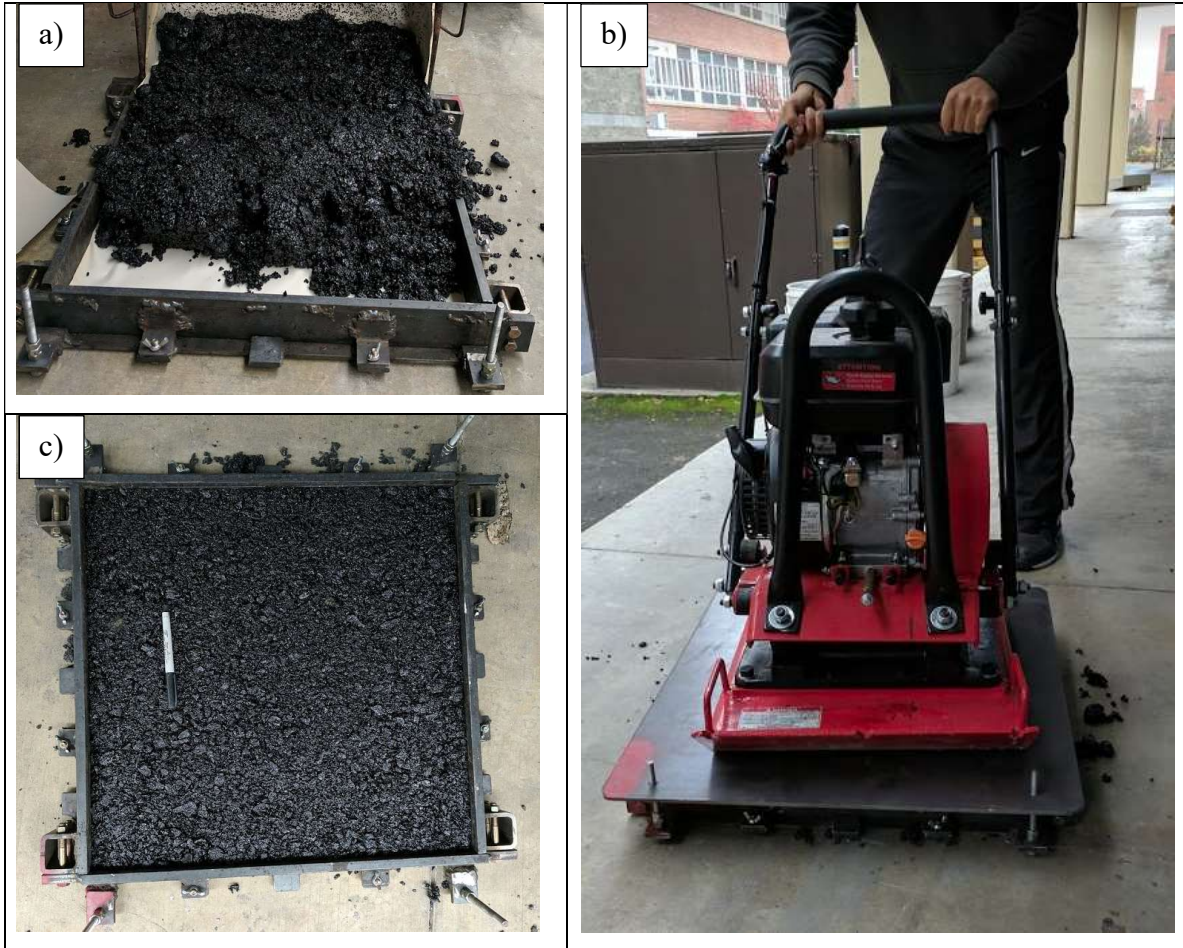


Figure 4-1. Preparation of HMA slabs; a) placing HMA inside the slab for compaction b), Compaction of the HMA slab, and c) HMA slab surface after compaction.

Table 4-2 summarizes the testing matrix for field tests. A total of 400 friction data points were recorded. Test field test sections were evaluated and distributed across Idaho. The field pavement sections included five HMA, three sealcoat, and two PCC surfaces with different aggregate sources (e.g., basalt, river gravel, etc.). The friction was measured at different speeds (e.g., 20, 30, 40, 50, and 60 mph) and about eight friction measurements were recorded for each test section. The following section provides detailed discussion of the laboratory and field testing conducted in this part of study.

Table 4-2. Testing matrix for the field test sections

Parameter	Description	Number
Field section	I 15 MP 08, I 15 MP 23, US 30 MP 365, I 15 MP 32, I 86 MP 16, US 95 MP 440, US 20 MP 326, US 26 MP 356 I 15 MP 96, and I 15 MM 78.	10
Test speed	20, 30, 40, 50, and 60 mph	5
Number of measurements	Eight measurements for each test section at each speed	8
	Total number of data points	400

4.4.1 Macrotexture Measurements for the Field Test Sections and Lab-Prepared HMA Slabs

The macrotexture of the pavements surface was measured using the volumetric sand patch test as shown in Figure 4-2. The tools and materials needed to perform this test are silica sand, graduated cylinder, cleaning brush, ruler and spreader. The test surface is cleaned properly using the cleaning brush. Then a known volume of sand is measured using the graduated cylinder and spread over the surface uniformly to form a circular patch. The diameter of the circular patch is measured at four different places using the ruler and the average diameter for the sand patch is calculated.



Figure 4-2. Measuring pavement macrotexture using the sand patch test.

The area of the patch is then determined from the average diameter. The MTD obtained using a volumetric measurement technique represents the surface characteristics in three-dimensional space [1]. The average diameter of the sand patch is measured and the mean texture depth (MTD) is calculated using Equation 4-9. The macrotexture for each pavement surface in this study was measured and reported in terms of the MTD.

$$\text{MTD} = 4V / (\pi D^2) \quad (4-9)$$

where,

MTD = mean texture depth (mm)

V = sand volume (mm³)

D = average diameter of sand patch circle (mm)

4.4.2 Microtexture Measurement of the Field Test Sections and Lab-Prepared HMA Slabs

There is no standardized method to directly measure the pavement microtexture [39]. While some laser texture scanners can be used to capture a portion of the microtexture range (0.02 mm to 0.5 mm) [40], these scanners are limited in their resolution to the size and spacing between the laser spots [40]. The DFT measurement of the coefficient of friction using the standard rubber slider at speed of 20 km/h (DFT₂₀) is widely accepted and used as indirect measurement of the microtexture [8-10, 13, 16]. The DFT measures the frictional force induced between rubber sliders and the test surface. The DFT₂₀ are measured using standard rubber sliders specified in ASTM E 1911. The DFT₂₀ value was measured for all field test sections and laboratory-prepared test slabs. The laboratory-prepared test slabs were polished using the three-wheel polishing device at different polishing cycles. After each set of polishing cycles, the DFT₂₀ was measured to capture the change in the slab microtexture due to polishing under repeated loading. The three-wheel polishing device consists of three pneumatic tires that rotate over the pavement slab as shown in Figure 4-3.

Three steel plates were placed on top of the wheel assembly with a total weight of 105 lb. The tires rotate with a constant speed of 60 rpm over the slab while water is continuously sprayed over the slab surface to wash out the fines and keep the tires cooler to avoid excessive tire wearing. The diameter of the wheel track is 284 mm similar to the diameter of the rubber sliders track on the DFT. A laser counter and reflector are attached to the side of the three-wheel polisher and the device is stopped once the desired number of cycles is reached.

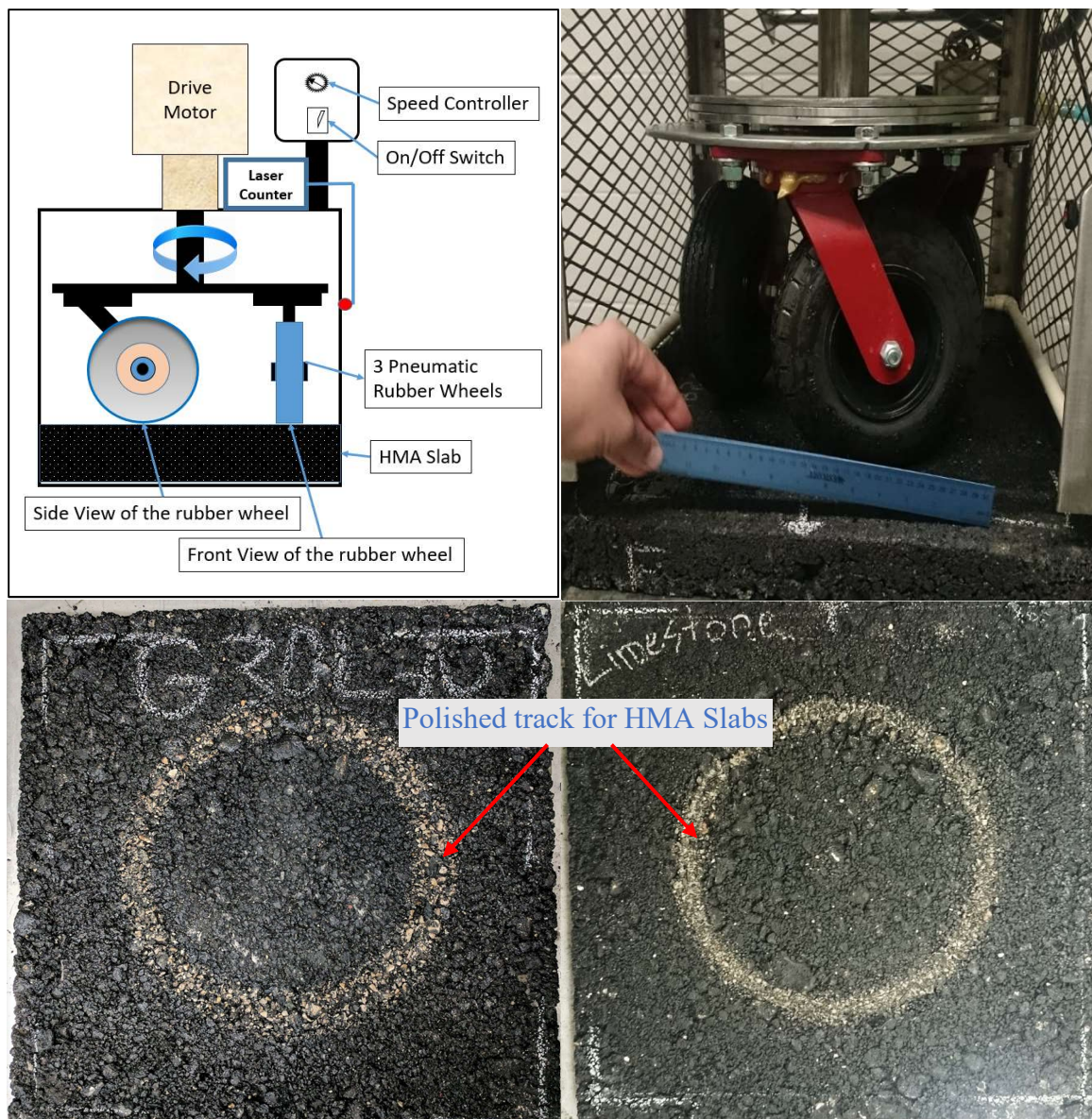


Figure 4-3. Polishing of HMA slabs using the three-wheel polisher

4.4.3 Measuring Pavement Surface Texture Characteristics Using the CRP Method

The research team explored the use of the CRP method to directly quantify pavement macrotexture and microtexture for the pavement surfaces. This process requires capturing a series of consecutive two-dimensional (2D) images for the area of interest of the pavement surface. The images were taken from multiple angles around the area of interest from close proximity (less than one foot from the pavement surface) to capture the details of the surface texture, especially for the microtexture wavelengths. A high-resolution (20.1 megapixel) hand-

held camera with 25 mm wide-angle lens was used to capture a series of images of the pavement surface. Nine to 12 images were captured from different angles for each surface. An overlap of at least 66% in both vertical and horizontal directions should be achieved between consecutive images. A 30-cm scale was placed on pavement surface and used as a reference when the images were imported for processing. Figure 4-4 shows a typical series of images captured for a laboratory prepared slab.

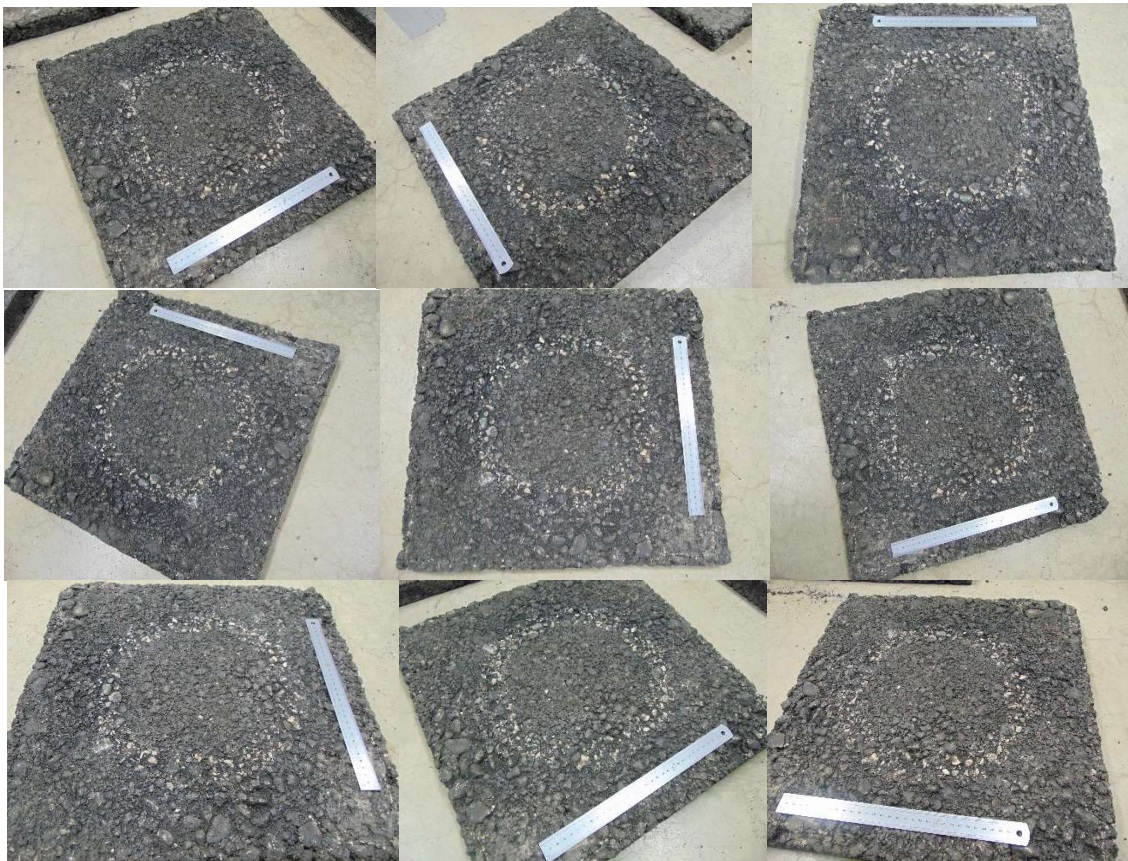


Figure 4-4. Typical set of 2D images captured using a hand-held camera from close proximity

The captured images were uploaded into an image processing software called 3DF Zephyr (version 4.003) (3DFlow, 2018). In this process, a camera calibration was performed to determine the focal length for each captured image. The angle and distance of the camera for each image with respect to pavement surface was calculated by matching overlapped-featured

points from different 2D images using triangulation techniques. The location of the camera can then be determined for each image using triangulation. A series of steps were performed in the 3DF Zephyr software to convert the 2D images into a 3D model of the surface of the pavement section. This was performed by creating a sparse point cloud from the image sequence. The sparse point cloud (Figure 4-5) was used as a benchmark to reconstruct the 3D surface model.

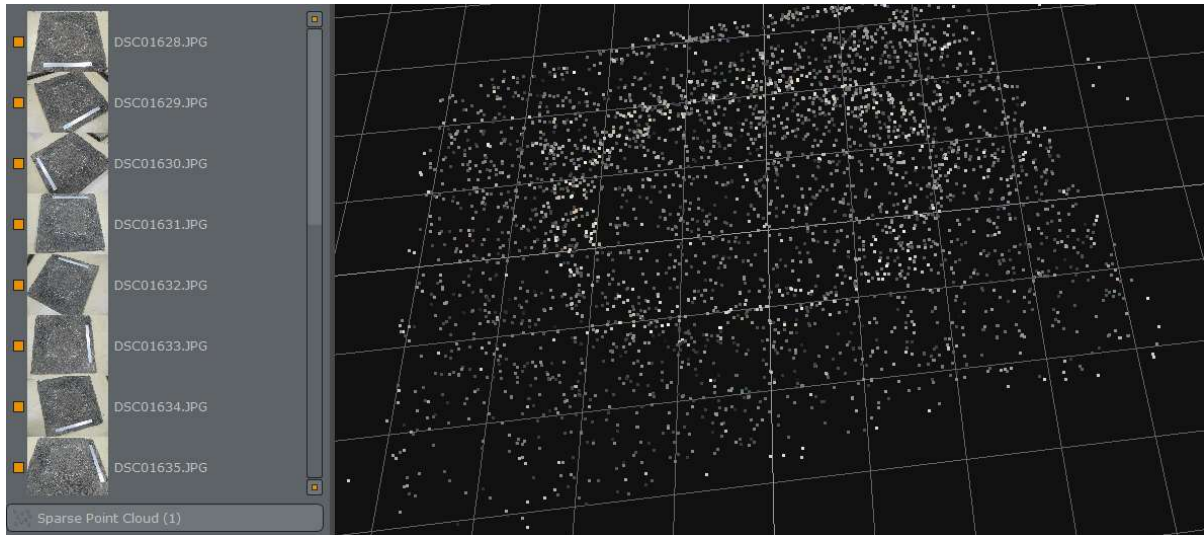


Figure 4-5. Example of sparse point cloud distribution for HMA slab

The next step was to perform a densification process, where the sparse point cloud was transformed into a 3D dense point cloud (DPC) that represents the sharp features of the pavement surface. The DPC was then used to create a 3D textured mesh of the pavement surface that represents the texture of the pavement surface with high definition in a 3D surface model as shown in Figure 4-6. The scale of the 3D model was established using a 30-cm scale that was placed on the pavement surface in order to determine the scale factor for each pavement section.

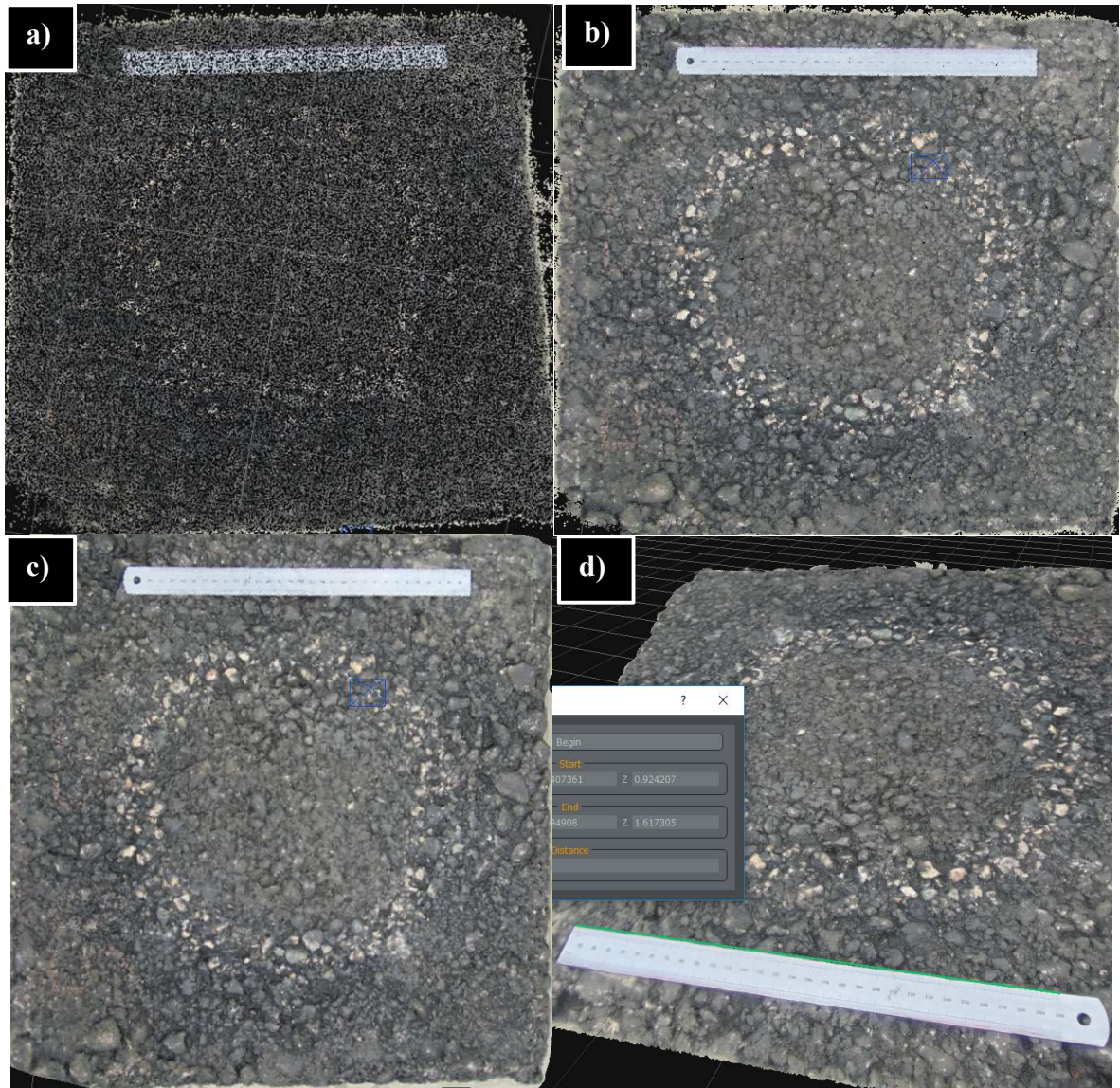


Figure 4-6. a) Densification process into a 3D dense point cloud; b) 3D sharp features mesh of the surface model; c) Textured mesh of the 3D surface model; d) Resizing the 3D surface model

The 3D surface model was exported to another software called the MountainsMap (version 7.4.8545) (Digital Surf, 2018) where the 3D model of the pavement surface was processed and prepared to extract surface texture parameters. The 3D surface was leveled to eliminate the effect of any artificial gradient on the height parameter. The surface form was removed using a third order polynomial to eliminate any surface rippling effect for the 3D surface model as shown in Figure 4-7. A surface profile was selected, and the profile height was extracted before

applying a Gaussian filter with a cutoff length of 0.8 mm [19] to separate the macrotexture height from the microtexture height as shown in Figure 4-8. The macrotexture and microtexture height profile were then exported separately into a spreadsheet and the mean macrotexture height and mean microtexture height are calculated for a baseline of 100 mm according to ASTM E 1845-09 [12] standard to calculate a mean profile depth from a pavement profile [23]. Equations 4-10 to 4-12 were used to measure macrotexture and microtexture, respectively in accordance with ASTM E 1845-9 [12]. Figure 4-9 shows a typical surface profile divided into segments to calculate the CRP texture depth. The mean macrotexture and microtexture heights were reported for each test section.

$$q_0 = (\sum_{i=1}^{i=n} MSD_{0,i})/n \quad (4-10)$$

$$q_1 = (\sum_{i=1}^{i=n} MSD_{1,i})/n \quad (4-11)$$

$$MSD_i = (p_1 + p_2) / 2 \quad (4-12)$$

where,

q_0 = the CRP calculated mean microtexture depth

q_1 = the CRP calculated mean macrotexture depth

MSD_i = the mean segment depth for segment i

n = the total number of segments in the profile length

p_1 = the peak level in the first half of the profile segment

p_2 = the peak level in the second half of the profile segment

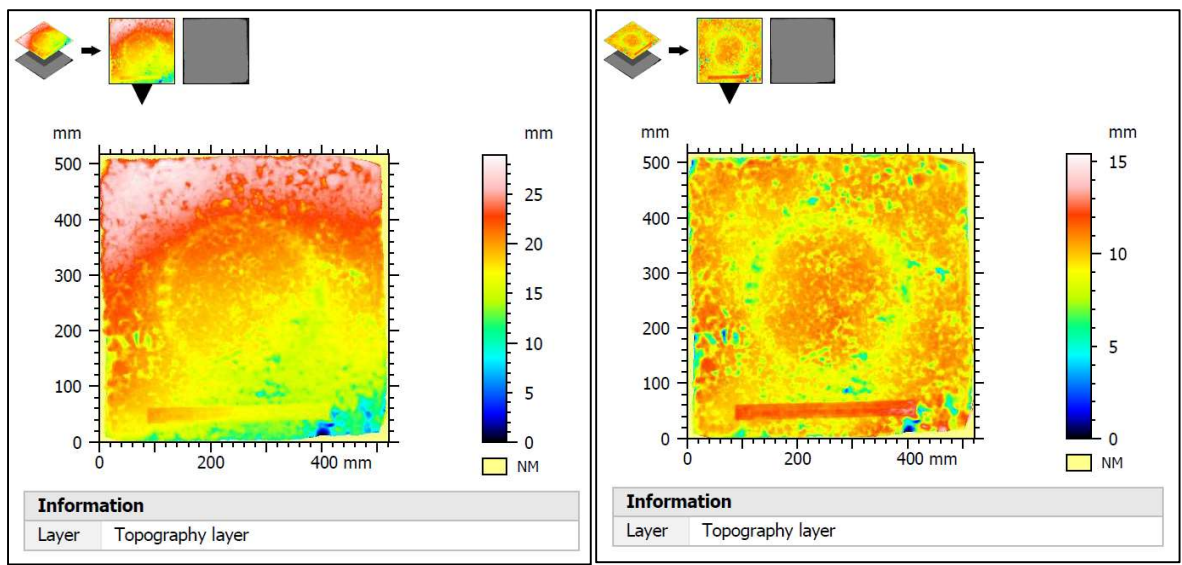


Figure 4-7. Example of a typical 3D surface model before and after applying the level and remove form operators

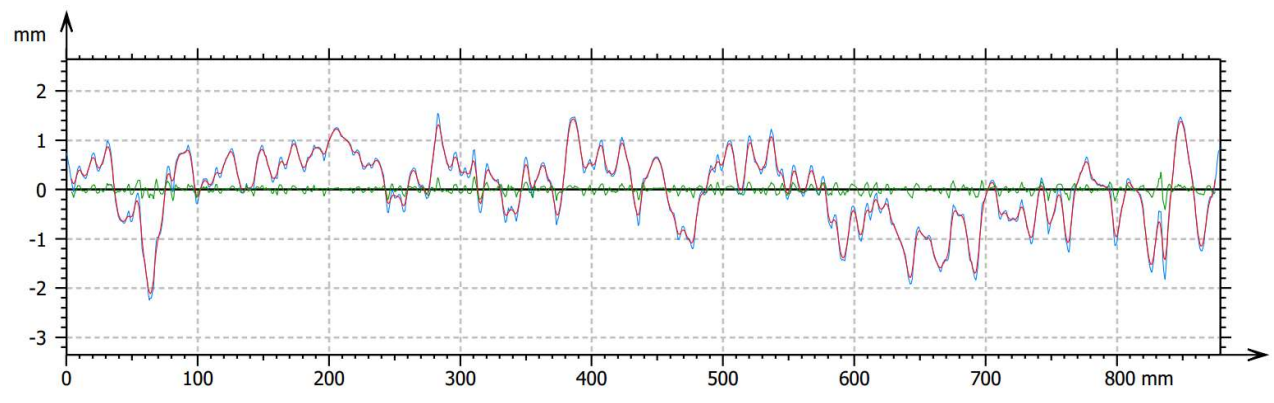


Figure 4-8. Example of a typical pavement profile height and separating the macrotexture and microtexture using a Gaussian filter

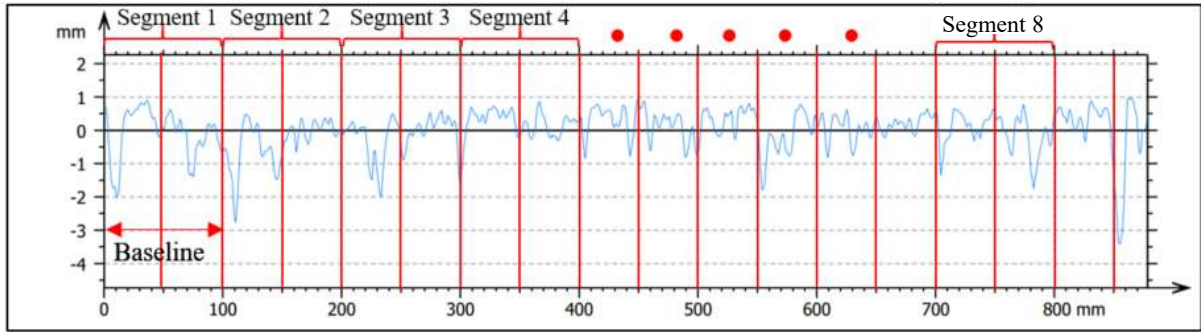


Figure 4-9. Calculating the CRP mean texture depth according to the ASTM E 1845-9 [12]

The CRP technique was used to measure the mean macrotexture and microtexture for the selected field sections and the laboratory-prepared slabs after each set of polishing cycles as described earlier. The CRP measurement results for the macrotexture and microtexture were compared to the sand patch test and the DFT_{20} measurements as discussed in Section 3.5.1.

4.4.4 Measuring Pavement Friction Using the DFT for Different Types of Rubber Materials

The coefficient of friction of the test slabs was measured using the DFT device. The rubber sliders of the DFT device were prepared using various rubber materials. A total number of six different types of rubber materials (i.e., Butyl, Neoprene, Nitrile, EPDM, SBR, and Pure Gum). These rubber sliders are attached to the DFT device for measuring the coefficient of friction between the test slabs and different rubber materials. The rubber materials were selected to cover a wide range of rubber material properties. The rubber materials were cut into the desired shape using a designed metal die as shown in Figure 4-10 in accordance with ASTM E 1911 [34]. Figure 4-11 shows rubber sliders prepared from different rubber materials.



Figure 4-10. Metal die used to cut the rubber sliders to the desired shape



Figure 4-11. DFT rubber sliders prepared in the laboratory

Each rubber material set consisting of three rubber sliders was attached to the bottom of the DFT rotating disk and the coefficient of friction was measured between the rubber sliders and the slab surface. The coefficient of friction was measured for each slab after different polishing cycles in the three-wheel polisher and at different temperatures (0, 20, 50 °C).

The material properties of the rubber specimens were measured using the Dynamic Mechanical Analyzer (DMA). The DMA at Texas A&M University was used in this study. Each of the rubber specimens (16.8 x 6.4 x 50 mm) was tested at a wide range of loading frequencies (i.e. 0.1, 0.5, 1, 5, 10, 25, 50, and 70 Hz) and test temperatures (i.e., 0, 10, 20, 35, 50, and 70 °C). The DMA was used to apply uniaxial sinusoidal loading on the rubber specimens. The uniaxial sinusoidal load is applied in a control strain mode with a strain level

of 6%. The dynamic modulus for each rubber material was measured at each loading frequency and test temperature. A master curve for each rubber material was developed using the measurements of dynamic modulus at different temperatures and loading frequencies utilizing the principle of time-temperature superposition. The reference temperature T_r was set as 20°C and the shift factors were determined for each temperature using the Williams-Landel-Ferry (WLF) model. The master curve was then fitted using the non-linear sigmoid function given in Equation 4-13.

$$\text{Log } |E^*| = \alpha + \frac{\beta}{1 + \frac{1}{\exp \gamma + \delta \log(f)}} \quad (4-13)$$

where,

E^* = the dynamic modulus of the rubber;

α , β , γ , and δ = the sigmoid function constants;

f = the frequency for the rubber material.

At a given temperature the reduced frequency f_r can be determined using the WLF model using the two temperature constants C_1 and C_2 as given in Equation 4-14.

$$\text{Log } (f_r) = \frac{-C_1(T-T_m)}{C_2(T-T_m)} \quad (4-14)$$

where,

T_m = the reference temperature for the master curve

T = the test temperature

4.4.5 Measuring Pavement Friction Using the Skid Trailer

The ITD pavement friction tester that uses a locked wheel skid trailer was used to measure the pavement skid number at the desired speed in the field. The skid trailer shown in Figure 4-12 is towed by the skid truck that travels at the test speed. In this study, a standard smooth tire was used in accordance with ASTM E 274 [37]. The skid number was measured at five different speeds (i.e., 20, 30, 40, 50, and 60 mph) for all field test sections evaluated in this

study. The skid trailer utilizes a force transducer that measures the traction between the wheel and pavement surface and used to calculate skid number as given in Equation 4-15.

$$SN = 100 \times \mu = 100 \times \frac{F}{W} \quad (4-15)$$

where,

μ = Coefficient of friction

F = Frictional force

W = Vertical load on a locked wheel



Figure 4-12. ITD Pavement Friction Tester

4.5 Results and Analysis

The surface texture characteristics (i.e., microtexture and macrotexture) calculated using the CRP method for both field sections and the laboratory-prepared slabs at different polishing cycles were found to correlate well with the measured macrotexture and microtexture using sand patch test and DFT_{20} , respectively. Figure 4-13 shows an example of two typical pavement surfaces with high and low macrotexture characterized using the sand patch test along with a 3D surface model developed using the CRP method. It can be seen that the CRP method could capture the difference in the macrotexture between the two surfaces. Similarly, Figure 4-14 shows another example of two typical pavement sections with low and high microtexture (DFT_{20}) along with 3D surface models for the microtexture roughness of the surface using the CRP method. It can be seen that good correlation exists between the CRP microtexture and DFT_{20} measurements.

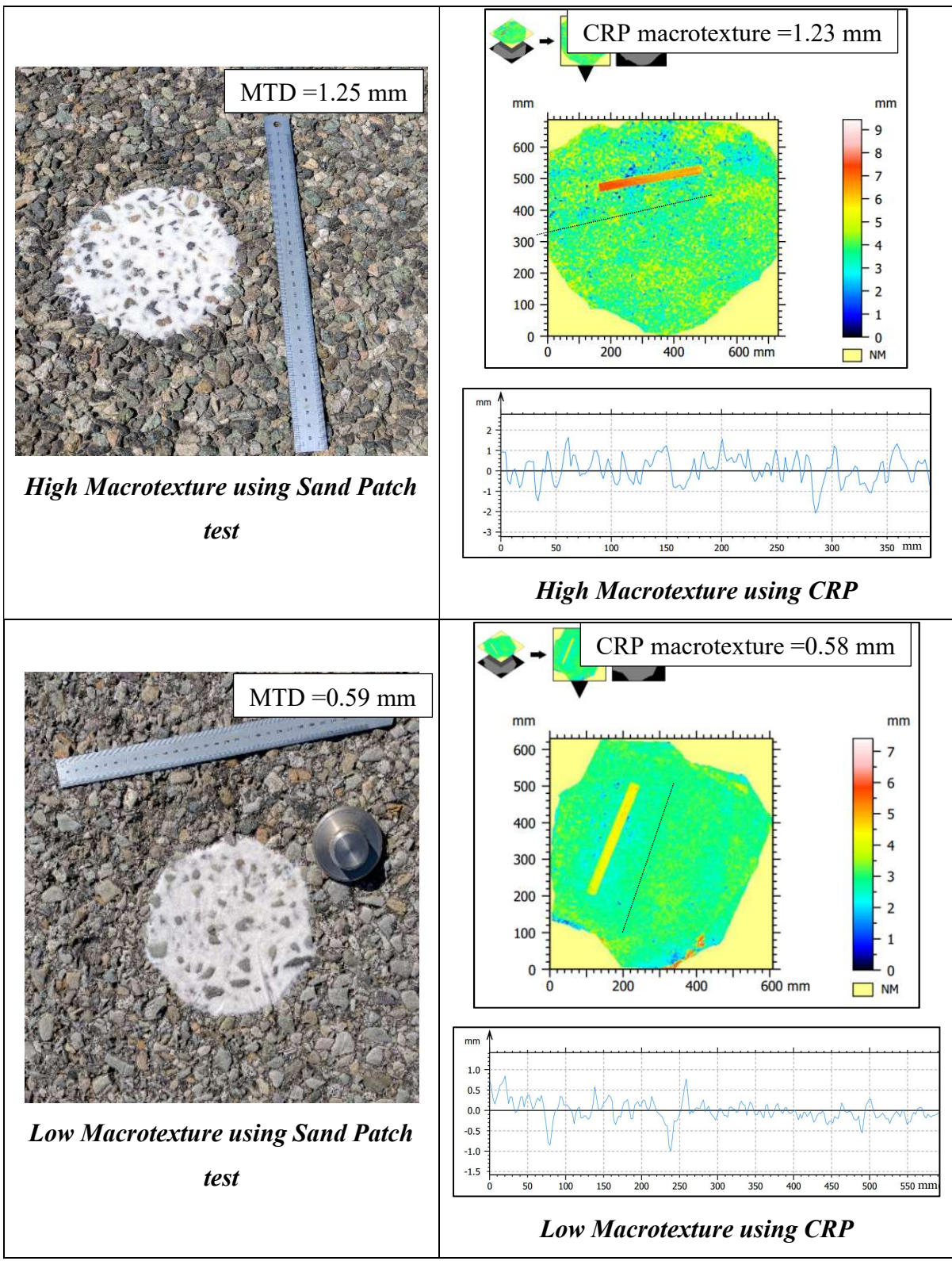


Figure 4-13. Examples of different macrotexture measured using Sand patch test and CRP

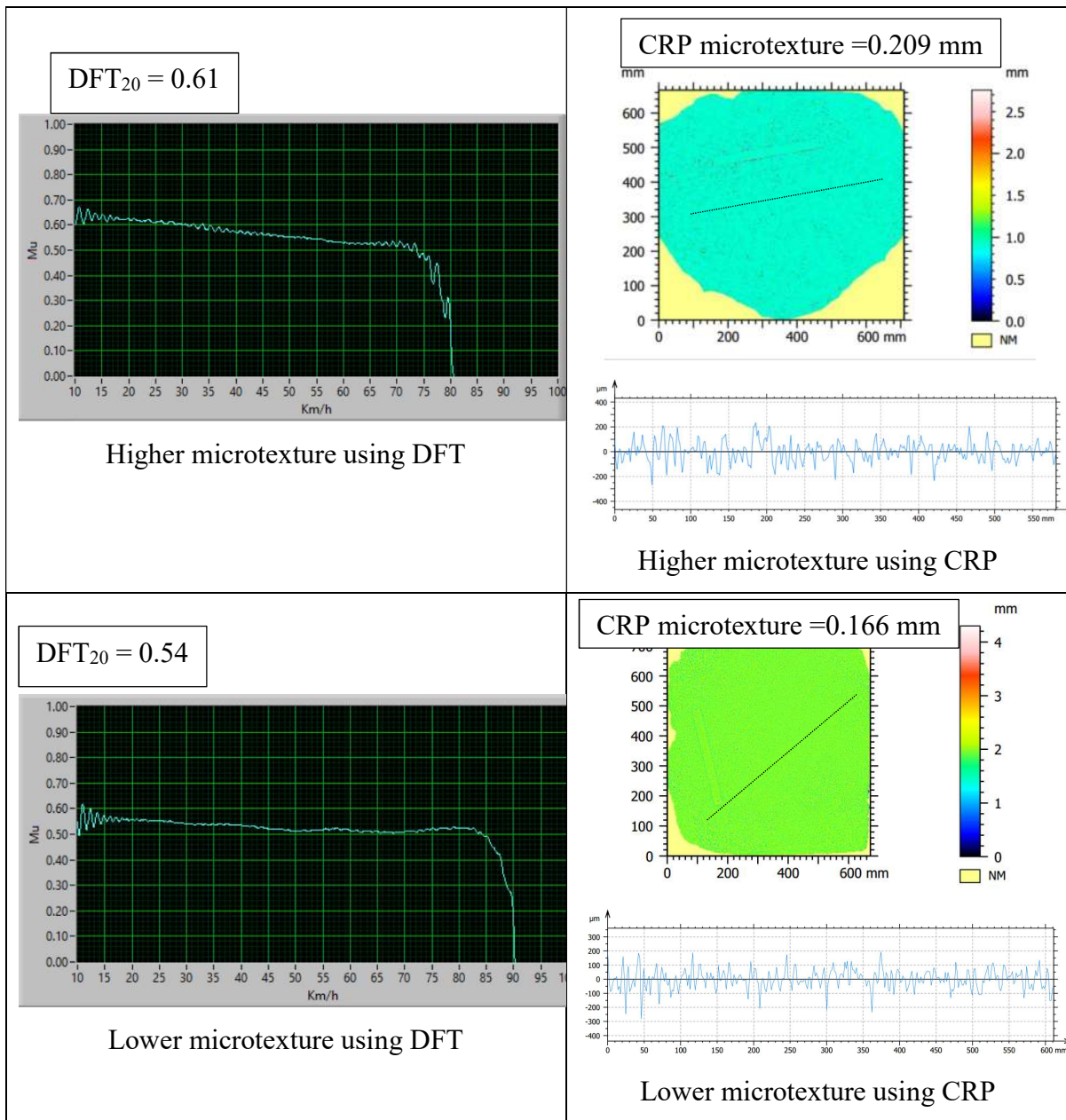


Figure 4-14. Examples of different microtexture measured using DFT and CRP

Figure 4-15 shows the correlation between MTD measured using the sand patch test and mean macrotexture depth of pavement surface measured using the CRP technique. The results showed there is a good correlation between these two parameters ($R^2 = 0.85$), so the CRP technique can be used to calculate the MTD. Similarly, there is a strong correlation between the measured DFT_{20} values and measured mean microtexture depth using the CRP technique ($R^2 = 0.91$) as shown in Figure 4-16. The CRP method was found to provide a good estimate

of both the surface macrotexture and microtexture. The results were comparable to the measurements of the macrotexture over a wide range of MTD measurements (0.4 to 1.54 mm). Similarly, the CRP measurements for the mean microtexture depth and the DFT₂₀ had a strong correlation over a wide range of the DFT₂₀ measurement (0.23 to 0.65).

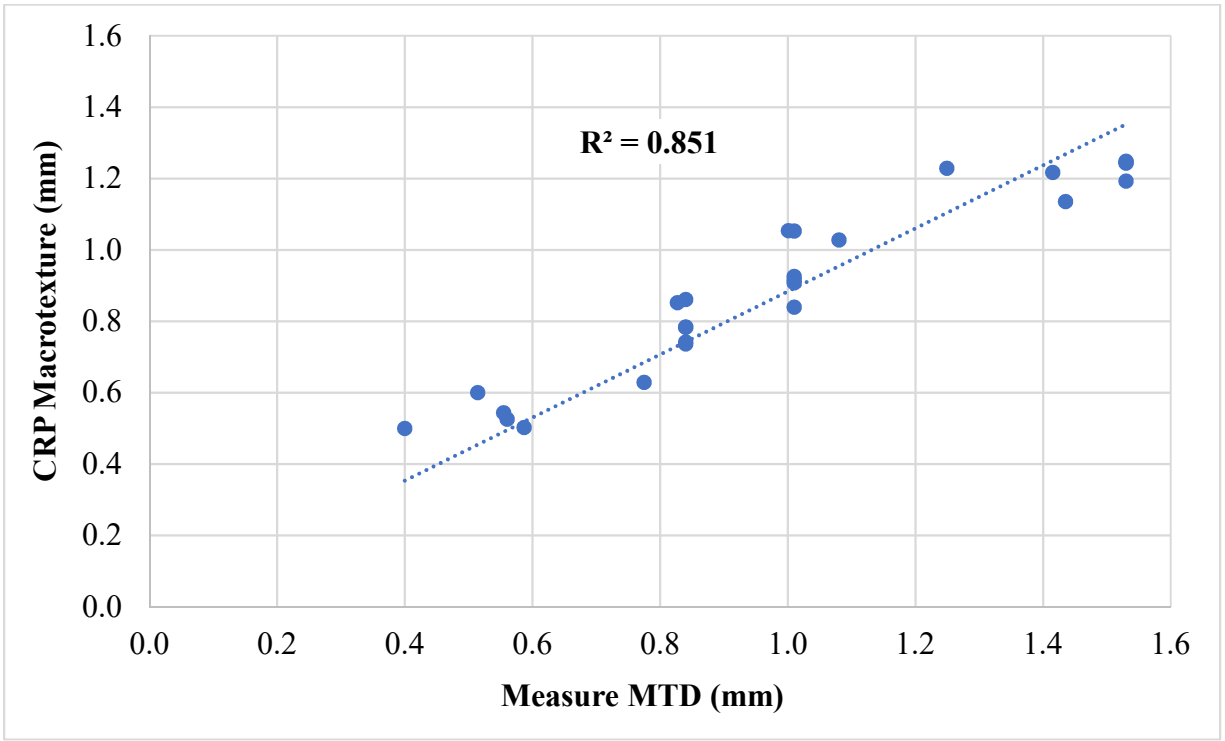


Figure 4-15. Correlation between CRP macrotexture and MTD measured using the sand patch test

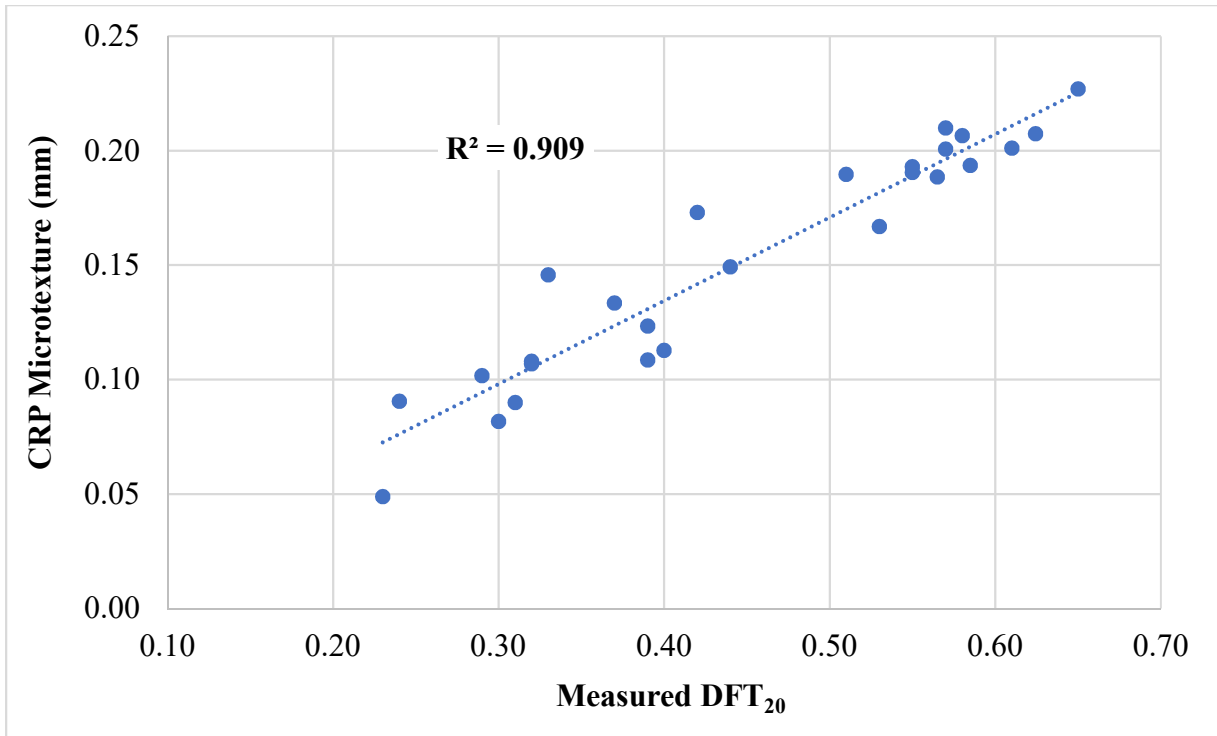


Figure 4-16. Correlation between CRP microtexture and DFT₂₀ measurements

4.5.1 Results for the Mechanical Properties of the Rubber Materials

The DMA was used to measure the dynamic modulus for each of the six rubber materials used as mentioned earlier. The results of the DMA testing for each rubber material at different temperatures and loading frequencies are presented in Appendix B (Figures B1 through B6). Figure 4-17 shows an example of the DMA curves for the Butyl rubber material. The results demonstrate the dynamic modulus of rubber decreased with the increase in temperature for all test materials. However, the dynamic modulus of rubber increased with loading frequency. The master curve, that describe the changed in dynamic modulus at reduced frequency, for each test rubber material was developed using the sigmoid function (Equation 4-13). The flow curves were fitted to the sigmoid function and sigmoid function coefficients (α , β , γ , and δ) were determined using the least square error method. Figure 4-18 shows the master curves for the rubber materials while Table 4-3 summarizes the sigmoid function coefficients for each rubber material.

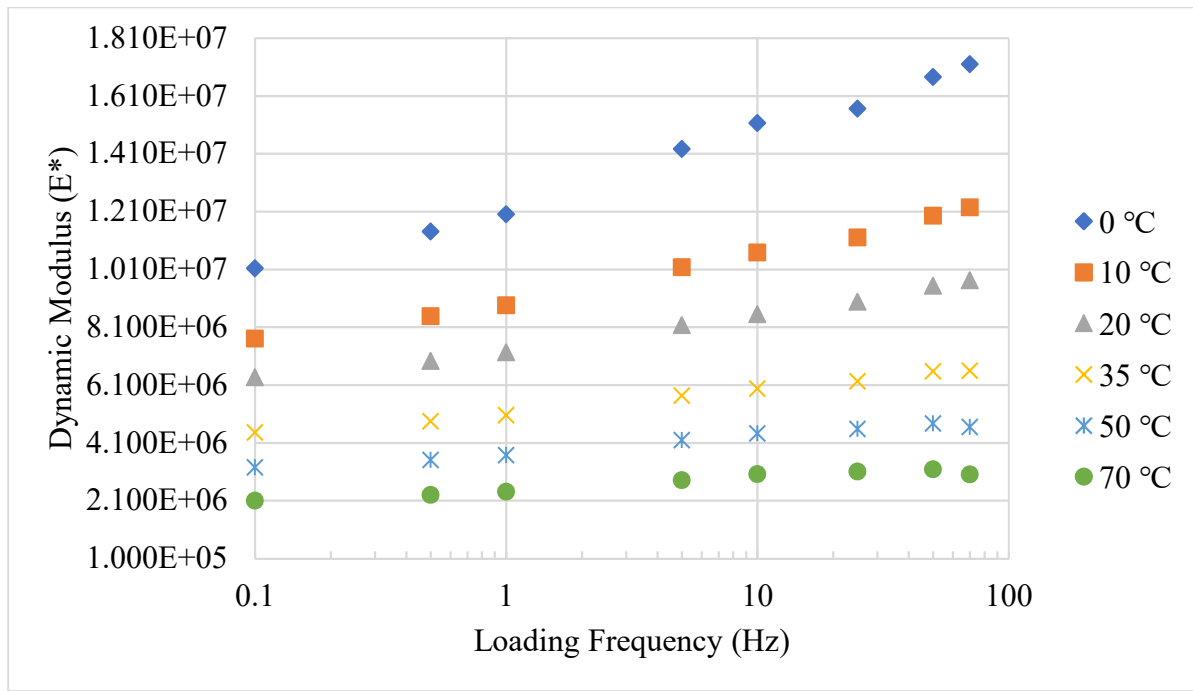


Figure 4-17. DMA curves for the Butyl rubber material

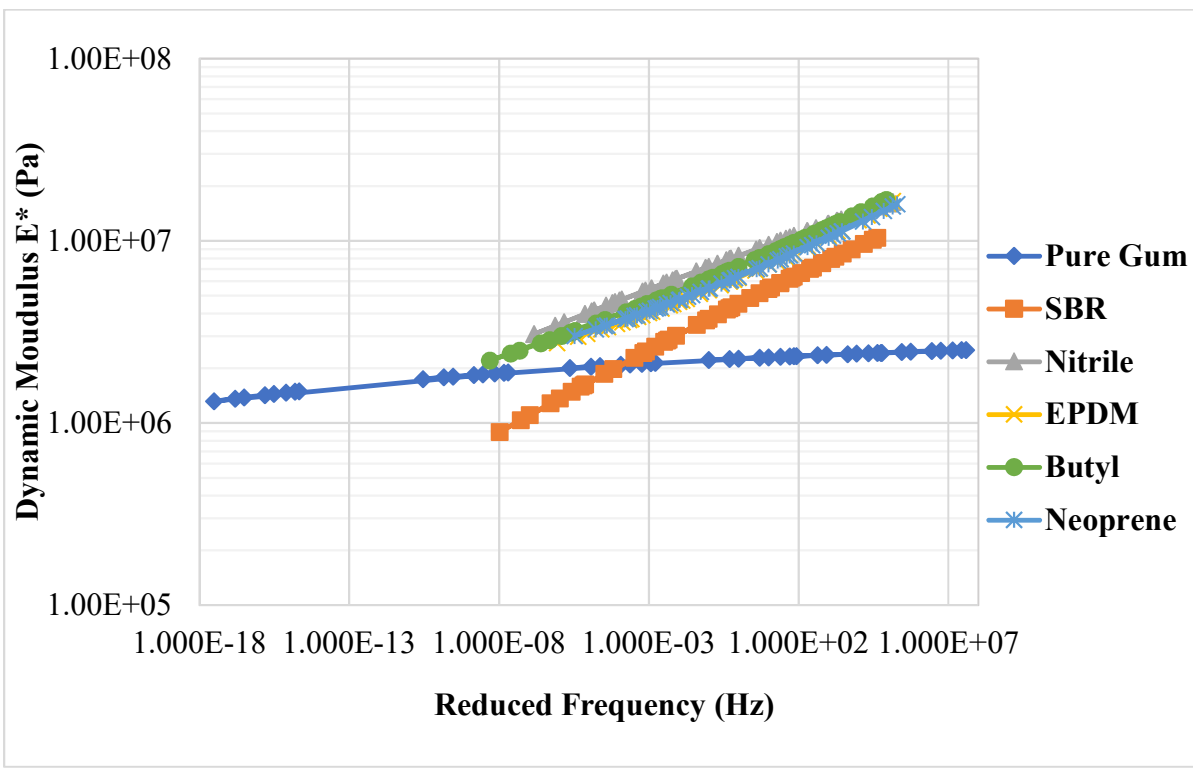


Figure 4-18. Master curves for the rubber materials

Table 4-3. Sigmoid function coefficients for the rubber master curves

Coefficient	Pure Gum	SBR	Nitrile	EPDM	Butyl	Neoprene
α	6.7190	9.4176	9.6246	20.1060	17.5406	16.4164
β	-2.9254	-0.6766	-0.8539	3.1303	2.2544	2.6144
γ	-0.2363	-0.1992	-0.1960	5.6488	4.7323	5.4126
δ	-0.0612	-0.0441	0.0821	-0.0648	-0.0373	-0.0525
C_1	0.3609	0.1396	0.0821	0.0556	0.0301	0.1405
C_2	-0.0006	-4.918E-6	0.0007	0.00091	0.00118	0.000114

4.5.2 Using the CRP Measurements to Predict Pavement Friction in the Laboratory

The texture measurements calculated using the CRP method were incorporated in the Persson friction model (Equation 4-5) to measure the coefficient of friction for the HMA test slabs. The model requires inputs for rubber rheological properties as well as surface texture parameters. The rubber rheological properties needed for the model [i.e., $E^*(\omega)$] were obtained from the master curve analysis of the rubber developed using the DMA measurements of the rubber dynamic modulus at various temperatures and loading frequencies.

The pavement surface power spectral density (PSD) was obtained from the CRP measurement of the pavement texture. A Fourier transformation was applied to the pavement surface profile measured using the CRP method to calculate the power spectral density. The Matlab software (MathWorks R2017b) was used to conduct the analysis. Figure 4-19 shows an example of power spectral density versus the spatial frequency (f) on a log-log scale. The slope of the line in Figure 4-19 represents the Hurst exponent (H) for each pavement surface which is a required parameter in Persson friction model.

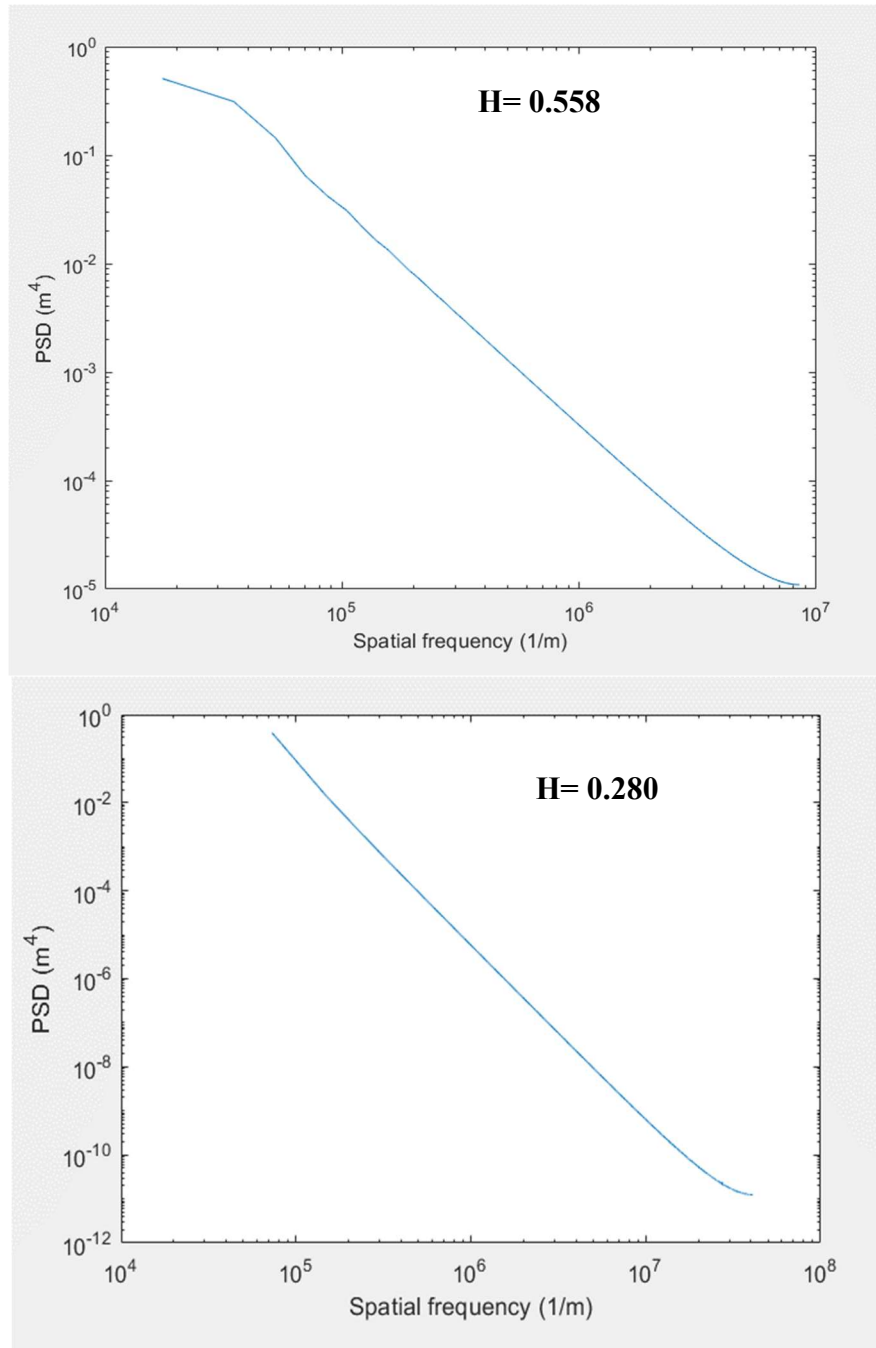


Figure 4-19. Examples of typical pavement surface power spectral density

The PSD parameter $C(q)$ was calculated using Equation 4-6 based on the lower and upper cutoff length of the wavenumber (q) and the calculated Hurst exponent of the surface (H). The nominal contact pressure (σ_0) in Equation 4-5 for the rubber sliders was calculated using Equation 4-16 where the normal applied load on each of the rubber sliders is 11.8 N and the

area of contact between the rubber slider and the pavement surface was measured to be 60.63 mm². The nominal contact pressure (σ_0) is 0.2 MPa for the rubber sliders.

$$\sigma_0 = P/A \quad (4-16)$$

The parameter $P(q)$ in Equation 4-5 was calculated as defined in Equation 4-4 while the parameter $S(q)$ was calculated according to Equation 4-8. The lower and upper cutoff lengths; q_0 and q_1 were calculated using Equations 4-10 and 4-11, respectively. Parameters q_0 and q_1 describe the mean microtexture and macrotexture depth for the pavement surface, respectively.

Poisson's ratio for all rubber materials was assumed to be 0.5 as the rubber materials [4, 31, 32] since rubber is incompressible. The dynamic modulus for each rubber material was calculated from the developed master curve using the sigmoid function to estimate the dynamic modulus of the rubber at a given frequency and test temperature as shown in Equation 4-13.

It was found that Persson's friction model was able to accurately predict the coefficient of friction (μ) between different rubber materials and the HMA slab surfaces based only on the material properties of the rubber and the surface texture characteristics that were calculated using the CRP method. The coefficient of friction (μ) was measured in the laboratory using the DFT device at 20 km/h. The results showed a strong correlation between the measured coefficient of friction and the predicted coefficient of friction using the Persson friction model. Figure 4-20 shows the correlation between the measured coefficient of friction and the predicted coefficient of friction between the HMA slabs and the rubber sliders. Such strong correlation of ($R^2 = 0.903$) clearly demonstrates that the texture parameters extracted from the CRP method can be used along with rubber properties to predict the coefficient of friction using Persson's friction model.

A check for normality was performed on the Persson model prediction of the coefficient of friction. Figure 4-21 shows that the residuals (error) histogram follows a normal distribution. In addition, Figure 4-22 shows that the Q-Q plot of the model predictions are distributed along

the normal quantile line which indicates the linearity of the model and shows that there is no bias in the model predictions.

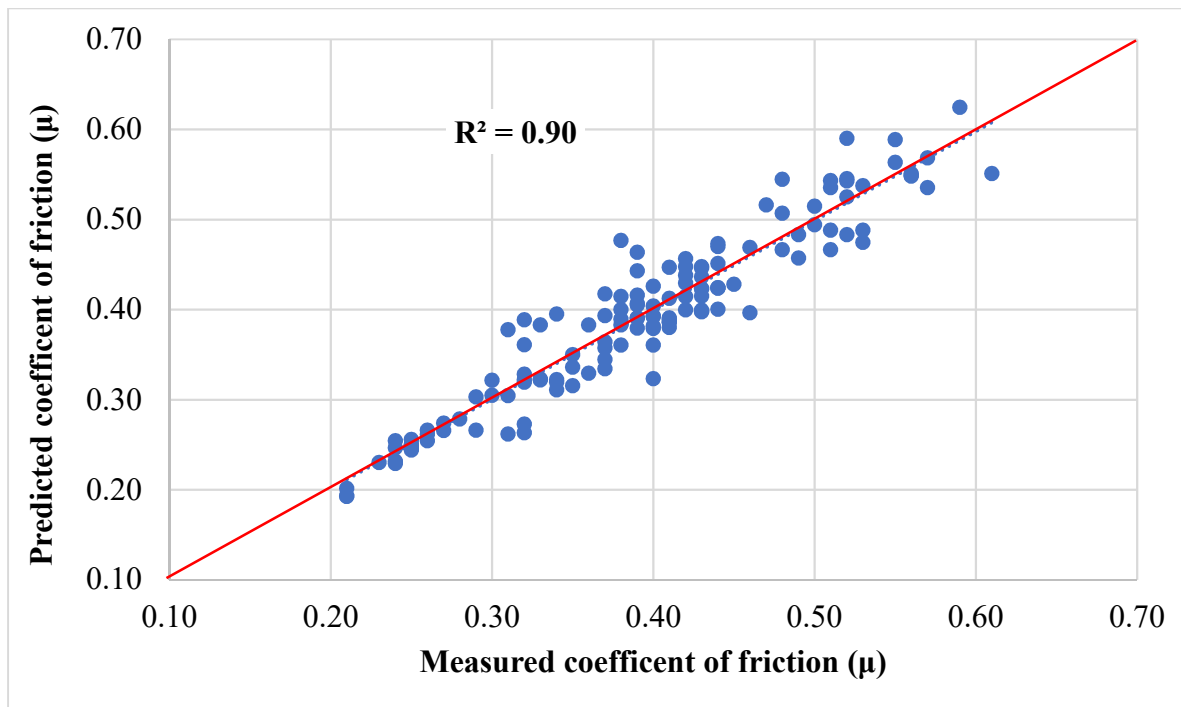


Figure 4-20. Measured coefficient of friction using DFT vs. predicted coefficient of friction using Persson model

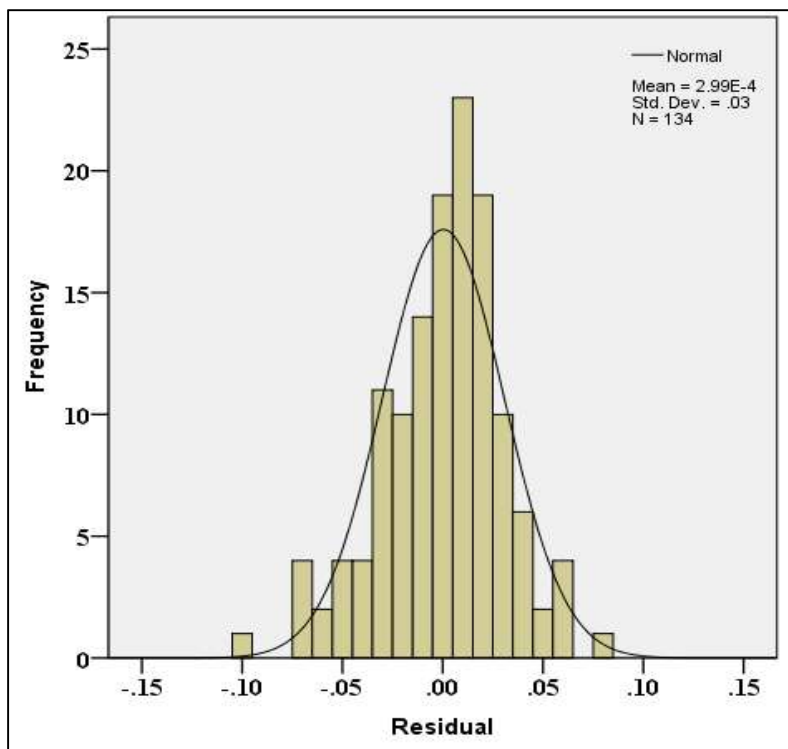


Figure 4-21. Histogram of the predicted coefficient of friction residuals

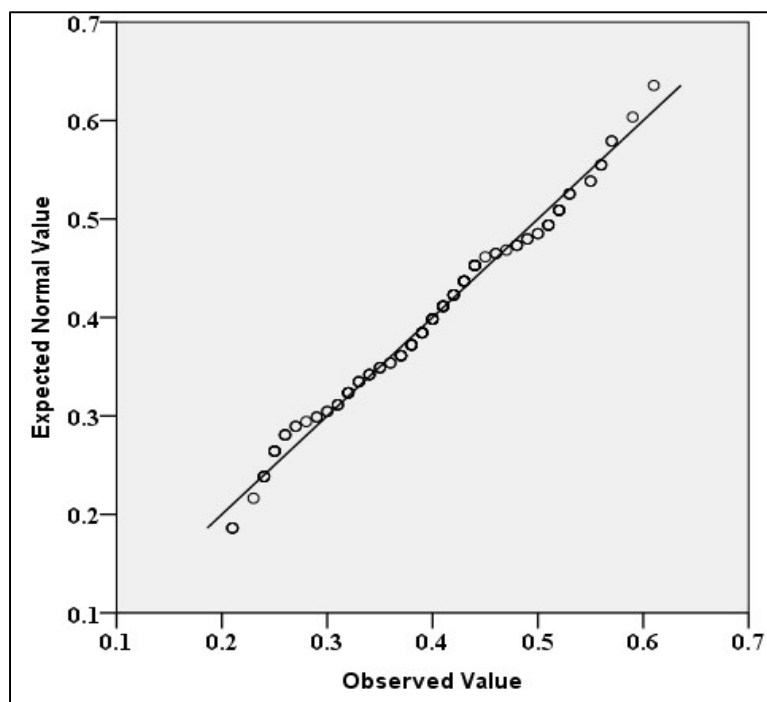


Figure 4-22. Q-Q plot for the model prediction of the coefficient of friction

4.5.3 Utilizing the CRP Measurements to Predict SN for the Field Test Sections

The CRP measurements for the field test sections surface texture were utilized to predict the SN between the skid trailer's smooth test tire (ASTM E 524) and field pavement sections at different speeds. The Persson friction model (Equation 4-5) was used to predict the SN. The SN is expressed as the predicted coefficient of friction multiplied by 100. According to the ASTM E 524 the standard smooth test tire is made from the SBR rubber and the properties of the tire were calculated from the master curve of the SBR rubber. Equation 4-17 was used to calculate the loading frequency (ω) for the rubber as it slides over the pavement surface at different speeds [41].

$$\Omega = v/\lambda \quad (4-17)$$

where,

v = the sliding velocity in m/s

λ = the wavelength of the pavement surface

The standard smooth tire is subjected to a constant axle load of 4800 N during the friction testing. The axle load of the skid trailer is calibrated before each test. The nominal contact area of the tire was measured in the laboratory using a pressure sensitive pressure sheet as discussed in Chapter 5 and was found to have a contact area of 25654 mm². The nominal contact pressure (σ_0) was calculated according to Equation 4-16 to be 0.19 MPa. The remaining parameters of the Persson friction model (Equation 4-5) (i.e., $P(q)$, $C(q)$, $S(q)$) were calculated as discussed in Section 4.2.3 and are reported in Appendix D.

The results demonstrated that the predicted skid numbers using Persson friction model correlated well with the measured skid numbers in the field as shown in Figure 4-23 ($R^2 = 0.972$). Furthermore, the model was able to accurately predict the skid number as a function of speed and surface texture characteristics of pavement surface. Figure 4-23 shows the correlation between the measured and predicted skid number for all the test sections at different speeds. The model was able to capture the effect of speed on the predicted SN based on the dynamic modulus of rubber. The loading frequency changes with speed according to Equation 4-17. As the speed increases the loading frequency increases which results in a higher rubber modulus leading to lower SN as the rubber becomes stiffer.

To verify the normality of the Persson model prediction of the skid number, a diagnostic check was performed. Figure 4-24 shows that the histogram of the residuals follows a normal distribution with a mean of 0.02 and standard deviation of 2.06. Figure 4-25 shows that the Q-Q plot of the model residuals. The residuals are distributed along the normal quantile line which indicates that the model errors are normally distributed and there is no bias in the model predictions.

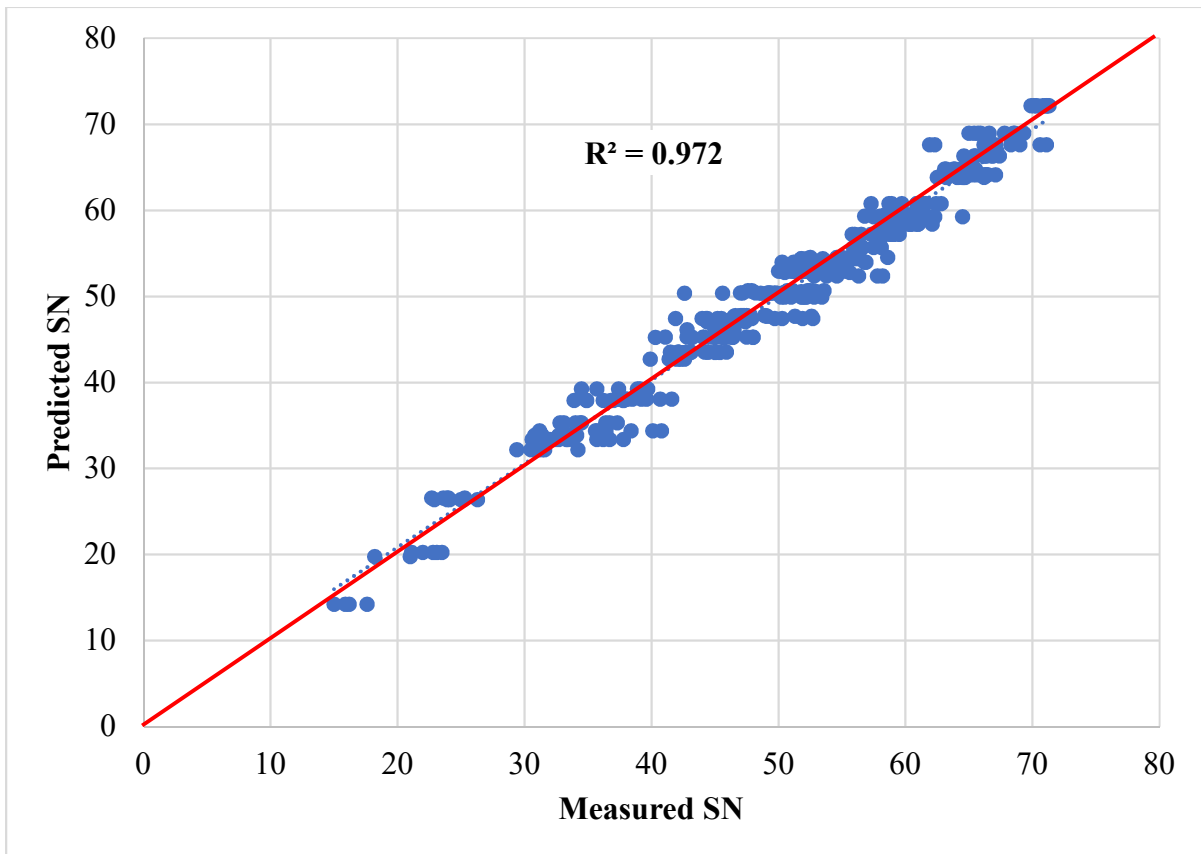


Figure 4-23. Correlation between the field measurements of the SN and the predicted SN using Persson friction model

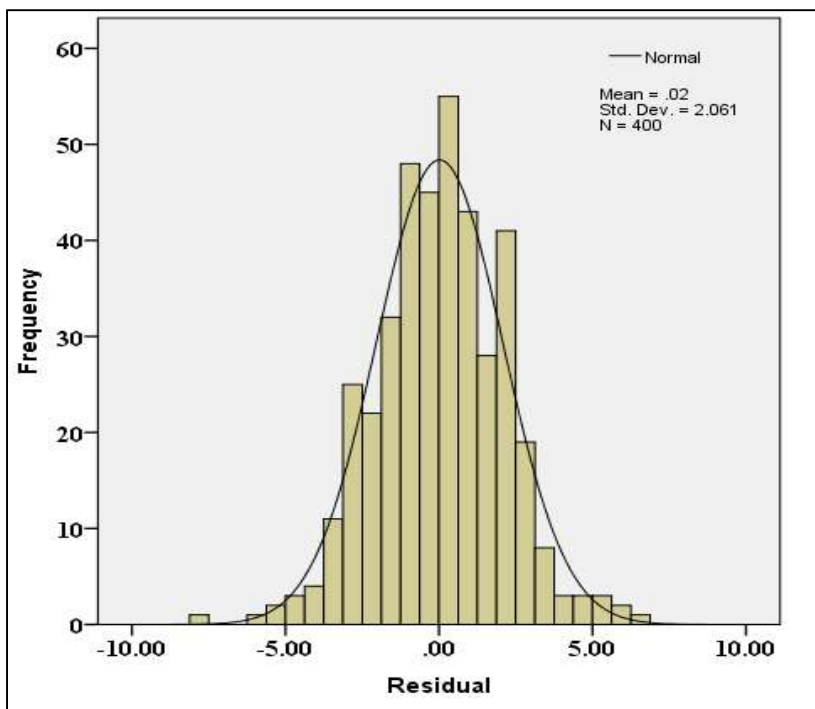


Figure 4-24. Histogram of the predicted SN residuals

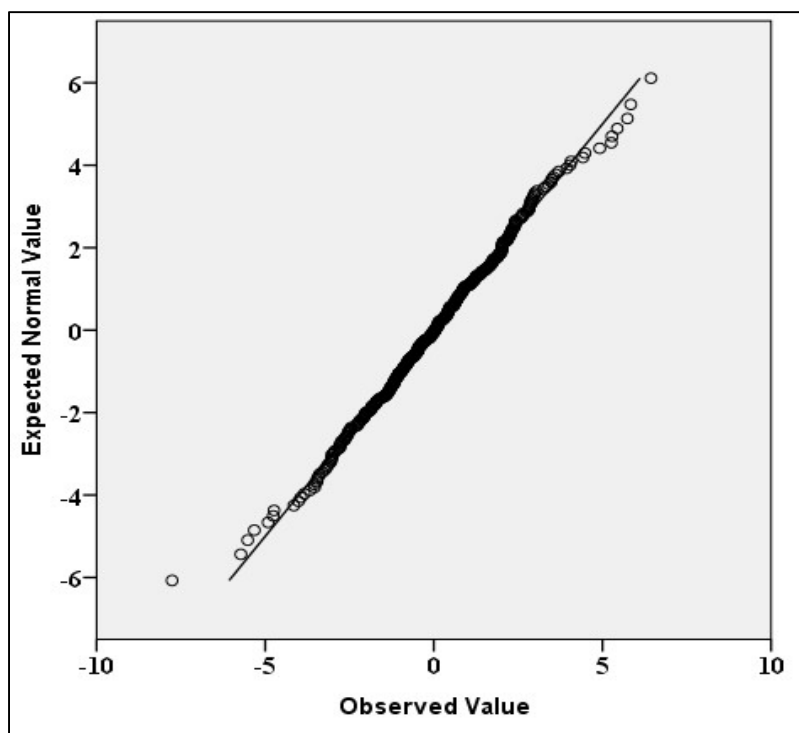


Figure 4-25. Q-Q plot for the model prediction of the coefficient of friction

4.6 Conclusions and Recommendations

This part of the study explored an innovative application of the CRP technique to measure the surface texture characteristics of pavement surfaces (macrotexture and microtexture). The results of CRP measurements of the macrotexture were in very good agreement with the results of the volumetric sand patch test. Similarly, the results showed a strong correlation between the CRP measured microtexture and DFT_{20} measurements using the standard rubber sliders. The DFT_{20} is accepted as an indirect method to quantify pavement microtexture. The CRP offers a simple and accurate, yet inexpensive alternative to the current methods used to measure surface macrotexture and microtexture. In addition, the CRP method only requires a hand-held camera to take measurements of the pavement surface at any desired location, while other methods such as atomic force microscopy (AFM) are limited to laboratory measurements.

The CRP measurements of the pavement surface characteristics along with the properties of different rubber materials were utilized to predict the pavement friction for pavement surfaces using the Persson friction model. The results demonstrated excellent correlation between measured and predicted friction. This study greatly simplified the texture parameter calculations needed in the Persson friction model and did so with good accuracy. This method can be used by highway agencies to estimate pavement friction especially when there are limitations on using the skid trailer (e.g., short test section, speed limit, or sharp horizontal curves).

The authors recommend further research to evaluate the light conditions (e.g., sunny, partially cloudy, cloudy, and artificial light) and surface conditions (e.g., wet and dry) on the results of CRP measurements. In addition, it is recommended to validate the results of this study and develop a system that can complement the current practice for measuring skid resistance of pavements. Such a system can be used to develop 3D models for surface texture using digital images to measure the texture parameters needed to predict skid number using non-contact methods.

4.7 References

- [1] Hall, J.W., Smith, K.L., Titus-Glover, L., Wambold, J.C., Yager, T.J. and Rado, Z., 2009. Guide for pavement friction. Final Report for NCHRP Project, 1, p.43.
- [2] Noyce, D.A., Bahia, H.U., Yambo, J.M. and Kim, G., 2005. Incorporating road safety into pavement management: maximizing asphalt pavement surface friction for road safety improvements. Draft Literature Review and State Surveys, Midwest Regional University Transportation Center (UMTRI), Madison, Wisconsin.
- [3] Henry, J.J., 2000. Evaluation of pavement friction characteristics (Vol. 291). Transportation Research Board.
- [4] Persson, B.N., 2001. Theory of rubber friction and contact mechanics. *The Journal of Chemical Physics*, 115(8), pp.3840-3861.
- [5] Roberts, A.D., 1988. *Natural rubber science and technology*. Oxford University Press.
- [6] Tomita, H., 1970. Tire-Pavement Friction Coefficients (No. NCEL-TR-672). Naval Civil Engineering Lab Port Hueneme, CA.
- [7] Dunford, A., 2013. Friction and the texture of aggregate particles used in the road surface course (Doctoral dissertation, University of Nottingham).
- [8] Kassem, E., Awed, A., Masad, E. and Little, D., 2013. Development of predictive model for skid loss of asphalt pavements. *Transportation Research Record: Journal of the Transportation Research Board*, (2372), pp.83-96.
- [9] Aldagari, S., Al-Assi, M., Kassem, E., Chowdhury, A. and Masad, E., 2018. Prediction Models for Skid Resistance of Asphalt Pavements and Seal Coat. *Transportation Research Board 97th Annual Meeting* (No. 18-05541) Washington DC.
- [10] Kogbara, R.B., Masad, E.A., Kassem, E., Scarpas, A.T. and Anupam, K., 2016. A state-of-the-art review of parameters influencing measurement and modeling of skid resistance of asphalt pavements. *Construction and Building Materials*, 114, pp.602-617.
- [11] Anderson, R. and Bahia, H., 1997. Evaluation and selection of aggregate gradations for asphalt mixtures using Superpave. *Transportation Research Record: Journal of the Transportation Research Board*, (1583), pp.91-97.
- [12] Asi, I.M., 2007. Evaluating skid resistance of different asphalt concrete mixes. *Building and Environment*, 42(1), pp.325-329.

- [13] Masad, E., Rezaei, A., Chowdhury, A. and Freeman, T.J., 2010. Field evaluation of asphalt mixture skid resistance and its relationship to aggregate characteristics (No. 0-5627-3). Texas Transportation Institute.
- [14] Jayawickrama, P. and Thomas, B., 1998. Correction of field skid measurements for seasonal variations in Texas. *Transportation Research Record: Journal of the Transportation Research Board*, (1639), pp.147-154.
- [15] Oliver, J.W., Tredrea, P.F. and Pratt, D.N., 1988. Seasonal variation of skid resistance in Australia. *SPECIAL REPORT, NO 37, ISSN: 0572-144X;*, (37).
- [16] Al-Assi, M. and Kassem, E., 2017. Evaluation of adhesion and hysteresis friction of rubber-pavement system. *Applied Sciences*, 7(10), p.1029.
- [17] Hernandez-Olivares, F., Barluenga, G., Bollati, M. and Witoszek, B., 2002. Static and dynamic behavior of recycled tyre rubber-filled concrete. *Cement and concrete research*, 32(10), pp.1587-1596.
- [18] ASTM E965-15, Standard Test Method for Measuring Pavement Macrotexture Depth Using a Volumetric Technique. ASTM International, West Conshohocken, PA, 2015.
- [19] Hanson, D.I. and Prowell, B.D., 2004. Evaluation of circular texture meter for measuring surface texture of pavements (No. NCAT Report 04-05). The Center.
- [20] ASTM E2157, Standard test method for measuring pavement macrotexture properties using the circular track meter. ASTM International, West Conshohocken, PA, 2012
- [21] Abe, H., Tamai, A., Henry, J.J. and Wambold, J., 2001. Measurement of pavement macrotexture with circular texture meter. *Transportation Research Record*, 1764(1), pp.201-209.
- [22] Hao, X., Sha, A., Sun, Z., Li, W. and Zhao, H., 2016. Evaluation and comparison of real-time laser and electric sand-patch pavement texture-depth measurement methods. *Journal of Transportation Engineering*, 142(7), p.04016022.
- [23] Fuentes, L.G., 2009. Investigation of the factors influencing skid resistance and the international friction index. Ph.D. Dissertation. University of South Florida, FL.
- [24] Fuentes, L., Gunaratne, M. and Hess, D., 2010. Evaluation of the effect of pavement roughness on skid resistance. *Journal of Transportation Engineering*, 136(7), pp.640-653.
- [25] Fisco, N.R., 2009. Comparison of macrotexture measurement methods. Master Thesis. Ohio State University.

- [26] McQuaid, G., Millar, P., Woodward, D., Friel, S. (2013). Use of Close Range Photogrammetry to Assess the Micro-Texture of Asphalt Surfacing Aggregate. International Journal of Pavements Conference, Sao Paulo, Brazil.
- [27] Millar, P., Woodward, D., Woodside, A. (2009). Use of Close Range Terrestrial Photogrammetry to Assess Accelerated Wear of Asphalt Concrete Surface Course Mixes. 6th International Conference on Maintenance and Rehabilitation of Pavements and Technological Control (MAIREPAVE6), pp. 734-740.
- [28] McQuaid, G., 2015. Development of non-contact 3D measurement of areal pavement texture parameters (Doctoral dissertation, Ulster University).
- [29] Kogbara, R.B., Masad, E.A., Woodward, D. and Millar, P., 2018. Relating surface texture parameters from close range photogrammetry to Grip-Tester pavement friction measurements. *Construction and Building Materials*, 166, pp.227-240.
- [30] Martino, M.M. and Weissmann, J., 2008. Evaluation of Seal Coat Performance Using Macro-texture Measurements. University of Texas at San Antonio, Department of Civil and Environmental Engineering.
- [31] Persson, B.N. and Scaraggi, M., 2014. Theory of adhesion: Role of surface roughness. *The Journal of chemical physics*, 141(12), p.124701.
- [32] Lorenz, B., Oh, Y.R., Nam, S.K., Jeon, S.H. and Persson, B.N.J., 2015. Rubber friction on road surfaces: Experiment and theory for low sliding speeds. *The Journal of chemical physics*, 142(19), p.194701.
- [33] Martinez, O.S., Cruz, D.M., Chavarin, J.U. and Bustos, E.S., 2014. Rough Surfaces Profiles and Speckle Patterns Analysis by Hurst Exponent Method. *J. Mater. Sci. Eng*, 3, pp.759-766.
- [34] ASTM E1911-09ae1, 2009. Standard Test Method for Measuring Paved Surface Frictional Properties Using the Dynamic Friction Tester (Withdrawn 2018), ASTM International, West Conshohocken, PA.
- [35] ASTM E524-08, 2015. Standard Specification for Standard Smooth Tire for Pavement Skid-Resistance Tests, ASTM International, West Conshohocken, PA.
- [36] ASTM E501-08, 2015. Standard Specification for Standard Rib Tire for Pavement Skid-Resistance Tests, ASTM International, West Conshohocken, PA.

- [37] ASTM E274 / E274M-15, 2015. Standard Test Method for Skid Resistance of Paved Surfaces Using a Full-Scale Tire, ASTM International, West Conshohocken, PA.
- [38] Fernando, E., Zimmer, R. and Mikhail, M., 2013. Comparative evaluation of locked-wheel and fixed-slip skid systems. Transportation Research Record: Journal of the Transportation Research Board, (2369), pp.125-134.
- [39] Florková, Z. and Pepucha, L. Microtexture Diagnostics of Asphalt Pavement Surfaces. IOP Conference Series: Materials Science and Engineering. 2017, 236, 012025.
- [40] Flintsch, G.W., de Leon, E., McGhee, K.K. and Al-Qadi, I.L., 2003. Pavement surface macrotexture measurement and applications. Transportation Research Record, 1860(1), pp.168-177.
- [41] Do, M.T. and Cerezo, V., 2015. Road surface texture and skid resistance. Surface Topography: Metrology and Properties, 3(4), p.043001.

Chapter 5. Finite Element Simulation of ASTM E 524 Standard Test Tire

5.1 Abstract

In this part of the study, a three-dimensional (3D) finite element model was developed for the ASTM E 524 standard test tire used in measuring skid number in the field to study the tire-pavement interaction. The finite element simulations were conducted in two main stages. In the first stage, the authors defined the tire geometry, cross section and material properties of various layers that form the test tire. Then, the author validated the finite element model of the test tire with laboratory measurements that included the application of various loads and recording the resulting deformation. In the second stage, the validated tire model was used to predict the normal and shear contact stress distribution under various parameters to study the effect of surface characteristics and temperature on the tire-pavement contact stress. The study parameters included coefficient of friction, rolling condition, texture, and temperature of rubber material.

The results of this study demonstrated that the magnitude and non-uniformity of the contact stress distribution depend on both the rolling condition and coefficient of friction of the tire-pavement interface. The results of the finite element simulations demonstrated that the stress distribution at the tire-pavement interface is non-uniform with maximum values towards the edges of the tire. These findings were consistent with the wearing pattern of the test tire in the field. The coefficient of friction was found to have a significant effect on the shear contact stresses at the tire-pavement interface. Higher values of the pavement coefficient of friction resulted in higher magnitudes of shear stress at the tire-pavement area of contact. The results also showed that the grooved (textured) pavement surface exhibited higher contact stresses (normal and shear) compared to the smooth pavement surface. Finally, the temperature was found to have significant effect of the contact stresses. The contact (normal and shear) stress decreased with the increase in temperature as the area of contact between the tire and pavement surface increases.

5.2 Introduction

Skid resistance of pavement surfaces is measured and monitored by highway agencies using the skid trailer to ensure that pavements provide an adequate level of skid resistance. The skid trailer uses standard smooth or ribbed test tires to measure pavement skid resistance. Accurate simulation of the tire-pavement interaction is of great importance for traffic and highway engineers to better understand the mechanisms developing at operational conditions (e.g., free rolling, skidding, acceleration, etc.). Calculating the stress distribution under the contact area between the tire and pavement is needed for pavement design. Excessive stress at the top of pavement surface may lead to pavement damage [1-3]. In addition, tire-pavement contact stresses contribute to the vehicle stability and its ability to perform different maneuvers while traveling on the road [4, 5]. Many previous studies were performed to simulate different truck and passenger vehicle tires and calculate the stress distributions at the tire-pavement interface. Finite element simulations of the tire-pavement interaction provide a better understanding of the mechanisms that affect the stresses and strains at the tire-pavement interface. Prediction of the tire-pavement contact stress distribution, while the vehicle is performing different maneuvers, was used to ensure the safety and stability of the vehicle on the pavement surface [3].

Numerical solutions can provide accurate results in less time compared to mathematical methods [2]. Higher stress concentrations at the pavement surface increase the potential of pavement distresses including rutting, shoving, and top-down cracking [20]. Pavement distresses are mainly caused by a high concentration of normal and shear stresses at the tire-pavement interface [3]. Numerical methods are useful to calculate the magnitude and distribution of contact stresses at the tire-pavement interface. These numerical approaches use the finite element method (FEM) to study the stresses and strains at the tire-pavement interface. The FEM considers numerous factors that affect the tire-pavement interaction such as the nonlinear behavior of the tire composite materials, and complex boundary conditions at the interface along with the effect of temperature on the tire-pavement interaction [2]. There are several models that have been used in previous studies to simulate the tire-pavement contact behavior (i.e., the distribution of contact stresses at the interface) [6-11]. The complexity of these models varies based on the features and types of the FE formulation used in the analysis (i.e., Lagrangian, Eulerian, and Arbitrary Lagrangian Eulerian), and material properties in the

FEM (e.g., linear elastic, hyperelastic, or viscoelastic). This section provides brief discussion about some of these models.

Tielking and Roberts [6] developed a finite element tire model to calculate the contact pressure at the tire-pavement interface. The pavement surface was modeled as a rigid flat (smooth) surface to simplify the analysis and reduce the required computational time. The tire was modeled after a bias-ply truck tire with two levels of inflation pressure (i.e., 75, and 125 psi) were applied on the tire. The tread pattern on the tire was not considered in the analysis. Instead, a smooth representation of the truck tire geometry was used in the FEA to simplify the model and reduce the computational time. The calculated contact shear stresses distribution was compared to laboratory-measured contact shear stresses. The results of FEA confirmed the non-uniformity of the stress distribution under the tire footprint. The edges of the contact area showed higher stress than the center of the contact area, which was also confirmed by laboratory measurements of the contact stresses under the tire contact area. The tire model was then used to calculate the critical maximum contact stresses resulting from a truck passing over a pavement surface. The analysis results were found to be more accurate than the conventional methods that assume that the stress is uniform under the tire contact area. The results of this study presented an analytical method to accurately calculate pavement stresses. The stress distribution was then used as input for the pavement design using design software. Such software utilizes the non-uniformity of the contact pressure distribution in calculating pavement strains for flexible pavements. The calculated strains are used in flexible pavement design in order to increase its life expectancy and carry higher repetitions of heavy truckloads.

Zhang [7], developed a nonlinear 3D finite element model of a ribbed tire to study the stress, strain, and deformation of the truck tire when subjected to axle load and inflation pressure under normal operating conditions. The results showed that the maximum contact pressure occurs inside of the inner ribs of the tire when subjected to light loads. However, the maximum pressure shifts outwards along the lateral direction of the tire when the applied normal load is increased. The contact area and deflection of the tire under a wide range of normal loads and inflation pressures were measured in the laboratory. Then the measured contact area and deflection were compared to the FE results in order to validate the model accuracy. The results of the finite element model were used to calculate the tire-pavement

contact pressure distribution as a function of the applied normal load. After the model was validated, the vibration modes and natural frequencies of the tire were evaluated for the radial truck tire. The model was able to accurately predict the shear stresses interaction between the tire layers (reinforcement layers) under different loading conditions.

Long [8] performed a finite element simulation to calculate rutting in flexible pavements for a heavy-vehicle simulator tire. The pavement was modeled using a viscoelastic material property. The laboratory measured rut depths using the heavy-vehicle simulator were found to be comparable to the finite element results of the average measured rut depth.

Kim et al. [9] investigated four types of tire-pavement interaction models. The material properties of the tire and pavement were defined as follows: 1) the tire was modeled as hyperelastic material and the pavement as a rigid body, 2) the tire modeled as a linear elastic material and the pavement as multi-layered with elasto-viscoplastic HMA layer, 3) applying a predefined pressure of a tire on an elasto-viscoplastic pavement model, and 4) the tire was modeled as hyperelastic material while an elasto-viscoplastic model was used for pavements. The tire part was modeled after a typical passenger car tire with a smooth tread to reduce the computational time and simplify the analysis. A pressure level of 30 psi was applied to simulate the typical inflation pressure in a passenger car and the applied load at the rim center was set at 4000 N. The results demonstrated that the pavement model does not affect the contact pressure distribution at the tire-pavement interface, while the material property and behavior of the tire was found to affect the stress distribution. The hyperelastic material model for the tire was found to accurately describe the contact behavior between the tire and pavement surface. The contact stress distribution of the tire was found to have larger concentrations at the outer edge of the contact area compared to the center of the contact area due to the high local strain of the sidewall of the tire, which is a typical for pneumatic tires.

Srirangam et al. [10] developed a finite element model to investigate the effect of the tire temperature on pavement friction measurements for the PIARC 165 R 15 standard smooth tire. The tire is made of SBR 1712 rubber and has a standard inflation pressure of 29 psi. A pressure sensitive film was used to measure the contact area imprint of the tire in the laboratory under different normal loads using an MTS machine. The material properties of the tire reinforcement layers were adjusted to match the contact area measured in the finite element analysis with the

lab measurements of the contact area at the different loads. The results showed a good agreement between the FE calculated thermal friction analysis with laboratory experimental measurements.

Wang et al. [11] developed a FEM to simulate a ribbed tire sliding over a smooth pavement surface to investigate the effect of surface friction on the contact stresses at the tire-pavement interface at different rolling conditions (e.g., braking, free rolling, cornering). The tire was modeled after a pneumatic tire structure with three layers of reinforcement embedded in the tire. The results showed that the stress distribution and magnitude at the tire-pavement contact area are non-uniformly distributed and depend on the rolling conditions of the tire. The results of the FEA showed that the increase in the surface coefficient of friction showed no effect on the vertical contact stress while there was a significant increase in the contact shear stress at both free rolling and fully skidding conditions.

5.3 Research Motivation

Measuring the skid resistance using the locked-wheel skid trailer is the most common method used by several highway agencies in the United States. This method uses the standard ASTM E 524 smooth test tire [12]. Yet to the best of the authors' knowledge, there are no previous studies that investigated the contact (vertical and shear) stress distribution for the ASTM E 524 standard test tire. Developing a finite element model (FEM) to calculate the contact stresses at the tire-pavement interface provides a fundamental understanding for the mechanisms of friction and the parameters that affect measurements of skid resistance using the ASTM standard test tire. The main goal of this research is to develop a 3D finite element model and evaluate the surface texture and rubber properties on the tire-pavement interaction. This part of the study investigates the effect of different parameters (i.e., pavement texture, coefficient of friction, rolling condition, and temperature) on the contact stress (normal and shear) distributions between pavement surface and the ASTM E524 smooth test tire. The developed model can be utilized to achieve a better understanding of the development of contact stress and traction distribution at the tire-pavement interface at different conditions (e.g., rubber-, pavement-, and vehicle-related). This understanding, for example, can assist us to explain the seasonal variation of skid resistance and the developed delamination stresses at

the intersection where vehicles break or speed. This will ultimately lead to better pavement design and tire configuration to improve performance.

5.4 Research Objectives

The main objectives of this part of the study were to:

- 1- Develop a full-scale 3D finite element model of the ASTM E 524 standard smooth test tire to understand its interaction with pavements.
- 2- Investigate the effect of pavement surface texture (e.g., coefficient of friction) and grooving conditions (e.g., smooth, grooved) on the resulting contact stress distribution (vertical and shear) at the tire-pavement interface at various rolling conditions (e.g., free-rolling, full skid).

5.5 Methods and Materials

5.5.1 Model Development

To achieve the objectives of this study, a full-scale 3D model of the ASTM E 524 tire was developed using Abaqus 2016 software (3DS SIMULIA 2016). The finite element modeling was carried out in two main stages. In the first stage, the authors defined the tire geometry, cross section and material properties of various layers that form the test tire. Then, the authors validated the finite element model of the test tire with laboratory measurements that include the application of various loads and recording the resulting deformation. In the second stage, the validated tire model was used to predict the normal and shear contact stress distribution under various parameters to study the effect of surface characteristics and temperature on the tire-pavement contact stress.

5.5.2 Tire Geometry

The first step was to define a two-dimensional (2D) cross section of the ASTM E 524 test tire that match the dimensions of a full-scale standard test tire. The cross-section of the tire was then revolved 360 degrees with a diameter of 15.5 inches (393.7 mm) to generate a full-scale 3D model of the tire. The tire was then reinforced with three shell element parts to model the tire reinforcement layers. Figure 5-1a shows 2D sketch of the tire cross-section with the reinforcement parts, while Figure 5-1b shows a 3D cut section of the tire showing the rubber tread part and the three embedded reinforcement layers (carcass and two belts). The number

of reinforcement layers was selected after Wang et al. [11]. A detailed description of each part is provided in the material properties section.

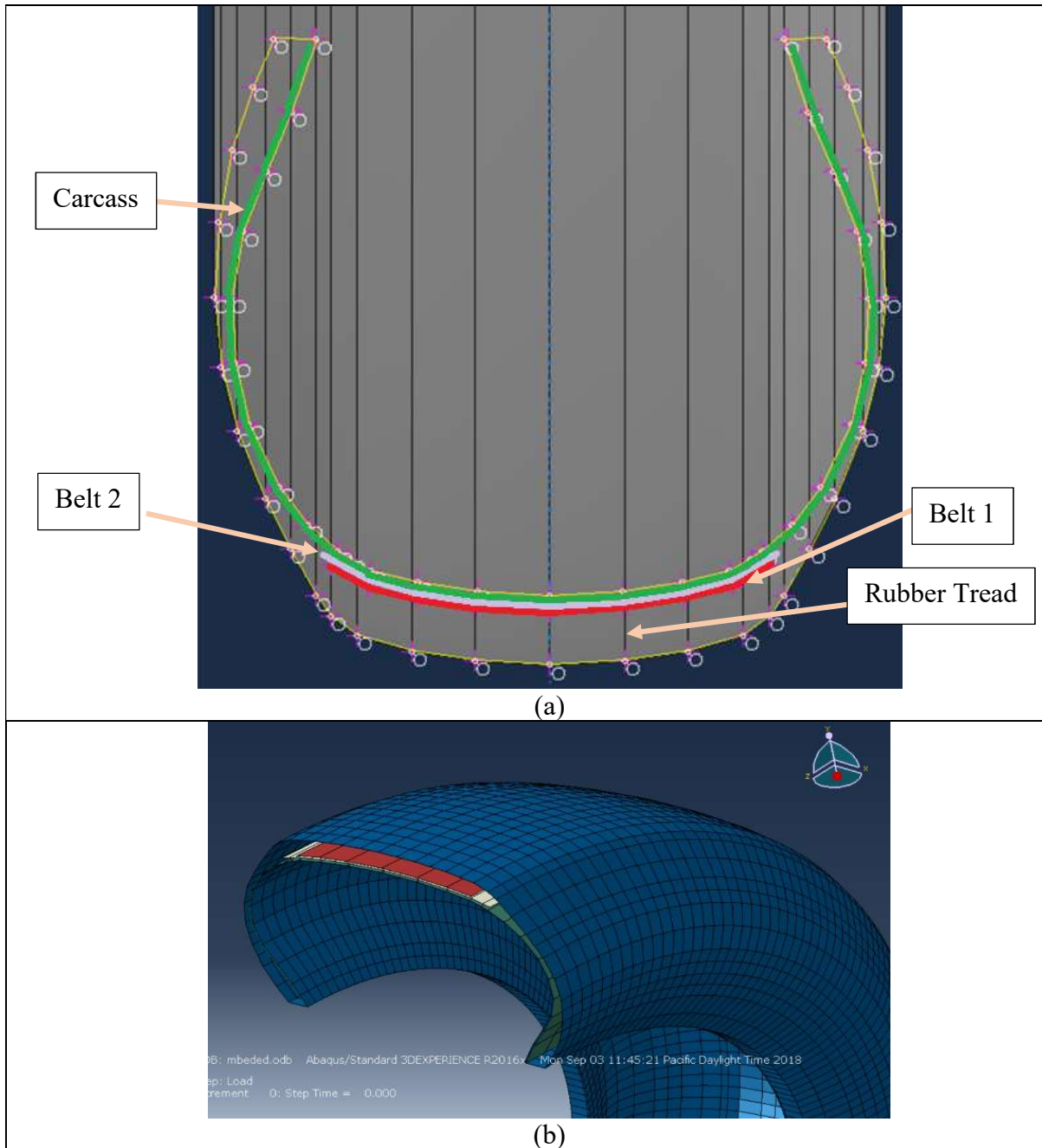


Figure 5-1. Cross section of the ASTM E 524 standard test tire model in Abaqus

5.5.3 Material Properties

The rubber tread of the ASTM E 524 standard test tire is made of SBR 1712 rubber. The rubber tread part material property was defined as hyperelastic [10] with a neo-Hookean strain energy potential as given in Equation 5-1.

$$U = C_{10}(\bar{I}_1 - 3) + D_1(J - 1)^2 \quad (5-1)$$

where,

U = the strain energy per unit of reference volume

C_{10} = material parameter equal to 0.5 of the shear modulus of the material (G)

D_1 = material parameter equal to $2/K$

\bar{I}_1 = the first deviatoric strain invariant defined as presented in Equation 5-2

J = the elastic volume ratio

G = shear modulus

K = bulk modulus

$$\bar{I}_1 = \bar{\lambda}_1^2 + \bar{\lambda}_2^2 + \bar{\lambda}_3^2 \quad (5-2)$$

Rubber is an incompressible material having a Poisson's ratio (ν) of 0.5 [1, 3, 10, 11] and thus D_1 in Equation 5-1 will be equal to zero as K_1 is approaching infinity according to Equation 5-3.

$$K = \frac{E}{3(1-2\nu)} \quad (5-3)$$

Similarly,

$$G = \frac{E}{2(1+\nu)} \quad (5-4)$$

Substituting Poisson's ratio (ν) of 0.5 in Equation 5-4, we obtain $C_{10} = \frac{E}{6}$, where E is the modulus of elasticity of the material.

An SBR rubber specimen was tested using the Dynamic Mechanical Analyzer (DMA) in uniaxial tension and the stress-strain curve was obtained for the SBR rubber at 20 °C as shown in Figure 5-2. The Abaqus solver was used to fit the rubber stress-strain curve of the SBR rubber to a neo-Hookean strain energy potential (Equation 5-1). The coefficients (i.e., D_1 , C_{10}) of the rubber tread were determined to model the rubber tread part of the tire. The coefficients are listed in Table 5-1. As expected, D_1 for the rubber tread was found to approach zero since rubber is an incompressible material.

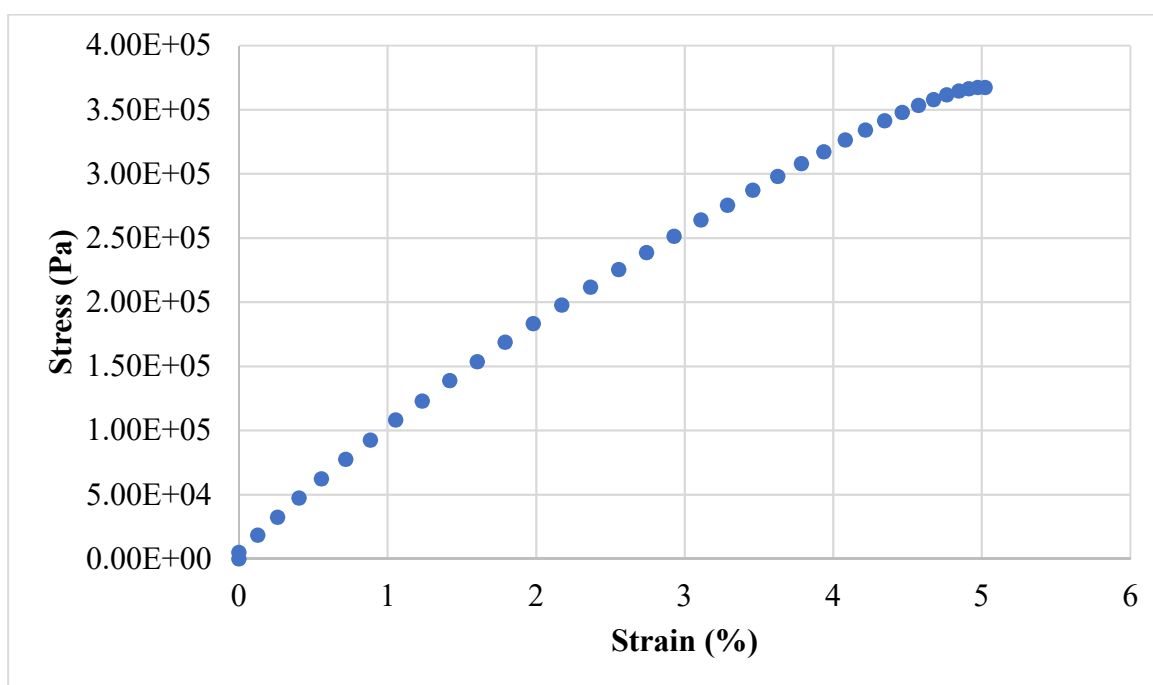


Figure 5-2. Stress-Strain curve for SBR Rubber at 20 °C

The tire reinforcement layers (i.e., the carcass and two belt layers) material properties are typically not specified by the tire manufacturer. The carcass layer provides support to the tire sidewall to withstand the inflation pressure and provides flexibility to accommodate the large tire deformation [3]. The belt layers provide additional stiffness to the rubber tread [10]. The carcass and the belts were modeled as linear elastic materials with Poisson's ratio equal to 0.35 [10]. The values of the elastic modulus of reinforcement layers were initially selected from

typical values found in the literature [1, 3, 10, 11]. The values of the elastic modulus were then adjusted in the FE model to match the contact area and deformation measured in the laboratory under various loadings.

Table 5-1 summarizes the material property used to model different component of the ASTM E 524 test tire. The same material properties were used to calculate the vertical and shear stress distribution in the second stage of the FE simulation.

Table 5-1. Material properties of various components of the test tire

Material	Density (kg/m³)	Modulus (MPa)	Poisson's Ratio
Rubber tread	1100	($C_{10} = 2.3955$, $D_1 = 8.4048 \text{ e-}8$)	0.49
Carcass	4000	65 (Elastic)	0.35
Belt 2	3500	25 (Elastic)	0.35
Belt 1	3000	12 (Elastic)	0.35

5.5.4 Surface to Surface Interaction Simulation

In first stage, the author tested the contact area between the test tire and fixed plate using the FE simulation which was later compared with the laboratory measurements. A surface to surface interaction was defined between both an upper and lower plate and the tire tread with hard contact behavior as shown in Figure 5-3. However, for the three reinforcement layers, a tie constraint was used to embed the reinforcement layers in the rubber tread. The rubber tread part was defined as the master surface while the reinforcement shell elements were set as a slave surface. Similarly, for the second stage of the analysis of the sliding tire over the pavement slab. As mentioned earlier, a surface to surface interaction (hard contact) was defined between the slab surface and the rubber tread. In addition, the penalty friction formulation was used to define the coefficient of friction through tangential contact behavior. In the second stage of the analysis, three levels of the coefficient of friction were defined (i.e., 0.2, 0.4, and 0.6) where a coefficient of friction of 0.2 represents a surface with low microtexture and a coefficient of friction of 0.6 represents a surface with high microtexture.

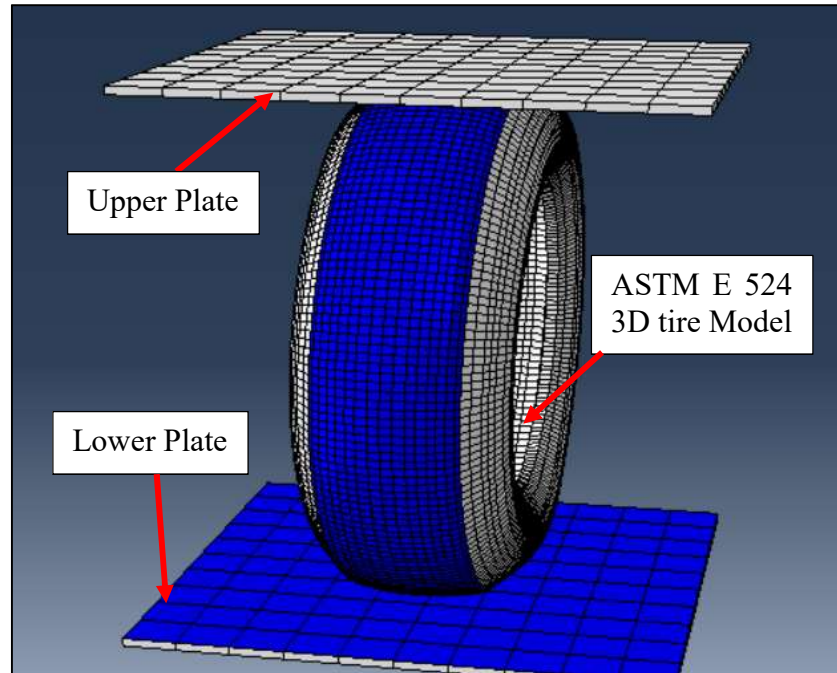


Figure 5-3. Contact between the tire part and two plates

5.5.5 Loads and Boundary Conditions

The applied loads and boundary conditions in these analyses are described in this section. First for the first stage of analysis with the tire between two plates, the bottom plate was fixed and not allowed to move or rotate in the x, y, or z directions. The upper plate was fixed in the x-z plane and was free to move in the vertical y-direction. Also, the upper plate was not allowed to rotate in the x, y, and z-directions. The boundary conditions for the tire part are applied on the rim edge of the tire as shown in Figure 5-4. The rim is only allowed to move in the vertical y-direction and is fixed from translation and rotation in all other directions. The vertical compressive load (P) is applied on the four corners of the upper plate with a magnitude of P/4 on each corner. A pressure of 24 psi (165,474 N/m²) was applied on the inner wall of the rubber tread to simulate the inflation pressure in the tire as specified in ASTM E 524 standard.

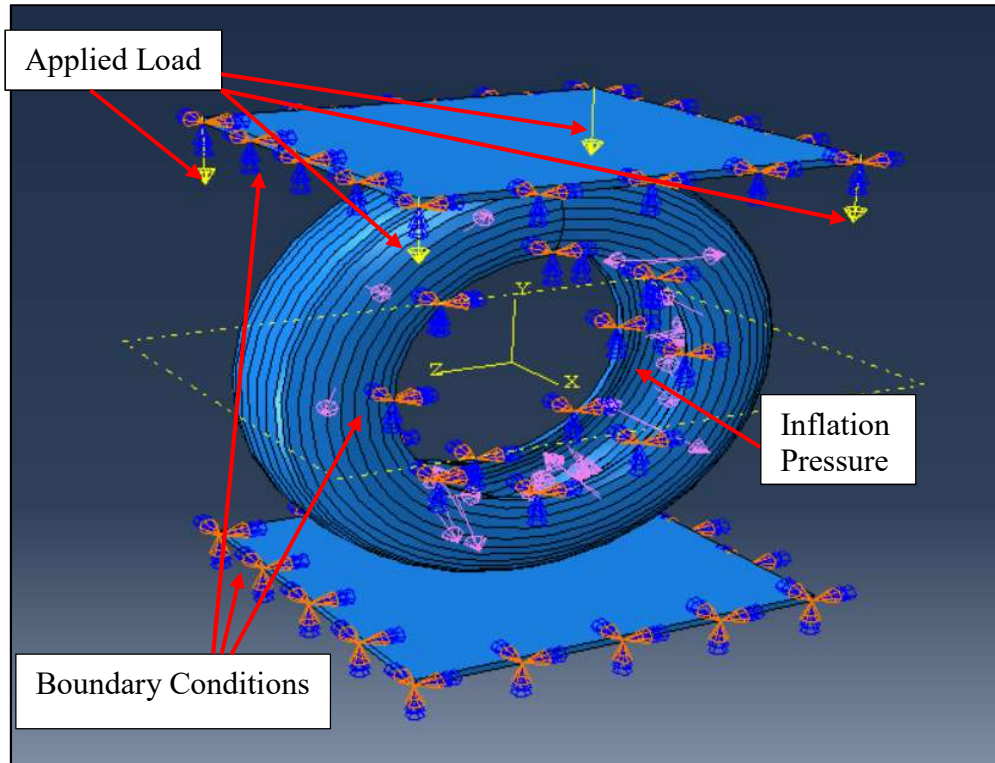


Figure 5-4. Loads and boundary conditions for the first stage of the analysis

For the second part of the analysis where the test tire is sliding over the pavement surface, the pavement slab shown in Figure 5-5 is fixed in all directions from translation and rotation. The tire was constrained from the rim edge to a reference point as shown in Figure 5-5. The tire was not allowed to translate in the lateral x-direction and was restricted from rotation in both the vertical y-direction and the longitudinal z-direction. A velocity boundary condition was defined on the reference point to move the tire at the desired speed (1 m/s) in the z-direction. The tire was not allowed to rotate in the x-direction when the tire was fully skidding. A rotational velocity (ω) of 3.16 rad/sec was defined at the reference point when the tire was allowed to rotate (i.e., free rolling) while the rotational velocity was set to zero for the full skidding condition. An inflation pressure of 24 psi was applied on the inner wall of the rubber tread to simulate the inflation pressure in the tire as specified in ASTM E 524 standard.

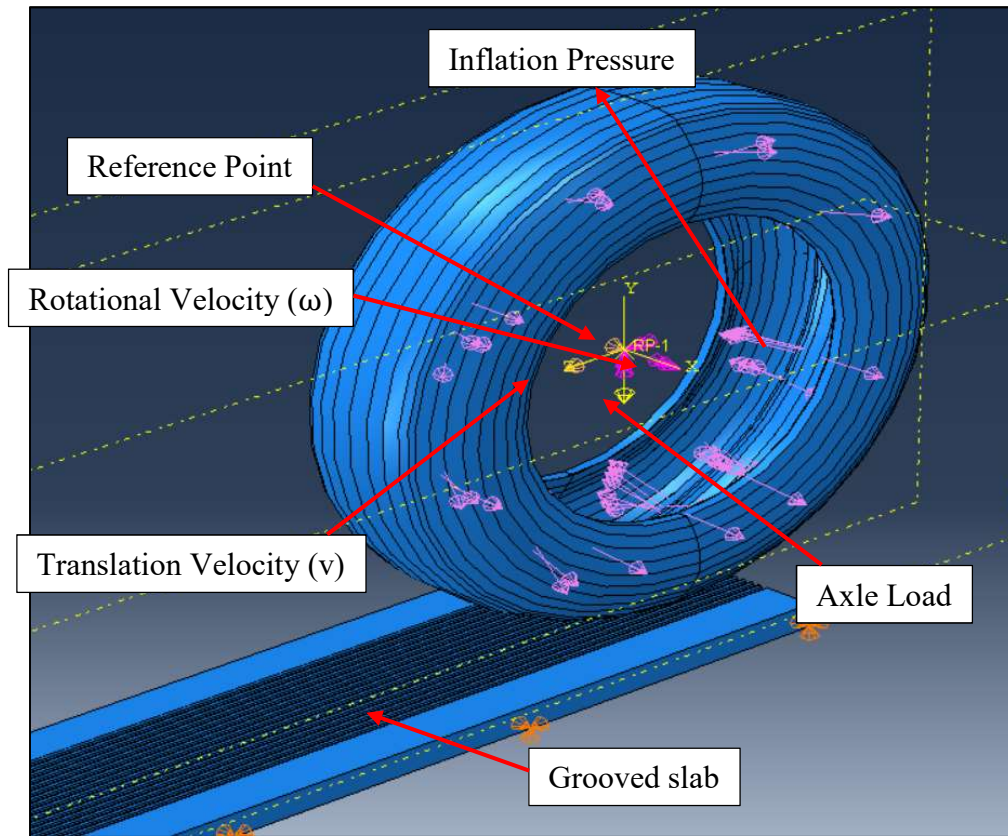


Figure 5-5. Loads and boundary conditions for the tire model sliding over pavement slab

5.5.6 Development of the Mesh for the Model Parts

The 3D stress mesh type with an eight-node linear brick element (C3D8R) was used for the tire model mesh. The three reinforcement layers (i.e., the carcass and two belt layers) were modeled as shell elements with four-node doubly curved shell elements (S4R). The tire was initially modeled using a coarse mesh (i.e., large element size) with a total number of 1080 elements. A mesh sensitivity analysis was performed, and the number of elements of the mesh was increased gradually to ensure that the mesh size does not affect the results. The maximum contact stress was reported for each mesh size. When the difference in the maximum contact stress was less than 5% as the mesh size changed, that mesh size was used for the analysis and the results were considered independent of the mesh size [21]. Figure 5-6 shows the mesh convergence analysis in this study. The same mesh size was used for both stages of the analysis with 17,226 elements as shown in Figure 5-7.

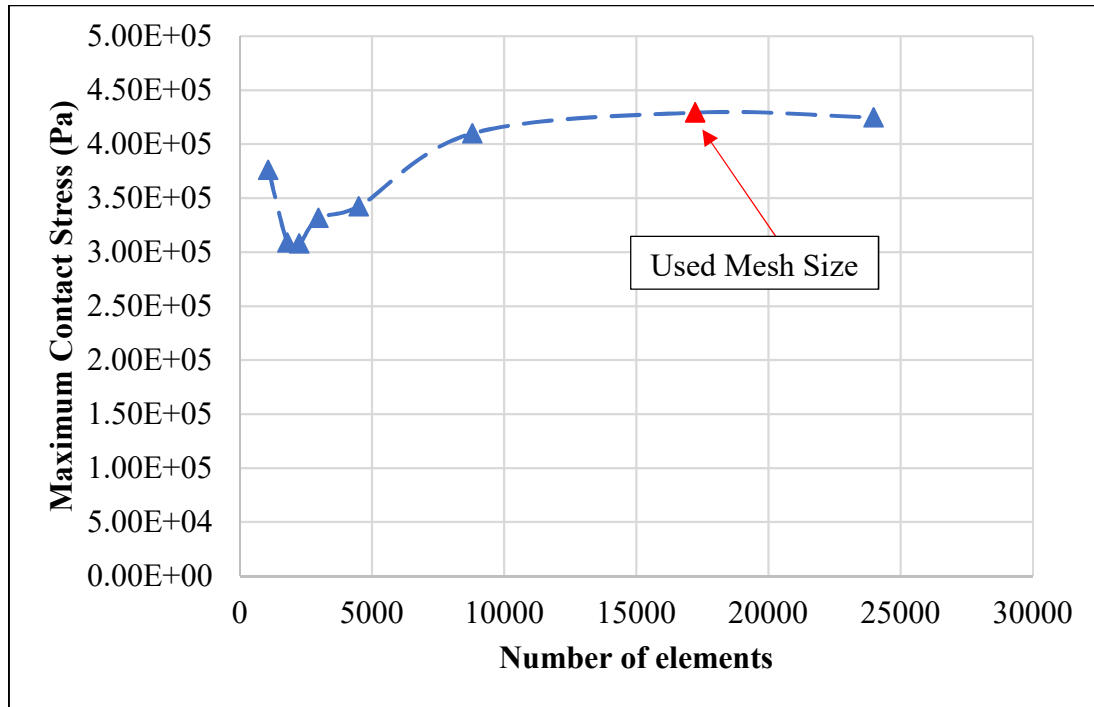


Figure 5-6. Mesh sensitivity analysis for the tire

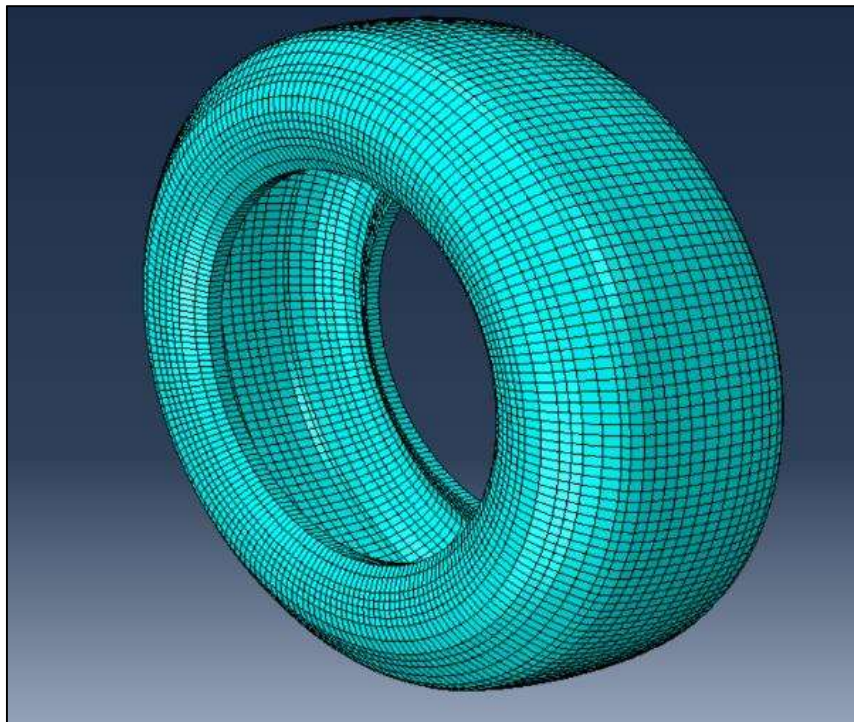


Figure 5-7. Mesh used for the 3D tire model

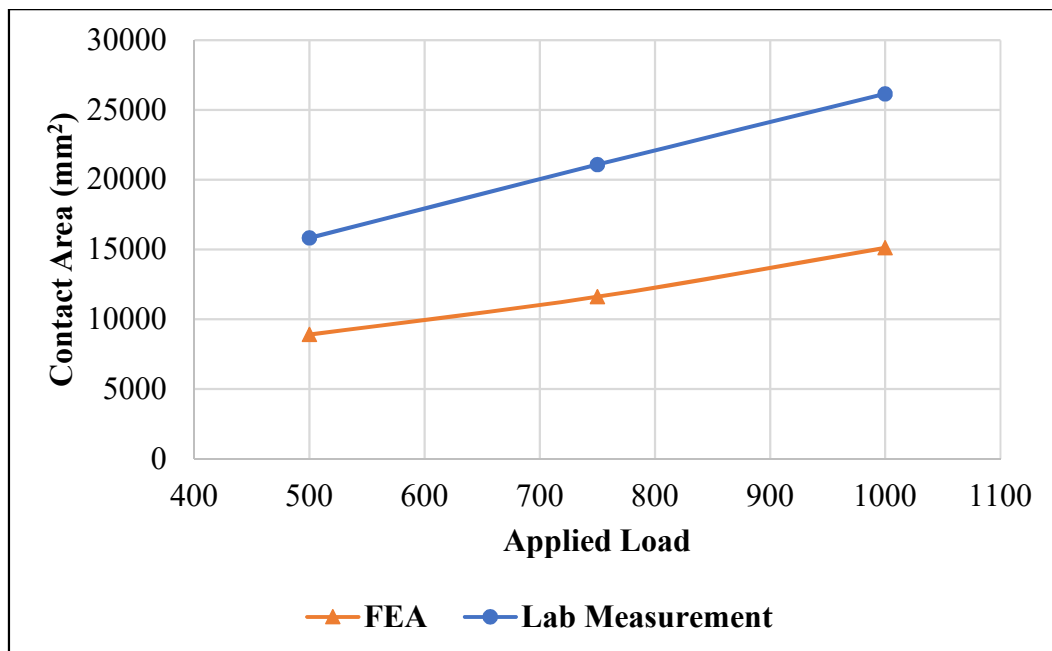
5.5.7 Model Calibration and Validation

To ensure that the results of the finite element simulation are comparable to the true behavior of the tire under different loading, the material properties of the tire reinforcement layers were adjusted to match the laboratory measurements of the contact area at different applied loads (i.e., 500, 750, and 1000 lbs.). In the laboratory, the standard smooth test tire was inflated to 24 psi according to ASTM E 524 standard, then a FujiFilm pressure-sensitive sheet was placed under the tire to measure the area of contact between the lower plate of the MTS and the tire as shown in Figure 5-8. Three levels of loading (i.e., 500, 750, and 1000 lbs.) were applied on the tire. The contact area was measured twice for each applied load and the average contact area was reported for each level of loading. The same levels of loading (i.e., 500, 750, and 1000 lbs.) were applied to the tire model in Abaqus and the contact area was measured. The material properties were adjusted for the three layers of reinforcement to match the laboratory-measured contact area at 500 lbs. and verified with the laboratory measurements at 750 and 1000 lbs. Figure 5-9 shows both the measured and calculated contact area of the tire before and after the material properties calibration.

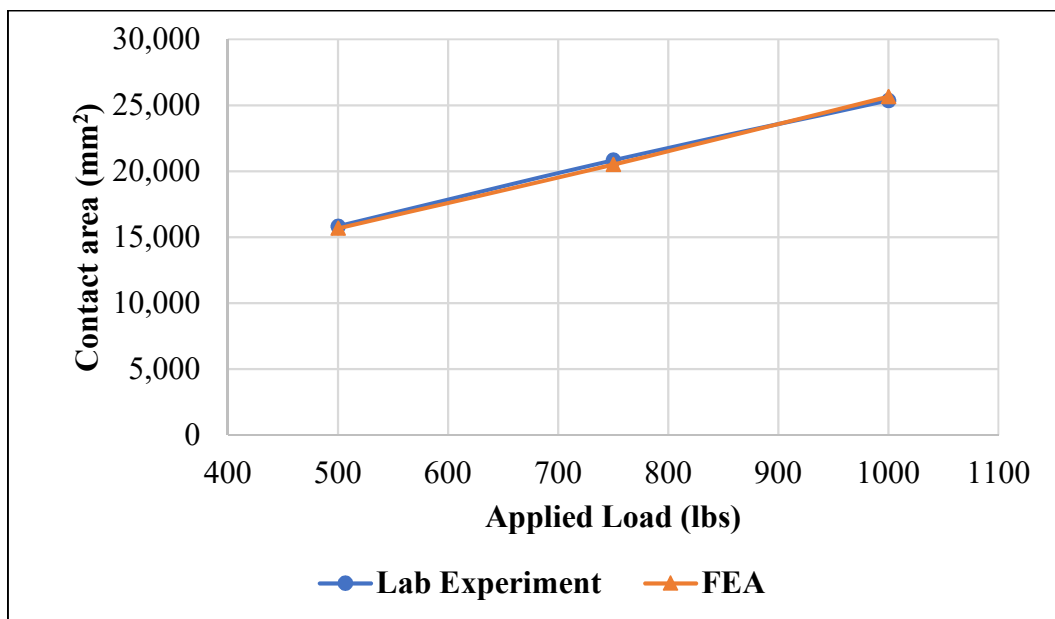
In order to validate the tire material properties after calibration, the tire was tested in the material test system (MTS). A load ranging from 100 to 1200 lbs. was applied on the tire to get the displacement in the tire at each load level. Then the full-scale 3D FE model of the ASTM E 524 tire was used to calculate the test tire displacement in Abaqus under different loads. The FE results of the tire displacement were compared to the laboratory measurements. Figure 5-10 shows the load-displacement curves obtained from both the lab measurement and the FE results. The results showed that the load-displacement curve from the experimental data matches the calculated displacement in the finite element results. These results demonstrate that the finite element model provided comparable results to the real behavior of the standard test tire and the FEM can be used to predict the behavior of the ASTM standard test tire under different loading conditions.



Figure 5-8. Measuring the contact area of the ASTM E 524 standard test tire using the MTS machine



a) Before adjusting material properties



b) After adjusting material properties

Figure 5-9. Change in contact area with applied load

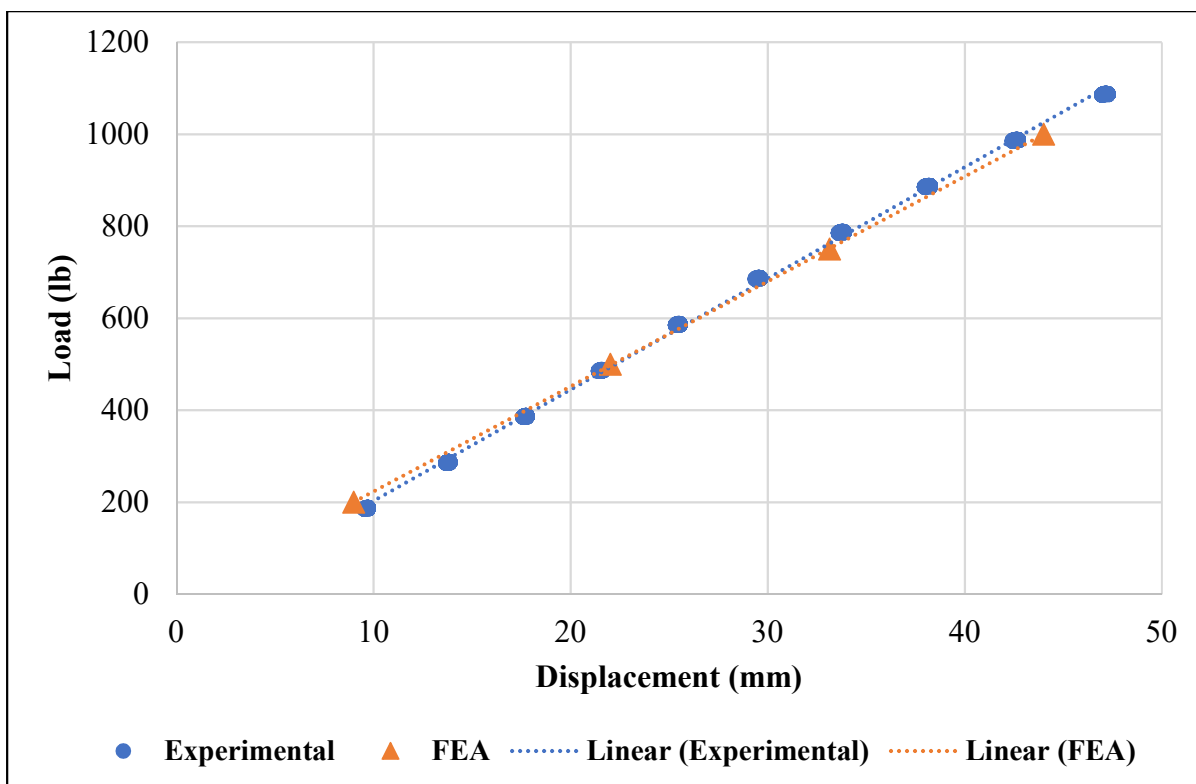


Figure 5-10. Comparing the load displacement curve between the experimental test data and the FE simulation results

5.5.8 Study Parameters

After the material properties were calibrated in the first stage of the finite element analysis, the second stage of the analysis focused on investigating the effect of several parameters on the contact stresses (i.e., vertical and shear) at the tire-pavement interface. These parameters included the coefficient of friction, texture of the pavement slab, rolling condition of the tire, and the temperature of the rubber tread of the tire. A summary of these parameters is provided in Table 5-2. The coefficient of friction was set at three different levels to cover surfaces that have low, intermediate, and high coefficients of friction. The levels of the coefficient of friction in Table 5-2 were selected based on the range of the coefficient of friction measured experimentally in the laboratory and field as discussed in Chapter 3 and Chapter 4. For the pavement texture, two types of slabs were used (a smooth slab surface, and a longitudinally-grooved slab surface with a mean profile depth [MPD] of 2.5 mm). Both the smooth and the grooved slab surfaces were assigned a value for coefficient of friction as shown in Table 5-2. The effect of changing the texture of the slab on the vertical and shear contact stresses at the

tire-pavement interface was investigated for the same coefficient of friction. The effect of the tire rolling condition was also investigated to understand the contact stress distribution at the tire-pavement interface when the tire is fully skidding and freely rolling over the pavement surface. Finally, the effect of changing the temperature of the rubber tread was investigated to understand the effect of temperature on vertical and shear contact stresses. This was achieved by changing the material properties of the rubber tread using measurements of the rubber properties in the laboratory at three different temperatures (i.e., 0, 20, and 50 °C). These temperatures represent the typical range experienced in the field.

Table 5-2. Study parameters used in the second stage of the analysis

Parameter	Description
Coefficient of friction	0.2, 0.4, 0.6
Pavement texture	Smooth slab, Grooved slab (MPD = 2.5 mm)
Rolling condition	Free rolling, Full skid
Temperature	0, 20, 50 °C

5.6 Results and Analysis

After the tire material properties were calibrated and validated, FE simulations were conducted to measure the contact shear stress and vertical stress distribution at the tire pavement interface under different conditions as described in the study parameters (Section 5.5.8). In this study, the pavement was assigned a large modulus of elasticity (i.e., $E = 20,000$ MPa) compared to the rubber material properties (Table 5-1). In addition, the deformation of the pavement slab is negligible since the tire deformation is much larger than the pavement deformation.

5.6.1 Contact Stress Distribution for a full-skidding tire

Figure 5-11 shows the stress distribution for a fully skidding tire on a grooved pavement surface. The results demonstrated that the stress distribution is non-uniform under the area of contact of the tire. There were higher stresses towards the edges of the tire and lower stresses at the middle for a transverse profile section across the center of the tire.

5-11b shows a typical contact stress distribution along a transverse cross section of the tire surface for a tire fully skidding over the pavement surface. The results of the stress distribution calculated using the finite element simulation explain the pattern of the tire wearing observed in the field for the ASTM E 524 standard test tire after several tests as shown in Figure 5-12. The tire starts to deteriorate from the edges of the tire rather than the center (Figure 5-12). This can be related to the high shear stress concentration during skidding at the edges of the tire. This confirms the non-uniformity of the stress distribution under the area of contact between the tire and pavement surface. These results were in agreement with the findings of previous studies that found a similar pattern of stress distribution for other types of test tires. In addition, these results were also confirmed by laboratory measurements of the tire contact stress under different loads when placed over a pressure sensor pad [6, 7].

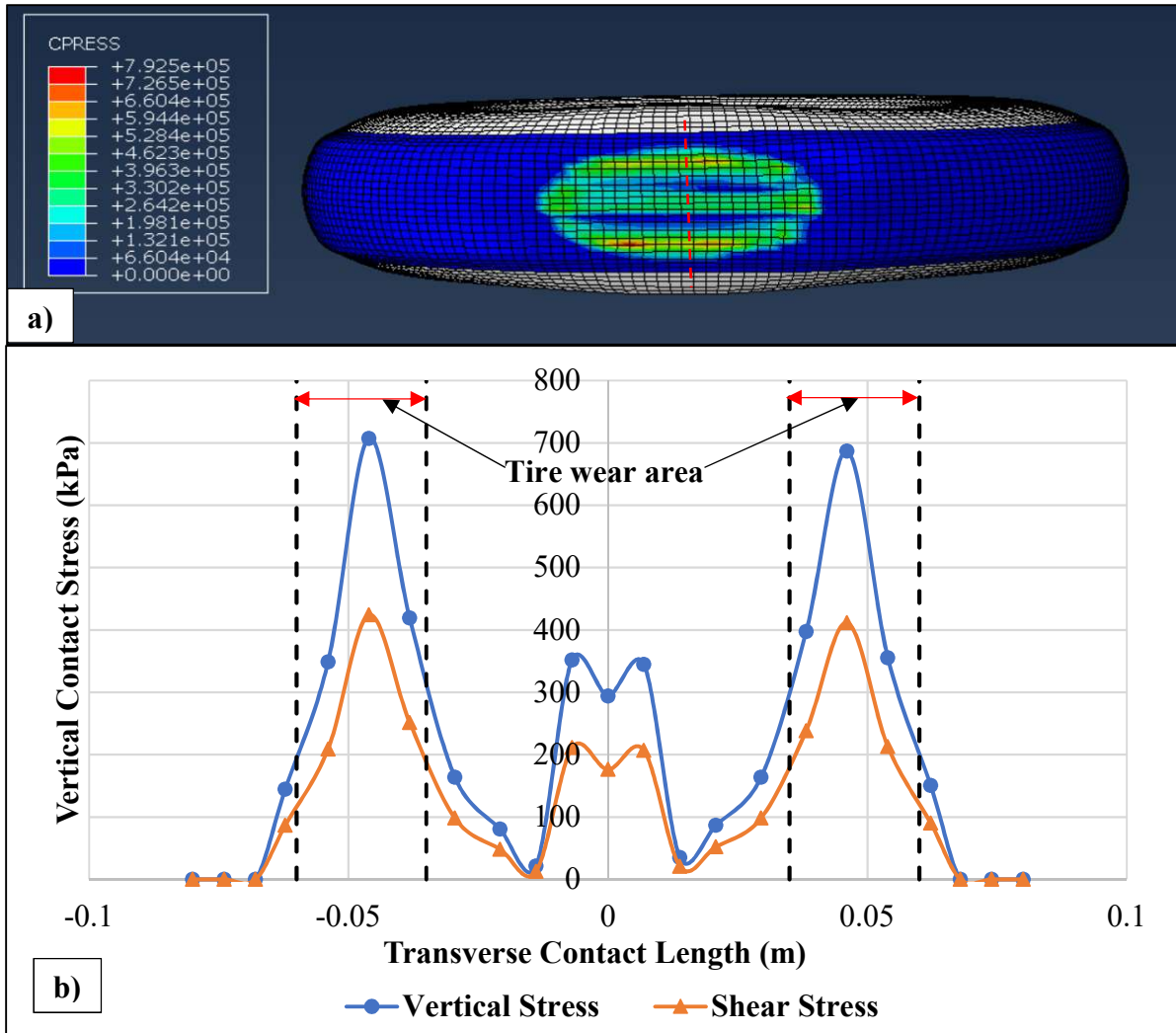


Figure 5-11. a) Nephogram of the contact stress distribution on the tire contact area, b) Contact stress distribution for a fully skidding tire on a grooved pavement surface



Figure 5-12. Wearing pattern of the ASTM E 524 standard test tire

5.6.2 Effect of the Coefficient of Friction on Contact Stress Distribution

The effect of the coefficient of friction of the pavement surface was investigated to study its effect on the vertical and shear stress distribution at the tire-pavement interface. The coefficient of friction was defined at three different levels (i.e., 0.2, 0.4, and 0.6). The selection of these values was based on the range of measured coefficients of friction in the laboratory and in the field. Pavement surfaces with a coefficient of friction around 0.2 are considered to have low frictional properties, and surfaces with a coefficient of friction of 0.6 are considered to have a relatively high frictional characteristic. Figure 5-13 and Figure 5-14 show shear stress distributions for grooved and smooth surfaces, respectively. The shear stress increases with the increase of the coefficient of friction and the maximum shear stress was located at the edges of the area of contact of the tire. Figure 5-15 and Figure 5-16 show the vertical contact stress at different levels of coefficient of friction for grooved and smooth surfaces, respectively. The results showed the coefficient of friction did not have an effect on the vertical contact stress. The results of this section were in agreement with the experimental measurements of the

skid number (SN) using the skid trailer as described in Chapter 3. Pavement surfaces with a higher coefficient of friction exhibit higher measured skid resistance. Since the applied normal force on the skid trailer wheel is constant, the shear forces are higher for pavements surfaces with higher coefficients of friction which is in agreement with the finite element results.

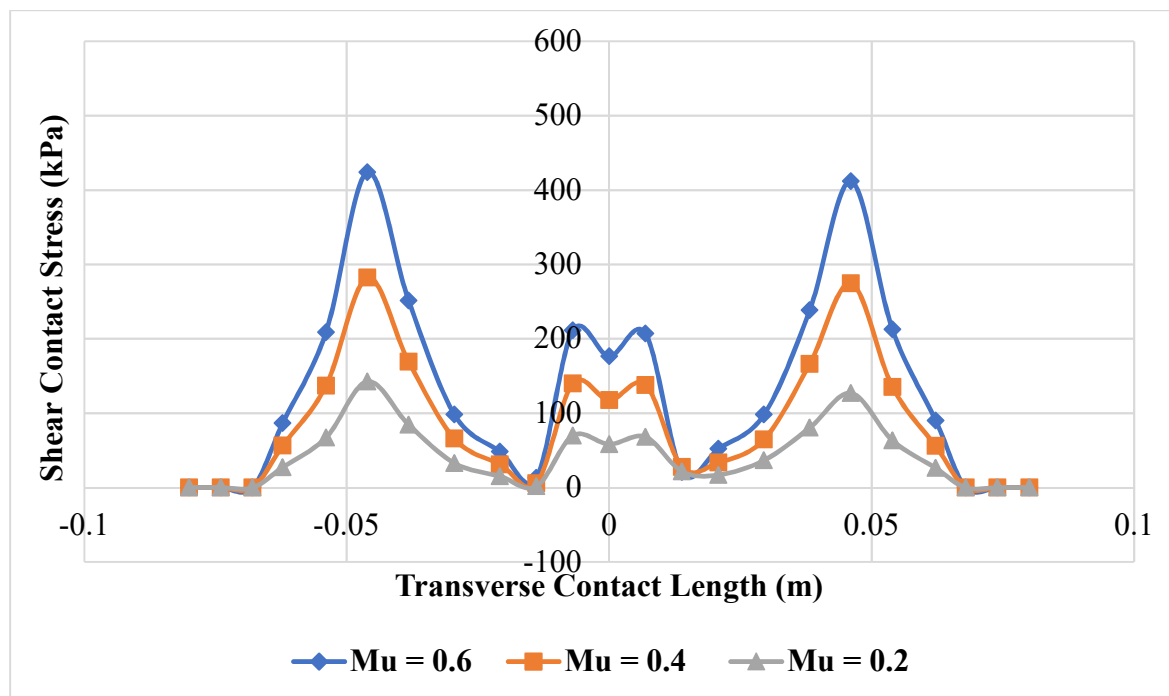


Figure 5-13. Shear contact stress for grooved pavement at different levels of μ

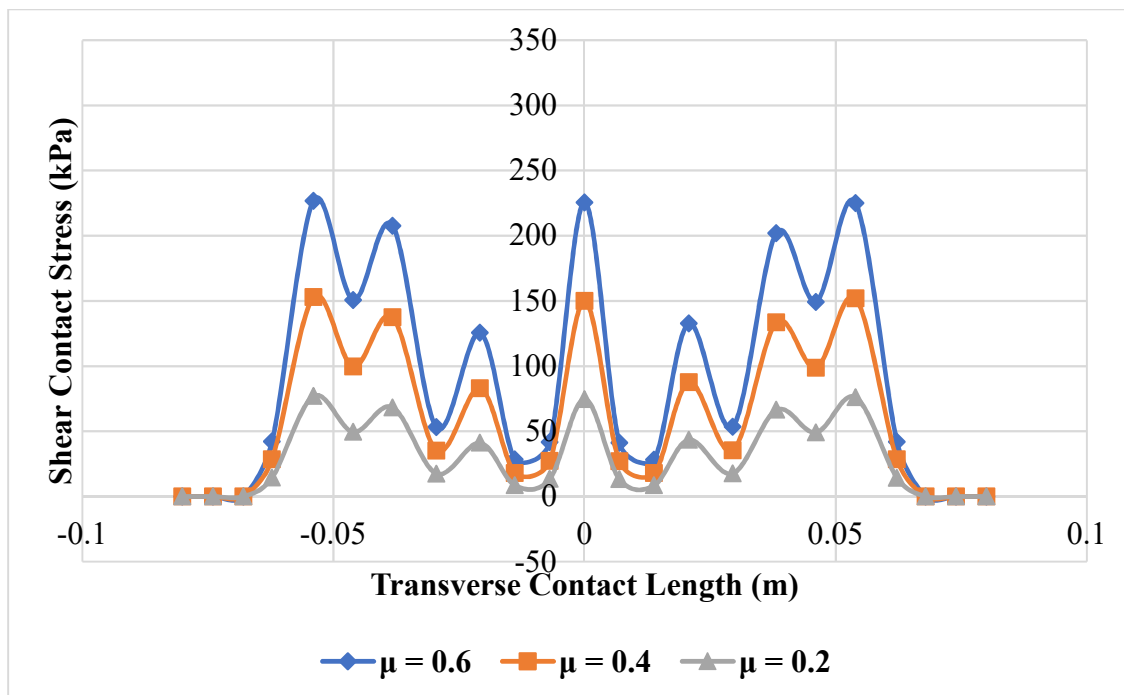


Figure 5-14. Shear contact stress for smooth pavement at different levels of μ

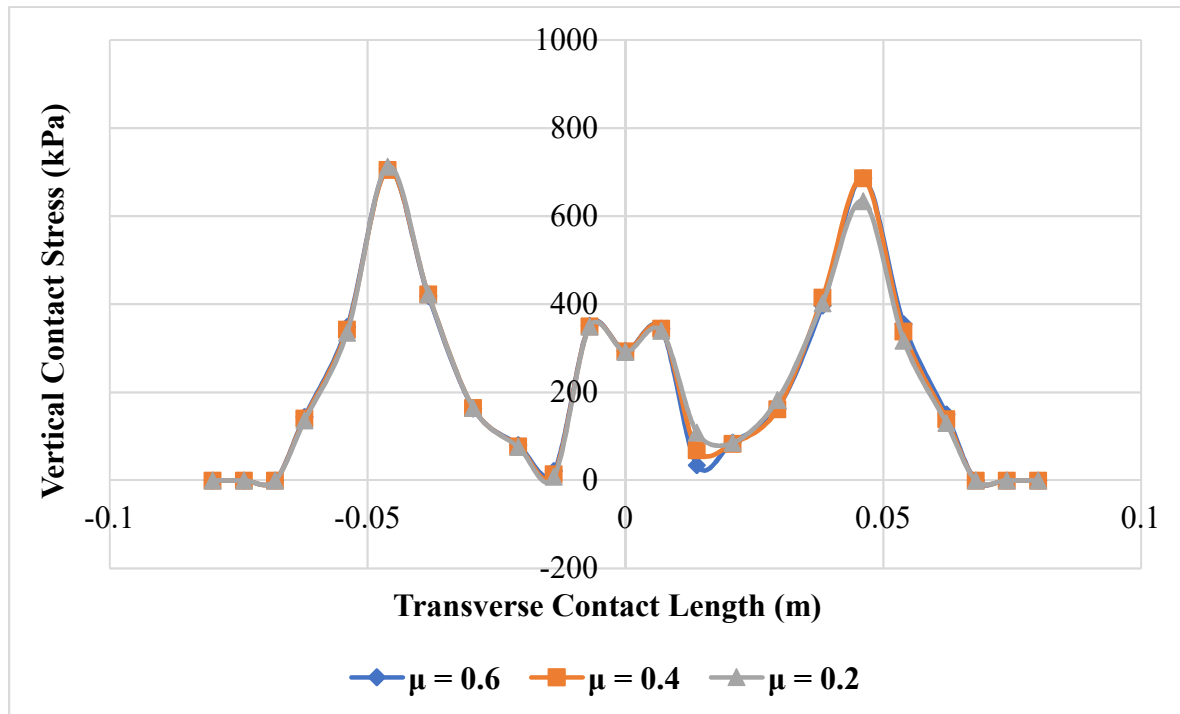


Figure 5-15. Vertical contact stress for grooved pavement at different levels of μ

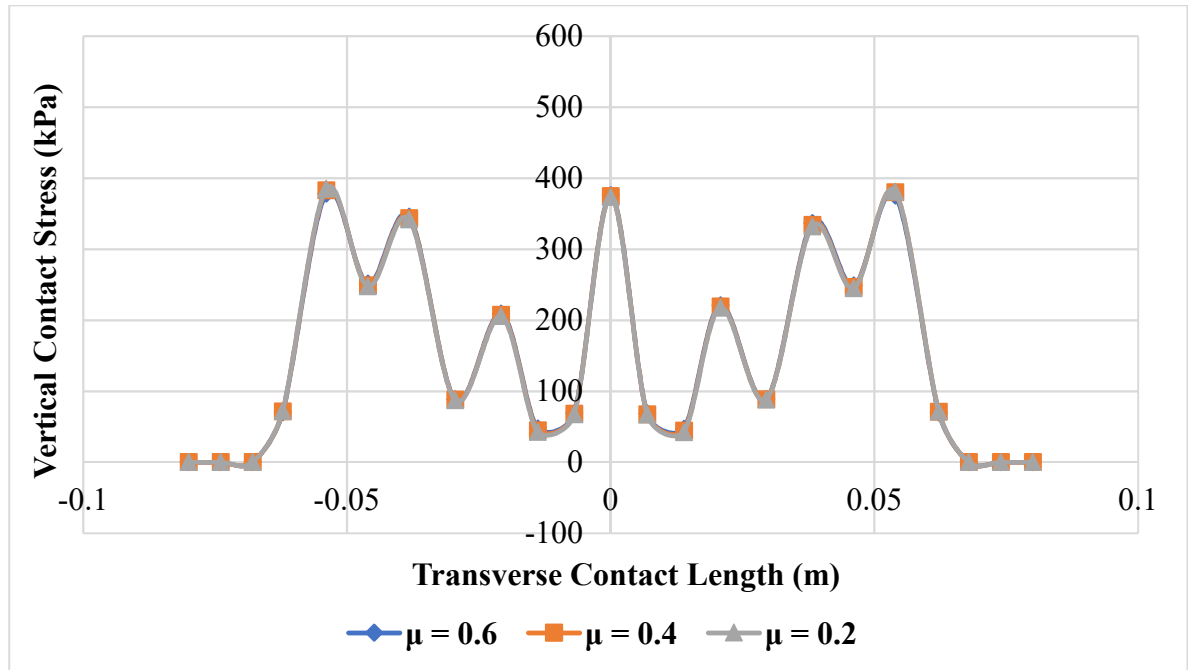


Figure 5-16. Vertical contact stress for smooth pavement at different levels of μ

5.6.3 Effect of Pavement Texture on Contact Stress Distribution

In order to investigate the effect of pavement surface texture on the contact stress distribution at the tire-pavement interface, two pavement textures were considered; smooth and grooved pavement surfaces, as shown in Figure 5-17. The grooved pavement surface has longitudinal grooves with a mean profile depth of 2.5 mm. The grooved surface is typically used in rigid pavements. These grooves are parallel to the direction of travel to reduce noise and improve the ride quality [13]. Figure 5-18 shows that the change in pavement texture affected both vertical stress and shear contact stresses, in addition to the stress distribution at the tire-pavement interface. Also, Table 5-3 summarizes the maximum contact stress at the tire-pavement interface at different coefficient of friction (i.e., 0.2, 0.4, and 0.6). The smooth pavement surface had lower vertical contact stress compared to the grooved pavement surface. The increase in the vertical contact stress for the grooved pavement surface can be attributed to the decrease in the area of contact between the pavement surface and the tire (due to the presence of peaks and valleys in pavement texture). As the vertical force applied on the tire remains constant, it is expected that the vertical contact stress increases as the area of contact decreases. Similarly, for the shear contact stresses, it was found that the grooved pavement

surface has larger contact shear stress than the smooth pavement surface. Moreover, the increase in the coefficient of friction was found to increase the contact shear stress.

The change in the coefficient of friction does not significantly affected the vertical contact stress at the tire-pavement interface for both smooth and grooved pavements (Table 5-3). Meanwhile, the slope of the line of the coefficient of friction and the maximum contact stress was noticeably higher for the grooved pavement surface compared to the smooth pavement surface as shown in Figure 5-19. These results are in agreement with the findings of Chapter 3 as both the macrotexture and microtexture affect the skid resistance and the friction force between the tire and pavement surface. This was also consistent with the findings of previous studies where it was documented that the microtexture has a significant role in determining the skid number of pavements [14-18].

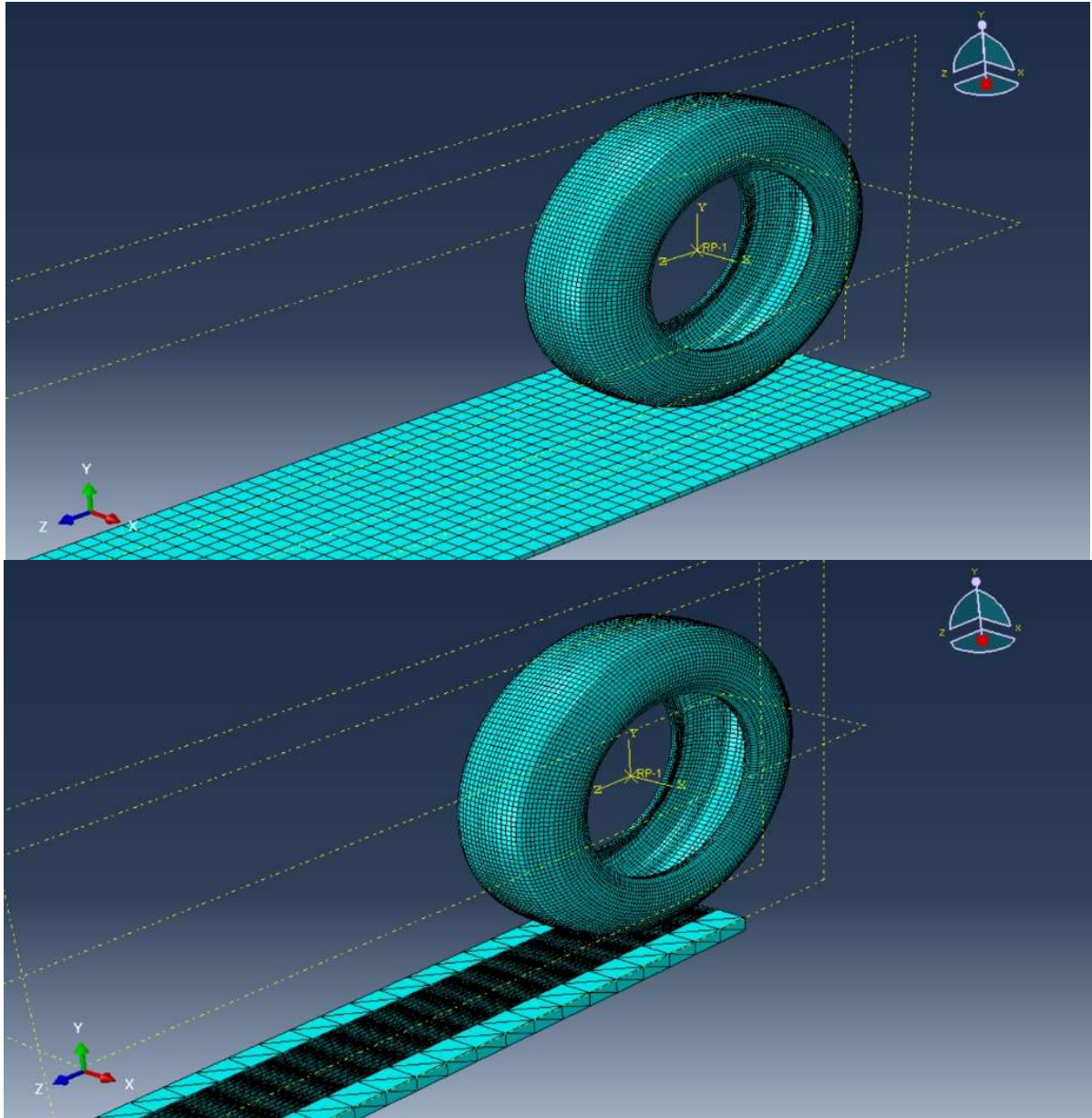


Figure 5-17. Pavement surfaces modeled in this study

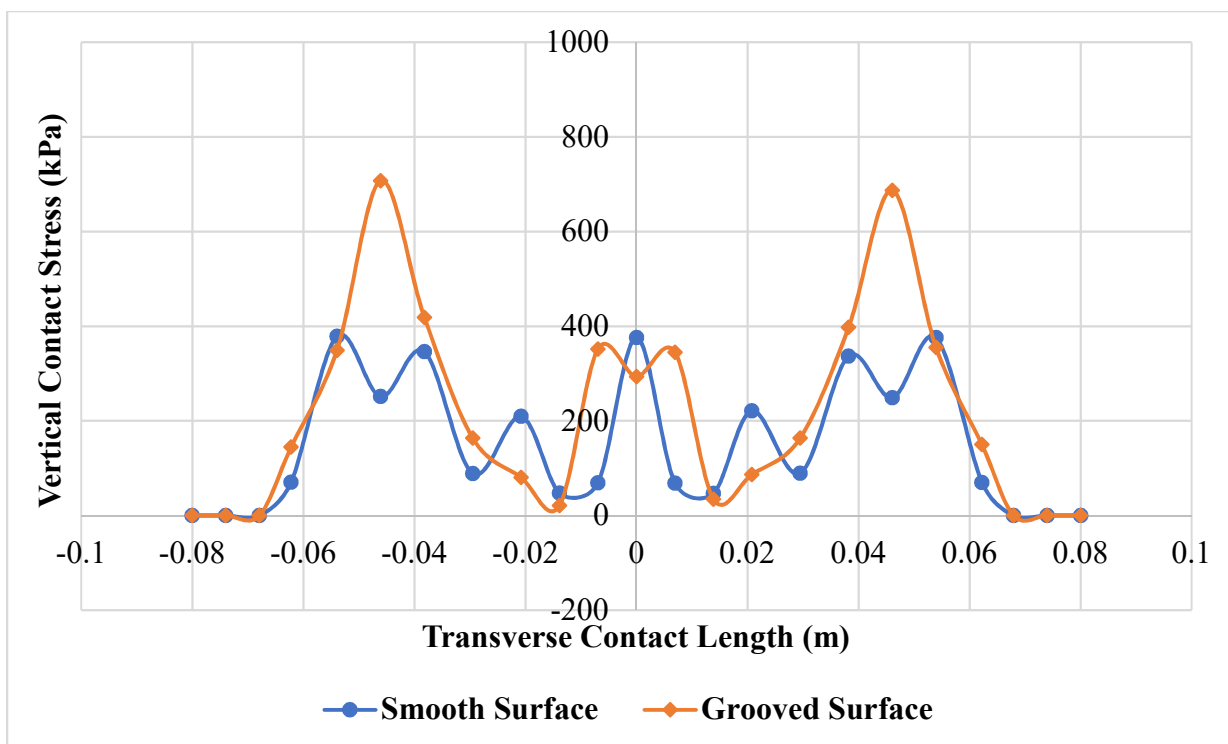


Figure 5-18. Comparing the vertical contact stress for smooth and grooved pavement slab

Table 5-3. Maximum contact stress at the tire-pavement interface

Coefficient of Friction	Smooth Surface		Grooved Surface	
	Vertical Contact Stress (kPa)	Shear Contact Stress (kPa)	Vertical Contact Stress (kPa)	Shear Contact Stress (kPa)
0.2	385.07	77.00	713.13	142.60
0.4	382.59	152.95	705.92	282.25
0.6	378.52	226.85	707.28	424.00

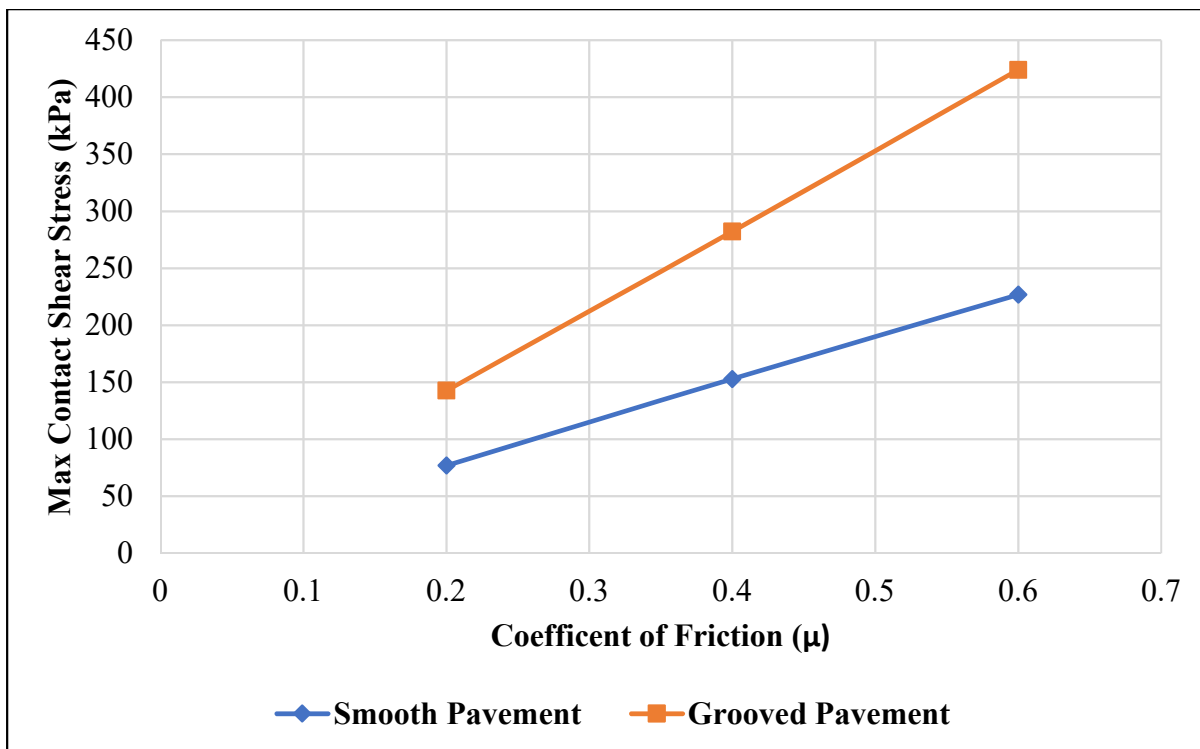


Figure 5-19. Effect of the coefficient of friction and surface texture on the maximum contact shear stress

5.6.4 Effect of Rolling Condition on Contact Stress Distribution

The researchers investigated the effect of the tire rolling condition on the contact stresses distribution at the tire-pavement interface. Two rolling conditions were investigated in this study: a freely rolling tire and a full skidding tire dragged over the pavement slab. The test tire rotates freely until it reaches the test speed and then fully locked and dragged by the skid truck for measuring the skid number. Figure 5-20 shows that the vertical contact stress distribution is similar for the two cases either free rolling or fully skidding over the pavement slab. However, along the longitudinal cross-section of the tire, the contact shear stress distribution is different for the two cases. For the freely rolling condition and at the point of impact of the tire with the direction of travel, the shear stress changed from positive (opposite to the direction of travel) to negative (along with the direction of travel) before it returned to a positive value after the setting stage and the rubber tread is released from contact with the pavement slab (Figure 5-21). Figure 5-22 shows the contact stress distribution for a fully

skidding tire along its longitudinal cross-section. The results showed that the contact shear stresses remain positive (opposite to the direction of travel) when the tire is fully skidding. These results are in good agreement with the findings of previous studies [19].

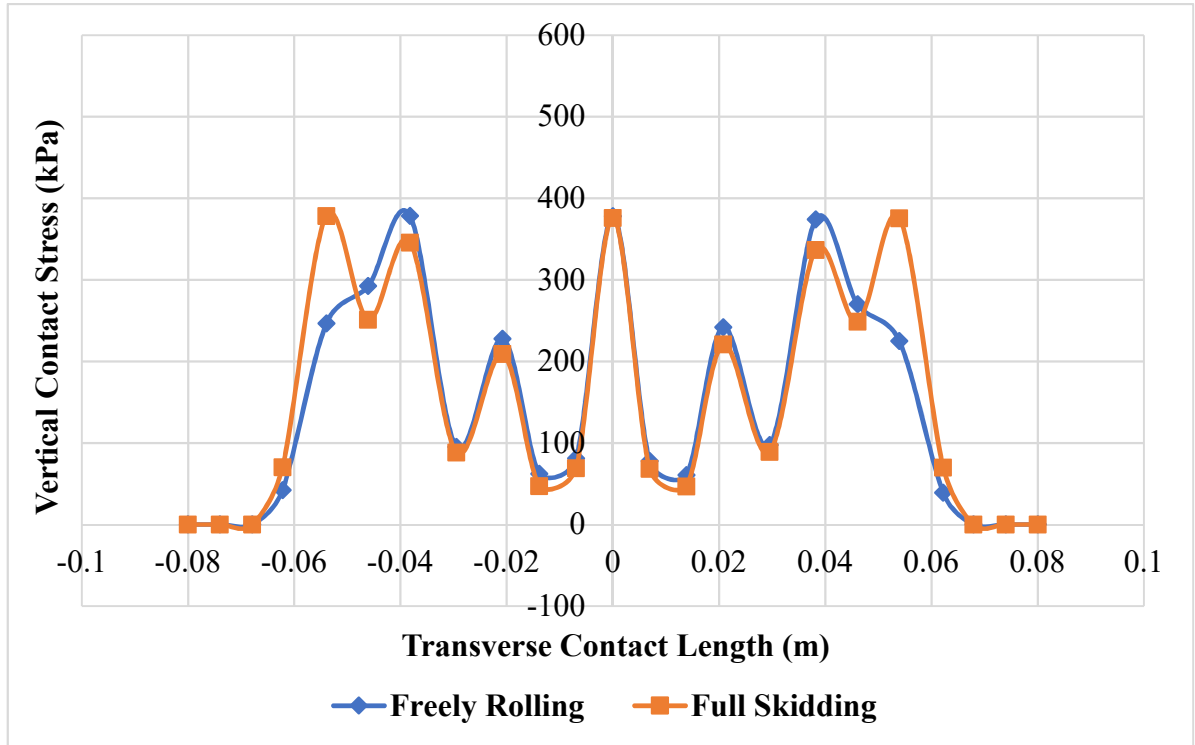


Figure 5-20. Comparing the vertical contact stress distribution for a fully skidding tire and a freely rolling tire

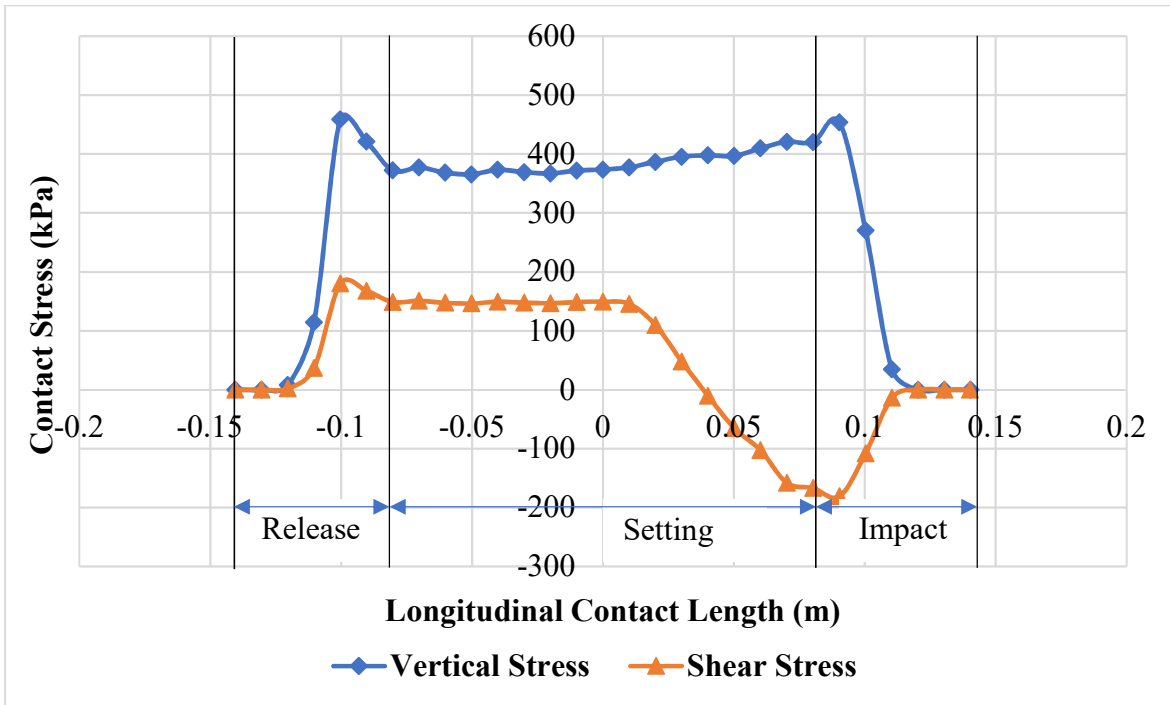


Figure 5-21. Contact stress distribution for a freely-rolling tire

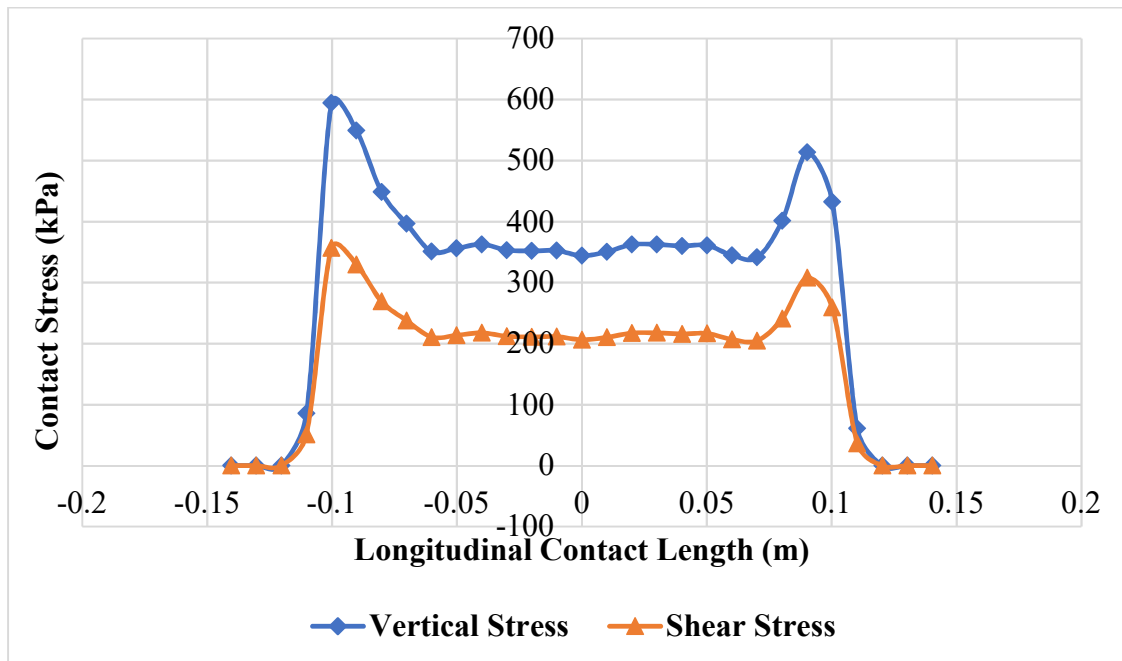


Figure 5-22. Contact stress distribution for a fully skidding tire

5.6.5 Effect of Temperature on Contact Stresses Distribution

The effect of pavement temperature on the vertical and shear contact stresses was investigated at three different temperatures (i.e., 0, 20, and 50 °C). The material properties for the rubber tread of the tire were defined based on the measured stress-strain curve for the SBR rubber using the dynamic mechanical analyzer (DMA) at each test temperature as shown in Figure 5-23. Based on DMA test results, it was found as the temperature increases, the rubber becomes softer (lower modulus) (i.e., easier to deform under applied loads) and the rubber is stiffer (higher modulus) at lower test temperatures. The FEA results in Table 5-4 demonstrate that both the vertical and shear contact stresses decreased with the increase in temperature. As the rubber temperature increases, it becomes softer and has a larger contact area as seen in the results in Figure 5-24. Thus, the vertical contact stress is reduced as the applied vertical load is constant and the contact area increases. The shear contact stress decreased with the temperature. These results are in good agreement with findings of several previous studies [22, 23]. The seasonal variation in pavement friction throughout the year is attributed to the seasonal variation in temperature [24]. Figure 5-25 shows the change in shear contact stress at different temperatures calculated from the finite element simulation had a similar pattern to the change in the skid number measurements at different times of year based on field measurements.

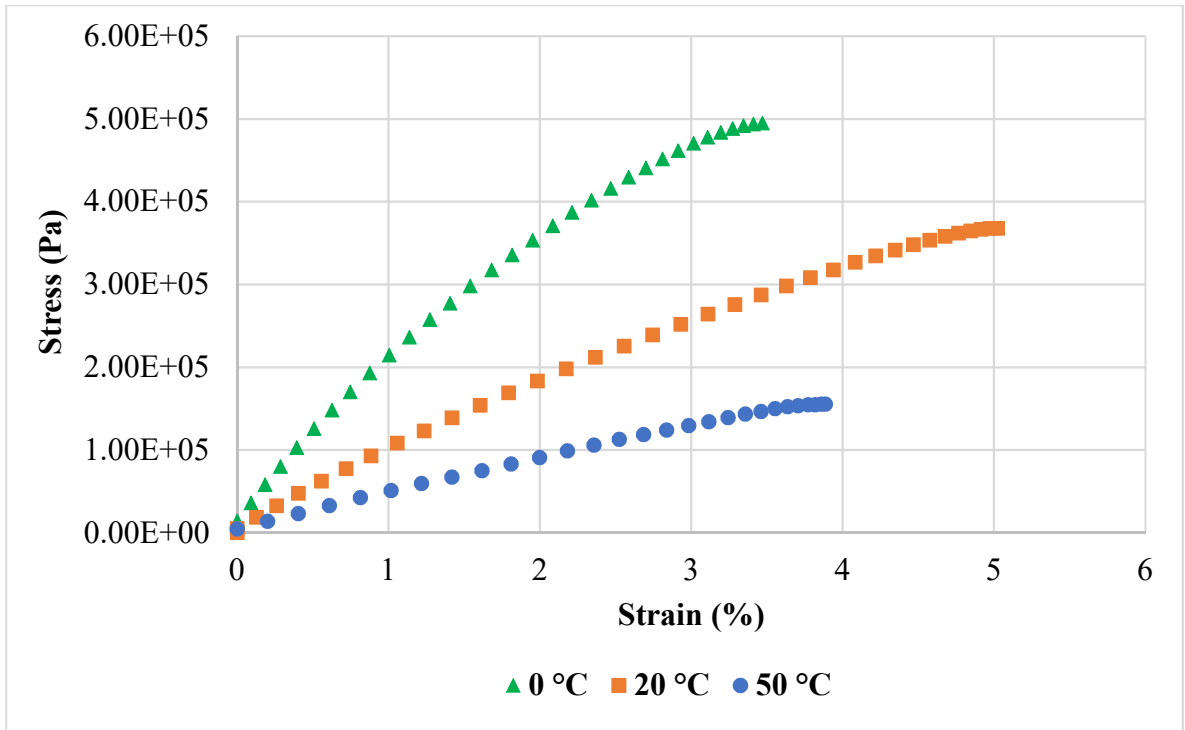


Figure 5-23. Stress strain curves for SBR rubber at different temperatures

Table 5-4. Change in the normal and shear contact stress with temperature

Temp °C	Max Normal Stress (kPa)	Max Shear Stress (kPa)
0	428.76	171.51
20	382.59	152.94
50	362.75	144.82

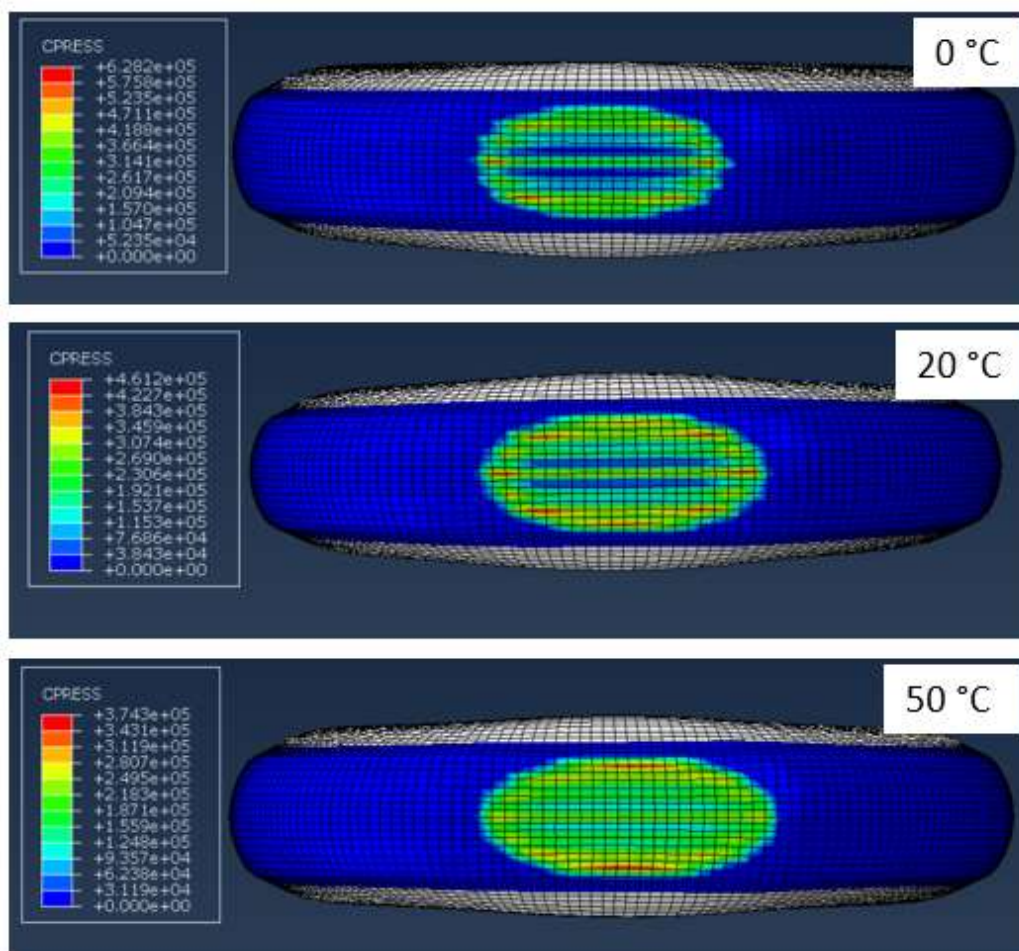


Figure 5-24. Vertical contact stress distribution at different temperatures.

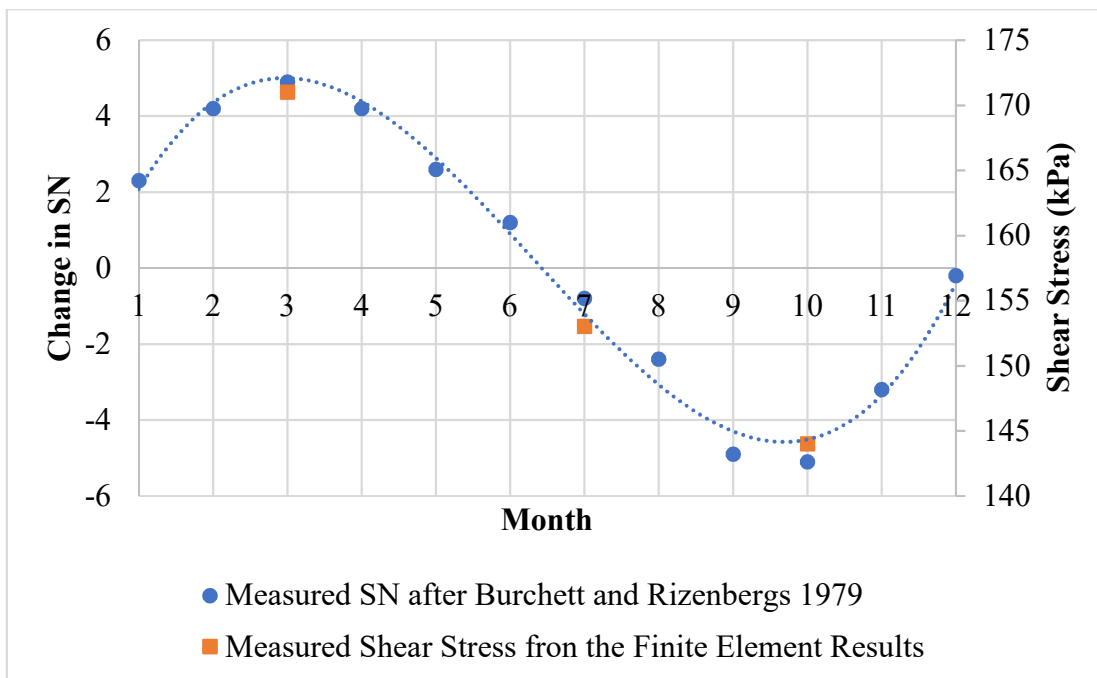


Figure 5-25. Comparison between the finite element calculated shear stress at different temperatures and SN measurements adapted from [24]

5.7 Discussion and Conclusions

In this Chapter, a finite element model of the ASTM E 524 standard test tire was created and used to investigate the effect of several parameters (i.e., coefficient of friction, surface texture, tire rolling condition, and temperature) on the contact stress distribution between the tire and pavements. The developed finite element model (FEM) for the tire-pavement interaction showed the potential to predict the tire-pavement contact stress distributions for various contact scenarios.

The stress distribution was found to be non-uniform under the tire with maximum values towards the edges of the tire. The results were consistent with the wearing pattern observed in the tire after typical skid testing. It was observed that the ASTM E 524 tire starts wearing from the outer edges where higher shear stress concentrations are present. The FEM was also able to capture the effect of changes in the surface coefficient of friction on the stress distribution under the area of contact of the tire. The shear stress increased with the increase in coefficient of friction. Higher shear stresses lead to higher skid resistance of pavements. This indicates the

importance of assigning an accurate coefficient of friction of pavements in FEM to study the contact shear stress distribution at the tire-pavement interface. Meanwhile, there was no significant effect of the coefficient of friction of vertical contact stress.

The effect of pavement texture on the contact stress was investigated in this study. Two different pavement textures (i.e., smooth and grooved) were considered. The results demonstrated that the texture affected both the vertical and shear contact stress. The grooved slab exhibited higher vertical and shear contact stress compared to the smooth slab. The grooved pavement surface has less true area of contact with the tire which leads to an increase in the normal contact stress. In addition, the grooves in the pavement slab cause the tire rubber tread to deform as it slides over the pavement leading to higher shear contact stress compared smooth pavements. The contact shear stress increased with the coefficient of friction for both the smooth and the grooved pavement slabs. However, the rate of increase in the contact shear stress was higher for the grooved pavement surface compared to the smooth surface.

The temperature of the tire was found to have a significant effect on the contact stress. As the temperature increases the rubber tread becomes softer (i.e., lower modulus). Both the vertical and shear contact stress decreases with temperature.

The FEM was able to predict the contact stress at the tire pavement interface and the FEA results were consistent and in agreement with field measurements of pavement friction and previous finite element models results. The FEM developed in this section can be used to investigate different parameters that affect the tire-pavement contact stresses and provide an in-depth understanding of the tire-pavement interaction for the standard ASTM E 524 test tire. It should be noted that there are no previous FE simulations conducted on the ASTM E 524 standard tire that investigated the contact stresses at the tire-pavement interface.

5.8 References

- [1] Wang, H. and Al-Qadi, I.L., 2009. Combined effect of moving wheel loading and three-dimensional contact stresses on perpetual pavement responses. *Transportation research record*, 2095(1), pp.53-61.
- [2] Wang, H., Al-Qadi, I.L. and Stanciulescu, I., 2010. Effect of friction on rolling tire-pavement interaction (No. NEXTRANS Project No. 049IY02). NEXTRANS Center (US).
- [3] Wang, H., 2011. Analysis of tire-pavement interaction and pavement responses using a decoupled modeling approach (Doctoral dissertation, University of Illinois at Urbana-Champaign).
- [4] Wong, J.Y., 2008. *Theory of ground vehicles*. John Wiley & Sons.
- [5] Pacejka, H., 2005. *Tire and vehicle dynamics*. Elsevier.
- [6] Tielking, J.T. and Roberts, F.L., 1987. Tire contact pressure and its effect on pavement strain. *Journal of Transportation Engineering*, 113(1), pp.56-71.
- [7] Zhang, X., 2001. Nonlinear finite element modeling and incremental analysis of a composite truck tire structure (Doctoral dissertation, Concordia University).
- [8] Long, F.M., 2001. Permanent deformation of asphalt concrete pavements: A nonlinear viscoelastic approach to mix analyses and design.
- [9] Kim, K., Ju, J., Kim, D.M. and Rhie, S., 2011, January. Finite Element Analysis of Tire and Pavement Interaction. In *ASME 2011 International Design Engineering Technical Conferences and Computers and Information in Engineering Conference* (pp. 813-820). American Society of Mechanical Engineers.
- [10] Srirangam, S.K., Anupam, K., Scarpas, A. and Kösters, A., 2013. Influence of temperature on tire-pavement friction-1: laboratory tests and finite element modeling (No. 13-4260).
- [11] Wang, H., Al-Qadi, I.L. and Stanciulescu, I., 2013. Effect of surface friction on tire-pavement contact stresses during vehicle maneuvering. *Journal of Engineering Mechanics*, 140(4), p.04014001.
- [12] ASTM E524-08(2015), *Standard Specification for Standard Smooth Tire for Pavement Skid-Resistance Tests*, ASTM International, West Conshohocken, PA
- [13] Skarabis, J. and Stöckert, U., 2015. Noise emission of concrete pavement surfaces produced by diamond grinding. *Journal of Traffic and Transportation Engineering (English Edition)*, 2(2), pp.81-92.

- [14] Henry, J.J., 2000. Evaluation of pavement friction characteristics (Vol. 291). Transportation Research Board.
- [15] Hall, J.W., Smith, K.L., Titus-Glover, L., Wambold, J.C., Yager, T.J. and Rado, Z., 2009. Guide for pavement friction. Final Report for NCHRP Project, 1, p.43.
- [16] Fülöp, I.A., Bogardi, I., Gulyas, A. and Csicsely-Tarpay, M., 2000. Use of friction and texture in pavement performance modeling. *Journal of Transportation Engineering*, 126(3), pp.243-248.
- [17] Al-Assi, M., Kassem, E., Nielsen, R., Poorbaugh, J., Mahmoud, E. (2019). Pavement Skid Number Prediction Using Surface Texture Characteristics. Manuscript Submitted for Publication.
- [18] Wu, Z., King, B., Abadie, C. and Zhang, Z., 2012. Development of design procedure to predict asphalt pavement skid resistance. *Transportation Research Record*, 2306(1), pp.161-170.
- [19] Liu, F., Sutcliffe, M.P.F. and Graham, W.R., 2010. Prediction of tread block forces for a free-rolling tyre in contact with a smooth road. *Wear*, 269(9-10), pp.672-683.
- [20] Emery, J.J. and Eng, P., 1986. Evaluation and mitigation of asphalt pavement top-down cracking. *Scientist*, p.2.
- [21] Khanal, K., Neopane, H.P., Rai, S., Thapa, M., Bhatt, S. and Shrestha, R., 2016. A methodology for designing Francis runner blade to find minimum sediment erosion using CFD. *Renewable energy*, 87, pp.307-316.
- [22] Baran, E., 2011, May. Temperature influence on skid resistance measurement. In *International Surface Friction Conference*, 3rd, 2011.
- [23] Oh, S.M., Ragland, D.R. and Chan, C.Y., 2010. Evaluation of Traffic and Environment Effects on Skid Resistance and Safety Performance of Rubberized Open-grade Asphalt Concrete (No. UCB-ITS-PRR-2010-14).
- [24] Burchett, J. L., Rizenbergs, R.L., 1979. Seasonal Variation in the Skid Resistance of Pavements in Kentucky

Chapter 6. Conclusions and Recommendations

6.1 Summary

Several transportation agencies periodically measure the skid resistance of pavements to ensure adequate surface friction. Providing an appropriate level of traction between rubber tires and pavements is essential for safe driving. The skid resistance of pavements is influenced by surface texture characteristics and rubber tire properties. The main goal of this study is to advance the current state of knowledge of the tire-pavement interaction mechanisms and modeling. This goal was achieved through 1) investigating the adhesion and hysteresis friction and the role of surface characteristics and rubber properties, 2) developing models to predict skid friction at various speeds using fundamental properties that describe the behavior of rubber and texture parameters extracted from close-range photogrammetry analysis of pavement surface, and 3) developing a finite element model of the skid trailer test tire to study the influence of surface texture characteristics and rubber properties on the tire-pavement stresses at typical operation conditions.

This first part of this study experimentally investigated the two main friction mechanisms (i.e., adhesion, and hysteresis) that contribute to tire-pavement friction. No previous experimental studies were conducted to explain the adhesion friction using the surface energy components of rubber and aggregates. The results demonstrated that there is a fair correlation between the adhesive bond energy and the measured coefficient of friction. Pavement surfaces with higher adhesion with rubber exhibited higher friction at low speed. The findings provide experimental verification of the relationship between adhesion and pavement surface friction. In addition, the results demonstrated a strong correlation between rubber-pavement friction and rubber properties. Softer rubber had higher friction with pavement compared with hard (higher modulus) rubber.

The second part of this study conducted comprehensive field tests to measure the pavement macrotexture, microtexture and skid number (SN) with the objective of developing a prediction model for skid resistance. The current standard model (ASTM E 274) can be used to predict skid number at a speed of 50 mph based on macrotexture and microtexture of pavement surface; however, no models are available to predict pavement skid number at different speeds based on solely the macrotexture and microtexture measurements of the

pavement surface. This study proposed a model that can be used to predict skid number at any speed between 20 mph and 60 mph as a function of macrotexture and microtexture. The model was found to provide a good correlation with skid number measurements in the field at different speeds. This model offers an alternative method that can be used to predict skid number at a given location when the skid trailer is not available.

The third part of this study investigated the use of close-range photography (CRP) method to accurately measure pavement macrotexture and microtexture. In addition, the developed texture parameters based on the CRP analysis were used along with the rheological properties of rubber in the Persson friction model to predict pavement friction at various operating conditions. The predicted friction values were found to have good correlation with the measurements collected in the field and laboratory. The CRP was found to offer a simple and accurate, yet inexpensive alternative to the current methods used to measure surface macrotexture and microtexture. This study greatly simplified the use of the Persson friction model for predicting skid number with good accuracy. In addition, the results of this research showed that there is room to enhance the CRP method of obtaining higher resolution details of the pavement surface efficiently and in a timely manner.

The last part of this study developed a 3D finite element model for a full-scale smooth test tire to investigate the effect of different parameters on the contact stresses at the tire-pavement interface. First, the tire geometry, cross section and material properties of various layers that form the test tire were defined, then the proposed model was validated with laboratory measurements that included the application of various loads and recording the resulting deformation. After validating the 3D model of the test tire, the model was used to examine the effect of surface characteristics and temperature on the tire-pavement contact stress. The finite element model was able to predict the effect of several parameters of the tire-pavement contact stresses including coefficient of friction, surface texture, tire rolling condition, and temperature. The normal and shear stress distributions were found to be non-uniform under the tire with maximum values towards the edges of the tire. The shear stress increased with the increase of the coefficient of friction of the pavement surface. In addition, higher macrotexture provided higher shear stress compared to pavement with low macrotexture. The contact stress was also found to be greatly affected by the temperature of the test tire. This model can be

utilized to run simulations that can assist pavement materials engineers to decide the best practices to improve the pavement friction as well as tire manufacturers to study different rubber compounds to provide better traction with the road.

6.2 Findings

The main findings of various components of this research are summarized in this section

6.2.1 Adhesion and Hysteresis Friction

- The adhesive bond energy was found to have a fair correlation ($R^2 = 0.51$) with friction between rubber and pavement surfaces. As the adhesive bond energy between rubber and pavement increases, the coefficient of friction increases.
- There is a strong correlation ($R^2 = 0.91$) between rubber-pavement friction and rubber elastic modulus. It was found that rubber materials with lower elastic modulus provide higher friction compared to rubber materials with higher elastic modulus.

6.2.2 Skid Number Prediction Models

- The macrotexture and microtexture of pavement surfaces can be used to predict the skid number (SN). Pavement SN changes with macrotexture, microtexture, and speed.
- The macrotexture of a pavement surface affects the rate of change in SN with speed, while the microtexture dictates the magnitude of the SN of pavements. Pavement surfaces with higher microtexture exhibit higher SN compared to pavements with lower microtexture.
- There is a strong linear correlation ($R^2 = 0.99$) between the mean profile depth (MPD) measured using a laser profiler, and the mean texture depth (MTD) measured using the volumetric sand patch test method.
- Both DFT_{20} and MTD measurements were found to be statistically significant ($p < 0.05$) in predicting the SN of pavement surfaces with 95% confidence interval. The DFT_{20} and the MTD can be modified during the design stage via using aggregate type and gradation to ensure adequate skid resistance at various operation speeds.

6.2.3 Close-Range Photogrammetry and Persson Model

- The CRP method can provide accurate and relatively inexpensive measurements of the pavement surface texture with high accuracy. The CRP measurements of the pavement

macrotexture and microtexture were comparable to the volumetric sand patch test and the DFT, respectively.

- The results showed good correlation ($R^2 = 0.85$) between the measured MTD and the CRP measurements of the macrotexture. Similarly, a good correlation ($R^2 = 0.91$) was found between the DFT₂₀ measurements and the CRP measured microtexture values.
- The CRP measurements of the pavement texture can be used to develop a 3D surface texture model that can be utilized along with the rubber material properties using Persson's friction model to accurately predict rubber-pavement friction. Good correlation was found between measured and predicted friction values in the field ($R^2 = 0.97$) and in the laboratory ($R^2 = 0.90$). The CRP method is a non-contact method that can be applied to provide accurate friction estimation of pavement surfaces without the need for complex and expensive tools.

6.2.4 Finite Element Simulation of Tire-Pavement Interaction

- The contact stress at the tire-pavement interface was found to be non-uniform. The center of the contact area was found to have lower contact stresses (vertical and shear) compared to the outer edges of the contact area.
- The coefficient of friction affected the contact shear stress for a tire skidding on the pavement surface as expected. However, the vertical contact stress was found to be independent of the coefficient of friction.
- Smooth pavements result in lower vertical and shear contact stresses compared to grooved surfaces.
- The contact shear stress was found to act opposite to the direction of motion along the contact profile while the tire is fully skidding. When the tire is free to roll over pavement surface, the contact shear stress changes in magnitude and direction along the contact profile as the tire impacts, sets on the pavement, and released contact between the tire and pavement surface.
- The temperature of the tire rubber material had a significant effect on the contact area and contact stresses at the tire-pavement interface. Rubber materials are softer (lower modulus) at higher temperatures. As the temperature increases, the contact area also increases. Both vertical and shear contact stresses decrease with temperature

- Finite element simulations provide us with in-depth knowledge of the factors that affect tire-pavement friction and help to optimize both pavement and tire design to enhance safety.

6.3 Recommendations for Future Research

Based on the findings of this study, the following recommendations are made for future research.

- The authors recommend testing additional rubber materials and aggregate combinations and validate the correlation between the adhesive bond energy and friction.
- Various models were developed to predict skid number as a function of macrotexture, microtexture, and speed. These models were developed based on field measurements collected using smooth tires. It is recommended to expand this work to include ribbed tires.
- It is recommended to use higher resolution cameras when using the CRP method to measure the surface microtexture and macrotexture.
- The authors recommend further research to evaluate the light conditions (e.g., sunny, partially cloudy, cloudy, and artificial light) and surface conditions (e.g., wet and dry) on the results of CRP measurements.
- The authors recommend validating the CRP prediction results for different pavement surfaces and develop a robust system that can complement the current practice for measuring skid resistance of pavements. Such system should be able to develop 3D models of the pavement surface texture from a number of digital images and utilize the 3D surface model to predict the skid number using a non-contact method that is relatively inexpensive and affordable.
- A mobile application can be developed to measure the microtexture and macrotexture and predict skid number using the CRP technique.
- Future work of finite element simulation of tire-pavement interaction can be expanded to include more realistic representation of pavement surface.

- It is recommended to utilize the finite element model in future studies to investigate various parameters that can be modified in the mix design stage (e.g., aggregate gradation and type) to provide higher friction and improve safety.

Appendix A - Improving Pavement Friction Through Aggregate Blending

“Al Assi, M., E. Kassem, R. B. Kogbara, and E. A. Masad. "Improving pavement friction through aggregate blending." In *Advances in Materials and Pavement Prediction: Papers from the International Conference on Advances in Materials and Pavement Performance Prediction (AM3P 2018)*, April 16-18, 2018, Doha, Qatar, vol. 100, no. 6.1, p. 277. CRC Press, 2018.”

A.1 Abstract

Maintaining an adequate level of skid resistance on highways is essential for the safety of motorists. Among other factors, the skid resistance of asphalt pavements depends on aggregate shape characteristics and its resistance to abrasion and polishing. This study investigated the effect of aggregate blending on improving the frictional characteristics of asphalt pavements. Test slabs prepared using different blends of limestone and gabbro were subjected to accelerated polishing. Gabbro is known to have better resistance to abrasion and polishing compared to limestone. A dynamic friction tester was used to measure the coefficient of friction at different polishing cycles; in addition, the macrotexture was measured using a sand patch test. The results showed that blending gabbro with limestone would improve the frictional characteristics of asphalt mixtures compared to the control mix prepared with only limestone. Based on the findings of this study, a blend of 50% gabbro and 50% limestone would provide comparable skid resistance and cut down the amount of gabbro imported for road construction leading to cost savings and maximizing the use of natural resources in Qatar. Meanwhile, the researchers recommend constructing trial test sites and monitoring their frictional characteristics alongside evaluating the mechanical properties of the proposed blend to ensure durability.

A.2 Introduction

Pavement friction or skid resistance of pavements is essential for safety of motorists on highways. Maintaining a satisfactory level of friction is one of the main factors that contributes

to reducing the number of crashes in wet conditions [1]. Adequate friction force between the tires and pavement surface prevents the vehicle from skidding while maneuvering and it provides stability to the vehicle while accelerating and decelerating. When the brakes are applied, the friction force between the tire and pavement surface causes the moving vehicle to stop safely without skidding or slipping over the pavement surface [2]. Pavement friction is often expressed in terms of the coefficient of friction, which is the ratio between the tangential friction force between the tire tread and pavement surface and the normal load on the tire [3]. There are several factors that contribute to pavement friction (e.g., aggregate mineralogy, aggregate size and gradation, pavement temperature, presence of lubricant on the surface, etc.) [4, 5]. Skid resistance is a function of both pavement macrotexture and microtexture, while the change of skid resistance with time is mainly related to the aggregate characteristics and its resistance to abrasion and polishing [6]. The pavement macrotexture is related to aggregate gradation and angularity, while pavement microtexture is a function of aggregate surface roughness its ability to resist polishing and abrasion [6].

Limestone aggregate is available in abundance in the State of Qatar; however, the state imports gabbro for road construction. Limestone is a sedimentary rock while gabbro is an igneous rock. Gabbro has better resistance to abrasion and polishing compared to the local limestone [7]. The objective of this study is to evaluate different blends of gabbro and limestone aggregates to optimize the asphalt mixture design with adequate skid resistance using more local materials. The use of more local materials will decrease the cost of pavement construction and maximize the benefits of the natural resources in Qatar.

A.3 Methodology

The researchers prepared 20-inch squared hot mix asphalt (HMA) slabs in the laboratory. The HMA slabs were prepared using limestone, gabbro, and different combinations of both limestone and gabbro. In addition, the asphalt binder (Pen 60/70), often used in asphalt pavements in Qatar, was used in preparing the HMA slabs. The slabs were compacted using a vibratory plate compactor and steel mold. Five different blends of gabbro and limestone aggregates were evaluated; 100% gabbro; 70% gabbro and 30% limestone; 50% gabbro and

50% limestone; 30% gabbro and 70% limestone; and 100% limestone. All the HMA slabs were prepared using the same aggregate gradation presented in Table A-1. The HMA slabs were mixed and compacted at 143 °C and 135 °C, respectively.

Table A-1. Aggregate gradation used to prepare the HMA slabs.

Sieve Size	% Passing (cumulative)	% Retained
1.5"	100	0
1"	98.6	1.4
3/4"	88.2	10.4
1/2"	76.9	11.3
3/8"	68.9	8.0
No. 4	47.1	21.8
No. 8	26.5	20.6
No. 16	15.8	10.7
No. 30	10.5	5.3
No. 50	7.9	2.6
No. 100	6.1	1.8
No. 200	4.2	1.9
Pan	0.00	4.2

The test slabs were polished using a three-wheel polisher at different polishing intervals (i.e., 0, 5000, 30000, 50000, and 100000 cycles) (Figure A-1). The three-wheel polisher has three pneumatic rubber tires that rotate on the slab with a load applied on the top to simulate the polishing due to traffic in the field. The polishing of the HMA slabs was conducted with the presence of water to wash away any loose material from the surface during the polishing process. The coefficient of friction for the HMA slabs was then measured using a dynamic friction tester (DFT) after each interval of polishing set (Figure A-2).



Figure A-1. Polishing HMA slabs using the three-wheel polisher

The DFT consists of three rubber sliders attached to a rotating disk at the bottom of the DFT device. The DFT disk is brought up to the desired rotational velocity and then is lowered on the slab surface to achieve full contact. The coefficient of friction is then continuously recorded, as the velocity of the disk decreases due to losses of the kinetic energy caused by the friction between the rubber sliders and the HMA slab surface. The DFT test for the HMA slabs was performed according to the ASTM E 1911 [8].

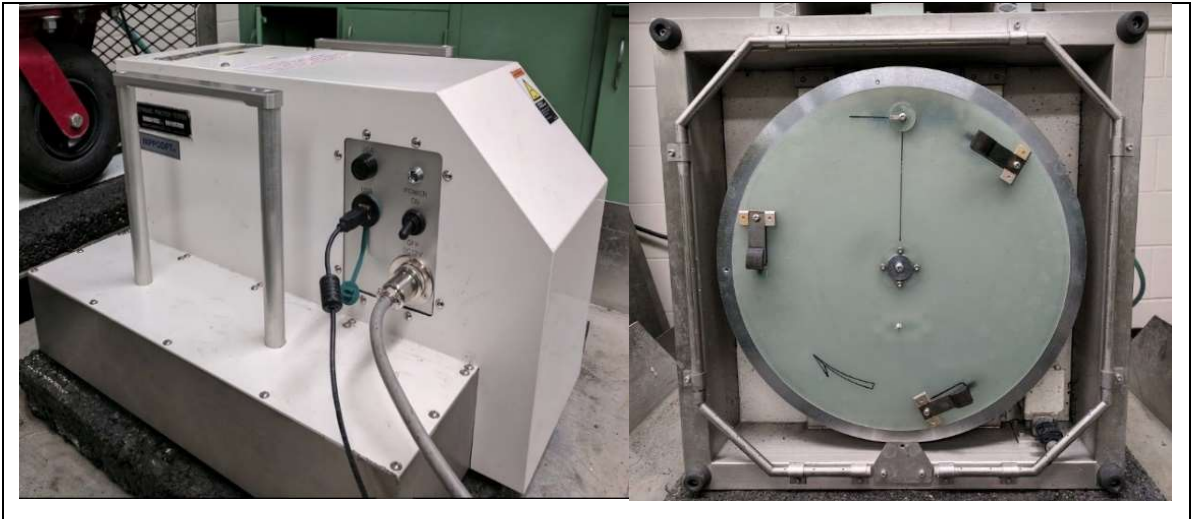


Figure A-2. Dynamic friction tester device and bottom view of the rotating disk and rubber sliders.

The surface macrotexture was measured using the sand patch test according to the ASTM E 965 [9]. The sand patch test measures the mean texture depth (MTD) of the pavement surface. The test is conducted by spreading a specific volume of sand on the pavement surface and spreading the sand in a circular shape. The diameter of the circle is then measured and the MTD is calculated using Equation A-1.

$$\text{MTD} = 4V / (\pi D^2) \quad (\text{A-1})$$

where, MTD = mean texture depth (mm); V = sand volume (mm^3); and D = average diameter of sand patch circle (mm).

The MTD is directly related to the mean profile depth (MPD). The MPD of the HMA slabs was measured using Equation A-2 as provided in the ASTM E 2157 [10].

$$\text{MTD} = 0.947 \text{ MPD} + 0.069 \quad (\text{A-2})$$

The international friction index (IFI) was measured according to the pavement international association of road congress (PIARC) formula (Equation A-3) as a function of both macrotexture and microtexture [11].

$$\text{IFI} = 0.081 + 0.732 \text{ DFT}_{20} \exp(-40/S_p) \quad (\text{A-3})$$

$$S_p = 14.2 + 89.7 \text{ MPD} \quad (\text{A-4})$$

where, DFT_{20} = coefficient of friction at 20 km/h measured using DFT; and S_p = speed constant.

A.4 Results and Discussion

The coefficient of friction was measured using the DFT for all test slabs after each set of polishing cycles. The DFT measurements at 20 km/h are considered an indication of the microtexture of pavement surface since there is no direct method for measuring the microtexture to date. The results (Figure A-3) showed that the HMA slab prepared with 100% limestone had the lowest initial and terminal values of the coefficient of friction compared to slabs with different blends of gabbro and limestone. In addition, the test slab prepared with 100% gabbro had the highest initial and terminal values of the coefficient of friction compared to the other slabs. The test slab prepared with 70% gabbro and 30% limestone had higher terminal coefficient of friction compared to the other two blends (50% gabbro and 50% limestone; and 30% gabbro and 70% limestone). The researchers observed that there was a slight increase in the coefficient of friction after 5000 cycles and this is attributed to removal of the asphalt film coating the aggregates at the surface.

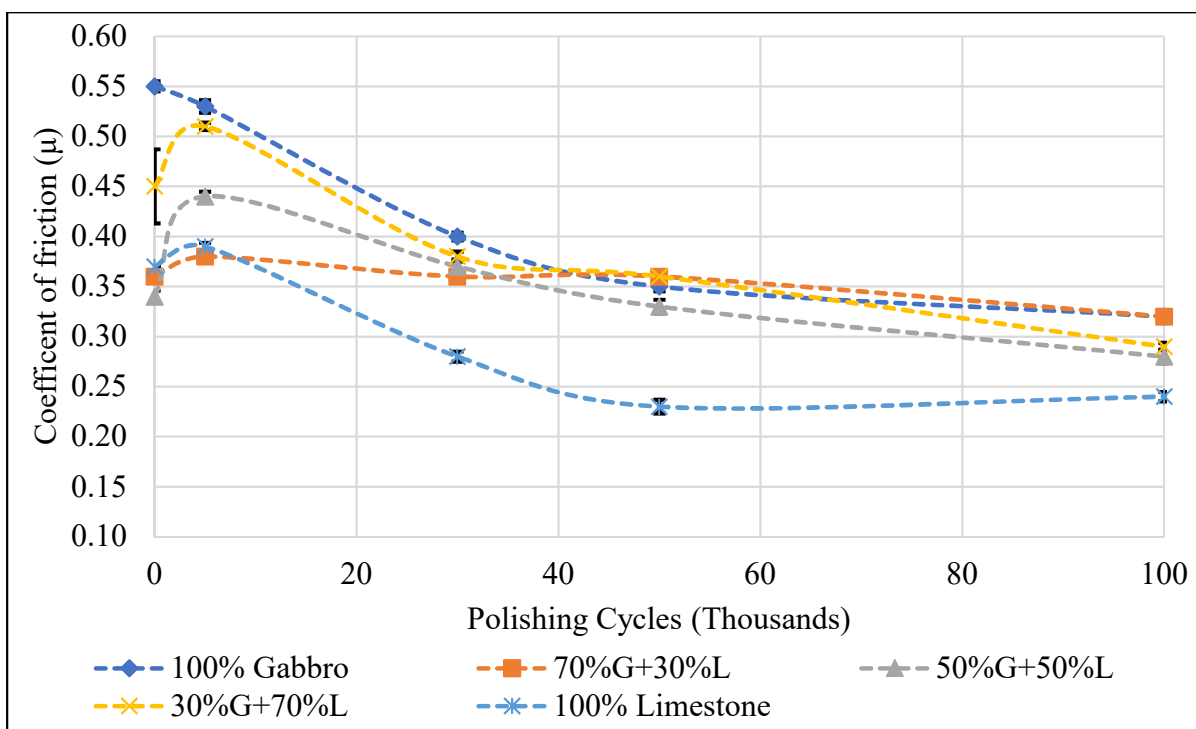


Figure A-3. Change of the coefficient of friction with polishing cycles of the lab-prepared HMA slabs.

Table A-2 presents the measured MTD and corresponding MPD for the test slabs. Although the same aggregate gradation was used in preparing all the test slabs of different aggregate blends, there were some differences in the macrotexture of the test slabs. This could be attributed to the effect of laboratory compaction.

Table A-2. Average measured MTD and calculated MPD for the HMA slabs.

Slab ID	MTD (mm)	MPD (mm)
Gabbro (G)	1.01	1.03
Limestone(L)	0.84	0.86
30% G + 70% L	1.08	1.09
50% G + 50% L	1.53	1.52
70% G + 30% L	0.87	0.89

The researchers calculated the IFI with polishing cycles using Equation A-3 for all test slabs as shown in Figure A-4. The IFI results clearly illustrated that blending gabbro with limestone improved the frictional characteristics of the HMA surface compared to slabs prepared using only limestone. Test slabs prepared using 100% gabbro; 70% gabbro and 30% limestone; and 50% gabbro and 50% limestone had relatively comparable terminal IFI but higher than the terminal IFI for slabs prepared using 30% gabbro and 70% limestone and 100% limestone test slabs. A blend of 30% gabbro and 70% limestone had improved frictional characteristics with a higher terminal IFI compared to 100% limestone. The results showed that blending aggregates with good resistance to abrasion and polishing, such as gabbro, with aggregates with poor resistance to abrasion and polishing, such as limestone, would improve the frictional characteristics of limestone mixtures.

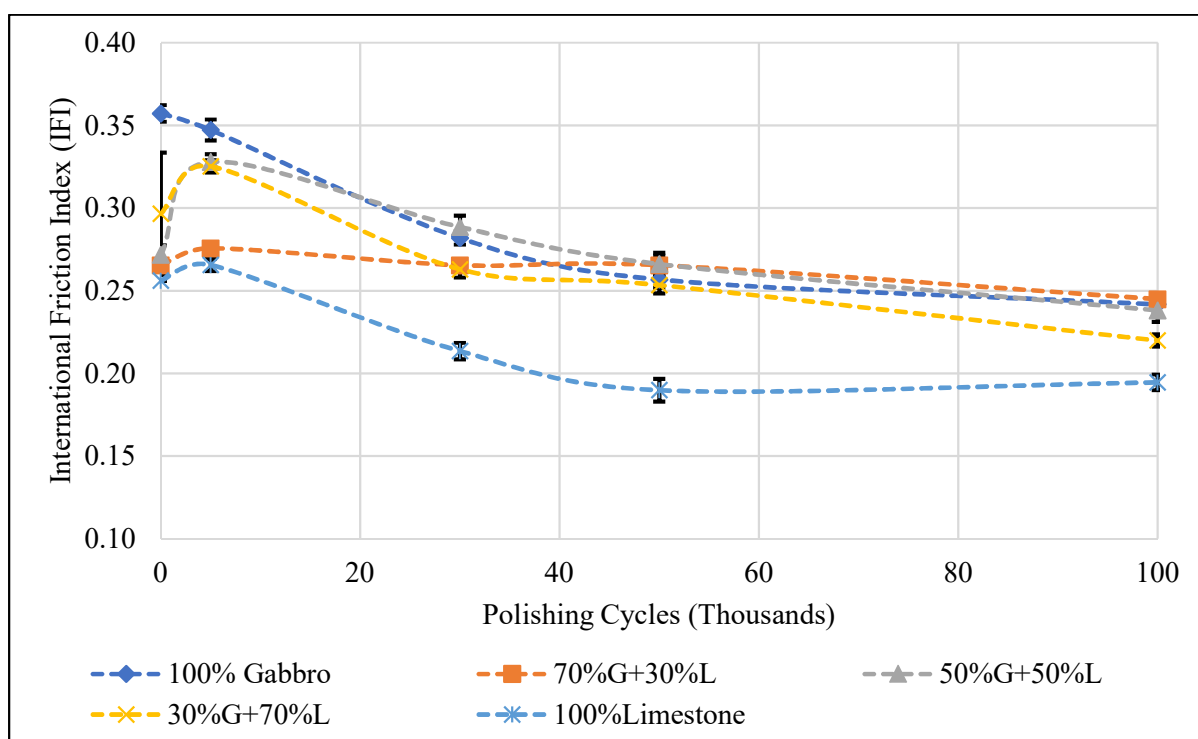


Figure A-4. Change of international friction index with polishing cycles of the lab-prepared HMA slabs.

In previous study by Aldagari et al., [12] prediction models were developed to predict the change the skid number with time for HMA and sealcoat pavements. The model can predict

the SN based on the aggregate gradation, texture, angularity and percentage of each aggregate source used in the mix design, the average annual daily traffic (AADT) and percent of truck traffic. Equation A-5 shows the model developed by Aldagari et al., [12] to predict the SN for HMA surfaces.

$$SN = 4.81 + 140.32 (IFI - 0.045) e^{-20/S_p} \quad (A-5)$$

where, IFI is the predicted international friction index given by Equation A-6, S_p is the speed parameter.

$$IFI = a_{mix} + b_{mix} * e^{-C_{mix}*N} \quad (A-6)$$

where a_{mix} , b_{mix} , and c_{mix} are parameters that are calculated based on the aggregate texture and angularity calculated as shown in Equations A-7 to A-9

$$a_{mix} = \frac{49.3144 + \lambda}{351.289 - 0.00193AMD^2} \quad (A-7)$$

$$a_{mix} + b_{mix} = 0.33 * \ln \left(\frac{1.43757*(a_{TX} + b_{TX}) + 46.8933*\lambda + 333.491*k}{2.42031*(a_{GA} + b_{GA})} \right) + 1.00801 \quad (A-8)$$

$$C_{mix} = 0.018 + 1.654C_{TX} + 1.346C_{GA} \quad (A-9)$$

where, λ , and κ are the scale and shape parameters for the Weibull distribution respectively, AMD is the texture after 105 minutes of polishing in the Micro-Deval, a_{TX} , b_{TX} are regression constants for aggregate texture, a_{GA} , b_{GA} are regression constants for aggregate angularity, C_{TX} is the rate of change in aggregate texture, C_{GA} is the rate of change in aggregate angularity.

The previous Equations A-5 to A-9 by Aldagari et al., [12] were incorporated into a software utility called the Skid Analysis of Asphalt Pavements (SAAP). The SAAP software was used in this research to predict the loss of skid resistance with time for different blends of

gabbro and limestone aggregates used in Qatar. The gabbro and limestone aggregate texture and angularity were characterized using the aggregate imaging system (AIMS) before polishing in the Micro-Deval and after 105 and 180 minutes of polishing in the Micro-Deval test. Figures A-5 and A-6 shows an example for entering into the SAAP software the texture and angularity data for the aggregate sources used in this study in order to predict the change in the skid resistance for the different combinations of gabbro and limestone.

AM Three Data Point Texture

Texture Data Points

Note: BMD > AMD105 > AMD180 > 0

Enter Number of Aggregate Sources

Enter Name of Aggregate Source 1

Enter Name of Aggregate Source 2

Limestone	Source 2
Proportion of Aggregate in the Mix (%)	Proportion of Aggregate in the Mix (%)
<input type="text" value="70"/>	<input type="text" value="30"/>
Percent Retained on Sieve #4	Percent Retained on Sieve #4
<input type="text" value="65"/>	<input type="text" value="43.5"/>
Texture Before Micro-Deval (BMD)	Texture Before Micro-Deval (BMD)
<input type="text" value="237.6"/>	<input type="text" value="351.2"/>
Texture After 105 Mins Micro-Deval (AMD)	Texture After 105 Mins Micro-Deval (AMD)
<input type="text" value="168.4"/>	<input type="text" value="321.8"/>
Texture After 180 Mins Micro-Deval (AMD)	Texture After 180 Mins Micro-Deval (AMD)
<input type="text" value="140.8"/>	<input type="text" value="289.3"/>

Figure A-5. Example for the aggregate texture input for two sources of aggregate.

AM Three Data Point Texture

Angularity Data Points

Note: BMD > AMD105 > AMD180 > 0

Enter Number of Aggregate Sources

Enter Name of Aggregate Source 1

Enter Name of Aggregate Source 2

Source 1		Source 2	
Proportion of Aggregate in the Mix (%)	<input type="text" value="70"/>	Proportion of Aggregate in the Mix (%)	<input type="text" value="30"/>
Percent Retained on Sieve #4	<input type="text" value="65"/>	Percent Retained on Sieve #4	<input type="text" value="43.5"/>
Angularity Before Micro-Deval (BMD)	<input type="text" value="3216.7"/>	Angularity Before Micro-Deval (BMD)	<input type="text" value="3541.4"/>
Angularity After 105 mins Micro-Deval (AMD)	<input type="text" value="2563.7"/>	Angularity After 105 mins Micro-Deval (AMD)	<input type="text" value="3165.2"/>
Angularity After 180 mins Micro-Deval (AMD)	<input type="text" value="220.1"/>	Angularity After 180 mins Micro-Deval (AMD)	<input type="text" value="2964.8"/>

Figure A-6. Example for the aggregate angularity input for two sources of aggregate.

The aggregate gradation along with the measured mean profile depth for each slab was provided as input to the SAAP software. The SAAP software accounts for the skid loss in years as a function of traffic. Based on previous traffic count data in Qatar, a divided 2-lane rural highway was considered for this analysis scenario. The AADT in each direction was provided to be 12,600 with 12% of truck traffic.

Figure A-7 shows the change in SN with years for the five different aggregate blends. The SAAP predictions shows that the limestone aggregate will provide the lowest level of skid resistance compared to all other combinations of aggregate blends. In addition, the results show that the limestone asphalt mix will have the highest rate of decrease in SN with time as it has lower texture and angularity when compared to the gabbro aggregate. The SAAP predictions for the SN showed that the use of a combination of gabbro and limestone will significantly

improve the frictional characteristics for pavements. The red dashed line shows the threshold of the SN for the pavement to be considered to have adequate skid resistance.

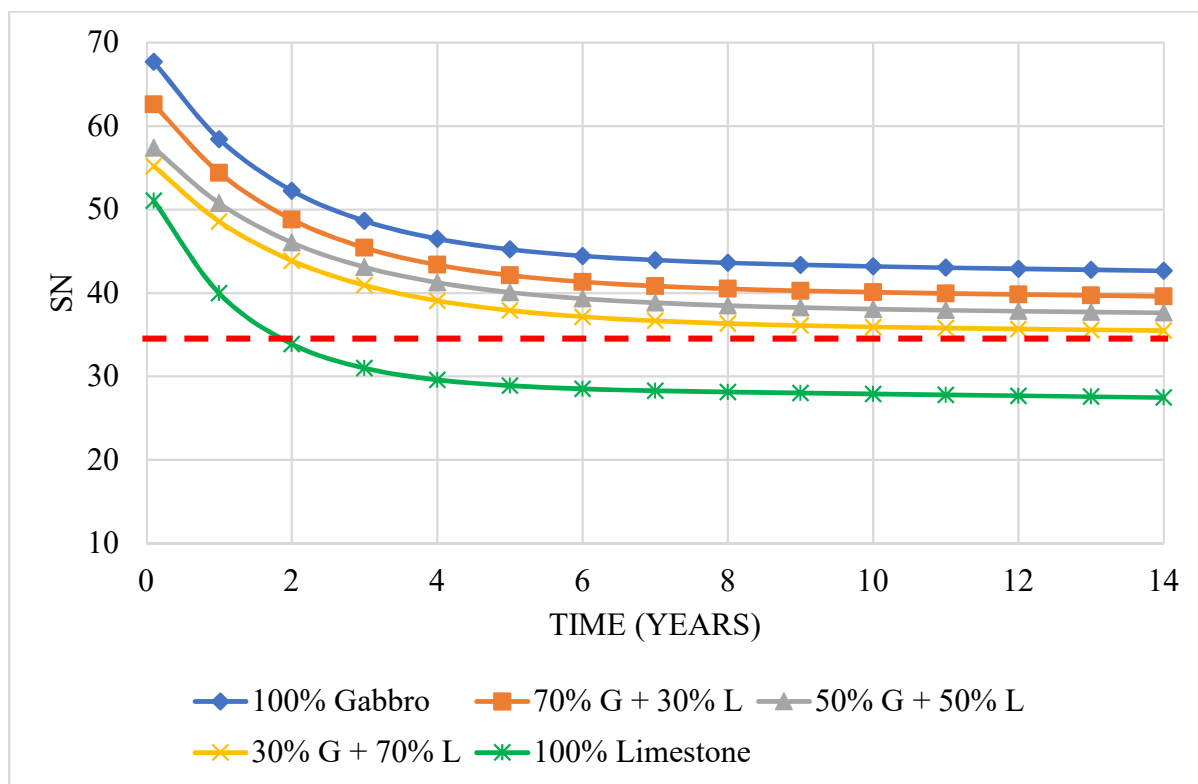


Figure A-7. SAAP predictions of SN with time for different blends of gabbro and limestone aggregate

A.5 Conclusions

This study examined the effect of aggregate blending on improving the frictional characteristics of the asphalt mixtures prepared using local limestone in Qatar. The researchers prepared HMA slabs with various blends of gabbro and limestone aggregates. The test slabs were subjected to polishing using a three-wheel polisher and both the microtexture and macrotexture were examined at different polishing intervals. The results showed that the HMA slabs prepared using gabbro aggregates had higher microtexture and IFI compared to limestone

slabs. The blend of gabbro and limestone provided comparable frictional characteristics to test slabs prepared using only gabbro aggregates. Based on the findings of this study, a blend of gabbro and limestone can be used in constructing asphalt pavements that provide adequate skid resistance. Such blend reduces the need to use 100% gabbro to about 30 to 50% gabbro leading to cost savings and maximizing the use of natural resources in Qatar. Meanwhile, the researchers recommend that trial test sites with different blends of gabbro and limestone be constructed alongside skid resistance monitoring over time. In addition, the mechanical properties of such blend should be thoroughly investigated to ensure durability.

A.6 References

- [1] Noyce, D. A. et al. (2005). Incorporating Road Safety into Pavement Management: Maximizing Asphalt Pavement Surface Friction for Road Safety Improvements; Midwest Regional University Transportation Center, p. 110.
- [2] Flintsch, G. W. et al. (2010). Speed Adjustment Factors for Locked-Wheel Skid Trailer Measurements; Transportation Research Record: Journal of the Transportation Research Board, 2155(1), pp. 117–123. doi: 10.3141/2155-13.
- [3] Wallman, C.-G. and Åström, H. (2001). Friction measurement methods and the correlation between road friction and traffic safety. A literature review; Swedish National Road and Transport Research Institute, Technical Report., p. 47. ISSN: 0347-6049.
- [4] Masad, E., Rezaei, A., Chowdhury, A., and Freeman, T. J. (2011). Field evaluation of asphalt mixture skid resistance and its relationship to aggregate characteristics; Texas Transportation Institute, Report No. 0-5627-3.
- [5] Kassem, E., Awed, A., Masad, E. and Little, D. (2013). Development of Predictive Model for Skid Loss of Asphalt Pavements; Transportation Research Record: Journal of the Transportation Research Board, 2372, pp.83-96.
- [6] Chowdhury, A., Kassem, E., Aldagari, S., Masad, E., (2017). Validation of Asphalt Mixture Pavement Skid Prediction Model and Development of Skid Prediction Model for Surface Treatments. Technical Report, Texas Transportation Institute 0-6746-01-1.
- [7] Masad, E., Kassem, E. and Little, D. (2011). Characterization of Asphalt Pavement Materials in the State of Qatar. Road Materials and Pavement Design, 12(4), pp.739-765.
- [8] ASTM E1911-09, (2009) Standard Test Method for Measuring Paved Surface Frictional Properties Using the Dynamic Friction Tester, ASTM International, West Conshohocken, PA, 2009.
- [9] ASTM E965 (2015), Standard Test Method for Measuring Pavement Macrotexture Depth Using a Volumetric Technique, ASTM International, West Conshohocken, PA, 2015.

- [10] ASTM E2157, (2015). Standard Test Method for Measuring Pavement Macrotexture Properties Using the Circular Track Meter, ASTM International, West Conshohocken, PA, 2015.
- [11] Wambold J. C., Antle C. E., Henry J. J., Rado Z., Descornet G., Sandberg U., Gothié M. and, Huschek S. 1995 International PIARC Experiment to Compare and Harmonize Skid Resistance and Texture Measurements (Paris: PIARC) Publication No. 01.04.T
- [12] Aldagari, S., Al-Assi, M., Kassem, E., Chowdhury, A. and Masad, E., (2018). Prediction Models for Skid Resistance of Asphalt Pavements and Seal Coat. Transportation Research Board (No. 18-05541).

Appendix B - DMA Flow Curves for Rubber Materials

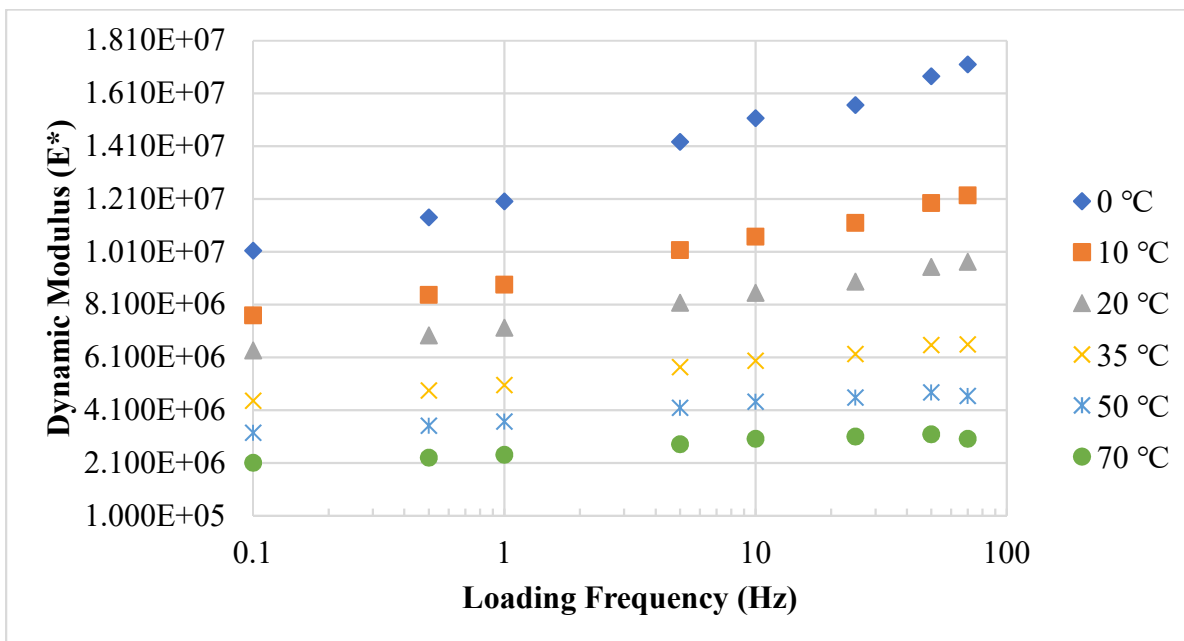


Figure B-1. DMA flow curves for the Butyl rubber material

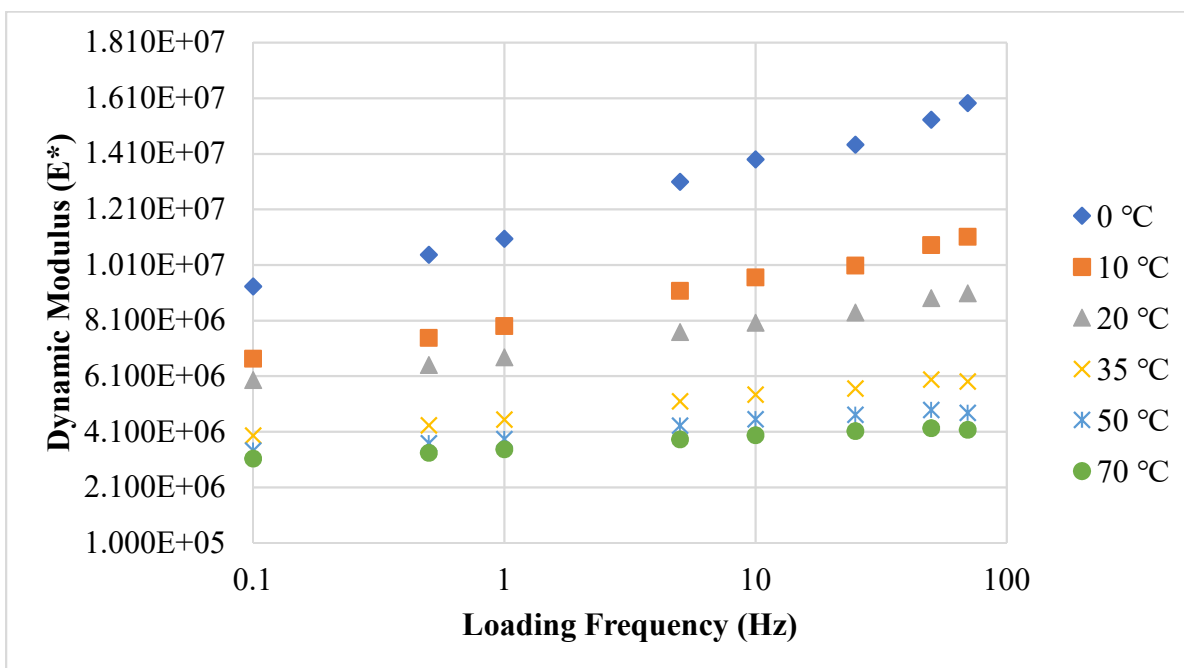


Figure B-2. DMA flow curves for the Neoprene rubber material

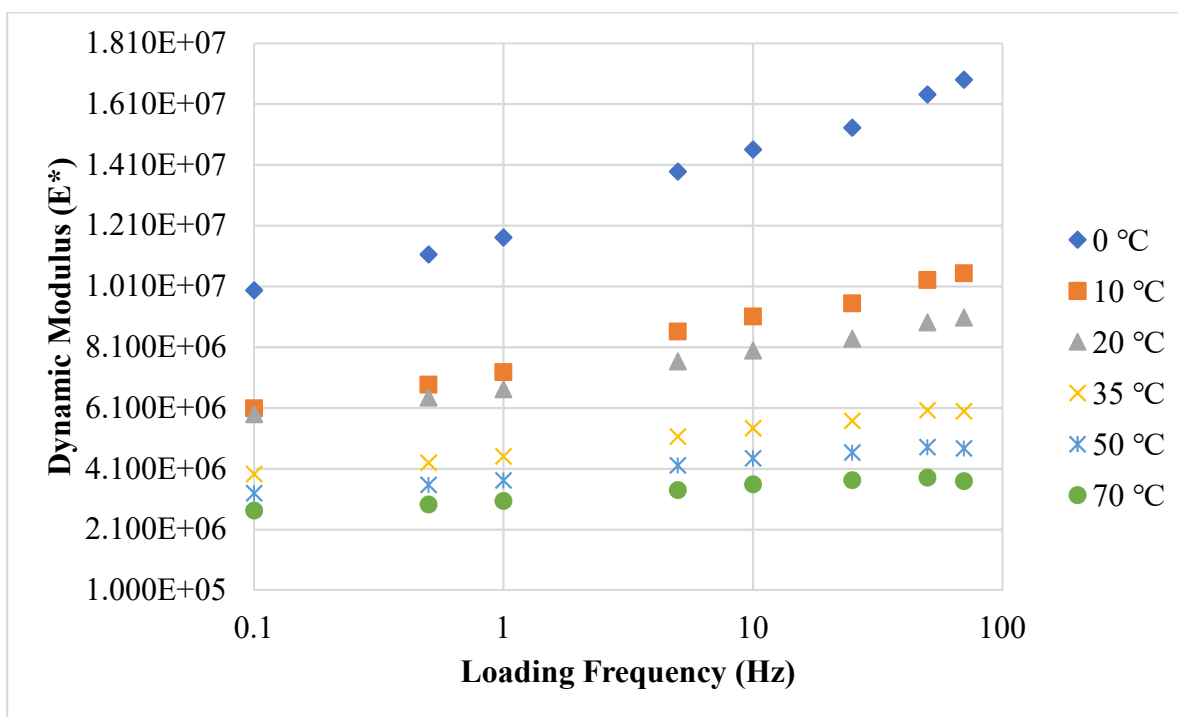


Figure B-3. DMA flow curves for the EPDM rubber material

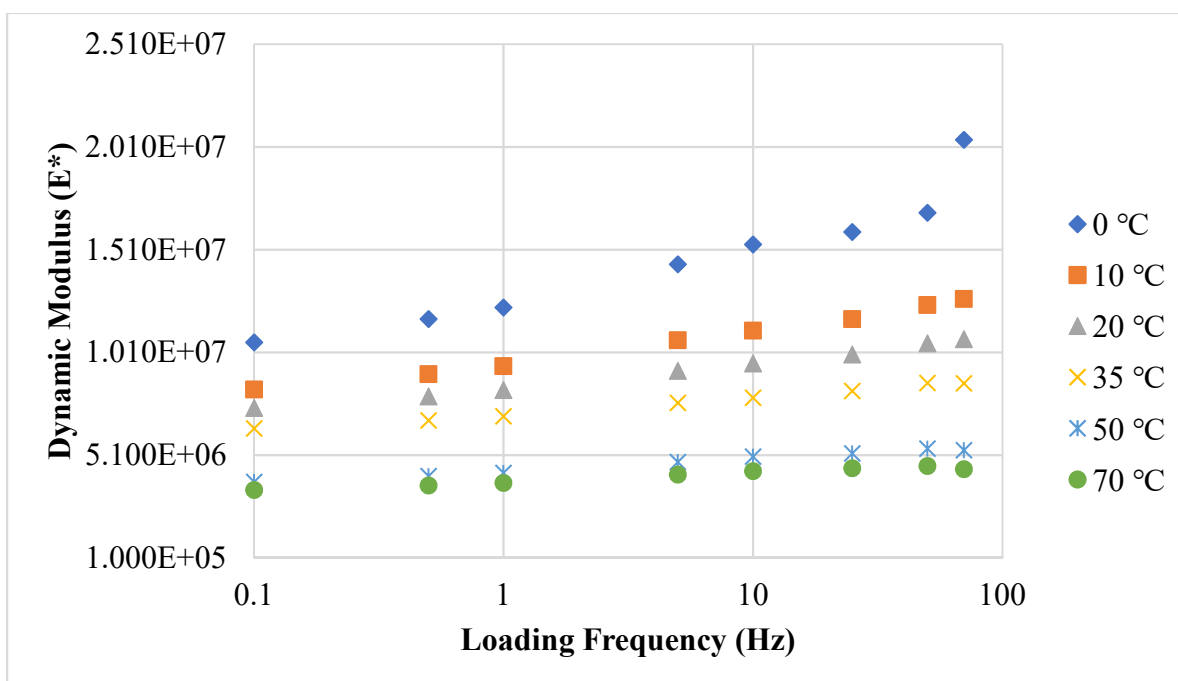


Figure B-4. DMA Flow curves for the Nitrile rubber material

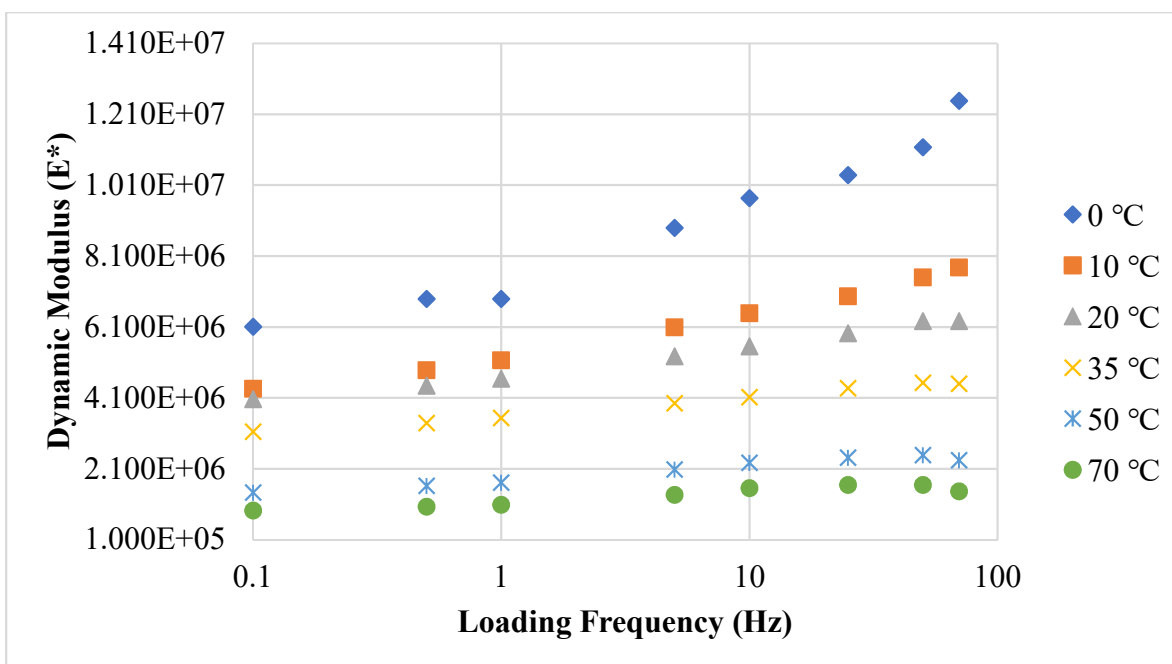


Figure B-5. DMA flow curves for the SBR rubber material

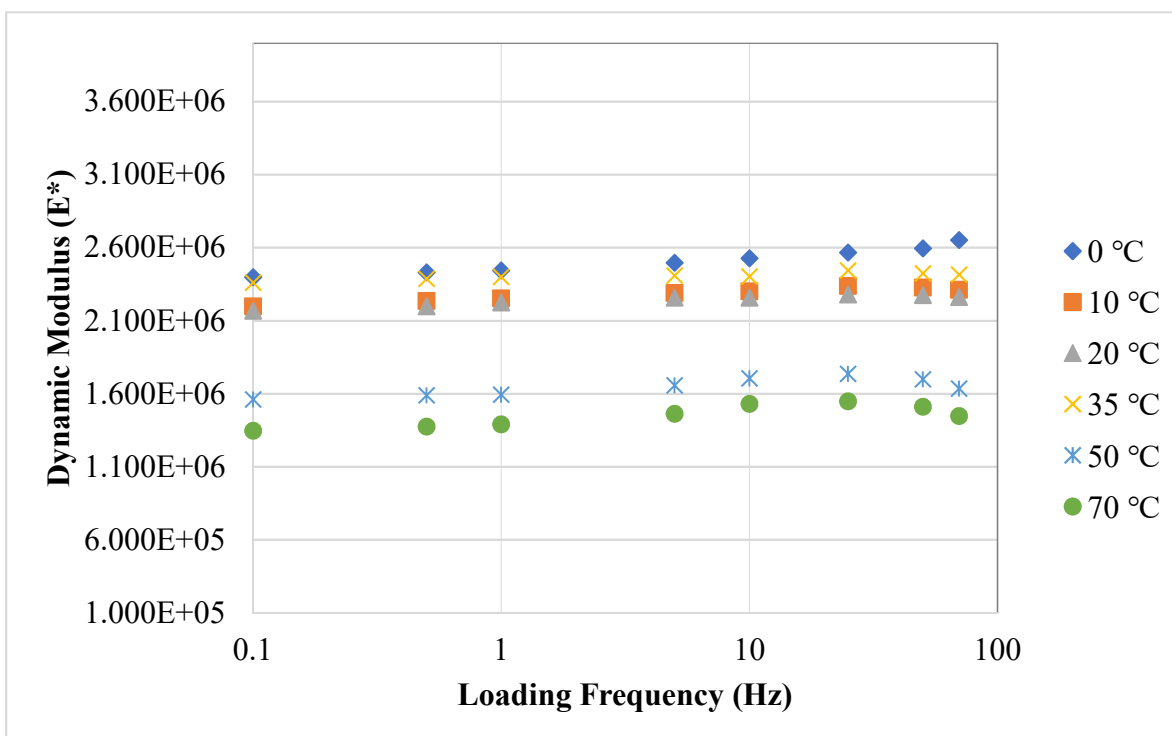


Figure B-6. DMA flow curves for the Pure Gum rubber material

Appendix C - Summary of Skid and Texture Measurements in Idaho

Table C-1. Collected Skid Number measurements for Idaho sections at different speeds

Test Section ID	Test Speed (mph)	Average Skid Number (SN)	Standard Deviation	Surface Type
1	20	75.09	0.95	Seal Coat
1	30	71.97	1.11	Seal Coat
1	40	66.19	1.33	Seal Coat
1	50	60.53	1.48	Seal Coat
1	60	52.02	6.12	Seal Coat
2	20	63.31	1.49	HMA
2	30	55.16	1.75	HMA
2	40	50.33	1.47	HMA
2	50	45.24	2.59	HMA
2	60	40.06	2.65	HMA
3	20	62.69	2.39	HMA
3	30	47.15	3.11	HMA
3	40	37.91	3.25	HMA
3	50	36.41	2.45	HMA
3	60	29.87	2.89	HMA
4	20	60.31	1.94	Seal Coat
4	30	53.17	2.67	Seal Coat
4	40	46.09	3.60	Seal Coat
4	50	41.36	6.69	Seal Coat
4	60	38.90	4.61	Seal Coat
5	20	69.83	1.88	Seal Coat
5	30	61.71	3.02	Seal Coat
5	40	51.53	3.28	Seal Coat
5	50	44.60	1.28	Seal Coat
5	60	45.10	3.05	Seal Coat
6	20	63.24	2.09	Concrete
6	30	56.38	2.20	Concrete
6	40	49.60	1.07	Concrete
6	50	43.16	1.72	Concrete

Table C-1. Collected Skid Number measurements for Idaho sections at different speeds
(Continued)

Test Section ID	Test Speed (mph)	Average Skid Number (SN)	Standard Deviation	Surface Type
7	20	57.03	0.94	HMA
7	30	50.08	0.86	HMA
7	40	44.16	2.77	HMA
7	50	40.21	2.20	HMA
7	60	35.96	1.76	HMA
8	20	70.72	0.49	Seal Coat
8	30	65.66	1.19	Seal Coat
8	40	60.20	1.08	Seal Coat
8	50	53.88	2.06	Seal Coat
8	60	48.99	2.78	Seal Coat
9	20	66.17	0.82	Seal Coat
9	30	59.78	1.55	Seal Coat
9	40	53.52	1.73	Seal Coat
9	50	51.37	1.58	Seal Coat
9	60	47.07	3.44	Seal Coat
10	20	60.46	1.67	Concrete
10	30	51.04	2.08	Concrete
10	40	43.21	1.10	Concrete
10	50	36.54	1.68	Concrete
10	60	34.05	2.13	Concrete
11	20	68.23	1.75	HMA
11	30	65.66	1.19	HMA
11	40	60.20	1.08	HMA
11	50	53.88	2.06	HMA
11	60	49.70	1.88	HMA
12	20	50.26	2.01	HMA
12	30	34.84	2.14	HMA
12	40	27.37	2.96	HMA
12	50	17.64	2.02	HMA
12	60	14.48	1.76	HMA

Table C-1. Collected Skid Number measurements for Idaho sections at different speeds
(Continued)

Test Section ID	Test Speed (mph)	Average Skid Number (SN)	Standard Deviation	Surface Type
13	20	64.31	0.90	Seal Coat
13	30	59.49	0.59	Seal Coat
13	40	56.62	0.64	Seal Coat
13	50	53.23	1.36	Seal Coat
13	60	49.39	1.71	Seal Coat
14	20	66.98	1.50	Seal Coat
14	30	60.93	1.90	Seal Coat
14	40	55.39	1.92	Seal Coat
14	50	45.80	1.20	Seal Coat
14	60	41.20	2.29	Seal Coat
15	20	71.98	1.07	Seal Coat
15	30	66.74	0.93	Seal Coat
15	40	63.03	1.07	Seal Coat
15	50	59.53	0.85	Seal Coat
15	60	55.44	1.98	Seal Coat
16	20	52.69	6.45	HMA
16	30	35.34	4.29	HMA
16	40	29.36	4.45	HMA
16	50	24.84	2.82	HMA
16	60	20.56	3.99	HMA
17	20	64.17	0.97	HMA
17	30	52.94	1.49	HMA
17	40	44.61	2.12	HMA
17	50	37.55	1.90	HMA
17	60	35.99	3.56	HMA
18	20	51.88	1.43	HMA
18	30	51.77	0.98	HMA
18	40	47.54	0.75	HMA
18	50	45.37	1.24	HMA

Table C-1. Collected Skid Number measurements for Idaho sections at different speeds
(Continued)

Test Section ID	Test Speed (mph)	Average Skid Number (SN)	Standard Deviation	Surface Type
19	20	57.81	1.35	HMA
19	30	43.82	1.52	HMA
19	40	32.54	2.14	HMA
19	50	24.57	3.07	HMA
19	60	22.50	3.85	HMA
20	20	48.97	4.57	Concrete
20	30	34.90	1.70	Concrete
20	40	23.90	2.46	Concrete
20	50	19.60	2.77	Concrete
20	60	16.18	1.92	Concrete
21	20	65.08	2.09	Sealcoat
21	30	58.32	2.80	Sealcoat
21	40	52.25	1.63	Sealcoat
21	50	46.60	2.08	Sealcoat
21	60	43.95	2.67	Sealcoat
22	20	73.20	1.94	HMA
22	30	63.74	1.64	HMA
22	40	58.78	1.63	HMA
22	50	53.80	1.54	HMA
22	60	51.17	2.24	HMA

Table C-2. Measurements of surface texture characteristics for Idaho sections

Test Section ID	MPD (mm)	MTD (mm)	DFT₂₀	Surface Type
1	1.19	1.20	0.69	Seal Coat
2	1.23	1.25	0.62	HMA
3	0.65	0.60	0.62	HMA
4	1.16	1.33	0.55	Seal Coat
5	1.02	0.86	0.55	Seal Coat
6	1.10	1.06	0.58	Concrete
7	1.02	0.89	0.52	HMA
8	1.63	1.32	0.59	Seal Coat
9	1.01	1.00	0.52	Seal Coat
10	0.58	0.56	0.55	Concrete
11	0.72	0.78	0.62	HMA
12	0.51	0.28	0.64	HMA
13	2.27	2.29	0.60	Seal Coat
14	0.82	0.83	0.57	Seal Coat
15	2.04	1.90	0.55	Seal Coat
16	0.52	0.42	0.61	HMA
17	0.66	0.59	0.58	HMA
18	1.37	1.42	0.57	HMA
19	0.61	0.56	0.65	HMA
20	0.57	0.51	0.55	Concrete
21	1.10	1.04	0.60	Sealcoat
22	1.30	1.25	0.63	HMA

Appendix D - CRP Measurements and Pearson Friction Model Parameters

Table D-1. Measurements of slabs friction, rubber properties, and surface texture using the CRP method

Number	Surface ID	E* (MPa) at 20 km/h	DFT ₂₀	CRP Microtexture (mm)	CRP Macrotecture (mm)	Hurst Exponent (H)
1	100G 5K	2.31	0.41	0.167	1.05	0.280
2	100G 5K	9.88	0.52	0.167	1.05	0.280
3	100G 5K	7.80	0.57	0.167	1.05	0.280
4	100G 5K	7.80	0.51	0.167	1.05	0.280
5	100G 5K	8.87	0.55	0.167	1.05	0.280
6	100G 5K	5.50	0.53	0.167	1.05	0.280
7	100G 20K	2.31	0.35	0.113	0.91	0.280
8	100G 20K	5.82	0.46	0.113	0.91	0.280
9	100G 20K	9.97	0.44	0.113	0.91	0.280
10	100G 20K	7.89	0.44	0.113	0.91	0.280
11	100G 20K	7.88	0.43	0.113	0.91	0.280
12	100G 20K	8.97	0.42	0.113	0.91	0.280
13	100G 20K	5.50	0.4	0.113	0.91	0.280
14	100G 30K	2.31	0.37	0.123	0.92	0.261
15	100G 30K	9.96	0.43	0.123	0.92	0.261
16	100G 30K	7.89	0.43	0.123	0.92	0.261
17	100G 30K	7.87	0.42	0.123	0.92	0.261
18	100G 30K	8.96	0.4	0.123	0.92	0.261
19	100G 30K	5.50	0.39	0.123	0.92	0.261
20	100G 50K	5.86	0.36	0.108	0.84	0.525
21	100G 50K	10.01	0.39	0.108	0.84	0.525
22	100G 50K	7.94	0.41	0.108	0.84	0.525
23	100G 50K	7.92	0.41	0.108	0.84	0.525
24	100G 50K	9.02	0.39	0.108	0.84	0.525
25	100G 50K	5.50	0.32	0.108	0.84	0.525
26	100G 100K	5.81	0.35	0.090	0.93	0.529
27	100G 100K	9.96	0.39	0.090	0.93	0.529

Table D-1. Measurements of slabs friction, rubber properties, and surface texture using the CRP method (Continued)

Number	Surface ID	E* (MPa) at 20 km/h	DFT₂₀	CRP Microtexture (mm)	CRP Macrotecture (mm)	Hurst Exponent (H)
28	100G 100K	7.88	0.38	0.090	0.93	0.529
29	100G 100K	7.87	0.41	0.090	0.93	0.529
30	100G 100K	8.96	0.45	0.090	0.93	0.529
31	100G 100K	5.50	0.31	0.090	0.93	0.529
32	50G 5K	2.31	0.4	0.149	1.24	0.522
33	50G 5K	9.78	0.59	0.149	1.24	0.522
34	50G 5K	7.71	0.56	0.149	1.24	0.522
35	50G 5K	7.70	0.61	0.149	1.24	0.522
36	50G 5K	8.77	0.55	0.149	1.24	0.522
37	50G 5K	5.50	0.44	0.149	1.24	0.522
38	50G 10K	2.31	0.37	0.173	1.25	0.516
39	50G 10K	9.78	0.51	0.173	1.25	0.516
40	50G 10K	7.70	0.51	0.173	1.25	0.516
41	50G 10K	7.70	0.53	0.173	1.25	0.516
42	50G 10K	8.77	0.47	0.173	1.25	0.516
43	50G 10K	5.50	0.42	0.173	1.25	0.516
44	50G 20K	2.31	0.4	0.133	1.19	0.508
45	50G 20K	5.69	0.43	0.133	1.19	0.508
46	50G 20K	9.81	0.48	0.133	1.19	0.508
47	50G 20K	7.73	0.52	0.133	1.19	0.508
48	50G 20K	7.73	0.49	0.133	1.19	0.508
49	50G 20K	8.79	0.5	0.133	1.19	0.508
50	50G 20K	5.50	0.37	0.133	1.19	0.508
51	50G 50K	2.31	0.31	0.146	1.25	0.250
52	50G 50K	9.78	0.52	0.146	1.25	0.250
53	50G 50K	7.70	0.48	0.146	1.25	0.250
54	50G 50K	7.70	0.51	0.146	1.25	0.250
55	50G 50K	8.76	0.48	0.146	1.25	0.250
56	50G 50K	5.50	0.33	0.146	1.25	0.250
57	50G 100K	2.31	0.3	0.097	1.22	0.500
58	50G 100K	5.68	0.4	0.097	1.22	0.500

Table D-1. Measurements of slabs friction, rubber properties, and surface texture using the CRP method (Continued)

Number	Surface ID	E* (MPa) at 20 km/h	DFT ₂₀	CRP Microtexture (mm)	CRP Macrotecture (mm)	Hurst Exponent (H)
59	50G 100K	9.79	0.44	0.097	1.22	0.500
60	50G 100K	7.72	0.44	0.097	1.22	0.500
61	50G 100K	7.71	0.44	0.097	1.22	0.500
62	50G 100K	8.78	0.43	0.097	1.22	0.500
63	100L 5K	2.31	0.34	0.109	0.74	0.500
64	100L 5K	5.92	0.44	0.109	0.74	0.500
65	100L 5K	10.09	0.5	0.109	0.74	0.500
66	100L 5K	8.02	0.42	0.109	0.74	0.500
67	100L 5K	8.00	0.41	0.109	0.74	0.500
68	100L 5K	5.50	0.39	0.109	0.74	0.500
69	100L 10K	2.31	0.32	0.107	0.78	0.497
70	100L 10K	10.05	0.37	0.107	0.78	0.497
71	100L 10K	7.98	0.32	0.107	0.78	0.497
72	100L 10K	7.96	0.38	0.107	0.78	0.497
73	100L 10K	9.06	0.31	0.107	0.78	0.497
74	100L 10K	5.50	0.32	0.107	0.78	0.497
75	100L 20K	2.31	0.29	0.082	0.78	0.500
76	100L 20K	5.89	0.32	0.082	0.78	0.500
77	100L 20K	7.96	0.37	0.082	0.78	0.500
78	100L 20K	5.50	0.3	0.082	0.78	0.500
79	100L 50K	10.09	0.25	0.049	0.74	0.493
80	100L 50K	8.01	0.25	0.049	0.74	0.493
81	100L 50K	9.10	0.25	0.049	0.74	0.493
82	100L 50K	5.50	0.23	0.049	0.74	0.493
83	100L 100K	5.84	0.24	0.090	0.86	0.501
84	100L 100K	10.00	0.26	0.090	0.86	0.501
85	100L 100K	7.92	0.25	0.090	0.86	0.501
86	100L 100K	7.91	0.24	0.090	0.86	0.501
87	100L 100K	9.00	0.24	0.090	0.86	0.501

Table D-1. Measurements of slabs friction, rubber properties, and surface texture using the CRP method (Continued)

Number	Surface ID	E* (MPa) at 20 km/h	DFT₂₀	CRP Microtextur e (mm)	CRP Macrotextur e (mm)	Hurst Exponen t (H)
88	100L 100K	5.50	0.24	0.090	0.86	0.501
89	30G 100K	5.68	0.34	0.102	1.23	0.550
90	30G 100K	7.71	0.38	0.102	1.23	0.550
91	30G 100K	7.71	0.42	0.102	1.23	0.550
92	30G 100K	8.77	0.43	0.102	1.23	0.550
93	30G 100K	5.50	0.29	0.102	1.23	0.550
94	Concrete1	5.50	0.57	0.210	0.50	0.277
95	50G 100K	1.87	0.21	0.097	1.22	0.500
96	50G 100K	5.68	0.38	0.097	1.22	0.500
97	50G 100K	4.40	0.4	0.097	1.22	0.500
98	50G 100K	4.62	0.43	0.097	1.22	0.500
99	50G 100K	4.38	0.41	0.097	1.22	0.500
100	100G 100K	2.50	0.4	0.090	0.93	0.529
101	100G 100K	15.35	0.56	0.090	0.93	0.529
102	100G 100K	14.85	0.52	0.090	0.93	0.529
103	100G 100K	14.43	0.53	0.090	0.93	0.529
104	100G 100K	15.31	0.56	0.090	0.93	0.529
105	100G 100K	1.87	0.34	0.090	0.93	0.529
106	100G 100K	5.78	0.52	0.090	0.93	0.529
107	100G 100K	4.47	0.49	0.090	0.93	0.529
108	100G 100K	4.70	0.46	0.090	0.93	0.529
109	100G 100K	4.46	0.42	0.090	0.93	0.529
110	30G 100K	2.50	0.32	0.102	1.23	0.550
111	30G 100K	15.11	0.39	0.102	1.23	0.550
112	30G 100K	14.47	0.43	0.102	1.23	0.550
113	30G 100K	14.10	0.34	0.102	1.23	0.550
114	30G 100K	14.97	0.39	0.102	1.23	0.550
115	30G 100K	1.87	0.21	0.102	1.23	0.550
116	30G 100K	5.68	0.32	0.102	1.23	0.550
117	30G 100K	4.40	0.33	0.102	1.23	0.550
118	30G 100K	4.62	0.37	0.102	1.23	0.550
119	30G 100K	4.38	0.33	0.102	1.23	0.550

Table D-1. Measurements of slabs friction, rubber properties, and surface texture using the CRP method (Continued)

Number	Surface ID	E* (MPa) at 20 km/h	DFT₂₀	CRP Microtexture (mm)	CRP Macrotecture (mm)	Hurst Exponent (H)
120	50G 100K	2.50	0.21	0.097	1.22	0.500
121	50G 100K	15.12	0.38	0.097	1.22	0.500
122	50G 100K	14.48	0.4	0.097	1.22	0.500
123	50G 100K	14.10	0.43	0.097	1.22	0.500
124	50G 100K	14.98	0.41	0.097	1.22	0.500
125	100L 100K	2.50	0.28	0.090	0.86	0.501
126	100L 100K	9.61	0.35	0.090	0.86	0.501
127	100L 100K	15.41	0.36	0.090	0.86	0.501
128	100L 100K	14.95	0.39	0.090	0.86	0.501
129	100L 100K	15.40	0.38	0.090	0.86	0.501
130	100L 100K	1.88	0.25	0.090	0.86	0.501
131	100L 100K	2.62	0.26	0.090	0.86	0.501
132	100L 100K	5.80	0.27	0.090	0.86	0.501
133	100L 100K	4.49	0.26	0.090	0.86	0.501
134	100L 100K	4.48	0.27	0.090	0.86	0.501

Table D-2. Summary of Persson model parameters for HMA slabs

Number	Surface ID	P(q)	S(q)	C(q)	H
1	100G 5K	0.01738	0.50015	0.34784	0.280
2	100G 5K	0.01738	0.50015	0.34784	0.280
3	100G 5K	0.01738	0.50015	0.34784	0.280
4	100G 5K	0.01738	0.50015	0.34784	0.280
5	100G 5K	0.01738	0.50015	0.34784	0.280
6	100G 5K	0.01738	0.50015	0.34784	0.280
7	100G 20K	0.01497	0.50011	0.28681	0.280
8	100G 20K	0.01497	0.50011	0.28681	0.280
9	100G 20K	0.01497	0.50011	0.28681	0.280
10	100G 20K	0.01497	0.50011	0.28681	0.280
11	100G 20K	0.01497	0.50011	0.28681	0.280
12	100G 20K	0.01497	0.50011	0.28681	0.280
13	100G 20K	0.01497	0.50011	0.28681	0.280
14	100G 30K	0.01512	0.50011	0.28179	0.261
15	100G 30K	0.01512	0.50011	0.28179	0.261
16	100G 30K	0.01512	0.50011	0.28179	0.261
17	100G 30K	0.01512	0.50011	0.28179	0.261
18	100G 30K	0.01512	0.50011	0.28179	0.261
19	100G 30K	0.01512	0.50011	0.28179	0.261
20	100G 50K	0.01386	0.5001	0.38224	0.525
21	100G 50K	0.01386	0.5001	0.38224	0.525
22	100G 50K	0.01386	0.5001	0.38224	0.525
23	100G 50K	0.01386	0.5001	0.38224	0.525
24	100G 50K	0.01386	0.5001	0.38224	0.525
25	100G 50K	0.01386	0.5001	0.38224	0.525
26	100G 100K	0.01527	0.50012	0.43834	0.529
27	100G 100K	0.01527	0.50012	0.43834	0.529
28	100G 100K	0.01527	0.50012	0.43834	0.529
29	100G 100K	0.01527	0.50012	0.43834	0.529
30	100G 100K	0.01527	0.50012	0.43834	0.529

Table D-2. Summary of Persson model parameters for HMA slabs (continued)

Number	Surface ID	P(q)	S(q)	C(q)	H
31	100G 100K	0.01527	0.50012	0.43834	0.529
32	50G 5K	0.02052	0.50021	0.55916	0.522
33	50G 5K	0.02052	0.50021	0.55916	0.522
34	50G 5K	0.02052	0.50021	0.55916	0.522
35	50G 5K	0.02052	0.50021	0.55916	0.522
36	50G 5K	0.02052	0.50021	0.55916	0.522
37	50G 5K	0.02052	0.50021	0.55916	0.522
38	50G 10K	0.02055	0.50021	0.54429	0.516
39	50G 10K	0.02055	0.50021	0.54429	0.516
40	50G 10K	0.02055	0.50021	0.54429	0.516
41	50G 10K	0.02055	0.50021	0.54429	0.516
42	50G 10K	0.02055	0.50021	0.54429	0.516
43	50G 10K	0.02055	0.50021	0.54429	0.516
44	50G 20K	0.01968	0.50019	0.53419	0.508
45	50G 20K	0.01968	0.50019	0.53419	0.508
46	50G 20K	0.01968	0.50019	0.53419	0.508
47	50G 20K	0.01968	0.50019	0.53419	0.508
48	50G 20K	0.01968	0.50019	0.53419	0.508
49	50G 20K	0.01968	0.50019	0.53419	0.508
50	50G 20K	0.01968	0.50019	0.53419	0.508
51	50G 50K	0.0206	0.50021	0.4463	0.250
52	50G 50K	0.0206	0.50021	0.4463	0.250
53	50G 50K	0.0206	0.50021	0.4463	0.250
54	50G 50K	0.0206	0.50021	0.4463	0.250
55	50G 50K	0.0206	0.50021	0.4463	0.250
56	50G 50K	0.0206	0.50021	0.4463	0.250
57	50G 100K	0.02017	0.5002	0.56255	0.500
58	50G 100K	0.02017	0.5002	0.56255	0.500

Table D-2. Summary of Persson model parameters for HMA slabs (continued)

Number	Surface ID	P(q)	S(q)	C(q)	H
59	50G 100K	0.02017	0.5002	0.56255	0.500
60	50G 100K	0.02017	0.5002	0.56255	0.500
61	50G 100K	0.02017	0.5002	0.56255	0.500
62	50G 100K	0.02017	0.5002	0.56255	0.500
63	100L 5K	0.01215	0.50007	0.36265	0.500
64	100L 5K	0.01215	0.50007	0.36265	0.500
65	100L 5K	0.01215	0.50007	0.36265	0.500
66	100L 5K	0.01215	0.50007	0.36265	0.500
67	100L 5K	0.01215	0.50007	0.36265	0.500
68	100L 5K	0.01215	0.50007	0.36265	0.500
69	100L 10K	0.01294	0.50008	0.09792	0.497
70	100L 10K	0.01294	0.50008	0.09792	0.497
71	100L 10K	0.01294	0.50008	0.09792	0.497
72	100L 10K	0.01294	0.50008	0.09792	0.497
73	100L 10K	0.01294	0.50008	0.09792	0.497
74	100L 10K	0.01294	0.50008	0.09792	0.497
75	100L 20K	0.01292	0.50008	0.3505	0.500
76	100L 20K	0.01292	0.50008	0.3505	0.500
77	100L 20K	0.01292	0.50008	0.3505	0.500
78	100L 20K	0.01292	0.50008	0.3505	0.500
79	100L 50K	0.01224	0.50007	0.3412	0.493
80	100L 50K	0.01224	0.50007	0.3412	0.493
81	100L 50K	0.01224	0.50007	0.3412	0.493
82	100L 50K	0.01224	0.50007	0.3412	0.493
83	100L 100K	0.0142	0.5001	0.3857	0.501
84	100L 100K	0.0142	0.5001	0.3857	0.501
85	100L 100K	0.0142	0.5001	0.3857	0.501
86	100L 100K	0.0142	0.5001	0.3857	0.501
87	100L 100K	0.0142	0.5001	0.3857	0.501
88	100L 100K	0.0142	0.5001	0.3857	0.501

Table D-2. Summary of Persson model parameters for HMA slabs (continued)

Number	Surface ID	P(q)	S(q)	C(q)	H
89	30G 100K	0.02026	0.50021	0.59691	0.550
90	30G 100K	0.02026	0.50021	0.59691	0.550
91	30G 100K	0.02026	0.50021	0.59691	0.550
92	30G 100K	0.02026	0.50021	0.59691	0.550
93	30G 100K	0.02026	0.50021	0.59691	0.550
94	Loading Dock	0.00825	0.50003	0.09075	0.277
95	50G 100K	0.02017	0.5002	0.56255	0.500
96	50G 100K	0.02017	0.5002	0.56255	0.500
97	50G 100K	0.02017	0.5002	0.56255	0.500
98	50G 100K	0.02017	0.5002	0.56255	0.500
99	50G 100K	0.02017	0.5002	0.56255	0.500
100	100G 100K	0.01527	0.50012	0.43834	0.529
101	100G 100K	0.01527	0.50012	0.43834	0.529
102	100G 100K	0.01527	0.50012	0.43834	0.529
103	100G 100K	0.01527	0.50012	0.43834	0.529
104	100G 100K	0.01527	0.50012	0.43834	0.529
105	100G 100K	0.01527	0.50012	0.43834	0.529
106	100G 100K	0.01527	0.50012	0.43834	0.529
107	100G 100K	0.01527	0.50012	0.43834	0.529
108	100G 100K	0.01527	0.50012	0.43834	0.529
109	100G 100K	0.01527	0.50012	0.43834	0.529
110	30G 100K	0.02026	0.50021	0.59691	0.550
111	30G 100K	0.02026	0.50021	0.59691	0.550
112	30G 100K	0.02026	0.50021	0.59691	0.550
113	30G 100K	0.02026	0.50021	0.59691	0.550
114	30G 100K	0.02026	0.50021	0.59691	0.550
115	30G 100K	0.02026	0.50021	0.59691	0.550
116	30G 100K	0.02026	0.50021	0.59691	0.550
117	30G 100K	0.02026	0.50021	0.59691	0.550

Table D-2. Summary of Persson model parameters for HMA slabs (continued)

Number	Surface ID	P(q)	S(q)	C(q)	H
118	30G 100K	0.02026	0.50021	0.59691	0.550
119	30G 100K	0.02026	0.50021	0.59691	0.550
120	50G 100K	0.02017	0.5002	0.56255	0.500
121	50G 100K	0.02017	0.5002	0.56255	0.500
122	50G 100K	0.02017	0.5002	0.56255	0.500
123	50G 100K	0.02017	0.5002	0.56255	0.500
124	50G 100K	0.02017	0.5002	0.56255	0.500
125	100L 100K	0.0142	0.5001	0.3857	0.501
126	100L 100K	0.0142	0.5001	0.3857	0.501
127	100L 100K	0.0142	0.5001	0.3857	0.501
128	100L 100K	0.0142	0.5001	0.3857	0.501
129	100L 100K	0.0142	0.5001	0.3857	0.501
130	100L 100K	0.0142	0.5001	0.3857	0.501
131	100L 100K	0.0142	0.5001	0.3857	0.501
132	100L 100K	0.0142	0.5001	0.3857	0.501
133	100L 100K	0.0142	0.5001	0.3857	0.501
134	100L 100K	0.0142	0.5001	0.3857	0.501

Table D-3. CRP measurements of surface texture and rubber properties at different speed for field test sections in Idaho

Test Section	CRP Microtexture (mm)	CRP Macrotecture (mm)	Speed (m/s)	Log Reduced Frequency (Hz)	E* (Mpa)	Hurst Exponent (H)
US30 MP383	0.2074	2.23	8.94	4.989	1.403	0.279
US30 MP383	0.2074	2.23	13.41	4.813	1.399	0.279
US30 MP383	0.2074	2.23	17.88	4.688	1.397	0.279
US30 MP383	0.2074	2.23	22.35	4.591	1.395	0.279
US30 MP383	0.2074	2.23	26.82	4.512	1.393	0.279
I15 MP08	0.1936	1.14	8.94	4.696	1.397	0.558
I15 MP08	0.1936	1.14	13.41	4.520	1.393	0.558
I15 MP08	0.1936	1.14	17.88	4.395	1.390	0.558
I15 MP08	0.1936	1.14	22.35	4.298	1.388	0.558
I15 MP08	0.1936	1.14	26.82	4.219	1.387	0.558
I15 MP23	0.1896	1.05	8.94	4.664	1.396	0.560
I15 MP23	0.1896	1.05	13.41	4.488	1.392	0.560
I15 MP23	0.1896	1.05	17.88	4.363	1.390	0.560
I15 MP23	0.1896	1.05	22.35	4.266	1.388	0.560
I15 MP23	0.1896	1.05	26.82	4.187	1.386	0.560
I15 MP32	0.1929	0.54	8.94	4.376	1.390	0.564
I15 MP32	0.1929	0.54	13.41	4.200	1.386	0.564
I15 MP32	0.1929	0.54	17.88	4.075	1.384	0.564
I15 MP32	0.1929	0.54	22.35	3.978	1.382	0.564
I15 MP32	0.1929	0.54	26.82	3.899	1.380	0.564
I15 MP78	0.2011	0.71	8.94	4.489	1.392	0.559
I15 MP78	0.2011	0.71	13.41	4.313	1.389	0.559
I15 MP78	0.2011	0.71	17.88	4.188	1.386	0.559
I15 MP78	0.2011	0.71	22.35	4.091	1.384	0.559
I15 MP78	0.2011	0.71	26.82	4.012	1.382	0.559
I15 MP96	0.2270	0.53	8.94	4.362	1.390	0.559
I15 MP96	0.2270	0.53	13.41	4.186	1.386	0.559
I15 MP96	0.2270	0.53	17.88	4.061	1.383	0.559
I15 MP96	0.2270	0.53	22.35	3.964	1.381	0.559

Table D-3. CRP measurements of surface texture and rubber properties at different speed for field test sections in Idaho (Continued)

Test Section	CRP Microtexture (mm)	CRP Macrotecture (mm)	Speed (m/s)	Log Reduced Frequency (Hz)	E* (Mpa)	Hurst Exponent (H)
I15 MP96	0.2270	0.53	26.82	3.885	1.380	0.559
I86 MP16	0.1905	0.57	8.94	4.396	1.390	0.280
I86 MP16	0.1905	0.57	13.41	4.220	1.387	0.280
I86 MP16	0.1905	0.57	17.88	4.095	1.384	0.280
I86 MP16	0.1905	0.57	22.35	3.998	1.382	0.280
I86 MP16	0.1905	0.57	26.82	3.919	1.380	0.280
US30 MP365	0.2006	0.85	8.94	4.571	1.394	0.551
US30 MP365	0.2006	0.85	13.41	4.395	1.390	0.551
US30 MP365	0.2006	0.85	17.88	4.270	1.388	0.551
US30 MP365	0.2006	0.85	22.35	4.173	1.386	0.551
US30 MP365	0.2006	0.85	26.82	4.094	1.384	0.551
US26 MP356	0.1885	1.22	8.94	4.726	1.397	0.550
US26 MP356	0.1885	1.22	13.41	4.550	1.394	0.550
US26 MP356	0.1885	1.22	17.88	4.425	1.391	0.550
US26 MP356	0.1885	1.22	22.35	4.328	1.389	0.550
US26 MP356	0.1885	1.22	26.82	4.249	1.387	0.550
US20 MP326	0.2065	0.50	8.94	4.341	1.389	0.552
US20 MP326	0.2065	0.50	13.41	4.165	1.386	0.552
US20 MP326	0.2065	0.50	17.88	4.040	1.383	0.552
US20 MP326	0.2065	0.50	22.35	3.944	1.381	0.552
US20 MP326	0.2065	0.50	26.82	3.864	1.379	0.552

Appendix E - Letters of Permission

Re: MDPI Contact Form: Permission to use manuscript

support@mdpi.com

Tue 5/7/2019 8:30 PM

To: Al Assi, Mohammad (alas9935@vandals.uidaho.edu) <alas9935@vandals.uidaho.edu>

Dear Mohammad,

Thank you for your email. As author of the paper and given that you are the owner of the copyrights, you are entitled to reproduce it in other publications. Please only remember to refer to the work properly.

Have a nice day.

Support

On 2019/5/8 6:26, Mohammad Al-Assi wrote:

> Hello,

>

> I am requesting permission to use my manuscript in my Ph.D. Dissertation.

> The manuscript was published in applied sciences

> Title: Evaluation of Adhesion and Hysteresis Friction of Rubber–Pavement
> System

> Appl. Sci. 2017, 7(10), 1029;

> <https://doi.org/10.3390/app7101029>

> Authors: Mohammad Al-Assi * and Emad Kassem

>

> Can you please advise on how to get this permission?

>

> Thank you

>

 Academic Books Permissions <mpkbookspermissions@tandf.co.uk>
Tue 5/7/2019 4:44 AM
Al Assi, Mohammad (alas9935@vandals.uidaho.edu) ✉

 T&F Generic Books Permissio...
41 KB

Dear Mohammad

9781138313095 | AM3P 2018 | Edn. 1 | Hardback | pp277-80

Further to your email, permission is granted for use of the above material in your forthcoming thesis, subject to the following conditions:

1. The material to be quoted/produced was published without credit to another source. If another source is acknowledged, please apply directly to that source for permission clearance.
2. Permission is for non-exclusive, English language rights, and covers **use in your thesis only**. Any further use (including storage, transmission or reproduction by electronic means) shall be the subject of a separate application for permission.
3. Full acknowledgement must be given to the original source, with full details of figure/page numbers, title, author(s), publisher and year of publication.

Kind regards

Annette Day
UK Books Permissions
www.tandf.co.uk



Taylor & Francis Group publishes Social Science and Humanities books under the Routledge, Psychology Press and Focal Press imprints. Our Science, Technology and Medical titles are published by CRC Press and Garland Science imprints.

If you require permission for the use of material from a Taylor & Francis book, please fill in the form below electronically. Any omissions may result in delay in processing your request. Do not leave any spaces blank. Handwritten forms cannot be accepted.

APPLICANT DETAILS

Applicant name	Mohammad Al-Assi
Company	University of Idaho
Address	875 Perimeter Dr MS Moscow, ID, USA 83844 Civil Engineering Department
Invoice Address (If different from above)	

Phone	+1 (208) 310- 4850
Email	Alas9935@vandals.uidaho.edu

REQUESTED MATERIAL

Please check the cover, spine and copyright page of the book. We do not keep physical copies of our books and are unable to check this material on your behalf.

Title	Advances in Materials and Pavement Prediction: Papers from the International Conference on Advances in Materials and Pavement Performance Prediction (AM3P 2018), April 16-18, 2018, Doha, Qatar
Author/Editor	Eyad Masad; Amit Bhasin; Tom Scarpas; Ilaria Menapace; and Anupam Kumar
Publisher/Imprint	CRC Press

ISBN (we categorically cannot process your request without this information)	9780429855795
Publication date & Edition	July 2018
Word Count - approximate	600
Chapter name, number, and chapter start and end pages	Improving pavement friction through aggregate blending, Section 11, Pages 277 - 280
Figure number (if applicable). Please	

include a photocopy of the figure (s) to be used	
Page Reference - start and end pages IMPORTANT	Pages 277 - 280
Any other information which may help identify the material	
Author's request to re-use their own material?	Yes

PROPOSED EXTRACT IN WHICH THE WORK IS TO BE USED

Your Publication Title and/or webpage name	Tire-Pavement interaction, Experimental Measurements and Modeling
--	---

Publisher of new work	Ph.D. Dissertation University of Idaho
Author/Editor	Mohammad Al-Assi
Website address and expected traffic (if applicable, <u>completing this field is mandatory if content is being uploaded to a website</u>)	
Will you be able to make this material secure so that it is not downloadable? (if applicable)	No
Language including translations	English

Distribution Territory	
Any other information, notes, comments, etc.	Ph.D. Dissertation

FOR PRINTED PUBLICATIONS

Proposed publication date	July 2019
Proposed price	N/A
Format (Hardback, Paperback)	
Print Run	
Description of your publication	Ph.D. Dissertation
Context in which the material would appear	Part of chapter in my dissertation

ELECTRONIC/E-book PUBLICATIONS

Title	
Authors	
Price	
1st year download forecast	

When you have provided as much information as possible, please email your completed form to mpkbookspermissions@tandf.co.uk including any attachments (for example, figures or tables) that are relevant to your application.

Important note:

Permissions requests currently have a processing time of up to **five weeks**, so please apply in good time. The process may take longer depending on the complexity of the request and any difficulties incurred whilst tracing records. We ask you to be patient during this process and to avoid sending repeated requests for information once you have received confirmation of receipt of your request form.

Under no circumstances are you entitled to assume consent on the basis of not having received a response within our or your own specified time frame, and no exceptions can be made to account for any pending print deadlines you yourself may face.